# INVESTIGATION OF FOULING MECHANISMS TO GUIDE THE DESIGN OF DIESEL ENGINE EXHAUST DRIVEN ABSORPTION HEAT PUMPS

A Thesis
Presented to
The Academic Faculty

by

Victor C. Aiello

In Partial Fulfillment
of the Requirements for the Degree
Master of Science in the
School of Mechanical Engineering

Georgia Institute of Technology
December 2016

# INVESTIGATION OF FOULING MECHANISMS TO GUIDE THE DESIGN OF DIESEL ENGINE EXHAUST DRIVEN ABSORPTION HEAT PUMPS

Approved by:

Dr. Srinivas Garimella, Advisor
School of Mechanical Engineering
*Georgia Institute of Technology*

Dr. William J. Wepfer
School of Mechanical Engineering
*Georgia Institute of Technology*

Dr. Peter Loutzenhiser
School of Mechanical Engineering
*Georgia Institute of Technology*

Date Approved: November 21, 2016

# ACKNOWLEDGEMENTS

I would first like to thank my advisor, Dr. Srinivas Garimella, for providing the opportunity to work on an intriguing and challenging research project. I am grateful for being given a balance of direction and autonomy that has allowed for an invaluable learning experience. I would also like to thank the members of the Sustainable Thermal Systems Lab for their unique willingness to provide technical guidance and support. I would particularly like to thank Marcel Staedter for his mentorship and Girish Kini for his incredible dedication to this research project. It has been an honor to work with and learn from such an inspiring and hard working group of people. Lastly, I would like to thank my family, for this accomplishment would not have been possible without their unwavering support.

# TABLE OF CONTENTS

# LIST OF TABLES

# LIST OF FIGURES

xiii

# LIST OF SYMBOLS AND ABBREVIATIONS

**Symbols**

| | |
|---|---|
| a | Atoms of Carbon |
| $A$ | Area, $m^2$ |
| $A_E$ | Specific optical extinction, $m^2$ $kg^{-1}$ |
| b | Atoms of Hydrogen |
| $C$ | Concentration by volume, $kg$ $m^{-3}$ |
| $C_f$ | Fanning friction factor |
| $c_p$ | Specific heat, $J$ $kg^{-1}$ $K^{-1}$ |
| $C_v$ | Flow Coefficient |
| $C_r$ | Heat capacitance ratio |
| $D$ | Diameter, m |
| $d$ | Molecular diffusivity, $m^2$ $s^{-1}$ |
| $e$ | Emissivity |
| $E_{th,\infty}$ | Thermophoretic deposition efficiency |
| $f$ | Darcy friction factor |
| F | View Factor |
| $g$ | Gravitational acceleration, $m$ $s^{-2}$ |
| $h$ | Heat transfer coefficient, $W$ $m^{-1}$ $K^{-1}$ |
| $k$ | Thermal conductivity, $W$ $m^{-1}$ $K^{-1}$ |
| $K$ | Thermophoretic Coefficient |
| $K_g$ | Mass Transfer Coefficient, $kg$ $m^{-2}$ $s^{-1}$ |
| $K_L$ | Loss Coefficient |
| $Kn$ | Knudsen Number |
| $K_p$ | Wedgemeter flow constant |
| $L$ | Length, m |
| $M$ | Molar mass, $kg$ $mol^{-1}$ |
| $\dot{m}$ | Mass flow rate, $kg$ $s^{-1}$ |
| $\dot{m}_g$ | Condensation rate, $kg$ $s^{-1}$ |
| n | Number |
| $Nu$ | Nusselt number |
| $NTU$ | Number of transfer units, $K^{-1}$ |
| $P$ | Pressure, Pa |
| $p$ | Pitch, m |
| Pr | Prandtl number |
| $\dot{Q}$ | Heat transfer rate, W |
| $r$ | Radius, m |
| $R$ | Thermal resistance, $K$ $W^{-1}$ |
| $R'$ | Thermal resistivity, $K$ $W^{-1}$ $m^{-1}$ |

| $r_{TD}$ | Turn down ratio |
| Re | Reynolds number |
| $Ro$ | Roshko number |
| $R_u$ | Universal gas constant, J mol$^{-1}$ K$^{-1}$ |
| $Sc$ | Schmidt number |
| $Sh$ | Sherwood |
| $St$ | Strouhal number |
| $St_m$ | Stanton number for mass transfer |
| $T$ | Temperature, $^{o}$C |
| $UA$ | Overall thermal conductance, W K$^{-1}$ |
| $V$ | Velocity, m s$^{-1}$ |
| $\dot{V}$ | Volumetric flow rate, m$^3$ s$^{-1}$ |
| $\dot{W}$ | Work, W |
| $x$ | Concentration by mass |
| $y$ | Mass fraction |
| $\tilde{y}$ | Mole fraction |

## Greek Symbols

| $\alpha$ | Thermal diffusivity, m$^2$ s$^{-1}$ |
| $\alpha_M$ | Linear Expansion Coefficient, K$^{-1}$ |
| $\beta$ | Volumetric Expansion Coefficient, K$^{-1}$ |
| $\Delta$ | Differential |
| $\eta$ | efficiency |
| $\varepsilon$ | Roughness, m |
| $\gamma$ | Specific Gravity, kg m$^{-3}$ |
| $\lambda$ | Wavelength, m |
| $\mu$ | Dynamic Viscosity, kg m$^{-1}$ s$^{-1}$ |
| $\upsilon$ | Kinematic Viscosity, m$^2$ s$^{-1}$ |
| $\omega$ | frequency |
| $\varphi$ | Stoichiometric ratio |
| $\rho$ | Density, kg m$^{-3}$ |
| $\sigma_{SB}$ | Stefan-Boltzmann Constant, W m$^{-2}$ K$^{-4}$ |
| $\theta$ | Influence Coefficient |

## Subscripts

| amb | Ambient |
| b | Bulk |
| c | Coolant |
| conv | Convection |
| cs | Concentrated solution |
| cwhx | Chilled water heat exchanger |
| dep | deposited |
| des | Desorber |
| ds | Dilute Solution |
| ex | Exhaust |

| | |
|---|---|
| elec | Electric |
| ent | Entrance |
| exit | Exit |
| fo | Fully open |
| foul | Fouling |
| h | Hydraulic |
| HX | Heat exchanger |
| I | Inner |
| in | In |
| ins | Insulation |
| int | Interphase |
| IT | Inner tube |
| lm | Log-mean |
| loss | loss |
| l | Liquid |
| maj | Major |
| meas | Measured |
| min | Minor |
| O | Outer |
| Opac | Opacimeter |
| OT | Outer tube |
| out | Out |
| PM | Particulate matter |
| prod | Products |
| pt | Per tube |
| rad | Radiation |
| s | Solution |
| Surf | Surface |
| tc | Thermocouple |
| TM | Turbine meter |
| tot | Total |
| v | vapor |
| wm | wedgemeter |
| x | Cross-sectional |

# SUMMARY

Waste-heat recovery systems that utilize diesel engine exhaust to provide useful forms of energy improve overall fuel utilization and address concerns related to energy security, energy cost, and climate change. The absorption heat pump is particularly useful in applications in which heating or cooling is required in combination with the work output of a diesel engine. A challenge in the performance of these systems arises overtime from the fouling of the heat exchanger that couples to the exhaust gas. While previous researchers have investigated diesel exhaust fouling mechanisms, they do not range the heat exchanger geometries and fluid conditions of an absorption heat pump. A detailed investigation into the fouling mechanisms in a 2.71 kW cooling capacity diesel engine exhaust driven absorption heat pump has been performed in the present study.

An experimental facility was designed to simulate the desorber, the component that couples the diesel engine exhaust to the working fluid pair in the heat pump, with a single-tube 12.7 mm in diameter and 285 mm in length. The exhaust from a 10 kW diesel generator was used in the experiments, and the use of a load bank allowed for variation in engine operation, exhaust temperature, and exhaust composition. Experiments were performed for generator loads ranging from 60 to 100%, exhaust flow rates from 0.8 to 2.6 g s$^{-1}$, coupling fluid inlet temperatures from 95.3 to 129.8 °C, and coupling fluid outlet temperatures from 160.4 to 182.3 °C. Fouling effects were most severe at a coolant inlet temperature of 95.3 °C, coolant outlet temperature of 160.4 °C, and 100% generator load. At these conditions, the fouling thermal resistance reached a steady state and was approximately 70% of the total thermal resistance ($R_{foul,1} = 2.85 \pm 0.11 \ K \ W^{-1}, R_{tot,1} =$

$3.99 \pm 0.03 \ K \ W^{-1}$). The fouling layer was 889 μm thick with a conductivity of 0.0362 W m$^{-1}$K$^{-1}$. The exhaust pressure drop at steady-state was 3.25 times greater than the initial value before fouling occurred.

These findings were used in a segmented heat transfer and thermodynamic model to optimize the design of the desorber. The desorber was fabricated and a fouling experiment was performed. The fouling resistances in the desorber experiment were slightly greater than those in the single-tube experiment at the same conditions. This resulted in a desorber heat duty 9.6% less than the heat duty predicted by the desorber model ($\dot{Q}_{des,exp} = 3.72 \pm 0.26, \dot{Q}_{des,mod} = 4.09 \ kW$). The measured exhaust pressure drop was 2.6% greater than the model predicted value and did not exceed the maximum allowable back pressure on the diesel engine. The fouling results and design methodology of this study may be used for the design of diesel engine exhaust coupled heat exchangers for a wide range of waste-heat recovery applications.

# CHAPTER 1.    INTRODUCTION

Growing concerns related to energy security and climate change have prompted efforts to reduce the reliance on fossil fuels for energy production. While strides have been made towards increasing energy production from renewable and non-carbon emitting sources in the last several decades, energy production from fossil fuels still constitutes 81% of total production in the United States (EIA, 2013). In addition, approximately two-thirds of the primary energy released in the combustion of fossil fuels, typically for the conversion of thermal-to-mechanical energy, is rejected as waste-heat. This waste-heat can be utilized in a variety of applications that do not require high grade thermal energy, including water heating, space conditioning, and refrigeration (Little and Garimella, 2011). Rattner and Garimella (2011) demonstrated that waste-heat recovery has the potential to reduce US primary energy demand by 12% and $CO_2$ emissions by 13%.

Space conditioning and refrigeration in the commercial and residential sectors constitute a significant portion (18%) of US energy consumption, and are most frequently provided through the use of vapor-compression systems (EIA, 2013). Vapor-compression systems require high-grade mechanical or electrical energy input, which contributes directly to increased consumption of fossil fuels and emission of greenhouse gases. These systems also use synthetic refrigerants, some of which have high global warming potential. One of the primary alternatives to the vapor-compression system is the absorption heat pump, a thermally driven system that can utilize mid- to low-grade thermal energy to provide cooling or heating. Substituting electrically driven vapor-compression systems with absorption heat pumps that use waste-heat to drive them would significantly reduce

fossil fuel consumption. For example, space heating, water heating, and air conditioning constitute 56.7% of residential energy consumption in the United States (EIA, 2013). Absorption heat pumps could utilize low-grade thermal energy from a variety of sources to provide these household services and reduce residential energy demand. In addition to the lower-grade energy input, absorption heat pumps use natural refrigerants with zero global warming potential. This makes absorption heat pumps attractive as a replacement for the vapor-compression system when waste-heat sources are available in sufficient quantities.

## 1.1 Absorption Heat Pump

A schematic of a simple absorption heat pump is shown in Figure 1.1. The working fluid pair consists of a refrigerant and an absorbent. A concentrated solution of the refrigerant absorbed in the solution mixture [1] is supplied at a high pressure to the desorber. The thermal energy from a waste-heat source is transferred to the desorber, often referred to as a vapor generator, to separate the refrigerant from the absorbent. The refrigerant vapor [2] then passes through the condenser, where heat is transferred to the ambient and the refrigerant exits as a liquid [3]. The liquid refrigerant then flows through an expansion valve [4] and the evaporator [5], where heat is transferred from the conditioned space to evaporate the refrigerant. Meanwhile, a dilute solution of refrigerant in the absorbent exits the desorber [6] and flows through the solution heat exchanger (SHX) where heat is transferred to the concentrated solution [7]. The dilute solution then passes through an expansion valve [8] and recombines with the refrigerant in the absorber where heat is rejected to the ambient [9]. The concentrated solution is pressurized by the pump [10] and gains heat in the SHX before completing the cycle. The condenser, expansion
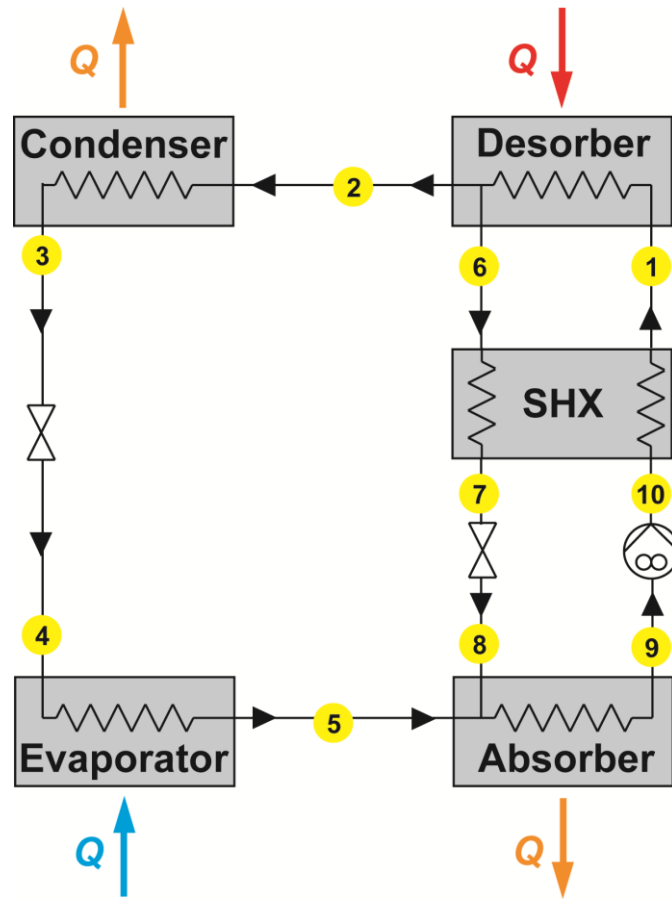
**Figure 1.1: Schematic of simple absorption heat pump**

valve, and evaporator replicate the components in a vapor-compression system. The mechanically or electrically driven compressor in a vapor-compression system is replaced by a thermal compressor that consists of the absorber, desorber, SHX, and pump. Pressurizing the liquid in a pump instead of compressing a vapor reduces the electrical consumption by an order of magnitude in comparison to vapor-compression systems. In practice, a single-effect absorption heat pump may include an additional recuperative heat exchanger and a rectifier to purify the refrigerant and improve system *COP*.

The additional heat exchangers in an absorption heat pump typically cause it to be larger, heavier, and more expensive. Historically, these barriers against implementation

are overcome when abundant waste-heat sources are available, such as in large-scale industrial processes. When a large amount of waste-heat is available, the additional size and cost of the system is overcome by the significant energy savings gained by waste-heat recovery. In contrast, the additional size and cost of absorption heat pumps has limited application in situations with lower quantities of waste-heat from sources that are highly distributed. Recent advances in miniaturized heat exchanger technology, resulting in greater heat fluxes, has renewed interest in the use of absorption heat pumps for use with distributed waste-heat sources. Determan and Garimella (2012) demonstrated a thermally activated absorption heat pump for miniaturized and mobile applications. The heat exchangers required for the absorption cycle were integrated into a single monolithic block with dimensions of $200 \times 200 \times 34$ mm and a mass of 7 kg. The heat pump delivered up to 300 W of cooling with a maximum *COP* of 0.4. The significant reduction in system size and weight was made possible through the use of microscale fluid passages that yield a several-fold enhancement in heat and mass transfer. The scalability of this technology was shown by Garimella *et al.* (2016) with a 3.2 kW cooling capacity gas-fired absorption heat pump with a cycle COP of 0.53. This absorption heat pump utilized similar monolithic microchannel heat and mass exchanger design principles, resulting in high heat fluxes and minimized system size and weight. The primary absorption components in the system made up only 35% of the total system size, while the rest of the space required was used for fluid routing and ambient heat rejection. This system demonstrated a ten-fold increase in cooling capacity over the proof of concept study by Determan and Garimella (2012), exhibiting the capability of the technology to effectively utilize a wide range of thermal energy sources.

## 1.2 Waste-heat Recovery Applications

Compact waste-heat driven absorption heat pumps have applications in a variety of energy sectors. Rattner and Garimella (2011) determined that only 6% of the input fuel for cars would be sufficient to serve as a source of waste-heat for sorption-based vehicle air-conditioning. This would save approximately 5% of total vehicle fuel consumption, as predicted by Lambert and Jones (2006). Refrigerated trucking is another application in transportation that shows significant potential for absorption heat pump technology. According to Tassou *et al.* (2009), refrigeration units used in food transport range in cooling capacity from 3.8 to 14.5 kW depending on the refrigerated volume, transport distance, and food temperature requirements. Waste heat in the exhaust from trucks used to haul refrigerated payloads ranges from 40 to 140 kW, which exceeds the necessary heat input in all cases for an absorption heat pump with a capacity corresponding to the respective cooling requirements for different trucks.

Absorption heat pumps also have a number of applications for waste-heat recovery in small-scale stationary power generation. Generators are often used in remote areas by developing countries and the military as a primary source of power generation. The use of these generators is often limited by the cost and availability of fuel transportation to the remote location. Replacing electrically driven vapor-compression systems for space cooling with an absorption heat pump that utilizes waste-heat from an on-site generator can significantly reduce fuel consumption. Keinath *et al.* (2012) demonstrated the feasibility of this concept with a 2 kW cooling capacity ammonia-water absorption heat pump that utilized the waste-heat in the exhaust stream of an 8 kW diesel generator.

Applications of waste-heat driven absorption heat pumps in transportation or small-scale power generation both utilize the waste-heat rejected from internal combustion engines. Rattner and Garimella (2011) estimated that 45% of the input energy in an internal combustion engine is rejected in the engine coolant at a temperature of 85°C and 25% of the input energy is released in the exhaust at a temperature of 400°C. The higher temperature of the exhaust makes it more suitable for the thermal input to an absorption heat pump in comparison with the engine coolant. Extraction of the thermal energy from the engine exhaust requires a heat exchanger that couples the exhaust to the working fluid pair in the heat pump, either directly or through an intermediate heat transfer fluid. Exhaust gases contain particulate matter and hydrocarbons that have the potential to be deposited on the heat transfer surface, resulting in the buildup of a fouling layer that can negatively impact heat exchanger performance. Particulate matter emission factors from diesel engines range from 30 to 50 mg km$^{-1}$, which is greater than that from spark-ignition engines that range from 0.5 to 13 mg km$^{-1}$ (Harris and Maricq, 2001). For this reason, fouling caused by diesel exhaust tends to be much more severe. This increased fouling is significant as diesel fuel makes up 25% of total fuel consumption in transportation in the United States (EIA, 2013), and an even a greater percentage when considering the refrigerated trucking and small-scale power generation markets alone.

Fouling due to diesel engine exhaust has been shown to have a significant effect on exhaust gas recirculation (EGR) cooler performance. Lance *et al.* (2009) found that an exhaust tube 8.11 mm in inner diameter exposed to diesel exhaust for 12 hours had a fouling layer thickness of 0.410 mm and thermal conductivity of 0.041 W m$^{-1}$ K$^{-1}$. Using these values to compare the conductive resistance of the fouling layer and convective

resistance of exhaust at a Reynolds number of 5,000 for a one-meter-long tube, the fouling resistance is 0.41 K W$^{-1}$ while the exhaust resistance is 0.39 K W$^{-1}$. Neglecting the presence of a fouling layer, the exhaust resistance is the greatest in an EGR cooler by an order of magnitude; therefore, addition of the fouling resistance results in a doubling of the resistance in a heat exchanger. For this reason, it is crucial that fouling be considered in the design of exhaust-coupled heat exchangers as it requires a significant increase in exhaust-side heat transfer area.

As will be discussed in Chapter 2, a number of researchers have investigated fouling mechanisms and their effect on the performance of EGR coolers. In their research they have found that the degree to which fouling occurs is highly dependent on geometry, exhaust temperature, exhaust composition, exhaust velocity, and tube temperature. All of these parameters differ in the exhaust-coupled heat exchanger of an absorption heat pump as compared to that in an EGR cooler. To maintain the compactness of the absorption heat pump that enables its use in the small-scale applications discussed previously, it is important that the exhaust-coupled heat exchanger be designed as compactly and efficiently as possible. Consequently, it is critical to determine the effects of fouling that are specific to the conditions present in an absorption heat pump and to design the desorber accordingly.

### 1.3 Scope of Work

The present work investigates the fouling mechanisms in diesel engine exhaust-coupled heat exchangers. The results guide the design of a direct exhaust-coupled desorber in a 2.71 kW ammonia-water absorption heat pump. The heat pump of interest utilizes waste-heat from diesel generator exhaust for combined cooling and power at military

forward operating bases.  A cycle model is used to predict the fluid properties of the exhaust and ammonia-water working pair within the desorber at a variety of heat pump and generator operating conditions.  The cycle model output parameters are subsequently used in a heat transfer and thermodynamic model to size and select components for an experimental facility that measures the effect of fouling on the thermal resistance and exhaust pressure drop of the desorber.  The facility simulates the desorber as a series of tube-in-tube heat exchangers that replicate the geometry and fluid conditions within the desorber.  A 10 kW diesel generator is used to produce the exhaust for the fouling experiments.  A resistive load bank is connected to the generator to allow variation in engine operating conditions, exhaust temperature, and exhaust composition.

Steady state experiments are performed to measure fouling thermal resistance and exhaust pressure drop for a wide range of coolant and exhaust temperatures, as well as exhaust composition and flow rates.  The experiments are performed for ten hours to ensure differences between the data points can be resolved and characterized, allowing for determination of the worst case heat pump and generator operating conditions with respect to fouling.  These conditions are used in a number of transient experiments that investigate the effect of heat pump and generator transients on fouling.  Two transient situations are considered for the purposes of this study: the first being when the generator is already running steady and exhaust is directed to the heat pump, and the second when the generator and heat pump start-up simultaneously.   With worst case steady state and transient conditions determined, the most severe effects of fouling are quantified by performing a final experiment, which allows for the fouling thermal resistance and exhaust pressure drop to approach a constant measured value.

In addition to measuring thermal resistance and exhaust pressure drop, exhaust tubes are removed from the facility after each experiment to perform ex-situ analysis of the deposit layer. The fouled exhaust tubes are split across the tube cross section and 50× magnification images of the tubes are taken to measure fouling layer thickness and calculate the effective thermal conductivity. This information, along with predicted particulate matter and hydrocarbon deposition rates, are used to develop an understanding of the mechanisms that most significantly affect fouling. The thickness and thermal conductivity results may be used in the design of exhaust coupled heat exchangers with similar geometries for a wide-range of engine exhaust waste-heat recovery applications.

The results of the fouling experiments are used in a heat transfer model of the full-scale desorber, at which point a parametric study of the number of parallel tubes and number of tube passes in the shell-and-tube style desorber is performed to select a design that meets performance requirements after fouling has occurred. The desorber heat transfer rates, refrigerant generation rates, refrigerant concentrations, and exhaust pressure drop are compared in the selection process. The size and weight of the most promising designs are also compared for feasibility within the available heat pump envelope. The desorber design that meets the performance requirements with the smallest size and lowest weight is fabricated for testing. This study is concluded by performing an experiment with the desorber at the most severe fouling conditions to validate the results of the single-tube experiments and the performance of the desorber as predicted by the computational model.

### 1.4 Organization of Thesis

The organization of the subsequent chapters of this thesis are as follows:

- Chapter 2 provides a review of diesel engine exhaust waste-heat recovery systems, diesel engine emissions, fundamental diesel exhaust fouling investigations, and component-level diesel exhaust fouling investigations.

- Chapter 3 describes the modeling framework for the single-tube experimental facility and the design and selection processes for facility components.

- Chapter 4 details the data reduction procedure for the single-tube experiments. The experimental results are presented along with a detailed analysis of the various fouling layer deposition mechanisms.

- Chapter 5 includes the desorber modeling effort and the selection process for the desorber design. It also contains the data reduction and results summary for the desorber test with a comparison to the single-tube results and the desorber computational model predictions.

- Chapter 6 summarizes the major findings and the conclusions of the present study and provides recommendations for further research.

# CHAPTER 2.    LITERATURE REVIEW

A review of the literature relevant to diesel engine exhaust waste-heat recovery systems, diesel engine emissions, fundamental diesel exhaust fouling investigations, and component level diesel exhaust fouling investigations is presented in this chapter.

## 2.1 Engine Exhaust Waste-Heat Recovery Systems

The exhaust gas from internal combustion engines contains a large fraction of the energy released in combustion.  In their review of relevant research, Saidur *et al.* (2012) found that 30-40% of the thermal energy of combustion is wasted in the engine exhaust. A range of technologies has been demonstrated to be effective in recovering the waste-heat of engine exhaust.

The Rankine cycle and the Organic Rankine cycle are of particular interest for vehicle applications in which the power output from the expansion device is directly coupled to the engine drive shaft.  A thorough review of these systems was performed by Wang *et al.* (2011).  Several strategies for extracting waste-heat from the engine coolant and exhaust were described, and it was found that Rankine cycles reduce brake specific fuel consumption by about 10%.  The Kalina cycle has also been analyzed for waste-heat recovery applications in transportation and power generation. Bombarda *et al.* (2010) compared Kalina and Organic Rankine cycles driven by the exhaust gas from a diesel generator.  The Kalina cycle had a heat recovery efficiency and electric power output of 17.5% and 1615 kW respectively, which was similar to 17.3% and 1603 kW for the Organic Rankine cycle.  The higher overall heat recovery efficiency of the Kalina cycle, despite

lower thermodynamic cycle efficiency, was due to the temperature glide of the $NH_3$-$H_2O$ working fluid in the exhaust-coupled heat exchanger.

Thermoelectric generators have also shown promise in converting the exhaust waste-heat directly to electricity for powering auxiliary vehicle components. In a review of these technologies, Saidur *et al.* (2012) found that thermoelectric generators were favorable due to their high reliability and a lack of moving parts. The downside to this technology is that it has a thermal efficiency typically less than 4%, which is far less than that of the Rankine cycle in these applications.

Adsorption and absorption heat pump technologies have been investigated for applications that have heating or cooling requirements in addition to engine work output. An adsorption system was studied by Wang *et al.* (2004) for making ice on fishing boats. They tested physical, chemical, and composite adsorption pairs, and determined that the composite pair had a cooling capacity 10 and 1.4 times greater than the physical and chemical adsorption pairs, respectively. The superior performance of the composite adsorption pair was attributed to the addition of activated carbon to the adsorbent, which has a porous structure that promotes mass transfer. An oil burner was used to simulate the diesel engine exhaust, which was coupled to a boiler that provided energy input to the desorption beds. Horuz (1999) modified a 10 kW commercial natural gas fired absorption chiller to couple it to the exhaust from a 6 L diesel engine. At high engine load, the absorption chiller was able to reach rated capacity. Substituting the absorption chiller for a vapor compression system in the vehicle eliminated the need for a refrigerant compressor, decreased fuel consumption, and reduced atmospheric pollution; however, the engine efficiency decreased by 2% due to the additional back pressure.

To address the issue of reduced engine performance, Talbi and Agnew (2002) developed a model to evaluate the overall efficiency of a diesel engine coupled with an exhaust driven absorption chiller. Several arrangements were analyzed such that cooling from the chiller could be used for a combination of air conditioning, charge pre-cooling, and intercooling to improve engine efficiency. It was determined that the use of both inter-cooling and air-conditioning had the greatest overall fuel utilization efficiency of 60.6%, compared to 58.2% for a system with only air-conditioning.

Keinath *et al.* (2012) modeled a single-effect ammonia-water absorption heat pump that utilized the exhaust waste-heat from an 8 kW diesel generator. It was assumed that 15% of the thermal energy of combustion was rejected through the exhaust at a temperature of 398°C and flowrate of 0.05 kg s$^{-1}$. The system was predicted to have a cooling capacity of 2.167 kW at a COP of 0.695 and a heating capacity of 5.039 kW at a COP of 1.66. A summary of the diesel engine waste-heat recovery systems is shown in Table 2.1.

A common component in all of these waste-heat recovery technologies is the heat exchanger that couples to the exhaust gas. A review of exhaust gas coupled heat exchangers was performed by Hatami *et al.* (2014). They found that double tube, shell and tube, heat pipe, helical, and plate heat exchangers have all been used to extract energy from diesel exhaust. Several enhancements such as twisted tape, finned tubes, baffles, and foamed inserts have also been used. In general, it was determined that finned shell-and-tube designs were the most effective due to minimal exhaust-side pressure drop and comparable heat transfer performance. A commercially available shell-and-tube heat exchanger was optimized by Bari and Hossain (2013) to improve exhaust heat recovery

**Table 2.1: Diesel engine waste-heat recovery system investigations**

| Author(s) (Year) | Type of Investigation | Type of System | Purpose |
|---|---|---|---|
| Wang et al. (2011) | Review | Rankine Cycle | Increase Brake Power for IC Engines |
| Saidur et al. (2012) | | Thermoelectrics, Rankine Cycle | Generate Electricity, Increase Brake Power for On-road Vehicles |
| Talbi and Agnew (2002) | Modeling | Absorption Chiller | AC, Inter-cooling, and Pre-cooling for On-road Vehicles |
| Bombarda et al. (2010) | | Rankine Cycle, Kalina Cycle | Electric Power Generation from Diesel Engine Exhaust |
| Keinath et al. (2012) | | Absorption Heat Pump | Military Generators with Combined Cooling, Heating, and Power |
| Horuz et al. (1999) | Experimental | Absorption Chiller | AC for On-road Vehicles |
| Wang et al. (2004) | | Adsorption Chiller | Ice Production on Fishing Vessels |

from a diesel engine. By manipulating shell diameter, the number of tubes, tube diameter, and tube length, the useful exhaust heat recovery was increased from 16% to 23.7%.

Mavridou *et al.* (2010) developed a numerical algorithm to evaluate the performance of shell-and-tube heat exchangers with smooth, dimpled, or finned circular tubes and compared it to that of plate-and-fin heat exchangers with plain fins or metal foam inserts. The algorithm considered the fouling resistance on the exhaust side of the heat exchangers and used a value of $1.76 \times 10^{-3}$ $m^2$ $K$ $W^{-1}$ for all of the heat exchangers evaluated. The analysis found that finned tubes were the most effective of all the shell-and-tube heat exchangers, reducing weight and pressure drop by 51% and 45%, respectively. The plate-and-fin heat exchanger with a 40 ppi metal foam insert was the most effective overall with a 38% reduction in volume and a twofold reduction in weight.

This makes the heat exchanger extremely beneficial for vehicle applications where weight and size are critical; however, there was a 96% increase in pressure drop that negatively affects engine performance.

A design and modeling analysis of a heat recovery system for an ammonia-water absorption refrigeration system was performed by Fernández-Seara *et al.* (1998). The system was designed to extract the waste-heat from diesel engine exhaust onboard trawler chiller fishing vessels and consists of a gas-to-liquid economizer coupled by a synthetic oil to the desorber of the absorption refrigeration plant. The exhaust flowed over the shell side of the economizer at an inlet temperature of 300ºC with synthetic oil on the tube side at a maximum temperature of 190ºC. A critical factor in the sizing of the economizer was the fouling factor on the exhaust side. Fin spacing was limited to 5 mm to prevent blockage, and a fouling heat transfer resistance of 21.23 $m^2$ K $kW^{-1}$ was implemented. These values were taken from the results of Semler *et al.* (1982), who evaluated the fouling of a finned-tube diesel flue gas heat recuperator. A summary of investigations into exhaust gas coupled heat exchangers is provided in Table 2.2.

The use of waste-heat recovery technologies has been shown to dramatically improve the overall efficiency of diesel engines in transportation, power generation, and combined cooling, heating, and power applications. However, the fouling of the heat exchanger that couples the exhaust to the waste-heat recovery system can significantly reduce system performance. Kuosa *et al.* (2007) modeled the impact of fouling on the performance of a Stirling engine that is driven by the combustion of solid biomass fuels. A parametric study in which the fouling resistance of the exhaust gas coupled heat exchanger was varied from 0 to 40 $m^2$ K $kW^{-1}$ was performed. Over this range of fouling

**Table 2.2: Exhaust gas coupled heat exchangers for waste-heat recovery**

| Author(s) (Year) | Type of Investigation | Type of WHR System | Heat Exchanger Design | Features |
|---|---|---|---|---|
| Hatami *et al.* (2014) | Review | Thermoelectrics, Rankine Cycle | Double tube, Shell and tube, Plate | Twisted Tape, Finned Tube, Foam Insert |
| Fernández-Seara *et al.* (1998) | Modeling | Absorption Chiller | Shell and Tube | Fins |
| Mavridou *et al.* (2010) | | Rankine Cycle | Shell and Tube, Plate | Fins, Metal Foam Insert |
| Bari and Hossain (2013) | Experimental | Rankine Cycle | Shell and Tube | Plain Tube |

factors, the brake power output of the engine decreased from 3.2 kW to 2.2 kW, respectively. While a few researchers (Mavridou *et al.* (2010); Fernández-Seara *et al.* (1998); Kuosa *et al.* (2007)) have considered a fouling resistance in exhaust coupled heat exchanger design, no efforts were taken to design the heat exchanger such that fouling was minimized. Likewise, fouling varies widely based on exhaust temperature, composition, heat exchanger geometry, and coupling fluid temperatures, but these factors were not thoroughly considered by previous researchers in their selection of fouling resistance values. This could result in exhaust gas coupled heat exchangers that are significantly over or under sized. The viability of waste-heat recovery systems often depends on cost effectiveness and compactness; therefore, accurate sizing of the exhaust-coupled heat exchanger is critical.

**2.2 Diesel Generator Emissions**

The concentration of emissions in diesel generator exhaust, particularly unburned hydrocarbons and particulate matter, has a significant effect on fouling in exhaust-coupled heat exchangers. For this reason, it is important to review the emissions from diesel generators so that the investigations in this study are representative. Diesel generator emissions are also highly dependent on the type of fuel used. To design an exhaust gas coupled desorber that meets the requirements for a wide range of applications, the effect of fuel on engine emissions has also been considered.

*2.2.1    In-use Diesel Generators*

Engine emissions from 18 in-use diesel back-up generators with capacities from 60-2000 kW were measured by Shah *et al.* (2006) using CE-CERT's Mobile Emissions Laboratory (MEL). All of the generators used a California no. 2 diesel fuel with a sulfur concentration of 500 parts per million by weight (ppmw). Diesel fuel is classified as low sulfur diesel for concentrations less than 500 ppmw and further classified as ultra-low sulfur diesel for concentrations of 15 ppmw or less. Ultra-low sulfur fuel has been implemented in the US for all on-road uses since 2010. Tests of each generator were conducted over the five mode cycle specified in the CFR for non-road compression ignition engines. Emission factors were calculated by a weighting of the mass emissions at each load, with higher weight given to mid-load operation and lower weight going to low and high load operation. In general, particulate matter, nitrous oxide, and total hydrocarbon emission factors were found to be greatest at low loads, decrease at mid-loads, and slightly increase at high-load. Generators with lower capacities had greater emission factors, which

is a result of more lenient emission regulations.  The average emission factors of all generators tested for particulate matter and total hydrocarbons were found to be 0.48 g kWh$^{-1}$ and 0.22 g kWh$^{-1}$, respectively.

Fuel-based emissions factors of 14 military diesel generators from 10 to 100 kW capacity were measured by Dongzi *et al.* (2009).  Diesel generators are widely used in the military to provide electricity to weapon systems, communications, and aviation ground support. Measurements of gaseous and particulate matter concentrations were made with the Desert Research Institute's In-Plume Emissions Test Stand.  The fuel used was either California no. 2 diesel with sulfur contents of 139 to 148 ppmw or JP-8 with sulfur contents of 311 to 349 ppmw.  Emission factors were similarly weighted based on engine load, and were reported on a fuel basis.  The fleet average emission factors for particulate matter and hydrocarbons were 1.2 g kgfuel$^{-1}$ and 11 g kgfuel$^{-1}$, respectively.  Using a brake specific fuel consumption of 9899 kJ kWh$^{-1}$ and a heating value of 44,889 kJ kg$^{-1}$, the particulate matter and hydrocarbon emission factors are converted to 0.26 g kWh$^{-1}$ and 2.43 g kWh$^{-1}$. These values are slightly greater than the values reported by Shah *et al.* (2006), but they still meet AP-42 emission standards for generators with a capacity less than 441 kW. During a cold start, emission factors were found to be higher than in steady operation, as much as 7 times higher for unburned hydrocarbons.  This could be an important factor in the fouling of exhaust gas coupled heat exchangers.

### 2.2.2    *Effect of Fuel Type*

The effect of fuel sulfur content and engine load on particulate matter emissions of non-road diesel engines was investigated by Saiyasitpanich *et al.* (2005).   Exhaust particulate measurements of a Generac 80 kW diesel generator at loads of 0, 25, 50 and 75

kW for three fuels of various sulfur contents were made. Exhaust particulate matter concentrations over the load range were found to be 15.6 to 36.8 mg m$^{-3}$, 10.2 to 31.6 mg m$^{-3}$, and 3.9 to 18 mg m$^{-3}$ for fuels containing 3700, 2100, and 500 ppm sulfur, respectively. A two-fold increase in particulate matter emissions was measured over the range of fuel sulfur content in this study.

Yost *et al.* (1996) compared the engine exhaust emissions from a GM 6.2L diesel engine for low sulfur diesel fuel to that of JP-8 containing various amounts of sulfur. The JP-8 fuel contained 600 ppmw sulfur and was doped to attain 1100 and 2600 ppmw, while the low sulfur diesel contained 350 ppmw sulfur. Tests were performed with a transient load command cycle that enabled a constant brake mean effective pressure irrespective of fuel type. The study showed lower unburned hydrocarbon emissions than the ultra-low sulfur diesel for all JP-8 fuels except the 600 ppmw; however, it was suspected that this was a result of engine oil consumption not yet stabilizing. All of the JP-8 fuels also produced less particulate matter emissions than the ultra-low sulfur diesel. They project that the particulate matter emissions of ultra-low sulfur diesel are more than that of JP-8 with sulfur content up to 3000 ppmw, which is the specified limit of the military for JP-8 sulfur content.

Diesel engine emissions for a wide range of on- and off-road applications were measured by Durbin *et al.* (2007) for ultra-low sulfur diesel, biodiesel blends, and JP-8. The applications included two medium-duty trucks, two Humvees, a heavy-duty diesel truck, a bus, two generators, a forklift, and an airport tow vehicle. A fleet wide average of emissions per kilogram of fuel used was compared for ultra-low sulfur diesel and a 20% blend of yellow-grease biodiesel. The comparison showed that the hydrocarbon and

particulate matter emissions of the biodiesel were 8.6% and 9.2% less than that of the ultra-low sulfur diesel, respectively. However, this difference was not found to be statistically significant, and the trends vary for each application. The applications most relevant to this study were the emissions of a 60 and a 250 kW standby generator. The difference in total hydrocarbon emissions for the 20% yellow-grease biodiesel and ULSD were less than 7% for both generators; however, the hydrocarbon emissions for JP-8 were as much as 32% greater than ULSD. Particulate matter emissions for the 250 kW generator varied minimally between fuels, but the PM emissions for the 60 kW generator with JP-8 were 50% less than that of ULSD and the 20% yellow-grease biodiesel.

A summary of the investigations of diesel engine emissions presented here is shown in Table 2.3. The particulate matter and hydrocarbon emissions of current in-use diesel generators as well as the effect of fuel on those emissions have been considered when selecting a generator and fuel for this study.

**Table 2.3: Investigations of diesel engine emissions**

| Author(s) (Year) | Type of Engine | Type of Fuel |
|---|---|---|
| Yost *et al.* (1996) | 1991 Prototype Series 60 Engine, 1990 GM 6.2L Engine | 600, 1100, and 2600 ppmw sulfur JP-8 |
| Saiyasitpanich *et al.* (2005) | Generac 80 kW Diesel Generator | 500, 2100, and 3700 ppm sulfur Diesel |
| Shah *et al.* (2006) | 60-2000 kW Diesel Generators | 500 ppmw sulfur Diesel |
| Durbin *et al.* (2007) | Medium Duty Truck, Humvee, HD Diesel, Bus, Back-up Generator, Forklift, Airport tow vehicle | ULSD, B20-YGA, B20-YGB, B20 Soy, JP-8 |
| Dongzi *et al.* (2009) | 10 to 100 kW Military Diesel Generators | 148 ppmw Diesel, 349 PPMw JP-8 |

**2.3 Fundamental Fouling Investigations**

While few studies have been performed to investigate fouling in exhaust coupled heat exchangers of waste-heat recovery systems, numerous studies have been performed to investigate the fundamental deposition and removal mechanisms of particulate matter and unburned hydrocarbons in exhaust gas recirculation (EGR) coolers. EGR coolers have been rapidly implemented in diesel engines due to stricter vehicle emissions standards. By recirculating cooled exhaust gas into the intake of a diesel engine, EGR coolers significantly reduce the emission of nitrous oxides. The performance of EGR coolers has been found to degrade over time due to fouling of the surfaces in the heat exchanger exposed to exhaust gas. Exhaust composition, coolant conditions, and tube geometry in EGR coolers are slightly different than that in the desorber of this study and may result in fouling effects that vary in magnitude; however, they are similar enough that the fundamental deposition and removal mechanisms in EGR coolers should be applicable to the diesel exhaust coupled desorber.

*2.3.1    Deposition Mechanisms*

A theoretical scaling analysis of different particulate matter deposition mechanisms in EGR coolers was performed by Abarham *et al.* (2010a). A representative case with a tube inner diameter of 5.5 mm, a wall temperature of 90ºC, an average exhaust temperature of 327ºC, and an average soot concentration of 30 mg m$^{-3}$ was used in the analysis. Thermophoresis, eddy diffusivity, turbulent impaction, electrostatic force, and gravitational force were the deposition mechanisms compared in the analysis. Thermophoresis, particle motion caused by a temperature gradient, was found to induce a

21

particle drift velocity at least two orders of magnitude greater than the other mechanisms, which led to the conclusion that thermophoresis is the dominant mechanism for fouling in EGR coolers. This analysis improved the understanding of EGR cooler fouling data and enabled model development.

### 2.3.1.1 Experimental Studies

Sluder and Storey (2008) investigated the effect of biodiesel fuel blends on EGR cooler performance degradation. Effectiveness loss and pressure gain were compared for ultra-low sulfur certification diesel (ULSD), 5% volume blend of soy biodiesel ULSD (B5), and a 20% volume blend of soy biodiesel ULSD (B20). For each fuel, exhaust flowed through a surrogate tube with an inlet temperature of 375ºC and flow rate of 3 kg hr$^{-1}$. The surrogate tube was surrounded by a coolant flowing through a tube jacket at a temperature of 95ºC. Tubes were exposed to exhaust for periods from a half hour to twelve hours. The effectiveness of the heat exchanger decreased rapidly at the beginning and asymptotically approached a steady value as time progressed. It was predicted that steady state would be reached after exposure to exhaust for 24 hours. A loss in effectiveness of 27% and pressure gain of 1 kPa were observed after a period of 12 hours; however, the difference in these values between fuel types was insignificant. Fractionation of the deposit mass showed that a greater mass of unburned hydrocarbons was deposited for the biodiesel fuels. The effect of coolant temperature was also studied. It was found that mass gain was greater at a coolant temperature of 40ºC than at 95ºC. The increased mass gain was expected at lower coolant temperature due to an increase in thermophoretic force; however, there was no significant decrease in effectiveness or increase in pressure drop. This could be attributed

to an increase in unburned hydrocarbons that condense on the tube surface, which have a higher thermal conductivity than dry particulate matter deposits.

Further measurements of total mass gain in surrogate tubes were performed by Sluder *et al.* (2009) with similar exhaust conditions and coolant temperatures of 40ºC, 70ºC, and 85ºC. Their study also found that total mass gain was greater at lower coolant temperature. Gas chromatography/mass spectroscopy analysis showed that the most common hydrocarbon chain in the deposits was $C_{20}$ (eicosane). The vapor pressure of $C_{20}$ sharply decreases in the coolant temperature range studied in this experiment from 1 Pa at 85ºC, to 0.82 Pa at 70ºC, and 0.27 Pa at 40ºC, making it much more likely to condense in the lower temperature case. The significant decrease in vapor pressure of $C_{20}$ helps to explain a mass gain as much as four times greater at the 40ºC case than at the 85ºC case. The use of an oxidation catalyst upstream of the surrogate tube showed dramatically lower mass gain at the lowest coolant temperature, but had little effect at the higher coolant temperatures, demonstrating that the catalyst was more effective at oxidizing lower boiling point hydrocarbons. The effect of exhaust flowrate was also studied. Exhaust flowrates in a 6.35 mm tube were varied from 5 to 30 SLPM while maintaining a constant coolant temperature. Total mass gain was found to increase with velocity; however, when normalized by the total particulate matter and hydrocarbon exposure, the trend was reversed. The efficiency of deposition decreased with increasing velocity. This was attributed to a reduction in the residence time for a particle to adhere to the tube surface, and the increased shear at the tube surface induced by higher exhaust velocity.

The effect of coolant temperature on deposit structure and composition was studied by Prabhakar and Boehman (2013). Exhaust was exposed to a single tube with a 5.33 mm

inner diameter at a temperature of 270$^{\circ}$C and coolant at a temperature of 85$^{\circ}$C. Tubes were exposed to the exhaust for intervals from 1.5 hours to 7.5 hours. High-magnification images of the deposit ex-situ showed large pores initially that were filled over time to build a denser and smoother deposit. Chromatographs of the deposit revealed that aromatic content marginally increases with time, which indicates that hydrocarbon condensation decreases as time progresses. These tests were also performed for a coolant temperature of 40$^{\circ}$C. When examining the microstructure of the two deposits, the 85$^{\circ}$C deposit was composed of coarse particulate while the 40$^{\circ}$C deposit consisted of larger particles formed due to greater hydrocarbon content. Chromatographs of the two deposits showed that 20% more alkanes ($C_{18}$ to $C_{25}$) were present in the deposit formed by the lower coolant temperature. While the deposit mass was much greater for the 40$^{\circ}$C case, the effectiveness loss was slightly less than that of the 85$^{\circ}$C. Prabhakar and Boehman (2013) suggested that this was because of wash out of the deposit layer due to water condensation at the lower temperature coolant; however, the change in properties of the deposit layer that results from additional hydrocarbon condensation could also cause this.

Storey *et al.* (2013) investigated the effect of hydrocarbon concentration in the exhaust on deposit microstructure. ULSD and ULSD (B20) were the fuels used in the experiments. Exhaust hydrocarbon concentration for both fuels was about 50 ppm. To further investigate the effect of hydrocarbon concentration, 50 ppm of hydrocarbons were added to the exhaust directly before the surrogate tubes for a high hydrocarbon case that resulted in a total hydrocarbon concentration of 100 ppm. Surrogate tubes 6.35 mm in diameter were exposed to exhaust for periods from 0.5 to 12 hours. The effect of the different fuels and exhaust composition on deposition mass and heat exchanger

24

effectiveness were important for the low exposure times, but the differences diminished at longer exposure times. This was also observed by imaging the microstructure of the deposit layer with a scanning electron microscope. The low HC deposits had a thick, dense bottom layer and a thin, dendritic top layer. The dendrites were visible at short exposure times, but disappeared at an exposure time of 12 hours. The dendrites were not observed for the high HC cases. It was concluded that hydrocarbon concentration has an initial effect on both performance and microstructure, but the difference diminishes as exposure time to exhaust increases.

The previous studies all used exhaust gas generated by a diesel engine. Hornig *et al.* (2011) used a model soot aerosol to investigate the mechanisms of EGR cooler fouling. The aerosol contained particulate of the size typically emitted from a turbo diesel engine as well as varying amounts of water, sulfuric acid, and diesel fuel. The model soot aerosol flowed through a single tube of 10 mm inner diameter that was surrounded by a coolant fluid. With no volatiles in the soot aerosol, mass deposition efficiencies varied from 7% to 14% for temperature differences between the exhaust and coolant of 80ºC and 280ºC, respectively. This showed the effect of thermophoresis on "dry" exhaust deposition. When water, hydrocarbons, and sulfuric acid were added to the model soot aerosol, mass deposition efficiencies increased to as much as 49%. They suggest this to be the result of diffusiophoresis, in which a vapor concentration gradient induces particle motion towards a surface where condensation is occurring. In this mechanism, condensing water, hydrocarbons, and sulfuric acid would drive particulate to the tube surface. To confirm this theory, one must be certain that the increased deposit mass is due to additional soot deposition and not due to mass added from condensation of volatiles.

A commercial soot generator was used by Hong *et al.* (2011) to produce a similar model exhaust gas. A parametric study was performed on particle size and soluble organic fraction (SOF) effect on EGR cooler fouling. For "dry soot", which contains less than a 10% SOF fraction, deposition efficiency was found to be as much as 84.18% for a mean particle size of 41 nm compared to 6.88% for a mean particle size of 190 nm. The effect of SOF fraction was determined by injecting various amounts of n-Dodecane into the model exhaust gas. With an injection rate of 0.4 ml hr$^{-1}$, exhaust temperature of 380ºC, and coolant temperature of 40ºC, deposit mass nearly doubled; however, at the same conditions with a coolant temperature of 80ºC, there was minimal change in the deposit mass. This is due to greater hydrocarbon condensation at the lower coolant temperature. The hydrocarbon deposit mass in the 40ºC case also resulted in an additional decrease in effectiveness of the single channel EGR cooler of about 6%. This result is contrary to that of Sluder and Storey (2008), who found that additional deposit mass from hydrocarbon condensation did not cause additional decrease in effectiveness.

Bika *et al.* (2012) determined soot deposition rates by measuring soot particle size and concentration upstream and downstream of a heat exchanger. This allowed for in-situ measurement of soot deposition efficiency. The effect of thermophoresis was first studied by exposing exhaust with an inlet temperature of 200ºC, hydrocarbon concentration of 40 ppmC$_3$, and filter smoke number of 2.0 to tubes 8 mm in diameter. Soot deposition rates of 38.3, 29.0, and 22.3 mg hr$^{-1}$ were measured for coolant temperatures of 25, 60, and 90ºC, respectively. This corresponds to a deposition efficiency ranging from 25-40%. These deposition rates match the trend of theoretical thermophoretic deposition, confirming thermophoresis as the primary deposition mechanism when low hydrocarbon

concentrations are present. To investigate the effect of hydrocarbon diffusiophoresis, particle motion caused by the gradient of a gas or vapor diffusing through air, inlet hydrocarbon concentrations were varied from 90 to 280 $ppmC_3$. It was found that soot deposition rate stayed constant while the hydrocarbon loss from the inlet to the outlet increased with increasing inlet concentration. This result suggests that hydrocarbon diffusiophoresis has little effect on soot deposition in EGR coolers.

The condensation of sulfuric acid in exhaust coupled heat exchangers can also cause fouling and corrosion that is detrimental to performance. Mosburger *et al.* (2008) developed a test facility to measure sulfuric acids and sulfates in the exhaust at the exit of an EGR cooler. The exhaust from a heavy duty diesel engine was analyzed when operating on a JP-8 fuel with 40 ppm sulfur and a JP-8 fuel with 2870 ppm sulfur. The EGR outlet temperature was between 90ºC and 110ºC, and sulfuric acid was not found in the exhaust stream for either fuel; however, the concentration of $SO_2$ was found to be ten times greater in the exhaust produced by the 2870 ppm sulfur fuel than in the 40 ppm sulfur fuel. They suggest that the temperatures were too high and timescales too small for oxidation of $SO_2$ to $SO_3$ and subsequent formation of sulfuric acid. If the temperatures in an exhaust coupled heat exchanger exceed those in this study, the only opportunity for condensation of sulfuric acid is during engine start-up and shut-down sequences.

A summary of experimental fouling deposition investigations is shown in Table 2.4 with the range of experimental conditions of each study plotted in Figure 2.1. Overall, the experimental investigations showed that deposition increased with increasing temperature difference between the exhaust and coolant, further suggesting thermophoresis as the dominant deposition mechanism. Conflicting results have been seen from different
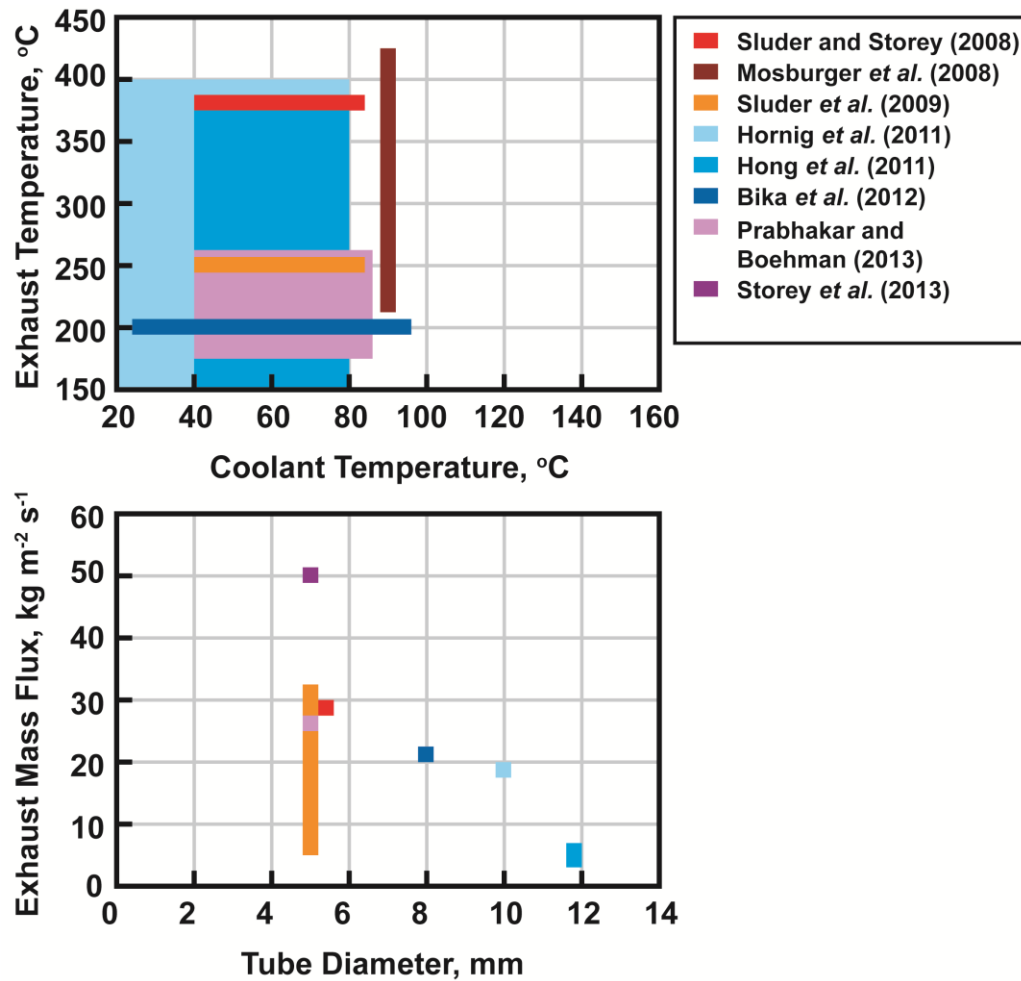
**Figure 2.1: Literature survey of experimental investigations into fouling deposition mechanisms**

investigators on the effect of lowering coolant temperature on fouling. Researchers were in agreement that lower coolant temperature resulted in greater mass gain; however, some results showed an increase in fouling resistance while others found that it remained the same. This was found to be the result of hydrocarbon condensation, which was greater at lower temperatures and increased the thermal conductivity of the fouling layer. This was observed through optical images that showed the layer to be less porous at conditions that promote hydrocarbon condensation. Efforts to model particulate matter deposition and

hydrocarbon condensation for prediction of EGR cooler degradation are presented in the following section.

**Table 2.4: Experimental fouling deposition investigations**

| Author(s) (Year) | Exhaust Source | Fuel | Heat Exchanger Geometry | Exhaust Temperature [ºC] | Exhaust Flow rate [kg hr$^{-1}$] | Coolant Temperature [ºC] |
|---|---|---|---|---|---|---|
| Sluder and Storey (2008) | 6.4 L V8 Diesel Engine | ULSD, ULSD (B5), ULSD (B20) | Square tube (5.33 mm) | 375 | 3 | 40, 95 |
| Mosburger *et al.* (2008) | Series 60 HD Diesel Engine | 40, 2870 ppmw sulfur JP-8 | Commercial EGR Cooler | 210-430 | NR | 87 |
| Sluder *et al.* (2009) | 1.7 L Diesel Engine | 300 ppmw diesel | Tube (4.93 mm) | 250 | 0.4, 1.1, 2.2 | 40, 70, 85 |
| Hornig *et al.* (2011) | Diffusion Burner | NA | Tube (10 mm) | 150-400 | 5.5 | 20, 80 |
| Hong *et al.* (2011) | Commerical Soot Generator | NA | Tube (11.7 mm) | 150-380 | 0.3, 0.7 | 40, 60, 80 |
| Bika *et al.* (2012) | 1.9 L Diesel Engine | ULSD | 19 Parallel Corrugated Tubes (8 mm) | 200 | 4 | 25-90 |
| Prabhakar and Boehman (2013) | 6.4 L V8 Diesel Engine | ULSD | 6 Parallel Tubes (5.33 mm) | 170, 270 | 13 | 40, 85 |
| Storey *et al.* (2013) | 6.4 L V8 Diesel Engine | ULSD, ULSD (B20) | Tube (4.57 mm), Square Tube (5.33 mm) | 375 | 3 | 40, 90 |

2.3.1.2 <u>Modeling Studies</u>

Several efforts have been made to model the fouling of EGR coolers. These models allow for a more thorough understanding of the mechanisms that drive fouling and can provide insight into experimental results.

Abarham *et al.* (2010b) developed an analytical model of thermophoretic particulate deposition in turbulent flows through a tube-in-tube heat exchanger. The model assumes a uniform radial and axial deposit distribution in the tube. This analytical solution provides qualitative trends of thermophoretic deposition. The model shows that deposition mass increases with exhaust inlet temperature, exhaust flowrate, and inlet particulate matter concentration. The exhaust and coolant conditions were matched to the experiments of Sluder and Storey (2008) for comparison purposes. Predictions of this analytical model match well with the experimental results for an exposure time of 3 hours, but results begin to deviate as exposure time increases throughout that period. This may be attributed to the assumption of constant interface temperature of the deposit layer. The interface temperature would tend to increase throughout the experiment, which would reduce thermophoretic deposition over time and cause improved agreement between the analytical model and experimental results.

The effect of increasing surface temperature was included in a 1-D computational model developed by Abarham *et al.* (2009b). The model considered thermophoresis as the primary deposition mechanism and neglected eddy diffusion and turbulent impaction. The model ran for a 3-hour exposure time, calculating deposition mass, deposition thickness, pressure drop, and effectiveness over that time period. The model predicted soot layer thicknesses at the inlet and outlet to be about 375 and 150 μm, respectively. Total mass

gain and effectiveness loss were predicted to be 42.7 mg and 18%. An experiment performed at these conditions resulted in a total mass gain of 17.9 mg and effectiveness loss of 15%. The model predictions showed improvement in agreement with these experimental results compared to the predictions of the analytical model; however, the mass gain and effectiveness loss predicted by the model still exceeded that seen in the measurements. Hydrocarbon condensation was added to this model as a deposition mechanism by Abarham *et al.* (2009a). The boundary condition inputs to the model were those reported by Sluder and Storey (2008) for a coolant temperature of 40°C. The model predicted 40 mg of soot deposition and 11.5 mg of condensed hydrocarbons. This is compared to test results that had 24-25.5 mg of soot deposition and 7.4-8.8 mg of condensed hydrocarbons. It was observed that hydrocarbons less volatile than $C_{20}$ did not condense, and condensation of all hydrocarbons ceased after an exposure time of two hours due to the increase in deposit interface temperature. While hydrocarbons had little effect on deposit thickness, they did have a more significant impact on effectiveness loss. With the inclusion of hydrocarbon deposits in the model, the asymptotic trend of effectiveness loss seen in experiments was more closely matched. This is most likely due to the effect hydrocarbons have on deposit properties.

An axi-symmetric model, developed by Abarham *et al.* (2013b) using ANSYS-FLUENT® (ANSYS, 2012), improved upon the prediction of deposit mass for exposure times of three and twelve hours. This model did not include deposition mechanisms for hydrocarbons. Compared to experiments, there was a 4% error in the deposit mass predicted by the axi-symmetric model while there was a 17% error for that of the 1-D model without hydrocarbons, described previously. The axi-symmetric model also

32

**Table 2.5: Modeling investigations of fouling deposition**

| Author(s) (Year) | Model Type | Modeled Deposition Mechanisms |
|---|---|---|
| Abarham *et al.* (2010a) | Scaling Analysis | Thermophoresis, Eddy Diffusion, Turbulent Impaction, Electrostatic and Gravitational Force |
| Abarham *et al.* (2010b) | 1D Analytical | Thermophoresis |
| Abarham *et al.* (2009b) | 1D Computational | Thermophoresis |
| Abarham *et al.* (2009a) | | Thermophoresis and HC Condensation |
| Abarham *et al.* (2013b) | Axisymetric (2D) Computational | Brownian diffusion, Turbulence, Thermophoresis |

performed better in the prediction of effectiveness; however, it did not closely match the asymptotic trend shown in experiments over long exposure times. They suggest that this is due to a discrepancy in the prediction of deposit layer properties and a lack of deposit removal mechanisms in the modeled physics. A summary of fouling deposition modeling investigations is provided in Table 2.5.

### 2.3.2    *Deposit Removal Mechanisms*

The asymptotic approach of fouling to a steady state has been partly attributed to deposit removal mechanisms. Drag, lift, weight, and turbulent lift force were investigated by Abarham *et al.* (2010a) as potential particulate matter removal mechanisms in EGR coolers. These forces were compared to the van der Waals force, which causes particles to adhere to the heat exchanger surface. The only plausible removal mechanism was found to be the drag force, which is on the same order of magnitude as the Van der Waals force for particles 400 nm in diameter and larger. This drag force is a result of the exhaust velocity and shear at the deposit surface.

The minimum gas speed to avoid particulate fouling in heat exchangers was studied by Abd-Elhady *et al.* (2004). An analytical model was developed to determine the minimum gas speed by equating the hydrodynamic rolling moment to the adhesion resting moment. The model was validated experimentally by passing air at 200°C over the shell side of a tube cooled to ambient temperature. Copper particles of 10 and 50 μm were injected into the flow. The 10 μm particles were predicted with the analytical model to need a minimum velocity of 10.5 m s$^{-1}$ to avoid fouling. It was shown experimentally that fouling occurred for flows with average velocities of 7.5 and 2.7 m s$^{-1}$, but did not occur at 9.5 m s$^{-1}$. The analytical model predicted the minimum velocity for 50 μm particles to be 4.5 m s$^{-1}$, while experiments showed that fouling occurred at 2 and 4.5 m s$^{-1}$ but not at 5.5 m s$^{-1}$. The analytical model accurately predicted the minimum gas speed to avoid particulate fouling for both the particle sizes.

Similar tests to determine the minimum velocity for gases containing particulate of the size typical in diesel engine exhaust were performed by Abd-Elhady *et al.* (2011). Soot particles with an average diameter of 130 nm with a standard deviation of 55 nm were generated by an ethylene-air burner. The particulate was mixed with air to a concentration of 100 mg m$^{-3}$ and heated to a temperature of 400°C before being passed through a shell-and-tube EGR cooler with coolant on the shell side at a temperature of 80°C. Typical exhaust gases contain a large distribution of particulate sizes. To prevent fouling, the critical flow velocity should be selected based on the smallest particle size. The smallest, average, and largest particulate sizes were 20 nm, 130 nm, and 300 nm, respectively. These particles sizes correspond to a minimum gas speed of 120, 67, and 40 m s$^{-1}$, respectively. For the test, velocities of 30, 70, and 120 m s$^{-1}$ were selected. The thermal resistance of

the deposit layer for the 30 m s$^{-1}$ case was 3.5 times greater than the resistance for the 70 m s$^{-1}$ case and 8.5 times greater than the resistance for the 120 m s$^{-1}$ case. Post fouling particulate size distribution was performed and showed a particulate distribution similar to that of the exhaust gas in the deposit for the 30 m s$^{-1}$ case, but a distribution of 65±20 nm for the 120 m s$^{-1}$ case. This demonstrates that the greater velocity was effective in removing particles of larger diameter, and that when designing EGR coolers, the velocity should exceed the minimum gas speed to avoid particulate fouling.

The hypothesis that fouling reaches a steady state due to flow-induced shear at the deposit surface was tested by Sluder *et al.* (2013) using in-situ and ex-situ methods. In the in-situ experiment, a surrogate tube was exposed to particulate laden exhaust gas at flow rates of 0.05 and 0.07 kg min$^{-1}$ for 8 hours. After this time, a particulate filter was installed upstream of the surrogate tube, and the tube was exposed to the exhaust for another two hours. The thermal resistance of the tube increased during the initial 8 hours and leveled off following the installation of the filter. This suggests that removal of the deposit layer due to flow-induced shear did not occur. Ex-situ measurements were performed by passing ambient temperature air through the surrogate tubes with an engine exhaust particulate sizer at the outlet. This test showed that some removal occurred at a velocity of 42 m s$^{-1}$, and more significant removal occurred at a velocity of 53 m s$^{-1}$. These velocities corresponded to a surface shear stress of 0.030 and 0.045 kPa, respectively. Sluder *et al.* (2013) concluded that flow induced shear can be a removal mechanism for deposit layers, but the required velocity is greater than those in typical EGR coolers. This suggests that flow induced shear is not the primary reason for a steady state fouling layer.

Another proposed removal mechanism is the washing away of the deposit by condensed water droplets in the exhaust. A facility for visualization of deposit removal mechanisms was developed by Abarham *et al.* (2013a). Exhaust from a medium duty diesel engine flowed through a rectangular cross section that was cooled at the bottom and covered by a pyrex window on top for imaging with a digital microscope. An analytical model was developed to calculate the dew point at the specified exhaust composition and the condensation mass flux as a function of coolant temperature. The dew point was calculated to be 49ºC, and the condensation mass flux was predicted to be more than two times greater at a coolant temperature of 20ºC than at 42ºC. The effect of coolant temperature on water condensation was investigated experimentally by creating a deposit layer at a coolant temperature of 80ºC and then reducing the coolant temperature to 20ºC or 42ºC so that water condensation would occur. At a coolant temperature of 42ºC, a crack developed and grew with time. For the 20ºC coolant temperature, water was observed to form below the deposit layer which weakened the bond forces and caused the deposit to float until it was removed by the exhaust flow. Significantly more removal was observed at the lower temperature, demonstrating that water condensation can be an important deposit removal mechanism at these conditions.

A similar visualization facility was designed by Warey *et al.* (2013) to quantify the amount of removal that occurs due to water condensation. Two deposits were formed with "dry" soot only by exhaust with a filter smoke number of 2.0 and hydrocarbon concentration of 40 $ppmC_3$ that was exposed to coolant at temperatures of 50ºC and 100ºC to prevent hydrocarbon condensation in the deposit. A third deposit was formed by exhaust with a filter smoke number of 2.0 and hydrocarbon concentration of 250 $ppmC_3$ that was

exposed to coolant at a temperature of 25ºC to promote hydrocarbon condensation and a "wet" soot layer. Measurements of deposit mass were made before exposing each deposit to humid air with a coolant temperature of 10ºC. For the 100ºC and 50ºC dry soot deposits, 81% and 65% of the deposit mass was removed after exposure; however, only 27% of the mass was removed for the wet soot layer formed by 25ºC coolant. Visualization showed that water condensed and diffused to the tube surface in the dry soot cases, but it remained on the deposit layer surface for the wet soot. The wet soot layer was less porous, which prevented water from diffusing to the tube surface and promoting greater deposit removal.

Based on these results, Warey *et al.* (2014) investigated the combination of an oxidation catalyst and water vapor condensation to mitigate fouling in EGR coolers. The oxidation catalyst was placed upstream of the EGR cooler, which oxidized unburned hydrocarbons in the exhaust and resulted in the development of a dry soot layer in the EGR cooler that could be removed by water condensation. Results for an active and inactive oxidation catalyst were tested for coolant temperatures of 25ºC and 50ºC. Deposit mass gain for the inactive oxidation catalyst was significantly greater than for the active oxidation catalyst for both temperatures due to hydrocarbon condensation into the deposit layer. After exposure to water condensation, the deposit mass gain for the active oxidation catalyst was 50% and 90% less than that of the inactive oxidation catalyst for the 50ºC and 25ºC coolant temperatures, respectively. This study shows that an oxidation catalyst in conjunction with deposit removal due to water condensation could be an effective means to regenerate the EGR cooler; however, this is only possible with coolant temperatures of 50ºC or less, which is the dew point of water at these conditions.

A summary of the reviewed deposit removal investigations is shown in Table 2.6. Two primary deposit removal mechanisms were addressed, flow induced shear and water condensation. Flow induced shear was found to be possible for the size of particulate in diesel exhaust for average flow velocities of 40 m s$^{-1}$ or greater. Water condensation was found to cause greater removal of "dry" deposit layers than "wet" deposit layers that contain a greater fraction of unburned hydrocarbons. It was also found that water condensation removal was only possible for coolant temperatures below the dew point of water. The conditions for deposit layer removal through flow induced shear and water condensation are shown in Figure 2.2. These removal mechanisms will be considered in analyzing the fouling results in this study.
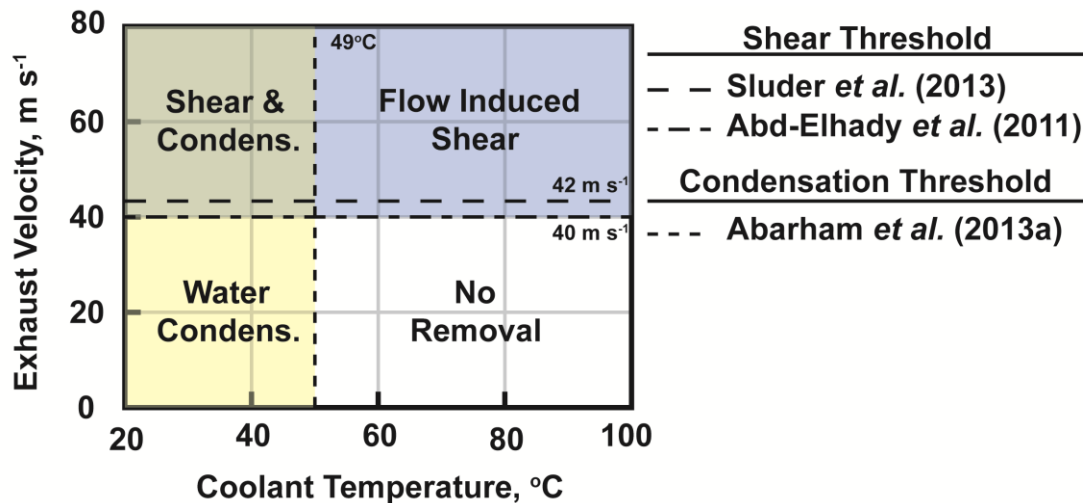


**Figure 2.2: Exhaust velocity and coolant temperature thresholds for deposit layer removal**

**Table 2.6: Investigations of deposit removal mechanisms**

| Author(s) (Year) | Exhaust Source | Heat Exchanger Geometry | Exhaust Temperature [ºC] | Exhaust Velocity or Flow Rate | Coolant Temperature [ºC] |
|---|---|---|---|---|---|
| Abd-Elhady *et al.* (2004) | Screw Feeder | Shell and Tube (Exhaust on Shell side) | 500 | 2-9.5 m s$^{-1}$ | 25 |
| Abd-Elhady *et al.* (2011) | Ethylene-Air Burner | Shell and Tube (Exhaust on Tube Side) | 400 | 30, 70, 120 m s$^{-1}$ | 80 |
| Sluder *et al.* (2013) | 6.4 L V8 Diesel Engine | Square tube (5.38 mm) | 375 | 42, 53 m s$^{-1}$ | 90 |
| Abarham *et al.* (2013a) | Medium Duty Diesel Engine | Rectangular Channel (11.5 x 22 mm) | 190 | 5.2 m s$^{-1}$ | 20, 40, 80 |
| Warey *et al.* (2013) | 1.9L Diesel Engine | Rectangular Channel | 215 | 14.7 kg hr$^{-1}$ | 10-100 |
| Warey *et al.* (2014) | 1.9L Diesel Engine w/ Oxidation Catalyst | Rectangular Channel | 250 | 14.7 kg hr$^{-1}$ | 25, 50 |

### 2.3.3    Deposit Properties

Determining the properties of the deposit layer is extremely useful in the design of exhaust gas coupled heat exchangers. Lance *et al.* (2009) measured the thermal properties of the deposit from the experiments performed by Sluder and Storey (2008). The surrogate tubes were removed and measurements were made ex-situ.  Specific heat was measured from 25ºC to 430ºC using a Stanton-Redcroft Differential Scanning Calorimeter, and for the fouling layer developed with ULSD fuel ranged from 0.82 J $g^{-1}$ $K^{-1}$ to 1.55 J $g^{-1}$ $K^{-1}$ over the temperature range considered.  The density of the sample was calculated by measuring the deposit volume and mass after heat treatment to remove adsorbed water and hydrocarbons.  The thickness of the deposit layer was measured from a micrograph of the tube cross section and used to find volume.  The thickness and density of the layer were found to be 410 μm and 0.0316 g $cm^{-3}$, respectively.  This density suggests a porosity of 98% when compared to primary soot particle density.  Thermal diffusivity was measured to be 0.0190 $cm^2$ $s^{-1}$ using the flash technique.  With these three properties, the thermal conductivities of the deposits created by ULSD, B5, and B20 fuels was calculated to be 0.057, 0.034, and 0.032 W $m^{-1}$ $K^{-1}$, respectively.

While the previous measurements were made ex-situ, a test facility to measure in-situ properties of EGR cooler deposit layers was described by Salvi *et al.* (2013).  The facility was designed for exhaust to flow through a rectangular channel that had coolant flowing on the bottom of the channel and optical access through glass from the top.  A microscope was used to image surface properties and an infrared camera was used to measure surface temperature.  The thermal conductivity was calculated using inner and outer surface temperatures, heat flux, and deposit layer thickness.  Results from this test

facility were reported in Salvi *et al.* (2014) for an exhaust inlet temperature of 280ºC, exhaust flow rate of 5 kg hr$^{-1}$, filter smoke number of 1.6, hydrocarbon concentration of 39 ppmC$_1$, and coolant temperature of 70ºC. After a 24-hour period, the deposit layer was found to have a thickness of 379 μm, a thermal conductivity of 0.047 W m$^{-1}$ K$^{-1}$, and an increase in surface area of 20%. These measurements were made again after heating the deposit to remove condensed hydrocarbons. This caused a decrease in the deposit layer thickness and the conductivity. If the layer had collapsed and become denser, the thermal conductivity would increase, but because it did not, it was determined that the presence of condensed hydrocarbons has a significant impact on the thermal conductivity and other layer properties. The thermal conductivity of the deposit layer after hydrocarbons were removed was similar to that of Lance *et al.* (2009), in which measurements were also made after hydrocarbon removal. Deposit layer property investigations are summarized in Table 2.7.

### 2.4 Component Level Fouling Investigations

Several experiments have also been performed on commercially implemented EGR coolers. These experiments investigated aspects of EGR cooler design, operating load cycles, and emission control strategies to mitigate fouling.

Kim *et al.* (2008) studied the effect of enhanced tube geometries on EGR cooler performance. Three coolers were analyzed, one with plain tubes 6 mm in diameter, a second with spiral tubes 6 mm in diameter, and a third with spiral tubes 8 mm in diameter. The EGR coolers were exposed to exhaust gas for a total of 78 hours. The EGR coolers with spiral tubes had an initial effectiveness of 77%, while the plain tube cooler had an effectiveness of 67%. Fouling in the spiral tube EGR coolers caused a more significant

decrease in the effectiveness than in the plain tube cooler.  After 78 hours, both the 8 mm spiral tube EGR cooler and plain tube EGR cooler had an effectiveness of 50%, while the 6 mm spiral tube EGR cooler showed the greatest decrease with a final effectiveness of about 30%. Cross sectional images of the EGR coolers after testing showed that several of the 6 mm spiral tubes had completely clogged, which caused the significant decrease in performance.  Kim *et al.* (2008) concluded that although spiral tubes enhance initial EGR cooler effectiveness, an increase in fouling that causes a greater reduction in effectiveness than that of plain tube EGR coolers occurs.

The effect of fouling on a small-scale six tube shell-and-tube heat exchanger was investigated by Zhang *et al.* (2004). The tubes were 4.6 mm in inner diameter and were exposed to exhaust at a temperature of 250ºC, flow rate of 1.4 kg hr$^{-1}$, and particulate matter concentration of 130 mg m$^{-3}$.  The thermal resistance and pressure drop of the cooler were found to increase by 150% and 200%, respectively, over an exposure time of 12 hours. The effective diameter of the tubes was found to decrease to two-thirds of the initial value. Load cycle tests in which the cooler was exposed to exhaust for a three-hour period each day for five days were also performed.  The final thermal resistance and pressure drop after each day increased; however, at the beginning of each new test, the thermal resistance and pressure drop were less than that at the end of the previous test. This either suggests that a portion of the fouling layer was removed between each test or the properties of the layer changed.  This result is significant because actual exhaust gas coupled heat exchangers will undergo intermittent exposure to exhaust gas as opposed to the constant long duration exposure that has been more thoroughly investigated.  These studies should be expanded

to determine if fouling of the heat exchanger also reaches a steady state after a certain number of typical load cycles.

The effect of PM control devices on reduction of EGR cooler fouling was investigated by (Zhan *et al.* (2009)). Four different PM control devices were installed upstream of an EGR cooler. They consisted of a diesel oxidation catalyst (DOC) substrate followed by a diesel particulate filter (DPF) substrate. Experiments were run with an exhaust inlet temperature of 500ºC and coolant temperature of 60ºC for 42 hours, which was the time required for pressure drop and exhaust outlet temperature to reach steady state. The baseline EGR cooler had an uncoated DOC substrate and uncoated flow-through DPF. This cooler showed a 61% increase in pressure drop. The other three coolers all had a 2.6 kg m$^{-3}$ platinum DOC with either an uncoated wall flow, uncoated flow through, or coated flow through DPF. These three coolers had increases in pressure drop of 13 percent, 53 percent, and 55 percent, respectively. The outlet temperature of the EGR cooler with the wall flow DPF showed virtually no increase in outlet temperature, indicating that very little fouling occurred in the cooler itself; rather, the increase in pressure drop was attributed to collection of particulate matter in the wall flow DPF. This study demonstrated that the use of a wall flow DPF can almost entirely eliminate fouling in exhaust gas coupled heat exchangers; however, these devices impose additional cost and operational complexity due to active regeneration of the filter. Component level fouling investigations are summarized in Table 2.8.

**Table 2.7: Investigations on fouling deposit layer properties**

| Author(s) (Year) | Type of Engine | Fuel | Heat Exchanger Geometry | Exhaust Temperature [°C] | Exhaust Flow rate [kg hr⁻¹] | Coolant Temperature [°C] |
|---|---|---|---|---|---|---|
| Lance *et al.* (2009) | 6.4 L V8 Diesel Engine | ULSD, ULSD (B5), ULSD (B20) | Square Tube (5.33 mm) | 375 | 3 | 40, 95 |
| Salvi *et al.* (2013) | 2008 MD Diesel Engine | NR | Rectangular Channel (21.5 x 12 mm) | 250 | 5 | 75 |
| Salvi *et al.* (2014) | 2009 MD Diesel Engine | NR | Rectangular Channel (21.5 x 12 mm) | 280 | 5 | 70 |

**Table 2.8: Component level fouling investigations**

| Author(s) (Year) | Exhaust Source | Heat Exchanger Geometry | Exhaust Temperature [°C] | Exhaust Flow rate [kg hr⁻¹] | Coolant Temperature [°C] |
|---|---|---|---|---|---|
| Zhang *et al.* (2004) | 5 kW Diesel Generator | Shell-and-Tube, 6 - 4.6 mm tubes | 250 | 1.4 | 15-22 |
| Kim *et al.* (2008) | 1.9 L Diesel Engine | Shell-and-Tube (Plain or Spiral) | 450 | 50 | 80-90 |
| Zhan *et al.* (2009) | 7.3L V8 Diesel Engine (DOC & DPF) | Coflow Shell and Tube EGR Cooler | 500 | 160-170 | 60 |

## 2.5 Summary

Overall conversion efficiency from diesel fuel to useful forms of energy can be improved in a wide range of applications through the use of waste-heat in diesel engine exhaust. Absorption heat pumps are particularly useful when combined heating and cooling is required in addition to the power generated by the diesel engine. Long term performance of these systems faces challenges due to the fouling of the heat exchanger that couples to the exhaust gas. As demonstrated by previous research, fouling is highly dependent on exhaust composition, temperature, and flow rate as well as heat exchanger geometry and coupling fluid temperature; however, the vast majority of studies have focused on the narrow range of fluid conditions and geometries pertinent to EGR coolers. Experiments must be performed for a broader range of fluid conditions and heat exchanger geometries to develop a database for exhaust-coupled heat exchanger design. Furthermore, there is a lack of understanding of the mechanisms that cause the deposit layer to reach steady-state. This has been demonstrated by modeling efforts that were unable to predict the asymptotic behavior of the deposit layer growth. Understanding this phenomenon is crucial to designing exhaust-coupled heat exchangers that limit or prevent fouling layer growth. A thorough design analysis of diesel exhaust-coupled heat exchangers is also absent from the literature. While some researchers have made allowances for fouling resistance, they have not made efforts to reduce fouling through design of the heat exchanger.

In this study, measurements of fouling resistance and exhaust pressure drops are made for the fouling conditions present in the desorber of an ammonia-water absorption heat pump. The exhaust temperatures, coolant temperatures, exhaust flow rates, and tube

diameter explored in this study are compared to those studied in the literature in Figure 2.3. The range of coolant temperatures is expanded significantly from 95ºC to 157ºC. Similarly, the tube diameter in this study, 12.7 mm, is greater than those previously investigated for EGR coolers.  Measurements at these conditions broaden the database of fouling results for exhaust-coupled heat exchanger design.  Fouling layer thermal resistance, thermal conductivity, and thickness as well as exhaust pressure drop are analyzed to understand which deposition mechanisms are most prevalent at various
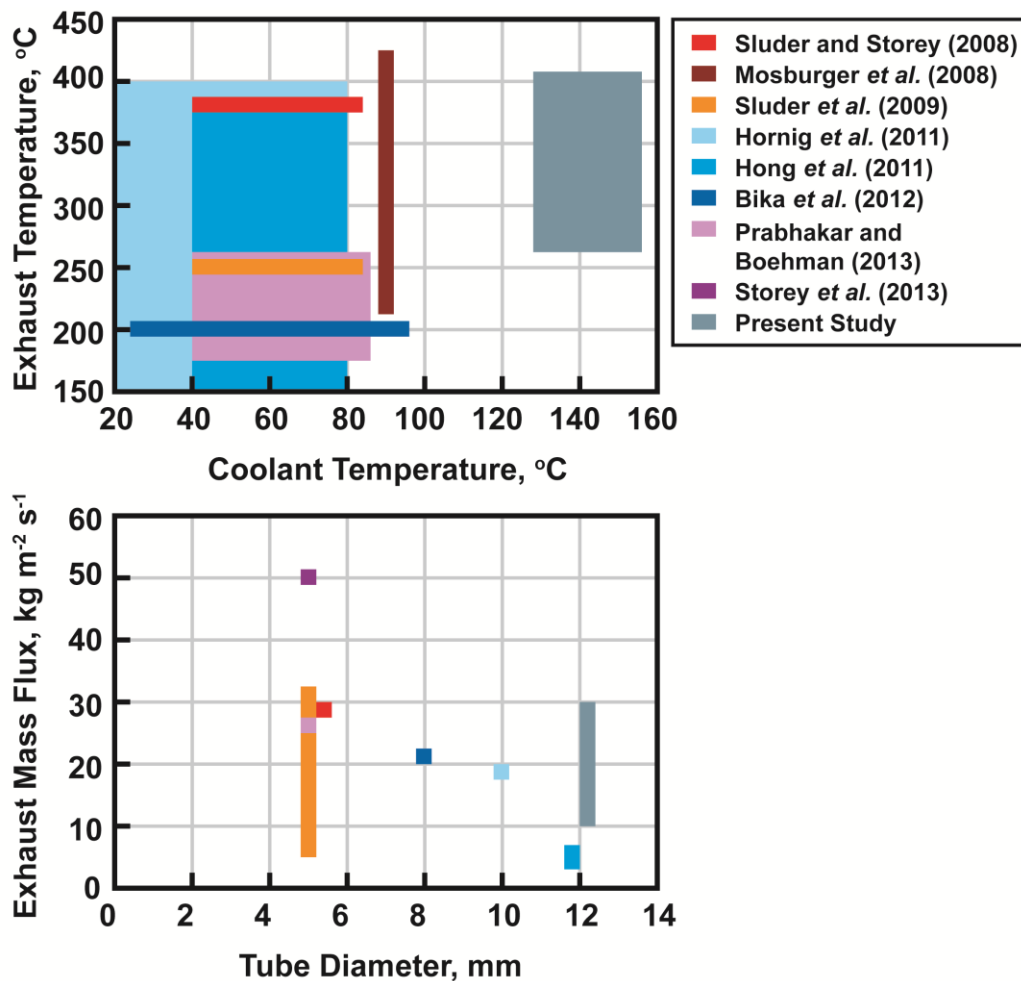


**Figure 2.3: Comparison of experimental conditions of this study to the literature**

conditions. The analysis provides further insight into the mechanisms that prevent fouling layer growth and cause it to reach steady-state. The results of these experiments are used to design a desorber that minimizes fouling through optimization of heat exchanger geometry. This will result in a desorber that is as compact and efficient as possible while meeting system level performance requirements after fouling has occurred. Ultimately, the methodology used to design a desorber that limits fouling in this study may be used in the design of exhaust-coupled heat exchangers for a wide range of waste-heat recovery applications. The methodology used to develop the test facility is discussed in the following chapter.

# CHAPTER 3.    EXPERIMENTAL FACILITY

The development of an experimental facility that simulates the fouling conditions in the desorber of a diesel engine exhaust driven absorption heat pump is presented in this chapter.  A thermodynamic cycle model is used to determine the conditions of the exhaust and ammonia-water solution in the desorber at various heat pump operating conditions. The results are used as inputs to a thermodynamic and heat transfer model of the experimental facility that allows for proper sizing of equipment and instrumentation.  The selected components of the facility and the experimental procedures are also discussed.

## 3.1 Cycle Model of Waste-Heat Driven Absorption Heat Pump

The system under consideration in the present study is a 2.71 kW cooling capacity ammonia-water absorption heat pump.  The heat pump utilizes waste-heat from the exhaust of a 10 kW diesel generator, which is at a nominal temperature of 398.9ºC and flow rate of 0.0235 kg s$^{-1}$.  The system is designed to operate in ambient temperatures up to 51.6ºC and provide chilled water for space-conditioning at 13ºC.  A thermodynamic cycle model was developed by Forinash (2015) to predict heat pump performance, heat and mass exchanger thermal conductance (*UA*), and inlet and outlet fluid conditions of each component.  A baseline model was developed with conservative estimates for the pressure drops, closest approach temperatures (*CAT*), and effectivenesses of the individual components.  The performance was then optimized through a parametric study that varied model inputs to determine their impact on the cooling capacity and coefficient of performance (*COP*).

**Table 3.1: Component heat duties and *UA*s ( Forinash (2015))**

| Component | Q (kW) | UA (kW K$^{-1}$) |
|---|---|---|
| Condenser | 2.53 | 0.188 |
| Precooler (RHX) | 0.34 | 0.025 |
| Evaporator | 2.71 | 0.846 |
| Absorber | 5.15 | 0.380 |
| Rectifier | 1.50 | 0.044 |
| Desorber | 4.94 | 0.055 |
| Solution Heat Exchanger (SHX) | 2.20 | 0.074 |

Values for the heat and mass exchanger *UA*s were modified to maximize heat pump performance and are shown in Table 3.1.

The cycle model also predicts the fluid inlet and outlet conditions of each component. The temperatures of the concentrated solution inlet and dilute solution outlet of the desorber are expected to have a significant effect on fouling; therefore, it is critical to determine and replicate these temperatures in the fouling experiments. At design conditions (an ambient of 51.6°C), the concentrated solution inlet and dilute solution outlet of the desorber were determined to be 137.6 and 190.4°C, respectively. By maintaining the same *UA*s for each component in the cycle model, which fixes the size of the system, a parametric study is performed to determine the inlet and outlet temperatures of the desorber at various ambient temperatures. The results are shown in Figure 3.1. As the ambient temperature is reduced from 51.6°C to 26.7°C, the temperatures of the concentrated solution inlet and dilute solution outlet drop to 99.03 and 165.6°C, respectively.
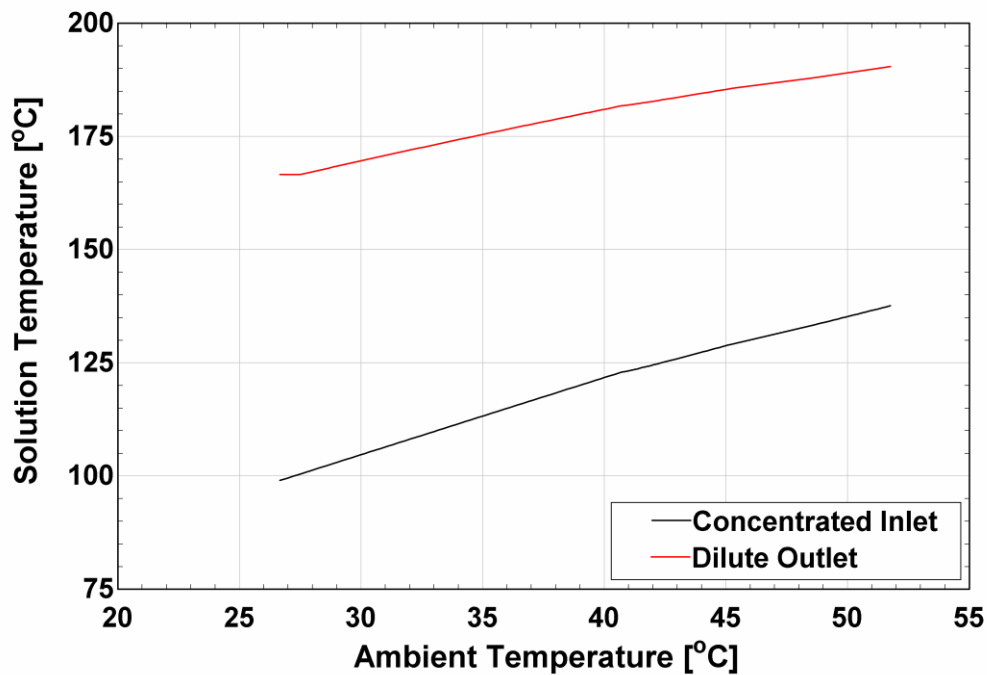
**Figure 3.1: Cycle model predictions of desorber inlet and outlet solution temperature at various ambient temperatures**

### 3.2 Fin-Tray Desorber

The desorber utilized in this absorption heat pump was developed by Staedter *et al.* (2016), and is shown in Figure 3.2. It consists of two columns, and each column contains 22 vertical tubes through which the exhaust flows. The tubes have a 12.7 mm outer diameter and a wall thickness of 0.9 mm, and are 254 mm in length. The tubes are all contained in a 114.3 mm diameter outer shell with a wall thickness of 6.0 mm. A schematic of exhaust and solution flow through the desorber is shown in Figure 3.3. Exhaust enters at the bottom of the column, flows upward through 11 parallel tubes, changes direction in a header, and flows downward through the remaining 11 parallel tubes, exiting at the bottom of the column. The ammonia-water solution flows on the shell side of the desorber with the concentrated solution entering at the top and dilute solution exiting at the bottom.

50
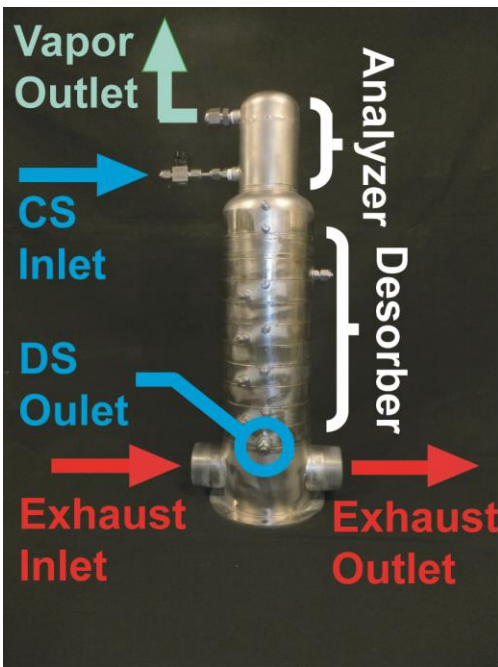
**Figure 3.2: Desorber column with labeled inlets and outlets**

The vapor that is generated flows counter to the liquid solution and exits at the top of the

desorber. A series of horizontal trays is installed on the shell side of the desorber to guide

and regulate liquid flow, and improve heat and mass transfer between the falling liquid and

rising vapor. The trays are circular and span the inner diameter of the column. Each tray

has 22 holes for the exhaust tubes and a weir down the center. On one side of the weir, the

holes are cut to the outer diameter of the exhaust tubes and brazed to the tray so that there

are no gaps between the tube and the tray. On the other side of the weir, the holes are

oversized to create an annulus between the tube and the tray. Liquid flows down through

these annuli to the next tray while vapor generated in lower trays flows upwards. A

downcomer tube allows liquid to flow down to subsequent trays if the liquid level grows

too high. This prevents complete flooding of the desorber with liquid.
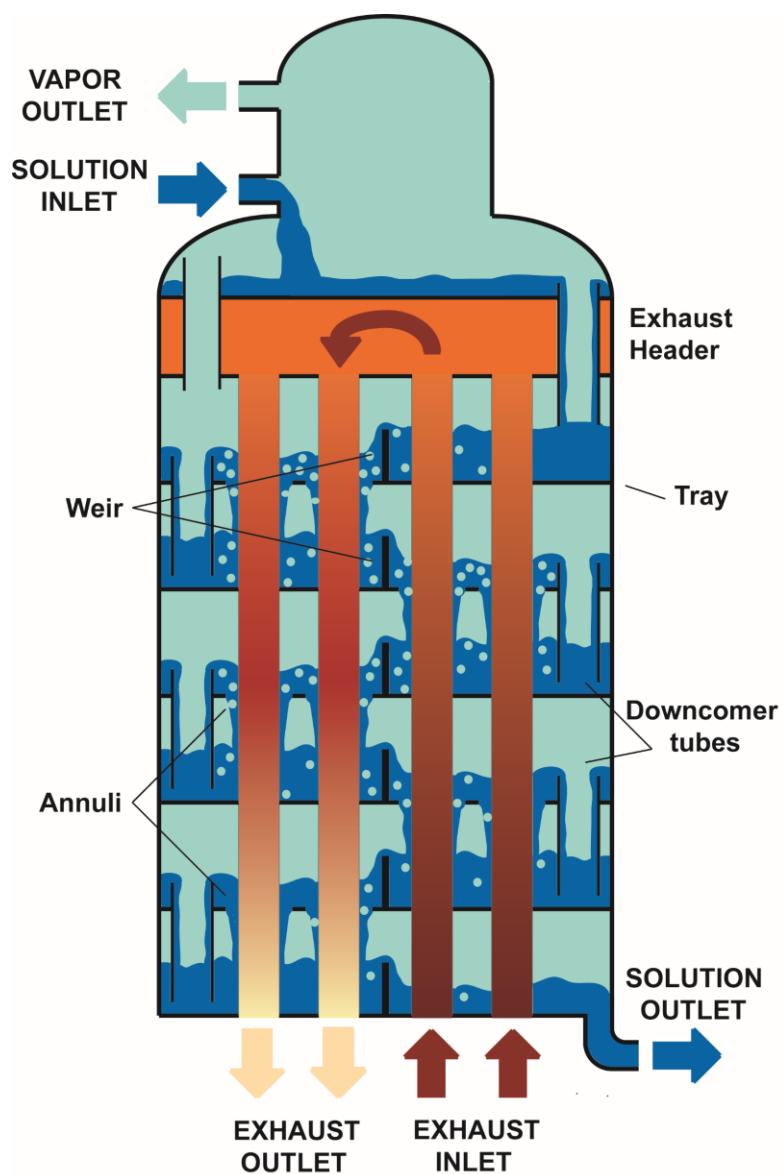
**Figure 3.3: Schematic of fin-tray desorber design**

To perform fouling experiments on the desorber, it is desirable to simplify the desorber design so that a wide range of test conditions can be analyzed with a minimal amount of material waste. This is done by isolating a single tube in the desorber and replicating its conditions with a tube-in-tube heat exchanger whose inner tube can be

readily removed for ex-situ analysis and replaced with a clean tube. It is possible to reduce each pass of 11 parallel tubes to a single tube because the exhaust inlet temperature, exhaust flow rate, and solution temperatures are approximately the same for each tube. A schematic of the tube-in-tube heat exchanger is shown in Figure 3.4. The exhaust flows through the inner tube, which has the same dimensions of the exhaust tubes in the desorber, and coolant flows between the annulus of the inner and outer tubes.

The coolant is shown in the schematic to flow in either direction with respect to the exhaust. This is so that the heat exchanger can either represent a tube in the first pass through the desorber column or a tube in the second pass. In the first pass, the solution and exhaust are in counter-flow, while in the second pass, they are in co-flow. To replicate the column, two tube-in-tube heat exchangers are connected with the exhaust in series. The coolant in the first heat exchanger is in counter-flow and the coolant in the second is in co-flow to represent the respective passes of a single column. By doing this, the exhaust conditions entering the second tube-in-tube heat exchanger closely resemble that entering the second pass in the desorber column.
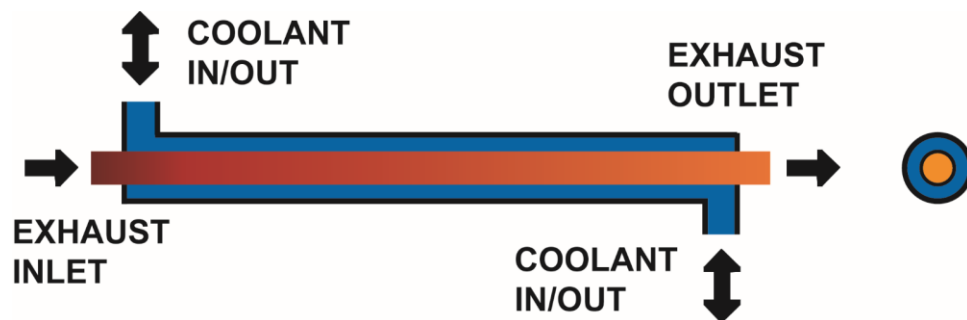


**Figure 3.4: Tube-in-Tube heat exchanger schematic**

It has been shown by several researchers (Sluder and Storey (2008); Sluder *et al.* (2009); Prabhakar and Boehman (2013); Hong *et al.* (2011); Bika *et al.* (2012)) that the exhaust tube temperature has a significant effect on fouling due to thermophoretic deposition and hydrocarbon condensation; therefore, it is critical to ensure that the tube temperature in the tube-in-tube heat exchanger is as close to that of the desorber as possible. The tube temperature in the desorber is primarily dependent on the liquid solution temperature. This is because the convective thermal resistance of the solution is far less than that of the exhaust. It is not critical to use ammonia-water as the coolant in the tube-in-tube heat exchangers as long as the tube temperature remains the same. Boiling ammonia-water would cause many challenges for accurate measurement of coolant temperature, calculation of heat transfer rate, and determination of fouling heat transfer resistance. The coolant also needs to be discharged and recharged into the experimental facility to install new tubes into the heat exchangers. The use of ammonia-water would incur additional cost and require additional safety precaution. For these reasons, pressurized liquid water is chosen as the coolant for these experiments. The tube temperature is kept constant by modifying the coolant inlet and outlet temperatures from the concentrated and dilute solution temperatures to account for the difference in heat transfer coefficients of the two fluids. The coolant inlet and outlet temperatures, flow rates, and a variety of other parameters are determined through the development of a heat transfer and thermodynamic model of the experimental facility.

## 3.3 Model of Experimental Facility

The design of the experimental facility is dependent on the arrangement of the two desorber columns in the absorption heat pump. The columns can be arranged in two ways,

with the exhaust connected in series or parallel. A schematic of the two arrangements is shown in Figure 3.5. In the series arrangement, each column receives the full flow rate of exhaust, but the second column receives exhaust at a lower temperature. In the parallel arrangement, each column receives exhaust at the same temperature and half of the flowrate. In both cases the solution is connected to the two columns in parallel. In the series arrangement, the exhaust makes a total of four passes through the solution, requiring four tube-in-tube heat exchangers in fouling experiments. In the parallel arrangement, the exhaust only makes two passes through the solution and only two tube-in-tube heat exchangers are required. The experimental facility is designed to accommodate both arrangements by incorporating four tube-in-tube heat exchangers.

A schematic of the facility is shown in Figure 3.6, and is described below with the state points contained in brackets. Exhaust flows in series through four tube-in-tube heat exchangers [1-5] with temperature measured at each state point. Pressure drop is measured
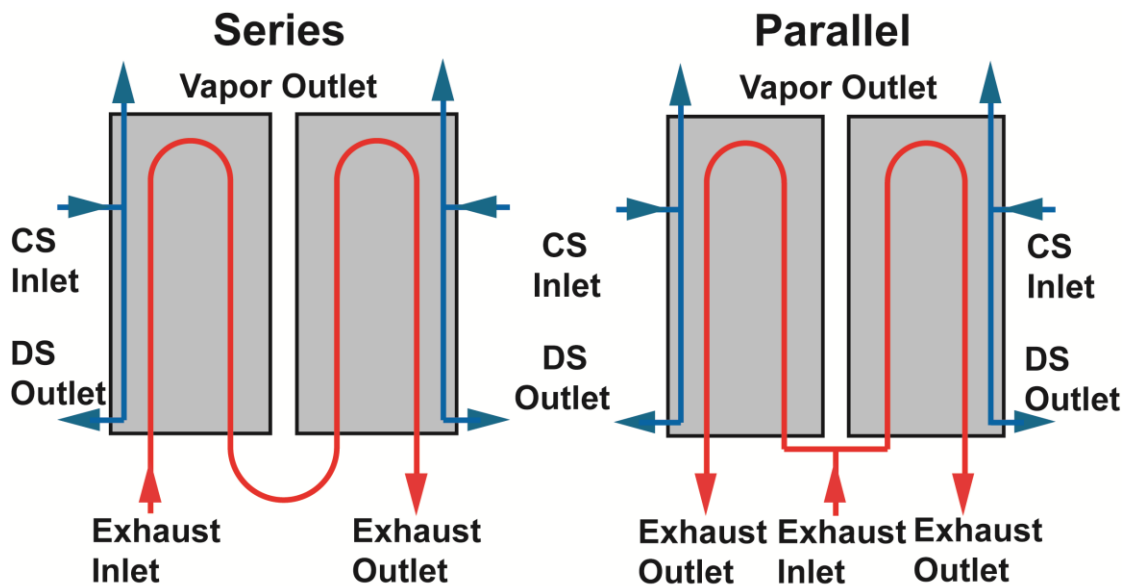


**Figure 3.5: Schematic of series and parallel arrangement of desorber columns**

55

across each heat exchanger, with absolute pressure measured at the outlet of the last heat exchanger [5]. The flow rate is measured downstream of the last heat exchanger [6]. The coolant loop starts at the outlet of the immersion heater, at which point the coolant splits into four parallel paths [7]. The flow rate of each path is controlled with a valve and measured before entering each heat exchanger [8-11]. The coolant through heat exchangers one and three is in counter flow while the coolant through heat exchangers two and four is in co-flow. Together, the first and second heat exchangers represent one desorber column and the third and fourth heat exchanger represent another desorber column connected in series. The coolant temperature is measured at the outlet of each heat exchanger [12-15], and coolant pressure is measured where they recombine [16]. An
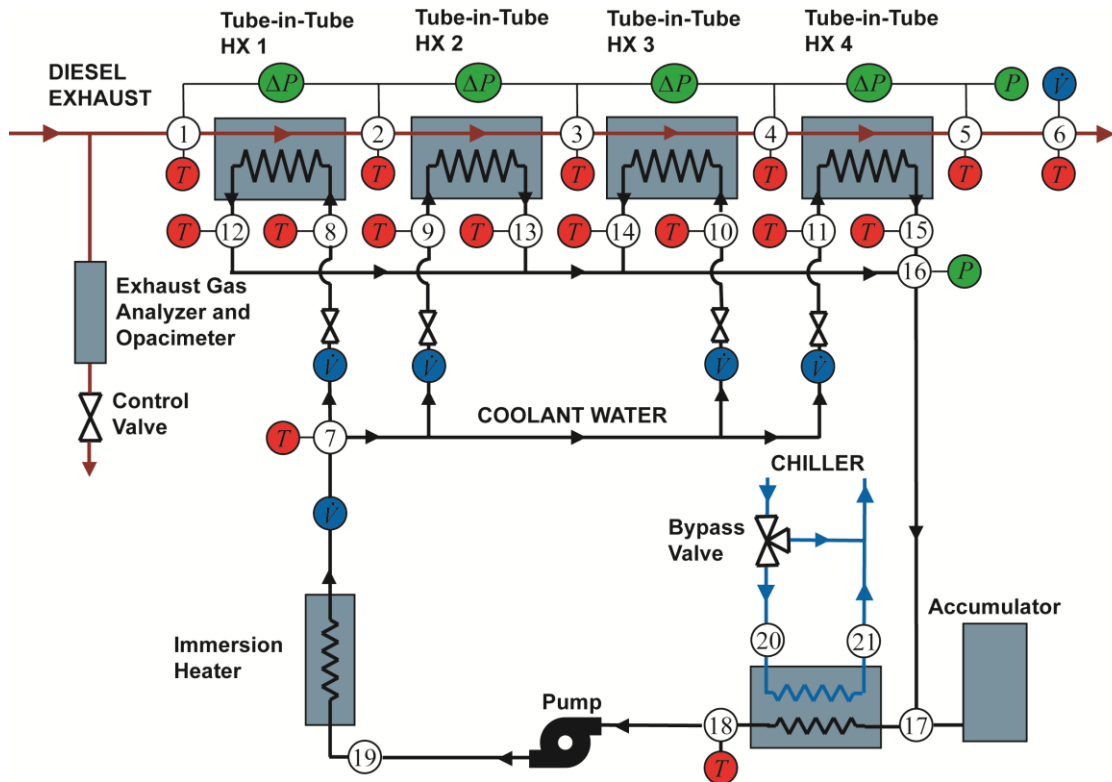


**Figure 3.6: Experimental facility schematic with four tube-in-tube heat exchangers**

56

accumulator is installed to account for any fluid expansion in the system [17] before the coolant passes through a chilled water heat exchanger to reject the heat gained by the exhaust [18]. The coolant pressure loss is recovered by the pump [19] and passes through the immersion heater where the inlet temperature to the heat exchangers is controlled. The coolant flows through a flow meter before splitting off to each heat exchanger [7].

A thermodynamic and heat transfer model is developed in the *Engineering Equation Solver* (EES) platform (Klein, 2016) to determine the fluid conditions and properties within the experimental facility so that instrumentation and equipment can be properly sized and selected. Inputs to the model come from the cycle model and include the exhaust inlet temperature, exhaust flow rate, concentrated solution inlet temperature, and dilute solution outlet temperature. The important outputs from the model are heat transfer rates from the exhaust to the coolant, the coolant temperatures, pressures, flow rates, and pressure drop across the system, and the exhaust pressure drop across each heat exchanger. The minimum and maximum values for each of these outputs are determined based on system arrangement and heat pump operating conditions.

### 3.3.1    Tube-in-Tube Heat Exchanger Model

The steady state heat transfer rates of the exhaust and coolant are predicted for each heat exchanger by assuming that each tube-in-tube heat exchanger is insulated from its surroundings; therefore, any heat rejected from the exhaust is gained by the coolant. This heat transfer rate is calculated from the heat capacitance rate and the inlet and outlet temperatures of the exhaust and coolant using Equations (3.1) and (3.2), respectively, and the *UA* and log mean temperature difference between the two fluids using Equation (3.3).

$$\dot{Q}_i = \dot{m}_{c,i} c_{p,c,i} (T_{c,out,i} - T_{c,in,i}) \tag{3.1}$$

$$\dot{Q}_i = \dot{m}_{ex,pt} c_{p,ex,i}(T_{ex,in,i} - T_{ex,out,i}) \qquad (3.2)$$

$$\dot{Q}_i = UA_i \times \Delta T_{lm,i} \qquad (3.3)$$

The subscript $i$ is used to indicate which tube-in-tube heat exchanger is being considered. The coolant mass flow rate is an unknown in this set of equations. The coolant specific heat is that for water at the average of the coolant inlet and outlet temperature. The coolant inlet and outlet temperatures are initially taken to be the concentrated solution and dilute solution temperatures for the heat pump design conditions. The exhaust flow rate per tube is determined based on the total desorber flow rate and the number of parallel tubes in the desorber, as shown in the following equation.

$$\dot{m}_{ex,pt} = \dot{m}_{ex,des}/n_{p,tubes} \qquad (3.4)$$

With a total desorber flow rate of 23.5 g s$^{-1}$ and 11 parallel tubes in the series arrangement, the exhaust flow rate per tube is 2.14 g s$^{-1}$. The exhaust inlet temperature to the first heat exchanger is know from the cycle model to be 398.8°C. The exhaust outlet temperature is an unknown obtained from the above equations. The inlet temperatures to the second, third, and fourth heat exchangers are taken as the outlets of the previous heat exchangers.

The specific heat of exhaust depends on the concentration of each constituent in the exhaust, which is determined from the chemical equation for combustion of diesel fuel with atmospheric air.

$$C_a H_b + \frac{n_{O_2}}{\varphi}(O_2 + 3.773 N_2) \rightarrow n_{prod}(\tilde{y}_{H_2O} H_2O + \tilde{y}_{CO_2} CO_2 + \tilde{y}_{O_2} O_2 + \tilde{y}_{N_2} N_2)$$

$$(3.5)$$

58
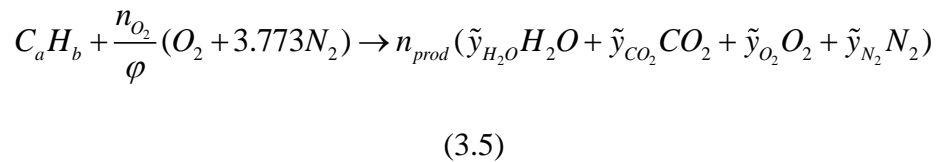
The exhaust products consist of water, carbon dioxide, oxygen, and nitrogen. Unburned hydrocarbons, particulate matter, carbon monoxide, nitrous oxides, and sulfur oxides are not considered in the calculation of specific heat due to their low concentration in the exhaust. The hydrocarbon ratio and stoichiometric ratio are taken to be $b/a = 1.8$ and $\varphi = 0.6$, respectively. These values are suggested by Heywood (1988) for diesel engines. The number of moles of oxygen for stoichiometric combustion is calculated as follows.

$$n_{O_2} = 1 + b/4a \tag{3.6}$$

The total moles of products and the mole fraction of each exhaust product are then determined from a balance of each species in Equation (3.5) and the summation of the mole fraction of each constituent to unity. This is shown in Equations (3.7) through (3.11).

$$n_{prod} = 3.773 \frac{n_{O_2}}{\varphi \tilde{y}_{N_2}} \tag{3.7}$$

$$\tilde{y}_{CO_2} = a/n_{prod} \tag{3.8}$$

$$\tilde{y}_{H_2O} = b/2n_{prod} \tag{3.9}$$

$$\tilde{y}_{O_2} = \frac{n_{O_2}}{\varphi n_{prod}} - \tilde{y}_{CO_2} - \frac{1}{2}\tilde{y}_{H_2O} \tag{3.10}$$

$$\tilde{y}_{N_2} = 1 - \tilde{y}_{H_2O} - \tilde{y}_{CO_2} - \tilde{y}_{O_2} \tag{3.11}$$

Mole fractions are converted to mass fractions.

$$y_x = \tilde{y}_x M_x / M_{tot} \tag{3.12}$$

The subscript $x$ represents any constituent of the exhaust. The specific heat of each constituent is taken as the ideal gas specific heat at the average exhaust temperature in each heat exchanger, except for the specific heat of water vapor, which is determined based on temperature and partial pressure within the mixture. The specific heat of the exhaust is

then calculated using Equation (3.13).  At the inlet exhaust temperature of 398.8°C, the specific heat of the exhaust is calculated to be 1.135 kJ kg$^{-1}$.

$$c_{p,ex,i} = y_{CO_2}c_{p,CO_2,i} + y_{H_2O}c_{p,H_2O,i} + y_{O_2}c_{p,O_2,i} + y_{N_2}c_{p,N_2,i} \qquad (3.13)$$

The overall heat transfer coefficient of each heat exchanger is determined from the total thermal resistance between the exhaust and coolant.  This consists of the convective exhaust resistance, conductive tube resistance, and convective coolant resistance, as shown in Equation (3.14).  The fouling resistance is not included here because the maximum heat transfer rates are required for component sizing.  This is representative of the condition at the beginning of the experiment before a fouling layer begins to develop.

$$R_i = R_{ex,i} + R_{tube,i} + R_{c,i} \qquad (3.14)$$

The convective exhaust resistance, shown in Equation (3.15), is dependent on the exhaust heat transfer coefficient and the inner surface area of the exhaust tube.

$$R_{ex,i} = \frac{1}{h_{ex,i}A_{IT,I}} \qquad (3.15)$$

The exhaust friction factor and Nusselt number are calculated using correlations developed by Churchill (1977a) and (1977b).

$$f = 8\left[\left(\frac{8}{Re}\right)^{12} + 1/\left(2.457\ln\left(\frac{1}{(7/Re)^{0.9}+(0.27\varepsilon/D)}\right)^{16} + (37530/Re)^{16}\right)^{1.5}\right]^{1/12}$$

$$(3.16)$$

$$Nu^{10} = 4.364^{10} + \left[\frac{e^{(2200-Re)/365}}{4.364^2} + 1/\left(6.3+\frac{0.079(f/8)^{1/2}\,Re\,Pr}{(1+Pr^{4/5})^{5/6}}\right)^2\right]^{-5} \qquad (3.17)$$

A stainless steel tube roughness of 15 μm is used in the determination of friction factor. These correlations conveniently allow for calculation of exhaust side parameters over laminar, transition, and turbulent flow regimes. The heat transfer coefficient in Equation (3.18) is calculated from the Nusselt number, thermal conductivity of exhaust, and the inner diameter of the inner tube.

$$h_{ex,i} = Nu_{ex,i} k_{ex,i} / D_{IT,I} \tag{3.18}$$

The thermal conductivity of air at the average exhaust temperature in each heat exchanger is used to approximate the thermal conductivity of the exhaust. Thermophysical properties of exhaust that are approximated with air and properties of water are determined using the Engineering Equation Solver platform. The thermal resistance of the tube is represented by Equation (3.19) for radial conduction through a hollow cylinder, and is dependent on the inner and outer tube diameter, the thermal conductivity of the tube, and the tube length.

$$R_{tube,i} = \frac{\ln(D_{IT,O} / D_{IT,I})}{2\pi k_{tube,i} L_{tube}} \tag{3.19}$$

For this analysis, the thermal conductivity of stainless steel is estimated by calculating the property at an average of the exhaust and coolant temperatures.

The convective resistance of the coolant is dependent on the coolant heat transfer coefficient and the outside surface area of the inner tube, as follows.

$$R_{c,i} = \frac{1}{h_{c,i} A_{IT,O}} \tag{3.20}$$

The Reynolds number of the coolant ranges from 31 to 226 over all test stand operating conditions; therefore, the heat transfer coefficient was calculated based on the Nusselt

number for laminar flow in a circular annulus with one surface insulated and the other at constant temperature recommended by Bergman *et al.* (2011). The Nusselt number is dependent on the ratio of the outer tube inner diameter and inner tube outer diameter, as shown in Table 3.2. A tube with a diameter of 19.0 mm and a thickness of 1.2 mm is selected for the outer tube in the tube-in-tube heat exchanger, resulting in a diameter ratio of 0.67. Linearly interpolating between points in Table 3.2 yields a Nusselt number of 5.27 for the coolant in each heat exchanger. The hydraulic diameter of the two concentric tubes is calculated using Equation (3.21), and in turn used to calculate the heat transfer coefficient in Equation (3.22). Coolant properties are determined at the average of the inlet and outlet temperatures.

$$D_h = D_{OT,O} - D_{IT,I} \tag{3.21}$$

$$h_{c,i} = \frac{Nu_{c,i} k_{c,i}}{D_h} = 5.27 \tag{3.22}$$

The exhaust, tube, and coolant resistances are summed to calculate the total thermal resistance. The *UA* for each heat exchanger is the reciprocal of the total thermal resistance.

$$UA_i = 1 / R_i \tag{3.23}$$

**Table 3.2: Nusselt number for laminar flow in an annulus with one surface insulated and the other at constant temperature (Bergman *et al.*, 2011)**

| $D_{IT,O}/D_{OT,I}$ | $Nu$ |
|---|---|
| 0.05 | 17.46 |
| 0.10 | 11.56 |
| 0.25 | 7.37 |
| 0.50 | 5.74 |
| 1.00 | 4.86 |

Log mean temperature difference is calculated based on the inlet and outlet temperatures of both the exhaust and coolant. The equation for *LMTD* varies based on a counter-flow or co-flow heat exchanger, as in Equations (3.24) and (3.25), respectively.

$$\Delta T_{lm,counter-flow,i} = \frac{\left(T_{ex,in,i} - T_{c,out,i}\right) - \left(T_{ex,out,i} - T_{c,in,i}\right)}{\ln\left(\left(T_{ex,in,i} - T_{c,out,i}\right) / \left(T_{ex,out,i} - T_{c,in,i}\right)\right)} \tag{3.24}$$

$$\Delta T_{lm,co-flow,i} = \frac{\left(T_{ex,in,i} - T_{c,in,i}\right) - \left(T_{ex,out,i} - T_{c,out,i}\right)}{\ln\left(\left(T_{ex,in,i} - T_{c,in,i}\right) / \left(T_{ex,out,i} - T_{c,out,i}\right)\right)} \tag{3.25}$$

This completes the system of equations for the tube-in-tube heat exchanger model and these equations are solved iteratively to determine the heat transfer rate, coolant flow rate, and exhaust outlet temperature for each heat exchanger.

During the tests, the coolant inlet and outlet temperatures are controlled to match tube temperature in the experimental facility to that in the desorber. Tube temperature in the desorber is dependent on the heat transfer rate, heat transfer coefficient, and temperature of the boiling ammonia-water solution.

$$T_{tube,O} = \frac{\dot{Q}}{h_s A_{tube,O}} + T_s \tag{3.26}$$

The heat transfer rate is approximated with the system of equations in the tube-in-tube heat exchanger model and the solution temperature is calculated using the cycle model. The heat transfer coefficient of the ammonia-water mixture is dependent on a variety of factors, such as desorber geometry, solution concentration, solution temperature, and solution flow rate. Delahanty (2015) performed experiments to determine the heat transfer coefficient of ammonia-water solution in a branched-tray desorber design that contained geometries

similar to the fin-tray desorber design in this study. Heat transfer coefficients were measured for a concentration of 40% ammonia by mass, solution temperatures from 170 to 190°C, and flow rates from 0.6 to 1.2 g s⁻¹. These conditions are also similar to those in the fin-tray desorber, which has a concentrated solution concentration of 42% ammonia by mass, a solution flow rate per tube of 0.4 g s⁻¹, and solution temperature ranging from 136.7 to 190.4°C. The measured heat transfer coefficients for the experiments of Delahanty (2015) ranged from 2000 to 3000 W m⁻² K⁻¹. A higher heat transfer coefficient results in a lower outer tube temperature; therefore, 3000 W m⁻² K⁻¹ is used as a conservative approximation because a lower tube temperature promotes fouling.

The tube temperature in the tube-in-tube heat exchanger is a function of the coolant temperature, the heat transfer rate, and the coolant heat transfer coefficient, as shown in the following equation.

$$T_{IT,O} = \frac{\dot{Q}_i}{h_{c,i} A_{IT,O}} + T_{c,avg,i} \qquad (3.27)$$

Substituting Equation (3.26) into (3.27) yields a relationship in Equation (3.28) for equating the tube temperature in the desorber to that in the tube-in-tube heat exchangers in the experimental facility.

$$T_{c,i} = T_s - \frac{\dot{Q}_i}{A_{IT,O}} \left( \frac{1}{h_{c,i}} - \frac{1}{h_s} \right) \qquad (3.28)$$

The coolant inlet or outlet temperatures for each heat exchanger are determined by inserting the concentrated or dilute solution temperature into Equation (3.28), respectively. Although the concentrated and dilute solution temperatures are the same for each tube pass

in the desorber, the coolant inlet and outlet temperature for each heat exchanger will vary based on the heat transfer rate. As shown in Equation (3.28), a greater heat transfer rate requires a lower coolant temperature for the same solution temperature. The first heat exchanger in the experimental facility has the greatest heat transfer rate because the exhaust is at the highest temperature; therefore, this heat exchanger requires the lowest coolant temperature to replicate the tube temperature in the desorber. However, the inlet coolant temp for each heat exchanger must be the same because a single heater controls these temperatures. In order to produce conservative results, the inlet temperature for all of the tube-in-tube heat exchangers is set to the temperature required for the first heat exchanger. Coolant inlet and outlet temperatures are compared to concentrated and dilute solution temperatures for the range of heat pump ambient temperatures in Figure 3.7. The coolant temperatures are about 10ºC less than the solution temperatures in all cases.
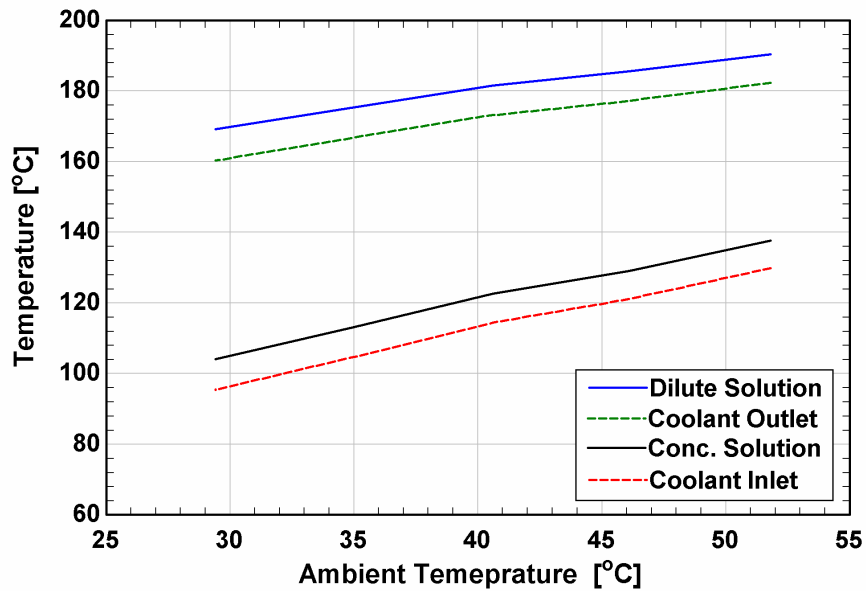


**Figure 3.7: Corrected coolant inlet and outlet temperatures to equate tube temperature in the desorber and tube-in-tube heat exchangers**

65

The heat transfer rates, coolant flow rates, and a variety of other parameters vary based on the coolant temperature and the desorber arrangement. It is important to specify the potential range of these parameters in order to size the equipment and instrumentation. A parametric study is performed considering the coolant temperature and the desorber arrangement that is being replicated. The variation in heat transfer rate is shown in Figure 3.8. For both arrangements, the heat transfer rate is greatest in the first heat exchanger and decreases in subsequent heat exchangers. At a given ambient temperature and for a specific heat exchanger, the heat transfer rate for the parallel configuration is about half that of the series configuration due to the reduced exhaust flow rate. Additionally, the heat transfer rate decreases with increasing coolant temperature due to lower temperature differences between the exhaust and coolant.
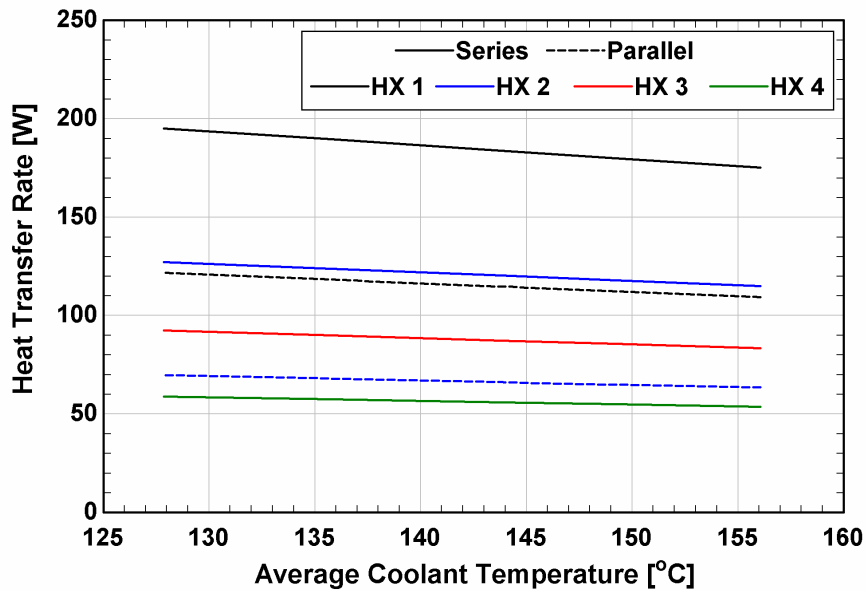


**Figure 3.8: Tube-in-Tube heat exchanger heat transfer rate range over test stand operating conditions**

The variation in coolant flow rate with test stand operating conditions is shown in Figure 3.9. The coolant flowrate follows the same trend as the heat transfer rate at a specific coolant temperature; however, flowrate increases with increasing coolant temperature. Flowrate would decrease with heat transfer rate as long as the coolant inlet and outlet temperature difference remained constant, but as depicted in Figure 3.7, the temperature difference decreases as heat pump ambient temperature and test stand coolant temperature increases. This decrease in temperature difference causes the increase in flowrate with average coolant temperature.

Another critical parameter for the design of the experimental facility is the coolant pressure. The coolant pressure must be high enough to prevent boiling, which is possible when the temperature of the outer side of the inner tube is greater than the saturation
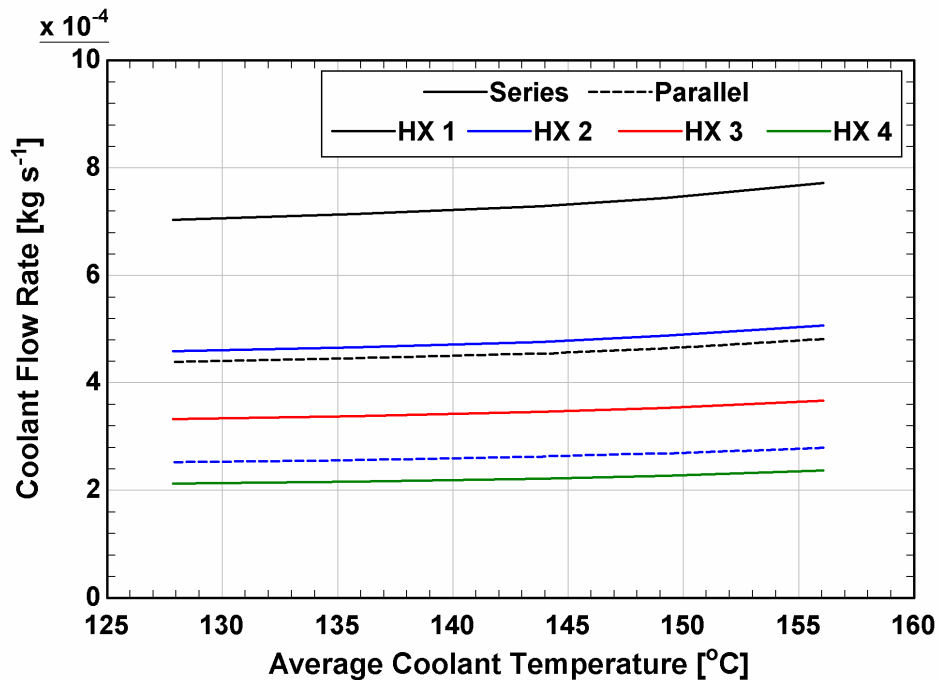


**Figure 3.9: Tube-in-Tube heat exchanger coolant flow rate range over test stand operating conditions**

temperature of the coolant. Therefore, the coolant pressure must be greater than the saturation pressure at the highest tube temperature. The tube temperature is highest at the coolant outlet of each tube-in-tube heat exchanger. The tube temperature at this location is calculated using Equation (3.29).

$$T_{IT,O,i} = \frac{\dot{Q}_i}{h_{c,i} A_{IT,O}} + T_{c,out,i} \tag{3.29}$$

The parametric study found that the tube temperature is greatest in the first heat exchanger, for the series configuration, and at the highest coolant temperature. This tube temperature is 196.2℃, and to insure boiling does not occur, the coolant pressure was specified to be the saturation pressure at a temperature ten degrees greater, 206.2℃. The saturation pressure at this temperature is 1.76 MPa, and the pressure was maintained at or above this value for all test cases.

A summary of the heat transfer and flow rate range along with other important design parameters are summarized in Table 3.3.

### 3.3.2   Pressure Drop Model

Coolant pressure drop values are required to size the pump and flow control valves in the system. Pressure drop values are calculated for each major component in the coolant loop. For the series configuration with the highest coolant temperature, the pressure drops through the Coriolis flow meter, flow control valve, turbine flow meter, and first tube-in-tube heat exchanger are 0.180, 68.9, 1.83, and 0.003 kPa, respectively. The control valves were selected to have a flow coefficient of $3.04 \times 10^{-9}$ $m^3$ $s^{-1}$ $Pa^{-0.5}$, which optimizes

**Table 3.3: Range of modeling results**

| Pressure [kPa] | | Temperature [°C] | |
|---|---|---|---|
| $P_{ex,5}$ | 101 | $T_{ex,in,1}$ | 398.8 |
| $P_{c,out,i}$ | 1764 | $T_{ex,out,2/4}$ | 200.0 - 255.1 |
| **Flow Rate [g s$^{-1}$]** | | $T_{sol,con}$ | 104.1 - 137.6 |
| $\dot{m}_{ex,pt}$ | 1.07 - 2.14 | $T_{sol,dil}$ | 169.2 - 190.4 |
| $\dot{m}_{c,1}$ | 0.48 - 0.77 | $T_{c,in,i}$ | 95.3 - 129.8 |
| $\dot{m}_{c,2}$ | 0.27 - 0.51 | $T_{c,out,i}$ | 160.4 - 182.3 |
| $\dot{m}_{c,3}$ | 0.33 - 0.37 | **Heat Transfer [W]** | |
| $\dot{m}_{c,4}$ | 0.21 - 0.24 | $\dot{Q}_1$ | 109.2 - 195.1 |
| $\dot{m}_{c,tot}$ | 0.75 - 1.88 | $\dot{Q}_2$ | 63.47 - 127.2 |
| **Reynolds Number** | | $\dot{Q}_3$ | 83.37 - 92.36 |
| $Re_{ex,i}$ | 3,819 – 9,395 | $\dot{Q}_4$ | 53.76 - 58.92 |
| $Re_{c,i}$ | 31 - 226 | **Resistances [K W$^{-1}$]** | |
| | | $R_{ex,i}$ | 1.069 - 1.859 |
| | | $R_{tube,i}$ | 0.0062 |
| | | $R_{c,i}$ | 0.1085 |
| | | $R_i$ | 1.186 - 1.974 |

controllability of flow rate while minimizing pressure drop. The total coolant pressure drop across the loop is predicted to be 71.0 kPa. With this pressure drop and a volumetric flow rate of $1.78 \times 10^{-6}$ m$^3$ s$^{-1}$, the required pump work is 0.13 W. For a pump efficiency of 0.9 and a motor efficiency of 0.6, the total power requirement for the pump is 0.23 W.

A model of the exhaust pressure drop across the test facility is used to select pressure measurement instrumentation. The pressure drop must also be less than the allowable back pressure on the diesel engine. The total exhaust pressure drop across the system is equal to the sum of the pressure drop across the four heat exchangers, the pressure drop across the wedge meter used to measure exhaust flow rate, and the pressure drop in the tubing at the outlet of the test stand. For both test stand configurations and across all

coolant temperatures, the pressure drop through each tube-in-tube heat exchanger ranges from 228 to 1153 Pa. This is used to select the differential pressure transducer that measures heat exchanger pressure drop. In the maximum case, the total exhaust pressure drop across the test stand is 6,771 Pa, which is much less than the maximum generator back pressure specified by the manufacturer to be 12,000 Pa.

A complete description of the methods used to calculate coolant and exhaust pressure drops is included in APPENDIX A.

### 3.3.3    Heater and Chiller Sizing

The immersion heater, between state points [19] and [7] in the experimental test facility, is sized to heat the coolant from ambient temperature to the coolant inlet temperature to the heat exchangers in a single pass of the fluid through the heat exchanger. This is required for start-up of the test facility from resting to operating temperature without having heat input from the exhaust. By assuming that the heater is thermally isolated from its surroundings, the heat transfer rate from the heater to the coolant is represented by Equation (3.30).

$$\dot{Q}_{heater} = \dot{m}_{19} c_{p,c,avg} \left( T_7 - T_{19} \right) \tag{3.30}$$

The heater outlet temperature is specified as the heat exchanger inlet temperature $(T_7 = T_{c,in,i})$, while the heater inlet temperature is equal to ambient temperature $(T_{19} = T_{amb})$. The heat transfer rate is greatest when the coolant flow rate and heat exchanger inlet temperature are greatest, which were determined from the heat exchanger model to be 1.88 g s$^{-1}$ and 129.8°C, respectively. For an ambient temperature of 20°C and

the specific heat determined at the average of the inlet and outlet temperatures, the maximum required heater power is 614 W.

The chilled water heat exchanger, between points [17] and [18] in the test facility, is designed to reject the heat gained by the coolant from the exhaust. The heat exchanger is coupled to a chilled water mixture of 25% propylene glycol in water that is provided by a Carrier 30RAN050 176 kW chiller. Assuming that the heat exchanger is thermally isolated from its surroundings, the heat transfer rate from the coolant to the chilled water is expressed with Equations (3.31), (3.32), and (3.33).

$$\dot{Q}_{cwhx} = \dot{m}_{17} c_{p,c,avg} (T_{17} - T_{18}) \tag{3.31}$$

$$\dot{Q}_{cwhx} = \dot{m}_{20} c_{p,cw,avg} (T_{22} - T_{21}) \tag{3.32}$$

$$\dot{Q}_{cwhx} = UA_{cwhx} LMTD_{cwhx} \tag{3.33}$$

It is assumed that there is no heat loss between components in the facility; therefore, the inlet temperature to the chiller is equal to the coolant temperature in the outlet header ($T_{17} = T_{16}$). The coolant temperature in the outlet header is calculated using Equation (3.34).

$$T_{16} = \frac{1}{\dot{m}_{16}} \sum_{i=1}^{n=2,4} \dot{m}_{c,i} c_{p,c,i} T_{c,out,i} \tag{3.34}$$

The coolant flow rate at state point [16] is equal to the sum of the heat exchanger flow rates. The test facility is designed such that the outlet temperature from each heat exchanger is equal. This results in a temperature in the outlet header that is equal to the coolant outlet temperature of the heat exchangers ($T_{17} = T_{16} = T_{c,out,i}$). The outlet

71

temperature of the chilled water heat exchanger is determined by working backwards from the inlet header. When the coolant has reached the desired inlet temperature and the system is being heated by exhaust flow through the tube-in-tube heat exchangers, there is no need to heat the coolant ($\dot{Q}_{heater} = 0$). This results in the heater inlet and outlet being at the same temperature ($T_7 = T_{19}$). Assuming no heat addition by the pump, the chilled water heat exchanger outlet temperature must be equal to the heater inlet temperature, and ultimately the inlet temperature to each tube-in-tube heat exchanger ($T_{18} = T_{c,in,i}$).

The coolant inlet and outlet temperatures and flow rate were calculated previously and are used to calculate the chilled water heat exchanger heat transfer rate with Equation (3.31). The inlet temperature and the flowrate of the chilled water are designated by the chiller to be 12.8°C and 0.1 kg s$^{-1}$. The *UA* and the outlet temperature of the propylene glycol-water are then calculated using Equations (3.32) and (3.33).

These outputs are critical to the design of the chilled water heat exchanger so that the outlet temperature of the chilled water does not exceed the boiling point and the heat exchanger is sized appropriately. The *UA* dictates the heat exchanger size and is equal to the inverse of the total thermal resistance, as shown in Equation (3.35).

$$UA_{cwhx} = 1 / R_{cwhx} \tag{3.35}$$

A tube-in-tube heat exchanger is also used as the chilled water heat exchanger. The inner tube has an outer diameter of 6.4 mm and a thickness of 0.9 mm and the outer tube has an outer diameter of 12.7 mm and a thickness of 0.9 mm. This results in a hydraulic diameter, calculated using Equation (3.21), of 3.9 mm. The total resistance in the chilled water heat

exchanger is composed of the convective coolant, conductive tube, and convective chilled

water resistance.

$$R_{cwhx} = \frac{1}{h_{c,cwhx}\left(\pi D_{IT,I,cwhx}L_{cwhx}\right)} + \frac{\ln(D_{IT,I,cwhx}/D_{IT,I,cwhx})}{2\pi k_{tube}L_{cwhx}} + \frac{1}{h_{cw,cwhx}\left(\pi D_{IT,O,cwhx}L_{cwhx}\right)}$$

(3.36)

The coolant heat transfer coefficient through the chilled water heat exchanger is calculated

using the correlation of Churchill (1977a), shown in Equation (3.17). The Reynolds number

for propylene glycol through the annulus of the chilled water heat exchanger is a maximum

of 2402, which is slightly greater than the threshold for transition from laminar to

transitional of 2300 as suggested by Bergman *et al.* (2011).  However, because the Nusselt

number for flow through concentric annuli are not well defined in the transitional regime,

the Nusselt number for laminar flow through an annulus is used, as shown in Table 3.2.

This will result in slight under prediction of heat transfer coefficient and result in a slight

over calculation of required heat exchanger size.  The Nusselt number for laminar flow

through the annulus of the chilled water heat exchanger is 5.6, and is used to calculate the

heat transfer coefficient.  Finally, the chilled water heat exchanger length was found using

Equation (3.36).

A plot of the required length and the propylene glycol-water outlet temperature is

shown Figure 3.10 for all coolant temperatures and test stand configurations. The length of

the heat exchanger is much greater for the series case than the parallel case because of the

larger heat duty.  The length also increases as the coolant temperature decreases.  This is a

result of a decreasing temperature difference between the coolant and the propylene glycol-
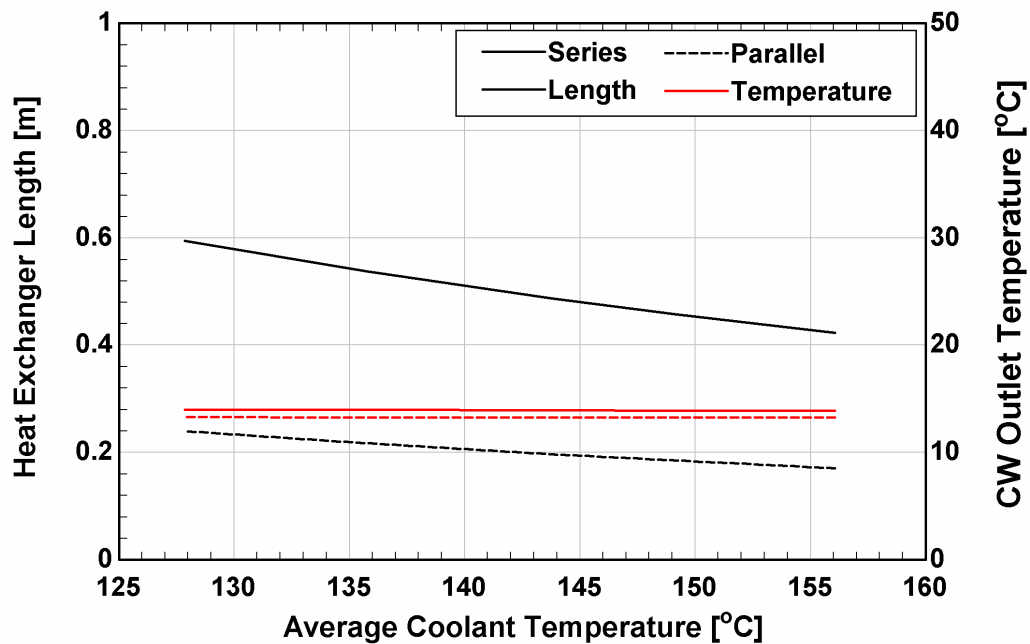
**Figure 3.10: Required chilled water heat exchanger length as a function of average coolant temperature and test stand orientation**

water mixture. In order to get the same heat transfer rate with a lower temperature difference, the *UA* must be larger. The propylene glycol-water outlet temperature is much less than the boiling point at atmospheric pressure, 102°C, for all cases. The maximum required length of the heat exchanger is 0.59 m; therefore, the component must be at least this length for proper facility operation at the lowest coolant temperatures. At the higher coolant temperatures and in the parallel configuration, the coolant outlet temperature is controlled to the desired value by decreasing the flow rate of the propylene glycol-water mixture with the bypass valve.

A set of sample calculations for all of the experimental facility modeling and design is shown in APPENDIX D.

## 3.4 Experimental Facility Design and Control

### 3.4.1    Equipment and Instrumentation

The thermodynamic, heat transfer, and pressure drop model of the experimental facility allows for the proper sizing and selection of the equipment and instrumentation for the facility.  The specifications for all of the components in the facility are shown in Table 3.4.   The assembled experimental facility is shown in Figure 3.11 with the visible components labeled.  Beginning at the Tuthill pump [1], coolant flows to the Watlow 1000 W immersion heater [2] where the coolant is heated to the desired heat exchanger inlet temperature.  Exiting the heater, coolant flows through a MicroMotion Coriolis flowmeter [3] to measure the total coolant flowrate.  The coolant then splits into four parallel paths to each heat exchanger with a Swagelok flow control valve [4] and Flow Technology turbine
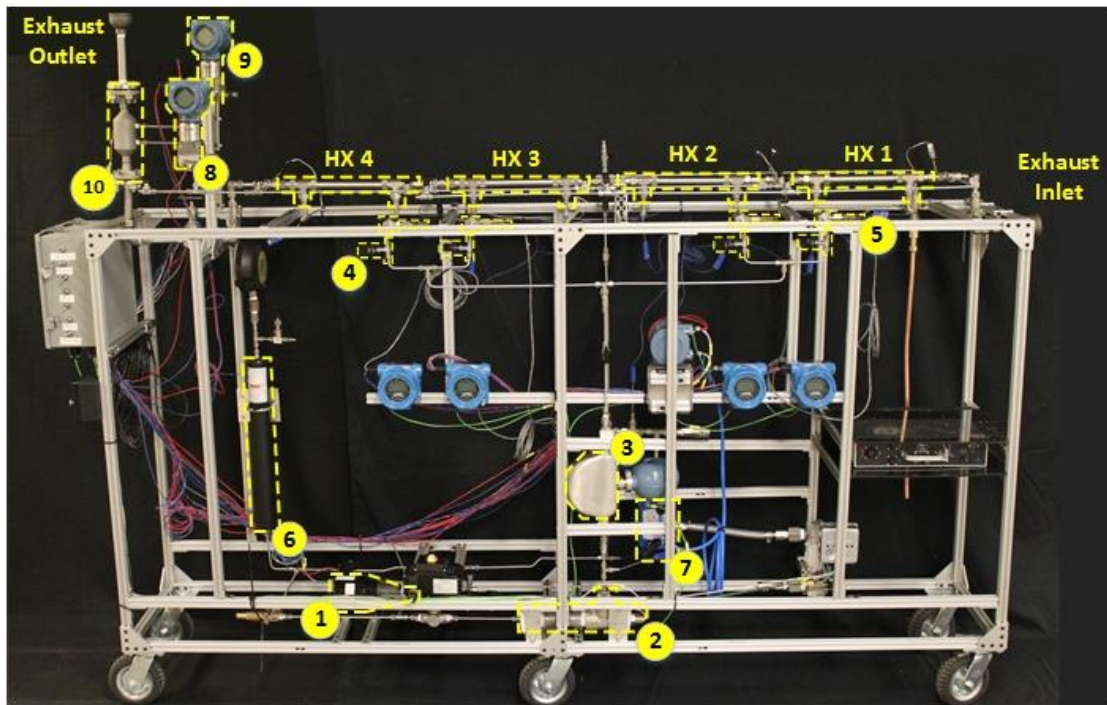


**Figure 3.11: Fouling test facility**

**Table 3.4: Equipment and instrumentation specifications**

| Fluid Loop | Name | Figure Label | Vendor and Model | Range | Accuracy |
|---|---|---|---|---|---|
| **Coolant** | Gear Pump | 1 | Tuthill DGS.38 | 5.30 g s$^{-1}$ @1.8 MPa | - |
| | Pump Motor | - | Fasco | 120 W | - |
| | Pump Drive | - | IronHorse GSD4-24A-5C | 124 W | - |
| | Heater | 2 | Watlow | 1000 W | - |
| | Heater Controller | - | Watlow DIN-A-MITE Style A | 25 A @ 600 VAC | - |
| | Total Flow Meter | 3 | Micromotion CMFS010M | 0.20 to 25 g s$^{-1}$ | 0.10% |
| | Flow Control Valve | 4 | Swagelok SS-SS4-VH | $3.04 \times 10^{-9}$ m$^3$ s$^{-1}$ Pa$^{-0.5}$ | - |
| | Turbine Meters | 5 | Flow Technology FTO-1 | 0.06 to 5.04 g s$^{-1}$ | 0.25% |
| | Pressure Transducer | - | Omega PX172-750GI | 0 to 5.171 MPa | 0.013 MPa |
| | Piston Accumulator | 6 | Parker | 1 L | - |
| | Thermocouple | - | Omega TMQSS | 0 to 350ºC | 0.5ºC |
| **Propylene Glycol - Water** | 3-Way Bypass Valve | - | JCI 41P762 | - | - |
| | Bypass Valve Actuator | 7 | JCI 41P484 | 6 N m | - |
| **Exhaust** | Opacimeter | - | Wager 7500 | 0 to 100% | 0.10% |
| | Exhaust Gas Analyzer | - | NOVA 7464K | 0-25% $O_2$ 0-20% $CO_2$ 0-5% CO | 1% FS |
| | Abs. Pressure Transducer | - | Rosemount 2088 A | 0 to 206.8 kPa | 0.065% FS |
| | Diff. Pressure Transducer | 8 | Rosemount 3051S | -62.2 to 62.2 kPa | 0.035 % FS |
| | Diff. Pressure Transducer | 9 | Rosemount 3051S | -62.2 to 62.2 kPa | 0.035 % FS |
| | Wedge Flow Meter | 10 | Coin PCOAA2AH1Z | 2.1 g s$^{-1}$ @ 1.5 kPa | |
| | Thermocouple | - | Omega JMQSS | 0 to 750ºC | 1.1ºC |

meter [5] along each path. After exiting the flow meter, the coolant flows through each tube-in-tube heat exchanger. The inner tube of the heat exchanger is 12.7 mm in outer diameter with a wall thickness of 0.9 mm and a length of 444.5 mm. The outer tube is 19.1 mm in outer diameter with a wall thickness of 1.2 mm and a length of 222.2 mm. A tee is connected at each end of the outer tube and the coolant enters through the branch of one tee, flows through the annulus between the two tubes, and exits through the branch of the other tee. Coolant inlet and outlet temperature is measured at these locations with Omega T-type thermocouples. The coolant flow length, the length from center to center of the tees, is 254.0 mm. Including the coolant that is stagnant in the end of each tee, the length of exposure of the inner tube to coolant is 285.0 mm. Exhaust temperature measurements are made with an Omega J-type thermocouple at the inlet and outlet of each heat exchanger. Exhaust pressure drop across the heat exchanger is measured at the same locations with a Rosemount 3051S differential pressure transducer [8]. Flow rate of the exhaust is determined by measuring the pressure drop with a Rosemount 3051 S differential pressure transducer [9] across a Coin wedge meter [10]. The dimensions of the tube-in-tube heat exchangers along with the fluid inlet and outlets are shown in Figure 3.12.

After the coolant exits each tube-in-tube heat exchanger, it recombines and the pressure is measured. This location was selected for pressure measurement because the coolant is hottest and has the greatest potential for vaporization. After the pressure is measured, the coolant flows through the chilled water heat exchanger to reject the heat gained from the exhaust. The chilled water is provided by a Carrier 30RAN050 176 kW chiller. The total cooled length is 600 mm, as sized in the chilled water heat exchanger model. The propylene glycol-water flow rate through the annulus of the chilled water heat

77
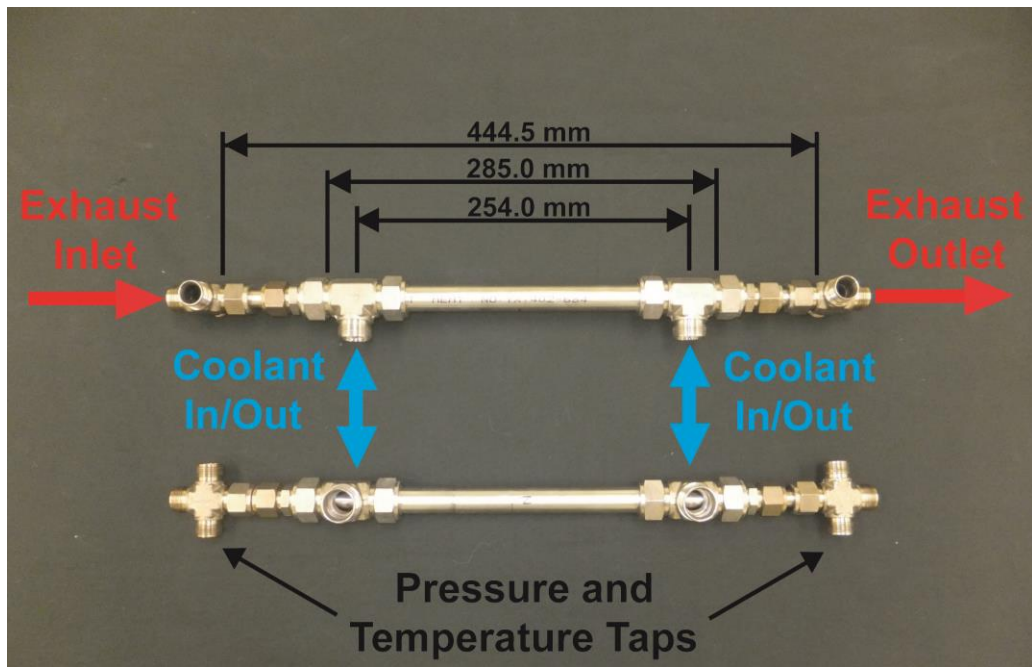
**Figure 3.12: Tube-in-Tube heat exchanger**

exchanger is controlled with a Johnson Controls 3-Way valve and actuator [7]. The valve

can be modulated to direct flow between the chilled water heat exchanger and a bypass.

This enables control of the coolant outlet temperature. After exiting the chilled water heat

exchanger, the coolant returns to the pump. A Parker piston accumulator is installed on

the suction side of the pump to account for fluid expansion and to pressurize the coolant to

prevent vaporization.

The exhaust that enters the test facility is provided by a Kohler 10REOZDC 10 kW

diesel generator. The load on the generator is provided by a Scotcher Model 627 0-10.8

kW adjustable load bank. This allows for control of load and engine operating conditions.

The exhaust exiting the generator can either be directed to the experimental facility or

rejected directly to the atmosphere. An Accuseal SPV132 control valve is installed on the

exhaust outlet to the atmosphere to control the flow rate of exhaust to the experimental

facility. The valve is sized such that when it is fully open, the flow rate to the experimental facility is less than the minimum required flow rate. This way closing the valve allows for control of the flow rate to the desired value. The specifications and arrangement of the generator, load bank, and control valve are shown in Table 3.5 and Figure 3.13.

The generator is selected based on the exhaust flow rate, temperature, and composition at rated power output. To provide the required heat input to the desorber, the generator must provide exhaust at a flow rate and temperature of at least 23.5 g s$^{-1}$ and 400ºC, respectively. The Kohler 10REOZDC is specified to produce 23.5 g s$^{-1}$ of exhaust
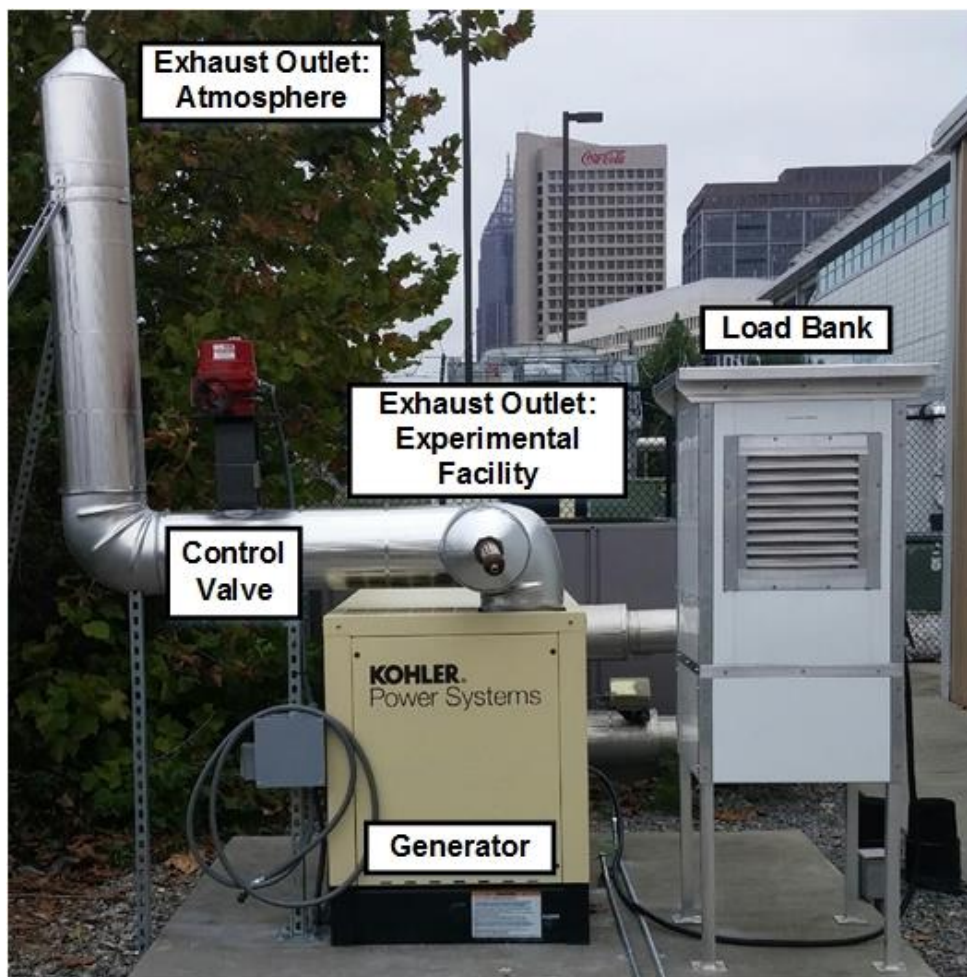


**Figure 3.13: Generator, load bank, and exhaust routing assembly**

**Table 3.5: Specifications of generator, load bank, and exhaust flow control valve**

| Name | Vendor | Model | Description |
|------|--------|-------|-------------|
| **Generator** | Kohler | 10REOZDC | 0.048 m$^3$ s$^{-1}$, 550ºC Exhaust @ 10 kW rated power |
| **Load Bank** | Sotcher Measurement | 627 | 0 to 10.8 kW capacity |
| **Control Valve** | Accuseal | SPV132 | 7.6×10$^{-5}$ C$_v$ |

at a temperature of 550ºC, which meets the requirements for flow rate and temperature.

The manufacturer specifies the emission factors of particulate matter and hydrocarbons to

be 0.42 g kWh$^{-1}$ and 8.85 g kWh$^{-1}$. These values are compared to those reported by Shah

*et al.* (2006) for 60-2000 kW diesel back-up generators (BUGs) and those found by Dongzi

*et al.* (2009) for 10 to 100 kW military diesel generators in Table 3.6. The emission factor

of hydrocarbons of the Kohler generator is much greater than that in either of the studies,

and the emission factor of particulate matter of the Kohler generator is greater than that of

the 10 to 100 kW military generators and slightly less than that for the 60 to 2000 kW

BUGs. This suggests that the emissions from the Kohler 10REOZDC used in this study

are either be greater than or approximately equal to that of in-use diesel generators. This

**Table 3.6: Generator emissions comparison**

| Generator | PM [g kWh$^{-1}$] | HC [g kWh$^{-1}$] |
|-----------|-------------------|-------------------|
| Kohler 10REOZDC | 0.42 | 8.85 |
| 60-2000 kW BUGs (Shah *et al.* (2006)) | 0.48 | 0.22 |
| 10-100 kW Military Generators (Dongzi *et al.* (2009)) | 0.26 | 2.43 |

provides fouling results that are valid for a wide range of diesel engine types and applications.

### 3.4.2    Data Acquisition and Controls

Data acquisition and control of the experimental facility is performed with a National Instruments cDAQ-9188. Data are acquired and control signals are output every second. The control process variables are the tube-in-tube heat exchanger inlet and outlet temperature, total coolant flow rate, and the exhaust flow rate.

The tube-in-tube heat exchanger inlet temperature is controlled with a combination of the chilled water heat exchanger and the immersion heater. The chilled water heat exchanger reduces the temperature of the coolant slightly below the required coolant inlet temperature. The coolant outlet temperature of the chilled water heat exchanger is controlled with the Johnson Controls 3-Way valve actuator. A signal input of 4 mA to the valve actuator directs all of the chilled water through the bypass, while a signal of 20 mA directs all of the flow through the chilled water heat exchanger. The input signal was controlled manually, and a value of 10 mA provided the required cooling for most test cases.

Fine adjustment of the tube-in-tube heat exchanger inlet temperature is achieved with the power output of the Watlow 1000 W immersion heater. This power output is varied with a Watlow Din-A-Mite Style A power controller. The controller varies the pulse width of the power supplied to the immersion heater based on a 4-20 mA input, where 4 mA signals no power to the heater and 20 mA signals constant power. The required control signal is determined through a PI controller in NI LabView. A block diagram of a generalized PI controller is shown in Figure 3.14.    In this case, the setpoint, *s(t)*, is the

desired heat exchanger inlet temperature, the control variable, $u(t)$, is the 4-20 mA output to the power controller, and the process variable, $y(t)$, is the actual heat exchanger inlet temperature. The control variable is determined from the error between the set point and process variables, $e(t)$, the proportional gain, and the integral time, as shown in Equation (3.37).

$$u(t) = K_p \left[ e(t) + \frac{1}{T_i} \int_0^t e(t)dt \right]$$  (3.37)

The proportional gain and the integral time are determined by increasing the proportional gain until the process variable begins to oscillate. The proportional gain is taken to be half of the value at which it oscillates. The integral time is then decreased until the steady state error is reduced to an acceptable value. The proportional gain and integral time for the heat exchanger inlet temperature are 0.001 and 1, respectively.

The total coolant flowrate is dependent on the voltage input to the pump, which can be varied from 0 to 24 VDC by the IronHorse pump drive. The 0 to 24 VDC output from the pump is based on a 4-20 mA signal input, where 4 mA results in a 0 VDC output and 20 mA a 24 VDC output. This 4-20 mA signal is also controlled with a PI controller in NI Labview with a proportional gain and integral time of 0.0005 and 0.1, respectively.
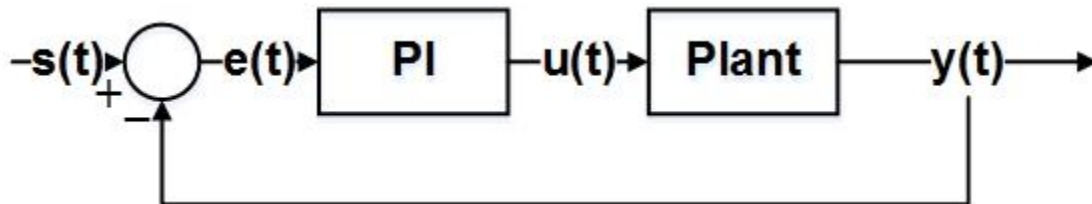


**Figure 3.14: PI block diagram**

The total coolant flowrate is controlled to a constant value during the start of the experiment. When exhaust first enters the tube-in-tube heat exchangers, the coolant inlet and outlet temperature are both at the desired inlet temperature. As heat transfer occurs from the exhaust to coolant, the coolant outlet temperature increases until it reaches a steady state value. The total coolant flow rate is selected such that the steady state outlet temperature is approximately equal to the desired value. As the experiment progresses, fouling of the exhaust tube causes the heat transfer rate to decrease, which results in a decrease in the outlet temperature if the coolant flow rate is held constant. To prevent this, when the coolant outlet temperature reached the desired value, the process variable for the pump output is changed from the total coolant flow rate to the coolant outlet temperature of the heat exchanger. This allowed for the coolant outlet temperature to remain constant throughout the experiment while the coolant flow rate decreased to account for the effect of fouling. The proportional gain and integral time for the control of coolant outlet temperature is -0.0005 and 0.7. The proportional gain is negative because an increase in flow rate causes a reduction in coolant outlet temperature and vice versa.

The last process variable is the exhaust flow rate through the experimental facility. The flow rate is controlled with the valve on the exhaust piping from the generator that goes directly to the atmosphere. If the valve was kept at a constant position through the test, the flow rate would decrease as the tubes fouled and caused increased restriction through the test stand; therefore, the valve was controlled to achieve a constant flow rate. The valve position was determined by a 4-20 mA signal input to the valve actuator, where 4 mA specifies a closed valve and 20 mA a fully open valve. The proportional gain and

integral time were determined to be -8 and 0.3. A summary of the process variables, control

variables, proportional gain, and integral time for each controller is provided in Table 3.7.

### 3.5 Experimental Methodology and Procedure

#### 3.5.1    Experimental Methodology

A two-step approach is developed to first determine the worst case conditions for

fouling and then quantify the most severe effect of fouling on heat transfer and pressure

drop. Determining the worst case condition for fouling is done through a series of steady

state experiments.  In these experiments, the coolant and exhaust inlet temperatures are at

their steady state values before exhaust enters the facility.  Performing experiments in this

matter eliminates the influence of start-up effects on fouling while investigating a wide

range of generator and heat pump operating conditions.

From the literature review performed in Chapter 2, it was found that the most influential

factors on fouling are the temperature difference between the exhaust and coolant, the

particulate matter and hydrocarbon concentration in the exhaust, and the velocity of the

**Table 3.7: Summary of controllers and PI gains**

| Process Variable | PV Range | Control Variable | CV Range | Proportional Gain | Integral Time |
|---|---|---|---|---|---|
| Coolant Inlet Temperature | 95.3 to 129.8°C | Heater controller input signal | 0.004 to 0.020 A | 0.001 | 1 |
| Total Coolant Flowrate | 2.7 to 6.8 kg hr$^{-1}$ | Pump drive input signal | | 0.0005 | 0.1 |
| Coolant Outlet Temperature | 160.4 to 182.3°C | Pump drive input signal | | -0.0005 | 0.7 |
| Exhaust Flowrate | 0.0011 to 0.0021 g s$^{-1}$ | Exhaust valve input signal | | -8 | 0.3 |

exhaust. Therefore, the generator and heat pump operating conditions that influence fouling are the coolant temperature, the generator load, and the exhaust flow rate. Coolant temperature affects the temperature difference between the exhaust and coolant. Generator load impacts both the exhaust inlet temperature and the composition of the exhaust. Exhaust velocity, which could be optimized in the design of the desorber to reduce the effect of fouling, has the potential to remove deposited particulate matter through flow induced shear. These factors are investigated sequentially, as shown in the flow chart in Figure 3.15. An initial test is performed at design conditions, and the following set of tests

## Steady State Testing

```
┌─────────────────────────────┐
│      Design Conditions      │
└─────────────────────────────┘
              ↓
┌─────────────────────────────┐
│   vary Coolant Temperature  │
└─────────────────────────────┘
          worst case
       coolant temperature
              ↓
┌─────────────────────────────┐
│      vary Generator Load    │
└─────────────────────────────┘
          worst case
        generator load
              ↓
┌─────────────────────────────┐
│    vary Exhaust Flow Rate   │
└─────────────────────────────┘
        ↓           ↓
┌─────────────────────────────┐
│    Worst Case Conditions    │
│         for Fouling         │
└─────────────────────────────┘
```
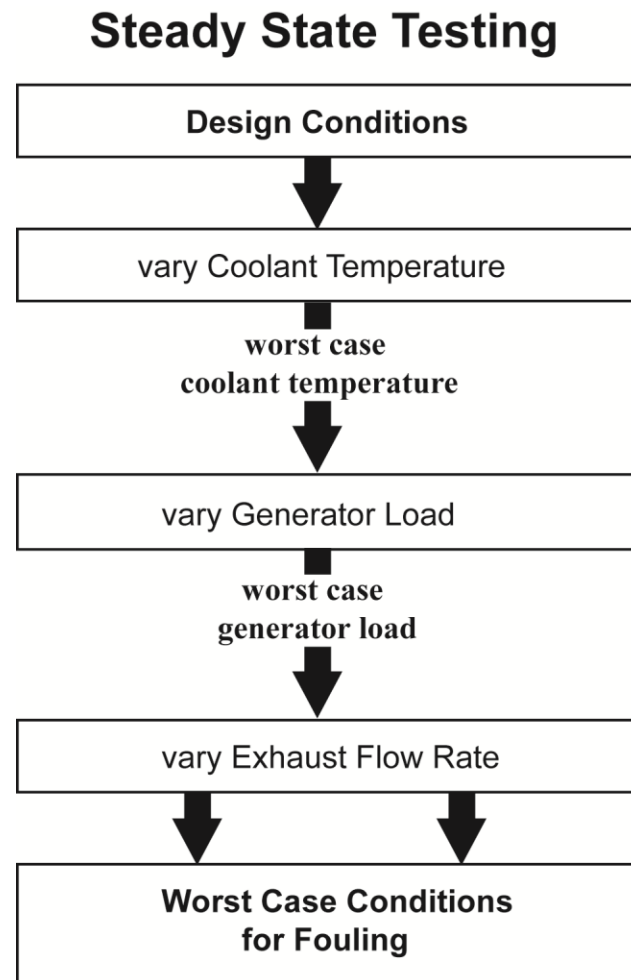
**Figure 3.15: Flow chart of steady state testing method**

vary the coolant temperature with the generator load and exhaust flow rate at design conditions. The coolant temperature that results in the greatest heat transfer resistance and pressure drop is used in the following investigation of the effect of generator load. Similarly, the worst case generator load is used in combination with the worst case coolant temperature while the exhaust flow rate is varied. Ultimately, this methodology produces the worst case conditions for fouling. The complete steady state test matrix is shown in Table 3.8. Experiments are performed for both the series and parallel test facility configurations.

Initial transients in the start-up of the generator and heat pump are also investigated in these experiments. Two practical generator and heat pump transient cases are investigated at the worst case fouling condition determined in steady state testing. The first case simulates a situation when the generator is already running to meet an electrical load and a cooling load is suddenly required. In this situation, referred to as engine steady experiments, the generator is started to bring the exhaust to the steady state temperature before it is directed into the experimental facility, but the coolant is initially near ambient temperature. The second case simulates a situation in which an electrical load and cooling load are needed simultaneously. In this situation, referred to as engine start-up

**Table 3.8: Steady state test matrix**

| Configuration | Coolant In/Out Temperature [ºC] | Generator Load [%] | Exhaust Flow Rate [g s⁻¹] |
|---|---|---|---|
| **Series** | 129.8/182.3 | 100 | 2.6 |
| | 114.4/173.2 | 80 | 2.1 |
| | 95.3/160.4 | 60 | 1.6 |
| **Parallel** | 129.8/182.3 | 100 | 1.4 |
| | 114.4/173.2 | 80 | 1.1 |
| | 95.3/160.4 | 60 | 0.8 |

**Table 3.9: Transient test matrix**

| Transient Case | Coolant Start-up Time [min] |
|---|---|
| **Engine Steady** | 0 |
| | 15 |
| | 30 |
| **Engine Start-up** | 0 |
| | 15 |
| | 30 |

experiments, the exhaust from the generator is directed into the experimental facility at the instant that it is started, and the coolant is again near ambient temperature. For both cases, the start-up time required for the coolant inlet temperature to reach the steady state value is varied, as this replicates the thermal transient for the ammonia-water solution in the desorber to reach operating temperature. The test matrix for transient experiments is shown in Table 3.9.

By executing the steady state experiments, the worst case conditions for fouling are determined, and performing transient experiments at that worst case quantify the most severe fouling resistance and pressure drop that result from fouling.

### 3.5.2 Experimental Procedure

Before beginning each experiment, the coolant loop of the experimental facility is charged with distilled water. The air side of the piston accumulator is first charged to a pressure greater than the pressure of the water that will be charged into the coolant loop. This ensures that the piston is at the bottom of the accumulator and no water would enter it at this time. Distilled water is then forced from a pressurized storage tank into the bottom of the facility. Initially, the water is allowed to flow to the top of the facility and exit

through an open valve, which forces the air out of the coolant loop. When most of the air is removed, the valve at the top of the facility is closed and the water in the facility reaches the same pressure as that in the storage tank. The accumulator is then filled with water by releasing the pressure on the air side of the piston. The weight of the water storage tank is monitored, and once 0.5 kg of water is added to the accumulator, water supply from the storage tank is closed off. This amount of water results in the accumulator being half full, allowing for expansion of the water as it is heated. Lastly, the water is pressurized by filling the air side of the accumulator with nitrogen to a pressure of about 2 MPa, which is above the saturation pressure corresponding to the coolant outlet temperature in all test cases.

To perform steady state experiments, the pump is started and the total flow rate is controlled to the required total flow rate value predicted in the facility model for each test case. With the pump running, the immersion heater is turned on and the coolant inlet temperature is controlled to the desired value. Prior to starting the generator, a valve in line with the exhaust flow on the facility is closed and the flow control valve to the atmosphere is fully opened. This ensures that no exhaust is directed into the experimental facility and that there is no excess back pressure on the generator. The generator is started, and after both the exhaust temperature near the inlet of the facility and the coolant inlet temperature to each heat exchanger reached steady state, the exhaust valve on the facility is opened and the exhaust flow is controlled to the desired value. Data acquisition begins at this time with data recorded every second, except for the exhaust pressure drop and composition measurements, which were taken manually every hour. Once the tube-in-tube heat exchanger coolant outlet temperature reaches the desired value, the pump control is

changed from controlling the total flow rate to controlling the coolant outlet temperature. The experiment continues in this manner until the fouling resistance reaches steady state, which is specified as less than two percent change in the fouling resistance per hour for two consecutive hours.

The start-up procedure for transient testing is slightly different than that for steady state testing. In the engine steady case, the engine is started first with the valve on the exhaust line of the experimental facility closed. Once the exhaust reaches a steady state temperature near the inlet of the facility, the valve is opened and the exhaust is controlled to the desired flow rate through the facility. At the same time, the immersion heater is turned on. The heat output is set to a constant value that was predetermined to achieve the desired coolant start-up time. Once the coolant inlet temperature reaches the desired value, automatic control of the heat exchanger inlet temperature begins. In the engine start-up case, the exhaust valve on the experimental facility is open and the flow control valve to the atmosphere is closed to the position that is predetermined to produce the desired exhaust flow rate. The generator is started, forcing exhaust through the facility before it has reached steady state temperature. The exhaust flow control is changed to automatic, and the process for controlling coolant inlet temperature is the same as in the engine steady case. Similar to the steady state fouling experiments, the tests are performed until the fouling resistance reaches steady state.

After a test is completed, all of the exhaust is directed to the atmosphere, the generator is shut down, and all of the chilled water flow is directed through the chilled water heat exchanger to cool the facility down. Once all of the coolant temperatures are below a safe

value, the coolant pump is turned off. Between each experiment, the facility is discharged

and the fouled exhaust tubes are extracted for further analysis.

**3.6 Fouling Layer Analysis**

In this section, the methodology to determine the thickness of the fouling layer

using optical imaging is explained.

*3.6.1    Imaging Procedure*

A manual action tube cutter is used to disassemble the tube-in-tube heat exchanger

while being held firmly in a vice. The inner tube is then cut at the midsection using a parting

tool on a lathe. A countersink tool is used to cut the tube at a slight angle to ensure that the

deposit layer is not contacted. All operations are done manually with care to ensure that

minimum disturbance is caused to the soot layer.   Coolant is not used in the cutting process,

and saddles support either side of the tube to prevent it from falling.  The cut tube is shown

in Figure 3.16. The tube is inserted into a jig that allows for consistent image analysis.  The

jig is designed so that a quarter image of the tube is taken and it is rotated by exactly 90°

to take the next quarter image. An Aven SPZ-50 microscope and Aven CMOS 26100-240
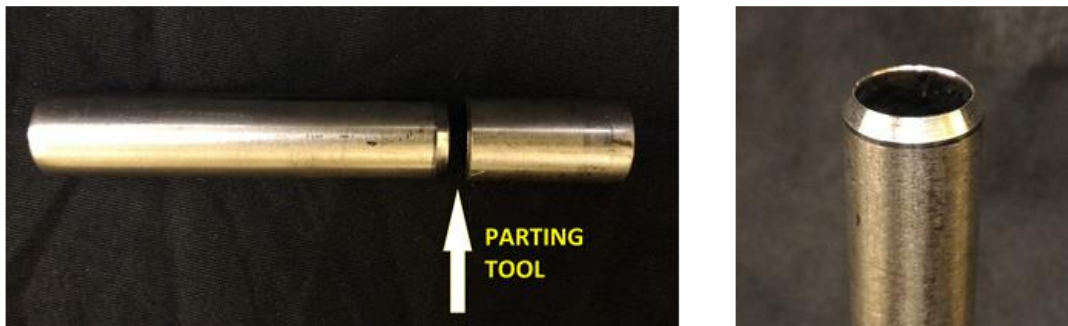


**Figure 3.16: Partitioned exhaust tube for cross sectional analysis**

camera are used to capture the magnified images. The images are taken at a magnification of 50× and a resolution of 1280 × 1024 pixels.

### 3.6.2    Image Processing

Four separate images are taken for each cut tube, one for each quarter. The images are captured in RGB format. In addition, an image of a clean tube is captured to determine the threshold index values to differentiate between the fouling layer and the void space. The raw image is then converted to a binary black and white image where the soot layer is in black. The binary image is further processed using a 2-D Gaussian filter to remove noise. The raw image and final processed image are shown in Figure 3.17.

A calibration image with a standard gage is also captured, and shown in Figure 3.18. A MATLAB (MathWorks, 2014) script is written to identify the edges of the standard
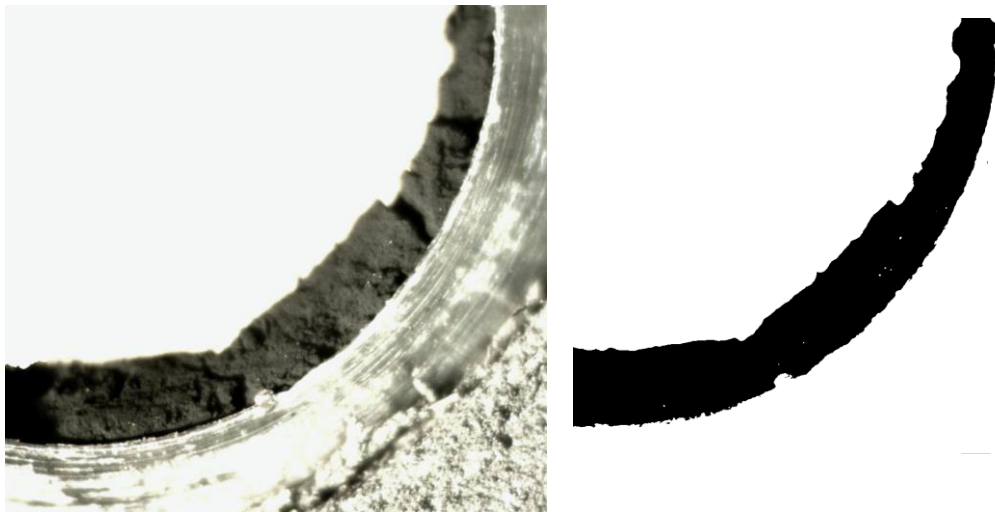


**Figure 3.17: Comparison of raw (left) and processed (right) cross-sectional image of exhaust tube**

**Figure 3.18: Raw (left) and processed (right) calibration image**

gauge and determine the number of pixels between them. The length of each pixel is then determined as follows.

$$L_{pixel} = \frac{L_{gage}}{n_{pixels}} \qquad (3.38)$$

The center of the tube is determined in order to quantify the thickness of the fouling layer. This is done by first identifying three points $(x_1, y_1)$, $(x_2, y_2)$ and $(x_3, y_3)$ on the inner wall of the tube. The MATLAB script identifies the inner wall by a black to white transition in pixel color. The center of the tube is then calculated with Equation (3.39) through (3.41)

.

$$x_{center} = \frac{(m \times n)(y_3 - y_1) + m(x_2 + x_3) - n(x_1 + x_2)}{2(m - n)} \qquad (3.39)$$

$$y_{center} = \frac{-1}{m}\left(x_{center} - \frac{x_1 + x_2}{2}\right) + \frac{y_1 + y_2}{2} \qquad (3.40)$$

92

$$m = \frac{y_2 - y_1}{x_2 - x_1}, n = \frac{y_3 - y_2}{x_3 - x_2} \qquad (3.41)$$

The starting point of soot layer is identified by a white to black transition. Since the thickness is in radial direction, the equation of the line joining the starting point and center is found. The number of black pixels is counted along the line through the fouling layer. The thickness is determined with Equation (3.42), and a schematic of this is shown in Figure 3.19.

$$t_{foul} = L_{pixel} n_{pixel} \qquad (3.42)$$

The thickness is measured at multiple points and is averaged over those points. The final thickness is calculated by taking the mean of the four images. A sensitivity study is
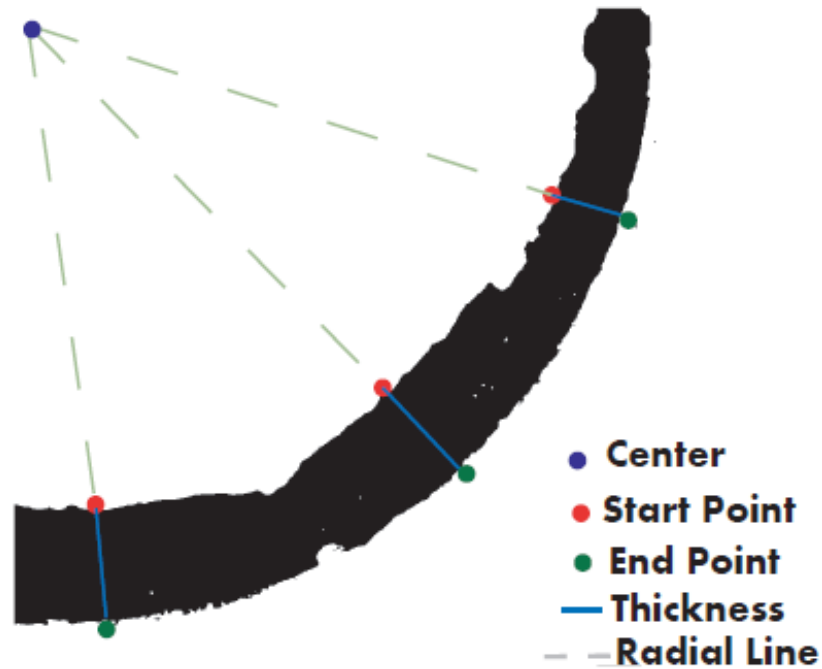


**Figure 3.19: Schematic of thickness measurement**

conducted to determine the number of points to consider for each image. The result is shown in Figure 3.20. It is observed that a minimum of 20 points are to be considered.

The uncertainty of the fouling thickness is calculated as the 95% confidence interval of the individual measurements, as shown in Equation (3.43).

$$\sigma_{t_{foul}} = \frac{1.96}{n_{points}} \sqrt{\sum \left( t_{foul,i} - \overline{t_{foul}} \right)^2} \qquad (3.43)$$

A sensitivity analysis was also performed to determine when the uncertainty converges on a constant value. Figure 3.21 shows the plot of uncertainty against the number of points to be considered. Considering both the sensitivity and uncertainty analysis, 40 measurements were made for each image.

The fouling thickness is used in the data analysis of the fouling experiments, described in Chapter 4, to calculate the thermal conductivity of the layer and to understand the influence of fouling mechanisms at various experimental conditions.
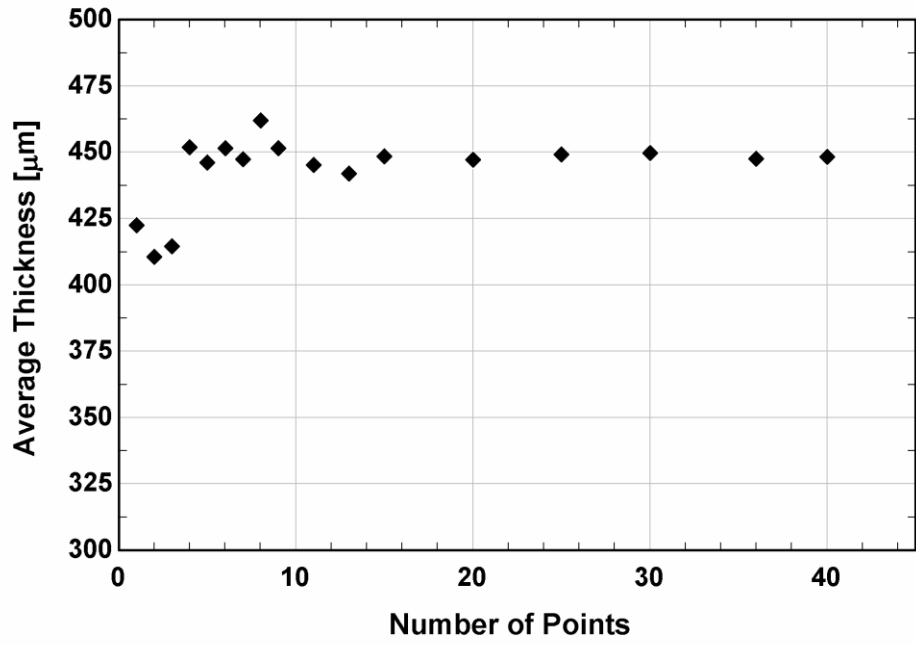
**Figure 3.20: Sensitivity analysis for the average fouling layer thickness**
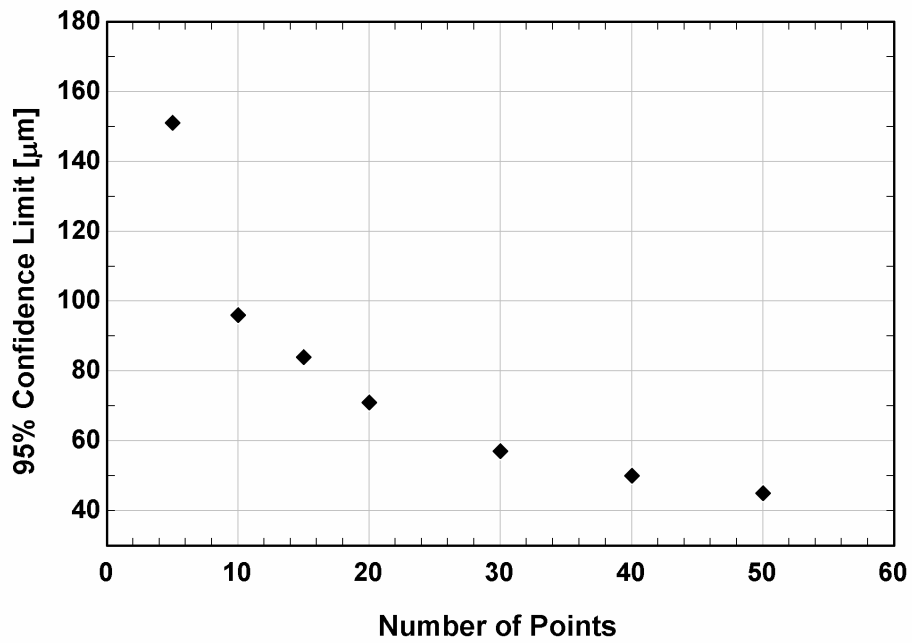


**Figure 3.21: Sensitivity analysis for the uncertainty in the fouling layer thickness**

# CHAPTER 4.        SINGLE-TUBE EXPERIMENTS

In this chapter, the results from the single-tube fouling experiments are presented, including data reduction procedures, validation of heat transfer rate measurements, data analysis, and a comparison of the results with the literature.

## 4.1 Data Reduction

In the modeling of the test facility, it was idealized that the heat rejected from the exhaust was equal to the heat gained by the coolant; however, in practice, there are differences in the measured heat transfer rates of each fluid due to heat losses to the surroundings. The heat losses from the exhaust and coolant to the ambient are depicted in Figure 4.1.  The temperatures shown in a box are measured temperatures, the remainder are calculated.  For the exhaust, there are heat losses between the thermocouple temperature measurements and the inlet and outlet of the heat exchanger.  For the coolant, there are
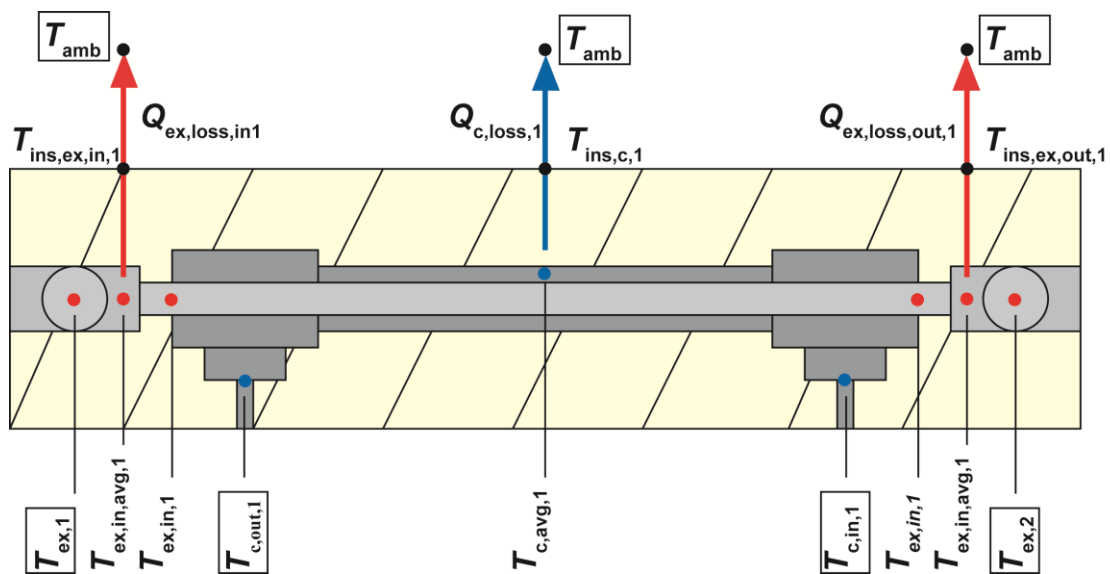


**Figure 4.1: Schematic of the heat losses from a tube-in-tube heat exchanger**

losses from the outer shell of the heat exchanger, through the insulation, and to the ambient. Including these losses, the heat transfer rate from the exhaust and to the coolant are shown in Equations (4.1) and (4.2), respectively.

$$\dot{Q}_{ex,i} = \dot{Q}_{ex,meas,i} - \dot{Q}_{ex,loss,in,i} - \dot{Q}_{ex,loss,out,i} \tag{4.1}$$

$$\dot{Q}_{c,i} = \dot{Q}_{c,meas,i} + \dot{Q}_{c,loss,i} \tag{4.2}$$

The values for these heat transfer rates should match within their experimental uncertainties.

### 4.1.1  Exhaust Heat Transfer Rate

As shown previously in Equation (4.2), the total heat transferred to the coolant from the exhaust is the measured heat transfer rate less the losses to the ambient. The measured heat transfer rate is calculated based on the specific heat of the exhaust, the exhaust flow rate, and the measured exhaust temperatures.

$$\dot{Q}_{ex,meas,i} = c_{p,ex,i} \dot{m}_{ex} \left( T_{ex,i} - T_{ex,i+1} \right) \tag{4.3}$$

The subscript $i$ represents the variable for heat exchanger one through four. The specific heat of the exhaust is calculated based on its composition, which is determined from the chemical reaction for combustion of diesel fuel, shown in Equation (4.4).

$$C_a H_b + \frac{n_{O_2}}{\varphi}(O_2 + 3.773 N_2) \rightarrow n_p(\tilde{y}_{H_2O} H_2O + \tilde{y}_{CO_2} CO_2 + \tilde{y}_{CO} CO + \tilde{y}_{O_2} O_2 + \tilde{y}_{N_2} N_2 + \tilde{y}_{C_a H_b} C_a H_b)$$

$$\tag{4.4}$$
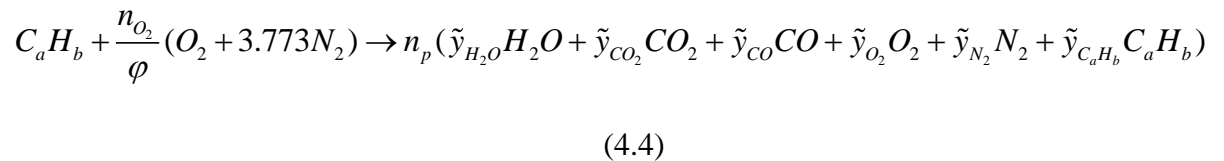
In contrast to the chemical equation used to obtain the specific heat in the modeling in Chapter 3, this includes the presence of unburned hydrocarbons in the exhaust. It is assumed that the unburned hydrocarbons have the same composition as the fuel, $a = 1$ and $b = 1.8$. The stoichiometric moles of oxygen are calculated as in the modeling in Chapter 3. Other knowns in the chemical reaction include the dry basis mole fraction measurements of oxygen, carbon dioxide, and carbon monoxide, which are converted to the wet basis mole fractions with Equations (4.5) through (4.7), respectively. The mole fraction of oxygen is measured with a paramagnetic analyzer, and the carbon dioxide and monoxide mole fractions are measured with a nondispersive infrared analyzer.

$$\tilde{y}_{O_2} = \tilde{y}_{O_2,dry}\left(1 - \tilde{y}_{H_2O}\right) \tag{4.5}$$

$$\tilde{y}_{CO_2} = \tilde{y}_{CO_2,dry}\left(1 - \tilde{y}_{H_2O}\right) \tag{4.6}$$

$$\tilde{y}_{CO} = \tilde{y}_{CO,dry}\left(1 - \tilde{y}_{H_2O}\right) \tag{4.7}$$

These equations are solved iteratively with a balance of the carbon, hydrogen, oxygen, and nitrogen species, along with a summation of the mole fractions to unity, shown respectively in the following equations.

$$a = n_p\left(a\tilde{y}_{C_aH_b} + \tilde{y}_{CO} + \tilde{y}_{CO_2}\right) \tag{4.8}$$

$$b = n_p\left(b\tilde{y}_{C_aH_b} + 2\tilde{y}_{H_2O}\right) \tag{4.9}$$

$$2n_{O_2}/\varphi = n_p\left(\tilde{y}_{CO} + 2\tilde{y}_{CO_2} + \tilde{y}_{H_2O}\right) \tag{4.10}$$

$$7.546n_{O_2}/\varphi = n_p(2\tilde{y}_{N_2}) \tag{4.11}$$

$$\tilde{y}_{N_2} + \tilde{y}_{H_2O} + \tilde{y}_{CO_2} + \tilde{y}_{CO} + \tilde{y}_{O_2} + \tilde{y}_{C_aH_b} = 1 \tag{4.12}$$

The specific heat of exhaust is calculated based on the mass fractions and the specific heat of each constituent in the exhaust. The specific heats are taken to be the ideal gas specific heat at the average of the exhaust inlet and outlet temperature, except for water vapor which is taken at the average temperature and partial pressure of the water in the exhaust. All fluid properties in this data analysis are obtained from Engineering Equation Solver (EES) software. The calculation of specific heat is shown in Equation (4.13).

$$c_{p,ex,i} = y_{CO_2} c_{p,CO_2,i} + y_{H_2O} c_{p,H_2O,i} + y_{O_2} c_{p,O_2,i} + y_{N_2} c_{p,N_2,i} + y_{CO} c_{p,CO,i} + y_{C_aH_b} c_{p,C_aH_b,i}$$

(4.13)

The exhaust flow rate is calculated based on the flow coefficient, the diameter, and expansion coefficient of the wedgemeter as well as the exhaust density, compressibility, and pressure drop across the wedgemeter, as in the following equation.

$$\dot{m}_{ex} = K_p D_{wm}^2 FaY \sqrt{\rho_{ex,wm} \Delta P_{wm}}$$

(4.14)

The diameter of the wedgemeter is specified by the manufacturer to be 0.158 m, and the expansion coefficient is 1.012. The flow coefficient was determined through calibration with a thermal anemometer over a flow rate range of 0.89 to 2.43 g s$^{-1}$. The flow coefficient at each flow rate is shown in Table 4.1. The flow coefficient is nearly constant over the flow range, as it is designed to be, and an average was taken for use over the full range of flow rates. The resulting average value along with its uncertainty is as follows.

$$K_p = (1.16 \pm 0.02) \times 10^{-3}$$

The calibrated flow coefficient allows for calculation of the exhaust flow rate.

**Table 4.1: Calibration of wedgemeter for flow coefficient**

| Flow rate [g s$^{-1}$] | Flow Coefficient, $K_p$ |
|---|---|
| 2.43 | 0.001159 |
| 2.02 | 0.001160 |
| 1.60 | 0.001162 |
| 1.25 | 0.001163 |
| 1.23 | 0.001165 |
| 0.93 | 0.001161 |
| 0.89 | 0.001161 |

The last variable in the measured exhaust heat transfer rate is the exhaust temperature at the location of the thermocouple. Due to the high temperature of the exhaust, there is potential for radiation to affect the temperature measurement. While exhaust flows over the thermocouple, there is convective heat transfer from the exhaust to the thermocouple. There is also radiation heat transfer from the thermocouple to the cross into which it is inserted and to the tube surface of the heat exchanger on either side. This results in the thermocouple temperature being slightly less than the bulk temperature of the exhaust. The method used to calculate the maximum possible temperature difference between the exhaust and thermocouple due to radiation is included in APPENDIX B. The difference is greatest at the first thermocouple and least for the fifth thermocouple. For an experiment at design conditions after 10 hours of exhaust exposure, the difference ranges from 0.6 to 2.0ºC. This difference in the measured and actual exhaust temperature causes no more than a 1.1% difference in exhaust heat duty.

The heat losses from the exhaust at the inlets of the heat exchangers are dependent on the temperature difference between the exhaust and the ambient temperature and the thermal resistance, as shown in Equation (4.15).

$$\dot{Q}_{ex,loss,in,i} = \left( T_{ex,in,avg,i} - T_{amb} \right) \Big/ R_{tot,ex,in,i} \qquad (4.15)$$

The ambient temperature is measured, the average inlet exhaust temperature is the average of the measured exhaust temperature and the exhaust inlet temperature to the heat exchanger, which is calculated using the following equation.

$$T_{ex,in,i} = T_{ex,i} - \dot{Q}_{ex,loss,in,i} \Big/ \dot{m}_{ex} c_{p,ex,in,i} \qquad (4.16)$$

The total thermal resistance between the exhaust and the ambient, in Equation (4.17), consists of the convective resistance from the exhaust to the tube, the conductive resistance of the tube, the conductive resistance of the insulation, and the resistance to the ambient. The resistance to ambient consists of two parallel resistances, for convection and radiation to the surroundings, as shown in Equation (4.18).

$$R_{tot,ex,in,i} = R_{ex,in,i} + R_{tube,ex,in,i} + R_{ins,ex,in,i} + R_{amb,ex,in,i} \qquad (4.17)$$

$$R_{amb,ex,in,i} = \frac{R_{amb,conv,in,i} \times R_{amb,rad,in,i}}{R_{amb,conv,in,i} + R_{amb,rad,in,i}} \qquad (4.18)$$

The convective exhaust resistance is dependent on the heat transfer coefficient of the exhaust, the inner diameter of the inner tube of the heat exchanger, and the length from the thermocouple measurement to the inlet of the heat exchanger, as follows.

$$R_{ex,in,i} = \frac{1}{h_{ex,in,i} \pi D_{IT,I} L_{ex,in}} \qquad (4.19)$$

The Nusselt number is calculated using the correlation of Churchill (1977a), shown in Chapter 3, and is in turn used to calculate heat transfer coefficient. A 25% uncertainty is

assigned to the heat transfer coefficient to account for the predictive capability of the correlation. All heat transfer coefficients determined from correlations are assigned this uncertainty. The inner diameter of the inner tube, 10.9 mm, and the distance between the thermocouple and the inlet of the heat exchanger, 97 mm, then provide the exhaust resistance. The tube and insulation resistances are calculated as radial conduction through a hollow cylinder, as shown in Equations (4.20) and (4.21), respectively.

$$R_{tube,ex,in,i} = \frac{\ln\left(D_{IT,O}/D_{IT,I}\right)}{2\pi k_{tube,ex,i} L_{ex,in}} \tag{4.20}$$

$$R_{ins,ex,in,i} = \frac{\ln\left(D_{ins,O}/D_{IT,O}\right)}{2\pi k_{ins,ex,i} L_{ex,in}} \tag{4.21}$$

The outer diameter of the inner tube is 12.7 mm, the outer diameter of the insulation is 172 mm, the thermal conductivity of the tube is that for stainless steel, and the thermal conductivity of the fiber glass insulation is specified by the manufacturer to be 0.053 W m$^{-1}$ K$^{-1}$. The convective ambient resistance is dependent on the convective heat transfer coefficient, the outer diameter of the insulation, and the exhaust tube length, as follows.

$$R_{amb,conv,in,i} = \frac{1}{h_{air,in,i} \pi D_{ins,O} L_{ex,in}} \tag{4.22}$$

The Nusselt number of the ambient air is taken to be that for natural convection over a horizontal cylinder, predicted using the correlation of Churchill and Chu (1975), as shown in Equation (4.23).

$$Nu_{air,ex,in,i} = \left[ 0.60 + \frac{0.387 Ra_{air}^{1/6}}{\left( 1 + \left( \dfrac{0.559}{\Pr_{air}} \right)^{9/16} \right)^{8/27}} \right]^2 \tag{4.23}$$

The Rayleigh number is calculated using Equation (4.24), and is dependent on the surface temperature of the insulation, which is obtained iteratively from Equation (4.25).

$$Ra_{air,ex,in,i} = \frac{g \beta_{air} \left( T_{ins,ex,in,i} - T_{amb} \right) D_{ins,O}^3}{\upsilon_{air} \alpha_{air}} \tag{4.24}$$

$$T_{ins,ex,in,i} = T_{air} + \dot{Q}_{ex,loss,in,i} R_{amb,ex,i} \tag{4.25}$$

The heat transfer coefficient is then computed from the Nusselt number, the thermal conductivity of the air, and the outer diameter of the insulation, as shown in the following equation.

$$h_{air,ex,in,1} = \frac{Nu_{air,ex,in,i} k_{air}}{D_{ins,o}} \tag{4.26}$$

Assuming that the surroundings are at the ambient temperature and that the insulation surface is gray and diffuse, the radiation resistance is represented by Equation (4.27).

$$R_{amb,rad,in,i} = \frac{1}{e_{ins} \pi D_{ins,o} L_{ex,in} \sigma_{SB} \left( T_{ins,ex,i}^2 + T_{amb}^2 \right) \left( T_{ins,ex,i} + T_{amb} \right)} \tag{4.27}$$

The emissivity of the insulation is taken to be 0.85, while the Stefan-Boltzmann constant is $5.67 \times 10^{-8}$ W m$^{-2}$ K$^{-4}$. Each individual resistance is summed to obtain the total thermal resistance, and the inlet exhaust heat loss is calculated. The outlet loss is calculated in a

similar manner. Finally, the measured, inlet loss, and outlet loss heat transfer rates are used to calculate the exhaust heat transfer rate.

### 4.1.2 Coolant Heat Transfer Rate

The coolant heat transfer rate, as shown by Equation (4.2), is dependent on the measured coolant heat transfer rate and the coolant losses. The measured heat transfer rate is calculated from the mass flow rate of coolant, the specific heat, and the inlet and outlet temperatures, as in the following equation.

$$\dot{Q}_{c,meas,i} = \dot{m}_{c,i} c_{p,c,i} \left( T_{c,out,i} - T_{c,in,i} \right) \tag{4.28}$$

The specific heat of water is calculated at the average of the coolant inlet and outlet temperatures. The coolant inlet and outlet temperatures are known from the thermocouple measurements. The volumetric flow rate is measured with the turbine flow meters at the inlet to each heat exchanger. The volumetric flow rate is calculated based on the frequency of turbine rotation. The manufacturer performed a correlation between volumetric flow rate and frequency in terms of $K_{factor}$, defined in Equation (4.29).

$$K_{factor,i} = \frac{\omega_{HZ,i} timebase}{\dot{V}_{c,GPM,i}} \tag{4.29}$$

As indicated by the symbols in the above equation, the frequency and volumetric flow rate are calibrated in Hertz and gallons per minute, respectively. The timebase is defined to be 60 s min$^{-1}$. The curve fits for $K_{factor}$ as a function of volumetric flow rate for each flow meter, provided by the manufacturer, are shown in Equations (4.30) through (4.33).

$$K_{factor,1} = 128,000 \ln \left( \dot{V}_{c,GPM,meas,1} \right) + 1,298,000 \tag{4.30}$$

$$K_{factor,2} = 124,000 \ln \left( \dot{V}_{c,GPM,meas,2} \right) + 1,285,000 \tag{4.31}$$

$$K_{factor,3} = 120,000 \ln\left(\dot{V}_{c,GPM,meas,3}\right) + 1,277,000 \tag{4.32}$$

$$K_{factor,4} = 128,000 \ln\left(\dot{V}_{c,GPM,meas,4}\right) + 1,294,000 \tag{4.33}$$

While this correlation works well at the fluid temperature used for calibration, 23.9°C, it is not valid for the temperature range used in the present experiments, 95.3°C to 129.8°C. To account for the difference in fluid properties and measurement at temperatures for non-reference conditions, a Roshko-Strouhal correction is used as suggested by Mattingly (1992). The non-dimensional Roshko number is shown in Equations (4.34).

$$Ro_i = \frac{\omega_i D_{TM}^2}{v_{c,i}} \tag{4.34}$$

The $K_{factor}$ for each flow meter is obtained by substituting the measured volumetric flow rate into Equations (4.30) through (4.33). This value is then input to Equation (4.29) along with the measured volumetric flow rate to get the frequency of rotation in Hertz. This value is converted to units of rad s$^{-1}$ using the following equation.

$$\omega_i = 2\pi\omega_{HZ,i} \tag{4.35}$$

This frequency, the kinematic viscosity of the coolant at the inlet temperature of the heat exchanger, and the diameter of the turbine meter are used to calculate the Roshko number. The diameter of the turbine meter is corrected for thermal expansion using Equation (4.36)

.

$$D_{TM,i} = D_{TM,o}\left(1 + \alpha_M\left(T_{c,in,i} - T_o\right)\right)^{1/3} \tag{4.36}$$

The diameter of the turbine meter at the reference temperature of 23.9°C is 12.7 mm, while the coefficient of thermal expansion is $1.72 \times 10^{-5}$ $K^{-1}$. This yields the Roshko number.

The original manufacturer calibration data are converted to a correlation of Strouhal number to Roshko number to determine flow rate at non-reference fluid conditions. The curve fit for each of the flowmeters is shown in Equations (4.37) through (4.40).

$$St_1 = 286 \ln(Ro_1) - 220 \tag{4.37}$$

$$St_2 = 278 \ln(Ro_2) - 146 \tag{4.38}$$

$$St_3 = 273 \ln(Ro_3) - 87 \tag{4.39}$$

$$St_4 = 286 \ln(Ro_4) - 223 \tag{4.40}$$

The Strouhal number, rotational frequency, and turbine meter diameter are used to determine the velocity of coolant in the following equation.

$$V_{c,i} = \frac{\omega_i D_{TM,i}}{St_i} \tag{4.41}$$

The mass flow rate of coolant through each heat exchanger is calculated using the velocity, turbine meter diameter, and density of the coolant at the inlet of the heat exchanger.

$$\dot{m}_{c,i} = \rho_{c,in,i} V_{c,i} \pi D_{TM,i}^2 / 4 \tag{4.42}$$

The determination of mass flow rate of the coolant provides all the necessary information for the calculation of measured coolant heat transfer rate.

The coolant heat transfer loss to the ambient is a function of the average coolant temperature, the ambient temperature, and the total resistance between the coolant and the ambient, as shown in the following equation.

$$\dot{Q}_{c,loss,i} = \left(T_{c,avg,i} - T_{amb}\right)\Big/R_{tot,c,i} \tag{4.43}$$

The total coolant heat transfer resistance is a summation of the coolant convective resistance, the tube and insulation conductive resistance, and the ambient resistance, as in Equation (4.44). The ambient resistance is a combination of two parallel resistances, the convective resistance and radiation resistance, as shown in Equation (4.45).

$$R_{tot,c,i} = R_{c,O,i} + R_{tube,c,i} + R_{ins,c,i} + R_{amb,c,i} \tag{4.44}$$

$$R_{amb,c,i} = \frac{R_{amb,conv,c,i} \times R_{amb,rad,c,i}}{R_{amb,conv,c,i} + R_{amb,rad,c,i}} \tag{4.45}$$

The convective resistance of the coolant is a function of the heat transfer coefficient on the outer surface in the annulus, the inner diameter of the outer tube, and the length of the annulus, as shown in the following equation.

$$R_{c,o,i} = \frac{1}{h_{c,O,i}\pi D_{OT,I}L_{annulus}} \tag{4.46}$$

The inner diameter of the outer tube is 16.6 mm and the length of the annulus is taken to be the total length for which the coolant is in contact with the exhaust tube, 285 mm. The heat transfer coefficient is a function of the Nusselt number, hydraulic diameter of the annulus, and thermal conductivity of the coolant at the average temperature, as shown in Equation (4.47). The Nusselt number is predicted for fully developed laminar flow in an

annulus with uniform heat flux at both sides, as presented by Bergman *et al.* (2011), Equation (4.48).

$$h_{c,O,i} = \frac{Nu_{c,O,i}k_{c,i}}{D_h} \qquad (4.47)$$

$$Nu_{c,O,i} = \frac{Nu_\infty}{1 - \left(q_I''/q_o''\right)\theta_o^*} \qquad (4.48)$$

The heat flux at the inner and outer surface are obtained iteratively using Equations (4.49) and (4.50), respectively.

$$q_I'' = \frac{\dot{Q}_{c,i}}{\pi D_{IT,O} L_{annulus}} \qquad (4.49)$$

$$q_O'' = \frac{\dot{Q}_{c,loss,i}}{\pi D_{OT,I} L_{annulus}} \qquad (4.50)$$

The influence coefficients, $Nu_\infty$ and $\theta_O^*$, are dependent on the ratio of the outer diameter of the inner tube to the inner diameter of the outer tube and are presented in Table 4.2.

The ratio of the two diameters is 0.77, which results in the following influence coefficients.

$$Nu_\infty = 5.217$$

$$\theta_O^* = 0.290$$

These values yield the Nusselt number, heat transfer coefficient, and the coolant convective thermal resistance on the outer surface of the annulus.

The tube, insulation, and ambient resistances for the coolant losses are obtained using the method for exhaust inlet losses. Calculation of these resistances yields the total

108

**Table 4.2: Influence coefficients for fully developed laminar flow through an annulus with uniform heat flux maintained at both sides (Bergman *et al.*, 2011)**

| $D_{IT,o}/D_{OT,i}$ | $Nu_{II}$ | $Nu_\infty$ | $\theta_i^*$ | $\theta_o^*$ |
|---|---|---|---|---|
| 0 | - | 4.364 | $\infty$ | 0 |
| 0.05 | 17.81 | 4.792 | 2.180 | 0.0294 |
| 0.10 | 11.91 | 4.834 | 1.383 | 0.0562 |
| 0.20 | 8.499 | 4.833 | 0.905 | 0.1041 |
| 0.40 | 6.583 | 4.979 | 0.603 | 0.1823 |
| 0.60 | 5.912 | 5.099 | 0.473 | 0.2455 |
| 0.80 | 5.580 | 5.240 | 0.401 | 0.2990 |
| 1.00 | 5.385 | 5.385 | 0.346 | 0.3460 |

coolant loss resistance to the ambient, the coolant loss heat transfer rate, and the coolant heat transfer.

### 4.1.3    *Heat Transfer Rate Comparison*

Accounting for the ambient heat transfer losses of both the exhaust and coolant to the ambient allows for direct comparison between the exhaust and coolant heat transfer rates, which should match within experimental uncertainty.  An uncertainty analysis is conducted on Engineering Equation Solver (EES) to propagate the error in the experimental measurements, which are included in Chapter 3, to the heat transfer rates.  The uncertainty propagation is performed using the method suggested by Taylor and Kuyatt (1994), as shown in Equation (4.51):

$$U_y^2 = \left(\frac{\partial y}{\partial x_1}U_{x_1}\right)^2 + \left(\frac{\partial y}{\partial x_2}U_{x_2}\right)^2 + \left(\frac{\partial y}{\partial x_3}U_{x_3}\right)^2 + ... \qquad (4.51)$$

where the uncertainty (u) of a calculated variable (y) is a function of the variables used in the calculation (x).  The variables influencing the exhaust and coolant heat transfer rate measurements for the first heat exchanger after exposure to exhaust for ten hours at design

conditions are shown in Table 4.3 and Table 4.4, respectively. The two heat transfer rates match within their experimental uncertainties. Due to less uncertainty in the coolant temperature and flow rate measurement, the coolant heat transfer rate has a lower

**Table 4.3: Relative uncertainty of each measured variable in the calculation of exhaust heat transfer rate**

| Variable | Percent of Total Uncertainty [%] |
|---|---|
| $\dot{Q}_{ex,1} = 116.60 \pm 3.99\ W$ | |
| $D_{IT,i}$ | 0.01 |
| $D_{ins,o}$ | 0.23 |
| $\Delta P_{ex,wm}$ | 0.40 |
| $h_{ex,in,1}, h_{ex,out,1}, h_{air,in,1}, h_{air,out,1}$ | 0.19 |
| $K_p$ | 4.15 |
| $L_{ex}$ | 0.03 |
| $T_{ex,meas,1}$ | 44.53 |
| $T_{ex,meas,2}$ | 45.09 |
| $T_{ex,wm}$ | 0.10 |
| $\tilde{y}_{CO,dry}$ | 0.09 |
| $\tilde{y}_{CO_2,dry}$ | 3.24 |
| $\tilde{y}_{O_2,dry}$ | 1.94 |

**Table 4.4: Relative uncertainty of each measured variable in the calculation of coolant heat transfer rate**

| Variable | Percent of Total Uncertainty [%] |
|---|---|
| $\dot{Q}_{c,1} = 112.00 \pm 0.80\ W$ | |
| $D_{IT,o}$ | 0.01 |
| $D_{OT,o}$ | 0.04 |
| $D_{ins,o}$ | 2.93 |
| $h_{c,o,1}, h_{air,1}$ | 0.22 |
| $L_{annulus}$ | 0.02 |
| $T_{air}$ | 0.03 |
| $T_{c,in,1}$ | 44.43 |
| $T_{c,out,1}$ | 41.16 |
| $\dot{V}_{c,1}$ | 11.13 |

uncertainty. This heat transfer rate is used for calculation of fouling resistance to reduce the uncertainty therein.

### 4.1.4    Fouling Thermal Resistance

The total thermal resistance between the exhaust and coolant in the tube-in-tube heat exchangers is calculated using Equation (4.52).

$$R_i = \Delta T_{lm,i} / \dot{Q}_{c,i} \qquad (4.52)$$

The coolant heat transfer rate was discussed above, and the log mean temperature difference is a function of the coolant and exhaust inlet and outlet temperatures. The total resistance circuit, shown in Figure 4.2, includes the exhaust, fouling, tube, and coolant
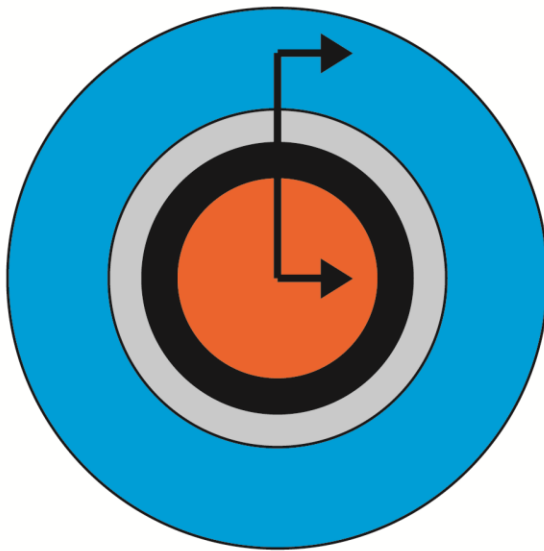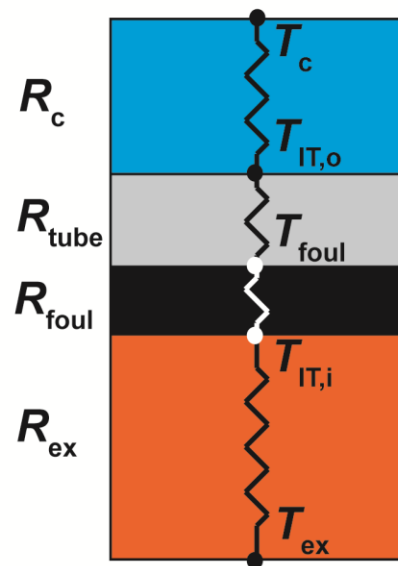


**Figure 4.2: Thermal resistance circuit for heat transfer from exhaust to coolant**

111

resistances. The fouling resistance is isolated from the total thermal resistance by subtracting the exhaust, tube, and coolant resistances.

$$R_{foul,i} = R_i - R_{ex,i} - R_{IT,i} - R_{c,i,i} \tag{4.53}$$

The tube resistance is calculated for radial conduction through a hollow cylinder using Equation (4.54).

$$R_{IT,I} = \frac{\ln\left(D_{IT,O}/D_{IT,I}\right)}{2\pi k_{tube,i} L_{annulus}} \tag{4.54}$$

The coolant resistance is dependent on the coolant heat transfer coefficient on the outer diameter of the inner tube, and the annulus length, as shown in Equation (4.55).

$$R_{c,I,i} = \frac{1}{h_{c,I,i}\pi D_{IT,O} L_{annulus}} \tag{4.55}$$

The coolant Nusselt number on the inner surface for laminar flow through an annulus with constant heat flux on both surfaces is calculated using the following equation according to Bergman *et al.* (2011).

$$Nu_{c,I,i} = \frac{Nu_{II}}{1-\left(q_o^{"}/q_I^{"}\right)\theta_I^*} \tag{4.56}$$

The Nusselt number is used to obtain heat transfer coefficient and coolant thermal resistance.    The exhaust heat transfer resistance is dependent on the heat transfer coefficient, the inner diameter of the inner tube, and the length of the annulus, as shown in

Equation (4.57). The heat transfer coefficient is dependent on the Nusselt number, thermal

conductivity of exhaust, and the inner diameter of the inner tube.

$$R_{ex,i} = \frac{1}{h_{ex,i} \pi D_{IT,I} L_{annulus}} \qquad (4.57)$$

$$h_{ex,i} = \frac{Nu_{ex,i} k_{ex,i}}{D_{IT,I}} \qquad (4.58)$$

The exhaust resistance is significantly greater than the other resistances. As an example,

for an experiment at design conditions in the series arrangement after ten hours of exhaust

exposure, the exhaust, coolant, and tube resistances are 0.785, 0.091, and 0.005 K W$^{-1}$,

respectively. Therefore, care must be taken to reduce the uncertainty in the values used to

calculate the exhaust thermal resistance, particularly the Nusselt number. The Nusselt

number could be predicted with the correlation of Churchill (1977a); however, assigning a

25% uncertainty to this value would result in a significant uncertainty in the fouling

resistance. To reduce the uncertainty in the fouling resistance, measurements of the Nusselt

number for a clean tube ($R_{foul} = 0$) are made with air at similar Reynolds and Prandtl

numbers. The air resistance can be obtained from Equation (4.59).

$$R_{air,i} = R_i - R_{c,I,i} - R_{IT,i} \qquad (4.59)$$

The method as described above for calculation of fouling resistance is used to determine

the total, coolant, and tube resistance. The heat transfer coefficient of the air is calculated

from Equation (4.60), and is used to calculate the Nusselt number of the air using Equation

(4.61).

$$h_{air,i} = \frac{1}{R_{air,i}\pi D_{IT,I}L_{annulus}} \quad (4.60)$$

$$Nu_{air,i} = \frac{h_{air,i}D_{IT,I}}{k_{air,i}} \quad (4.61)$$

The properties of air are calculated at the average of the air inlet and outlet temperatures. By making measurements at the same Reynolds and Prandtl number of air as the exhaust, the Nusselt number can be assumed to be the same for both cases, as follows.

$$Nu_{air,i} = Nu_{ex,i} \quad (4.62)$$

Determination of the exhaust Nusselt number and the exhaust thermal resistance in this manner, when used with Equation (4.62) above, provides the fouling resistance.

The air test results for Nusselt number are presented in Section 4.2.1, resulting in a decreases in the uncertainty in the Nusselt number to 10%. This significantly reduces the overall uncertainty in the fouling resistance. Table 4.5 compares the results of the uncertainty analysis for an uncertainty of 10%, if the exhaust Nusselt number is predicted from the air test results, and an uncertainty of 25%, if the exhaust Nusselt number is predicted using the correlation of Churchill (1977a). The table shows that exhaust heat transfer coefficient has the most significant effect on fouling resistance uncertainty, accounting for 85% and 97% of the total uncertainty when the heat transfer coefficient is predicted with the air test and correlation, respectively. This results in a significant reduction in the uncertainty in the fouling resistance from 14.3% when using correlation to 6.0% when using the air test results. This allows for the determination of trends in fouling resistance between different test cases with more experimental certainty.

**Table 4.5: Comparison of uncertainty analysis for fouling resistance calculation**

| Variable | Percent of Total Uncertainty [%] | |
|---|---|---|
| | 10% Uncertainty in $h_{ex,1}$ | 25% Uncertainty in $h_{ex,1}$ |
| | $R_{foul,1} = 1.322 \pm 0.084$ | $R_{foul,1} = 1322 \pm 0.202$ |
| $D_{IT,o}$ | 1.47 | 0.25 |
| $D_{OT,o}$ | 0.50 | 0.09 |
| $D_{ins,o}$ | 0.10 | 0.02 |
| $\Delta P_{ex,wm}$ | 0.04 | 0.01 |
| $h_{c,o,1}, h_{c,i,1}$ | 6.99 | 1.24 |
| $h_{ex,in,1}, h_{ex,out,1}$ | 0.26 | 0.05 |
| $h_{air,1}, h_{air,in,1}, h_{air,out,1}$ | 0.00 | 0.00 |
| $\boldsymbol{h_{ex,1}}$ | 85.19 | 97.36 |
| $K_p$ | 0.47 | 0.08 |
| $L_{annulus}$ | 0.06 | 0.01 |
| $T_{c,in,1}$ | 1.44 | 0.25 |
| $T_{c,out,1}$ | 2.12 | 0.37 |
| $T_{ex,1}$ | 0.50 | 0.09 |
| $T_{ex,2}$ | 0.47 | 0.08 |
| $T_{ex,wm}$ | 0.01 | 0.00 |
| $\dot{V}_{c,1}$ | 0.46 | 0.08 |
| $\tilde{y}_{CO_2,dry}$ | 0.08 | 0.01 |
| $\tilde{y}_{O_2,dry}$ | 0.06 | 0.01 |

*4.1.5    Pressure Drop*

The change in exhaust pressure drop across each tube-in-tube heat exchanger caused by fouling is also important to the design of the desorber. The differential pressure drop measurement made between the two union crosses in the tube-in-tube heat exchanger consists of the minor pressure losses in the union crosses, the major pressure drop between the pressure measurement and the inlet and outlet of the heat exchanger, and the major losses through the heat exchanger. These pressure losses are labeled in Figure 4.3. Each
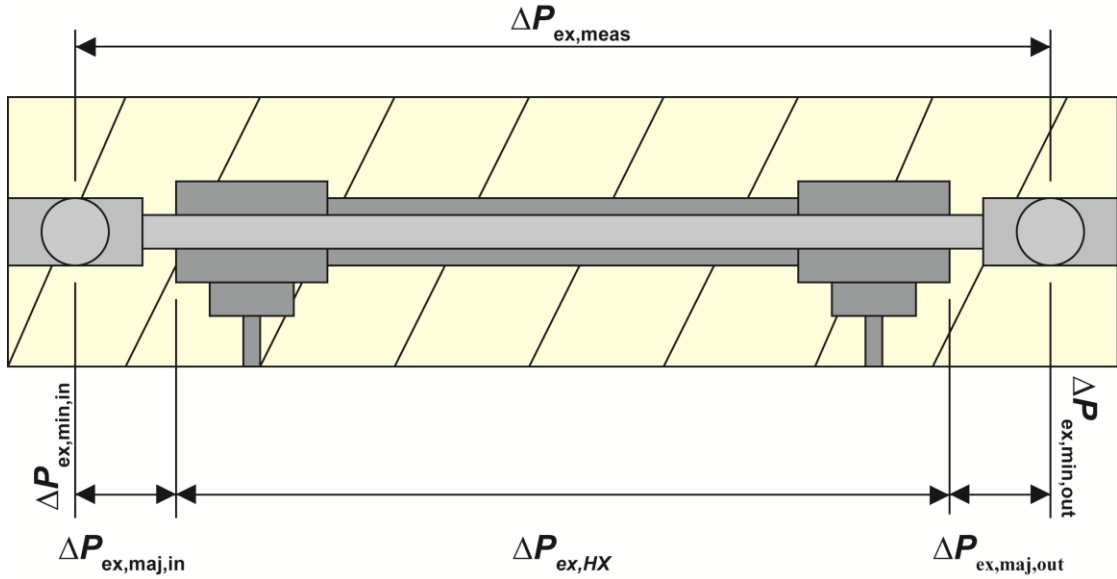
**Figure 4.3: Pressure drop through tube-in-tube heat exchanger assembly**

component of the pressure drop is summed to equal the measured pressure drop in Equation (4.63).

$$\Delta P_{ex,meas,i} = \Delta P_{ex,\min,in,i} + \Delta P_{ex,\min,out,i} + \Delta P_{ex,maj,in,i} + \Delta P_{ex,maj,in,i} + \Delta P_{ex,HX,i} \quad (4.63)$$

The minor losses at the inlet and outlet are flow through half of a union cross. The inlet and outlet minor pressure drops are calculated from the loss coefficient, the exhaust mass flow rate, the exhaust density, and the diameter of the inner tube, as Equation (4.64) and (4.65), respectively.

$$\Delta P_{ex,\min,in,i} = 4 K_{L,cross} \frac{\dot{m}_{ex}^2}{\rho_{ex,in,i} \pi^2 D_{IT,I}^4} \quad (4.64)$$

$$\Delta P_{ex,\min,out,i} = 4 K_{L,cross} \frac{\dot{m}_{ex}^2}{\rho_{ex,out,i} \pi^2 D_{IT,I}^4} \quad (4.65)$$

The loss coefficient is taken from Munson *et al.* (1990) for branch flow through a tee to be 0.9, while the exhaust density is taken at either the average exhaust inlet or outlet temperature. The major pressure drops through the inlet, outlet, and annulus are dependent on the friction factor, the diameter of the fouling layer, the exhaust mass flow rate, the exhaust density, and the length of tubing, shown in the following equations.

$$\Delta P_{ex,maj,in,i} = \frac{f_i}{D_{foul,i}^5} \frac{8}{\pi^2} \frac{\dot{m}_{ex}^2 L_{ex,in}}{\rho_{ex,in,i}} \qquad (4.66)$$

$$\Delta P_{ex,maj,out,i} = \frac{f_i}{D_{foul,i}^5} \frac{8}{\pi^2} \frac{\dot{m}_{ex}^2 L_{ex,out}}{\rho_{ex,out,i}} \qquad (4.67)$$

$$\Delta P_{ex,HX,i} = \frac{f_i}{D_{foul,i}^5} \frac{8}{\pi^2} \frac{\dot{m}_{ex}^2 L_{ex,annulus}}{\rho_{ex,i}} \qquad (4.68)$$

Due to fouling that occurs, both the friction factor and the diameter change throughout the experiment. By assuming that the friction factor and diameter are the same in the inlet, through the heat exchanger section, and outlet of the exhaust tube, the system of equations can be solved to determine the individual pressure drops. The pressure drop through the heat exchanger section is the value that is important to the design of the desorber.

To compare the effect of fouling on pressure drop at different flow rates, the ratio of the fouled pressure drop to that of a clean tube is calculated as shown in Equation (4.69) .

$$\frac{\Delta P_{ex,HX,i}}{\Delta P_{ex,HX,o,i}} = \frac{f_i / D_{foul,i}^5}{f_{o,i} / D_{IT,I}^5} \qquad (4.69)$$

This ratio eliminates the influence of mass flow rate, and also allows for the use of the findings in this study to be applied to cases with a different tube length and exhaust density. The friction factor for the clean tube is determined using the correlation of Churchill (1977b), shown in Chapter 3, and the inner diameter of the inner tube is known. This provides a standard reference for comparison among all of the test cases.

### 4.1.6   Predicted Deposition

To understand and describe the trends of fouling resistance and pressure drop ratio over different coolant temperatures, generator loads, and exhaust flow rates, a prediction of the deposition of particulate matter and hydrocarbons is made.

Particulate matter deposition is calculated due to thermophoresis, as this was determined to be the dominant mechanism in a scaling analysis performed by Abarham *et al.* (2010a). A relationship for the thermophoretic deposition efficiency, the ratio of particulate mass deposited to that entering the tube, was developed by Housiadas and Drossinos (2005) for turbulent flow through an infinitely long tube. The relationship is shown in Equation (4.70).

$$E_{th,\infty} = 1 - \left( \frac{T_{foul,i}}{T_{ex,in,1}} \right)^{\mathrm{Pr}\,K} \tag{4.70}$$

The rate of deposition is found by multiplying the mass flow rate of particulate matter entering by the efficiency.

$$\dot{m}_{PM,dep} = \dot{m}_{PM,in} E_{th,\infty} \tag{4.71}$$

This value is numerically integrated for each data point over the duration of the experiment to predict the total deposition mass of particulate matter. These equations show that thermophoretic deposition increases with the temperature difference between the exhaust and tube as well as the particulate matter concentration.

The mass rate of hydrocarbons that condense onto the deposit surface of each heat exchanger is dependent on the surface area of the inner tube, mass transfer coefficient, and the mole fraction of hydrocarbons in the bulk and at the interface, shown in Equation (4.72)

$$\dot{m}_{g,i} = K_{g,i} A_{IT,i} \ln\left( \frac{1 - \tilde{y}_{C_{20}H_{42},\text{int},i}}{1 - \tilde{y}_{C_{20}H_{42},b,i}} \right) \tag{4.72}$$

Hydrocarbon condensation increases with as inlet concentration increases and as tube temperature decreases. After performing ex-situ analysis on the deposit layer, Sluder *et al.* (2009) found that eicosane ($C_{20}H_{42}$) is the most prevalent hydrocarbon that deposits into the fouling layer. For simplicity, it is assumed that all of the hydrocarbons in the exhaust are eicosane, which is sufficient to show the trend of hydrocarbon condensation at different operating conditions. A thorough discussion of procedure for determining deposition rates is included in APPENDIX C. Sample calculations for the single-tube experiment data analysis are shown in APPENDIX E.

## 4.2 Experimental Results

### 4.2.1   Exhaust Nusselt Number

The exhaust side Nusselt number for a clean tube was determined using air at Reynolds and Prandtl numbers similar to that of the exhaust in the fouling experiments.

To validate the results, a comparison is made between the coolant and air heat transfer rates in Figure 4.4. The agreement of the heat transfer rates within 10% validates the coolant heat transfer rate, exhaust flow rate, and exhaust temperature measurements. Accurate measurements of these parameters yield an accurate determination of exhaust-side Nusselt number. The measured Nusselt numbers from the air test are compared with the predictions of several correlations for Nusselt number for fully developed flow through smooth tubes in Figure 4.5. The experimental results show good agreement with the correlations at Reynolds numbers from about 3,000 to 7,000; however, the measured data deviate from the correlation of Churchill (1977a) by as much as 25% at Reynolds numbers from 9,000 to 11,000. It should be noted that during the development of this correlation, Churchill also found the greatest deviation, as much as 20%, at Reynolds numbers from 10,000 to
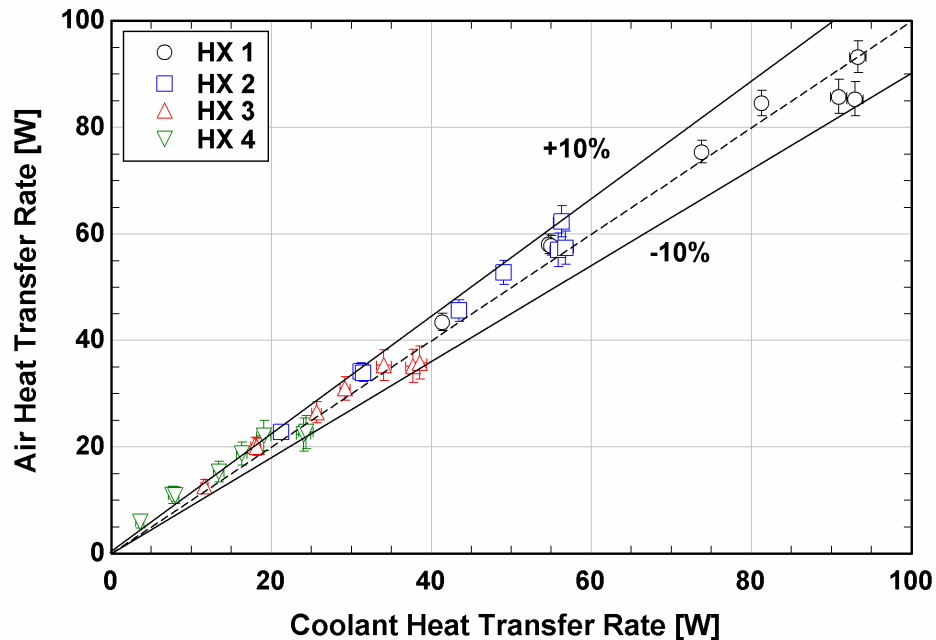


**Figure 4.4: Comparison of heat transfer rates for determination of exhaust side Nusselt number**
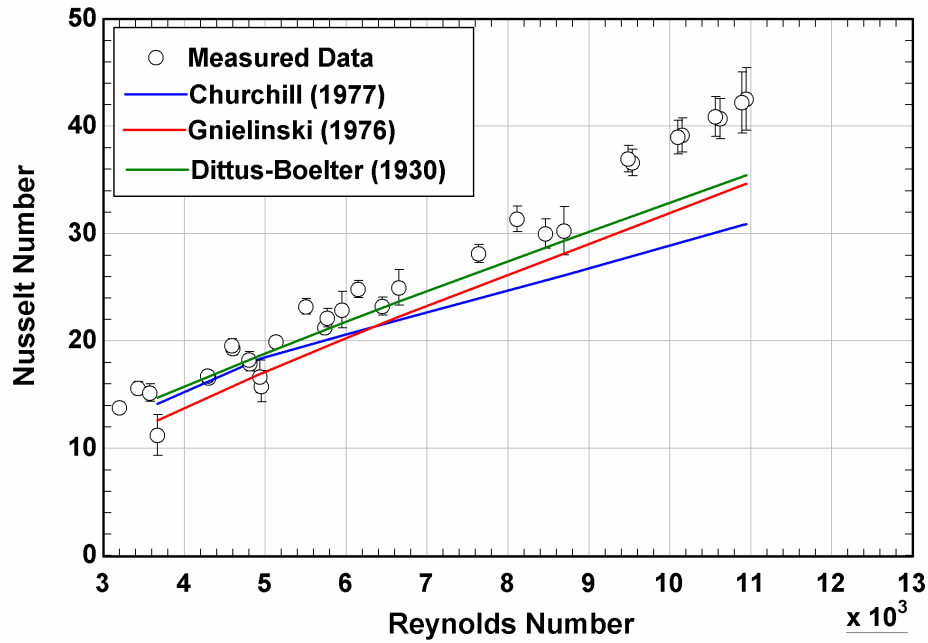
**Figure 4.5: Air test results for exhaust side Nusselt number**

12,000, between the data and predicted values. Therefore, the measured data from the present study are not far outside the bounds of the correlation. Differences in the Nusselt number can be attributed to uncertainty in tube roughness, inner diameter, and entrance effects.

To achieve more accurate prediction of the exhaust side Nusselt number, a curve fit was made to the measured data from this study. The form of the Dittus-Boelter (1930) correlation, shown in Equation (4.73), is used to fit the measured data.

$$Nu = A\,\mathrm{Re}^{b}\,\mathrm{Pr}^{c} \tag{4.73}$$

The coefficients $A$, $b$, and $c$, were defined by Dittus-Boelter to be 0.023, 0.8, and 0.3, respectively. To improve the accuracy of the correlation for this application, the coefficients $A$ and $b$ were modified to minimize the absolute average deviation (*AAD*)

between the correlation and the measured values. The coefficient *c* was not modified because Prandtl number was not varied in the experiments. As shown in Table 4.6, modifying *A* to 0.0045 and *b* to 0.995 reduces the absolute average deviation to 5.6%. A comparison of the measured Nusselt number and the predicted Nusselt number for both the correlation of Churchill (1977a) and the correlation of the present study is shown in Figure 4.6. The measured Nusselt number and predicted Nusselt number of the correlation in this study all fall within 10%, while the difference is as much as 25% for the correlation of

**Table 4.6: Modified correlation coefficients for exhaust Nusselt number correlation fit**

| | A | b | c | AAD [%] |
|---|---|---|---|---|
| **Dittus-Boelter (1930) Coefficients** | 0.023 | 0.8 | 0.3 | 9.3 |
| **Modified Coefficients** | 0.0045 | 0.995 | 0.3 | 5.6 |
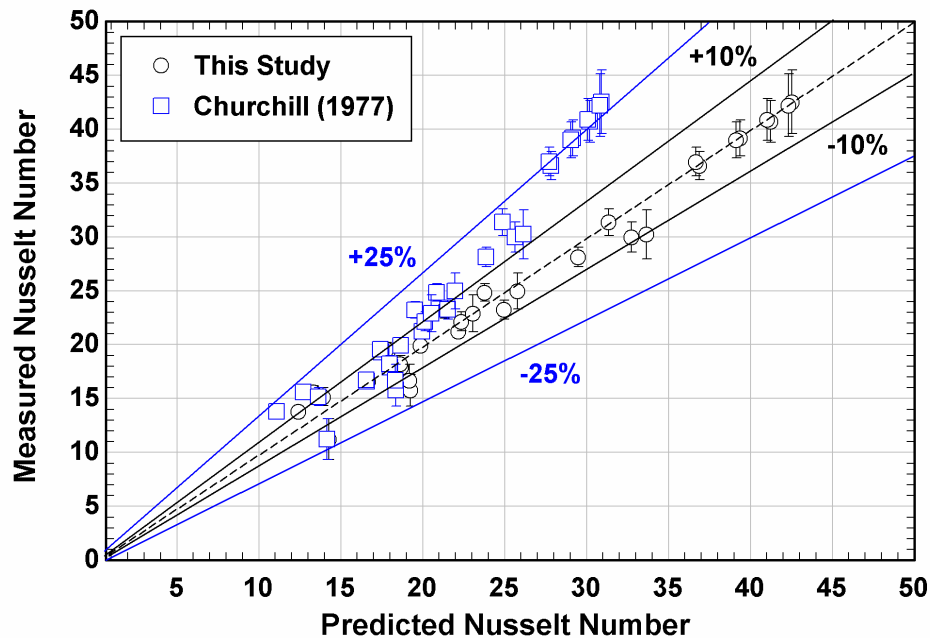


**Figure 4.6: Comparison of predictions of Churchill (1977a) and the present study with measured Nusselt number results**

Churchill (1977a). Calculating the exhaust side Nusselt number with the correlation of this study with a relative uncertainty of 10% significantly reduces the uncertainty in the calculated fouling resistance.

### 4.2.2    Validation of Experimental Results

An initial fouling test was performed at design conditions for the series configuration and the data were analyzed to ensure accurate determination of fouling resistance. The fouling resistance reached steady state, a less than 2% change for two consecutive hours, after exposure to exhaust for 24 hours, as shown in Figure 4.7. Data points are shown as five minute averages at about every hour. The decrease in fouling resistance at the start of the experiment is due to the time required for the exhaust and coolant outlet temperatures
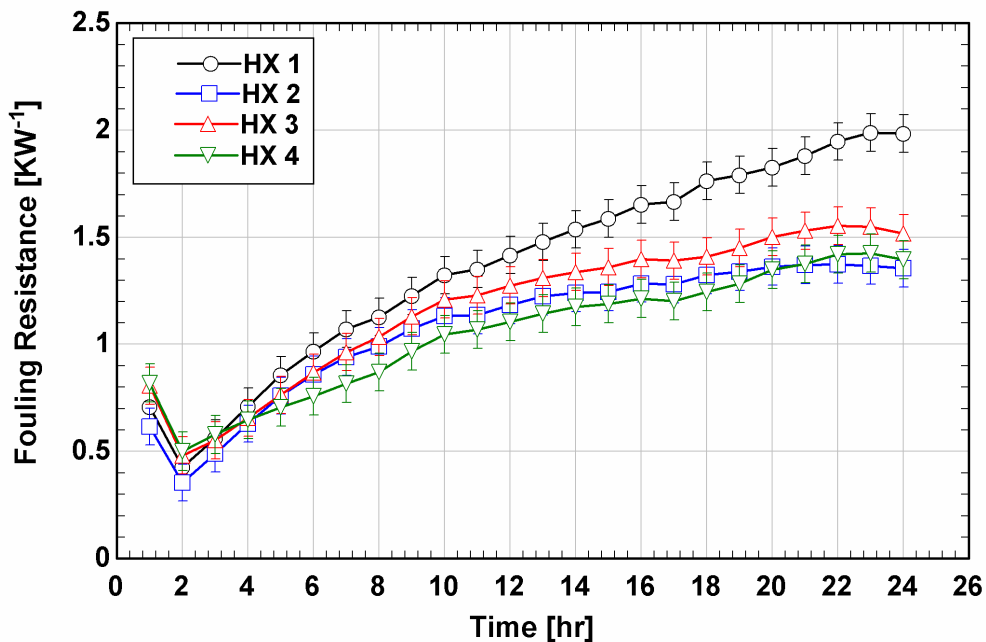


**Figure 4.7: Fouling resistance as a function of time for series configuration at design conditions**

to reach steady state. After this, the fouling resistance for each heat exchanger increases sharply with the rate of increase decaying over time. The fouling resistance of the first heat exchanger is greater than that of the three others. This is to be expected, because the temperature difference between the exhaust and coolant, the concentration of particulate matter, and the concentration of unburned hydrocarbons are all greatest in this heat exchanger. The fouling resistances of the other three heat exchangers are approximately equal, considering the uncertainty in the measurement. The magnitude of the steady state fouling resistance for the first heat exchanger is compared to the exhaust, tube, and coolant resistances in the same heat exchanger in Figure 4.8. The fouling resistance is the greatest resistance in the circuit and 2.5 times greater than the exhaust resistance, the dominant resistance of a clean tube. This makes the consideration of fouling extremely important to
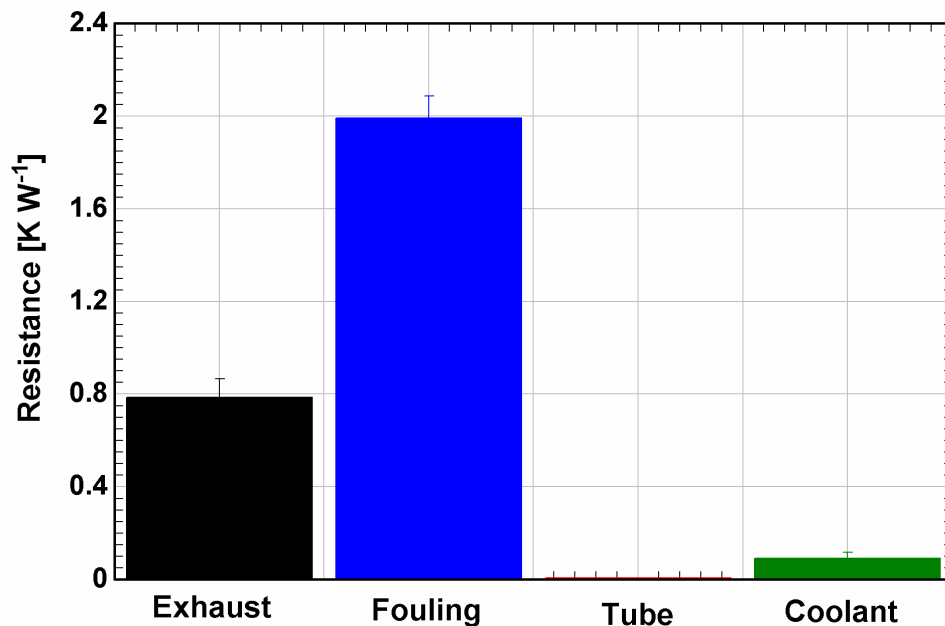


**Figure 4.8: Comparison of resistances in the first heat exchanger after 24 hours of exhaust exposure at design conditions**

the design of the desorber. Design of the desorber without the consideration of fouling would result in significant under sizing.

To evaluate the validity of the fouling resistance results, the exhaust and coolant heat transfer rates are compared as shown in the following equation.

$$EB_i = \frac{\dot{Q}_{ex,i} - \dot{Q}_{c,i}}{\dot{Q}_{c,i}} \times 100\% \tag{4.74}$$

The energy balance for each heat exchanger is plotted versus time for the entire fouling experiment in Figure 4.9. The coolant and exhaust heat transfer rates for the second and third heat exchangers are within 5% of each other for the duration of the experiment. The difference in heat transfer rates for the fourth heat exchanger starts at about 15% and decreases to 5% by the end of the experiment. This is attributed to the changing exhaust
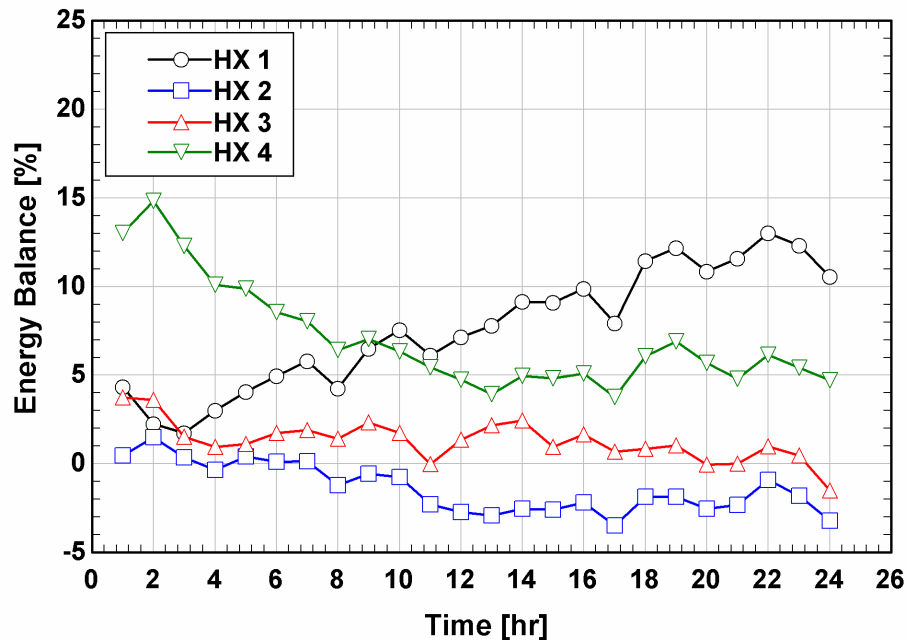


**Figure 4.9: Energy balance for each heat exchanger over the duration of the fouling test at design conditions**

temperature at the inlet to last heat exchanger. As the upstream heat exchanger fouls, the outlet exhaust temperature increases, resulting in a higher inlet temperature for the last heat exchanger. When the growth of the fouling resistance of the heat exchangers begins to slow down at about 10 hours, the energy balance of the fourth heat exchanger converges to an acceptable value. The energy balance between the two sides of the first heat exchanger starts at less than 5% discrepancy, but grows steadily throughout the experiment to a value of about 15%. The difference between the heat transfer rates at this point is outside the uncertainty in the two measurements and suggests either an inaccurate heat transfer rate measurement or additional heat transfer from the exhaust that is not gained by the coolant.

To investigate the accuracy of the coolant heat transfer rate measurement, an electric heater was inserted into the exhaust tube of the tube-in-tube heat exchanger, as shown in Figure 4.10. The power dissipated by the electric heater was measured and compared to the measured heat transfer rate of the coolant. This provided a means to isolate and validate the accuracy of the coolant heat transfer rate measurement. This was done for
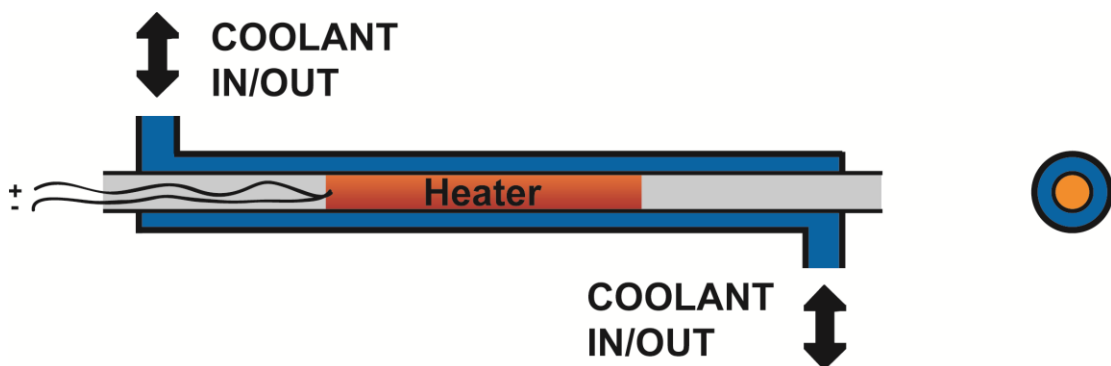


**Figure 4.10: Tube-in-tube heat exchanger with electrical resistance heater inserted into exhaust tube**

both the first and second tube-in-tube heat exchanger, comparing the heater energy balance defined by the following equation.

$$EB_{heater,i} = \frac{\dot{Q}_{heater} - \dot{Q}_{c,i}}{\dot{Q}_{heater}} \times 100\% \qquad (4.75)$$

The results of the tests are shown in Figure 4.11. The heater heat transfer rate is originally greater than the coolant heat transfer rate due to the time required for the coolant outlet temperature to reach steady state. This transient is due to the thermal capacitance of the heater, tubing, and fluids in the tube-in-tube heat exchanger. After this time, the energy balance for both heat exchangers converges to about 10%. The fact that the first heat exchanger converges to the same value as the second suggests that the coolant heat transfer
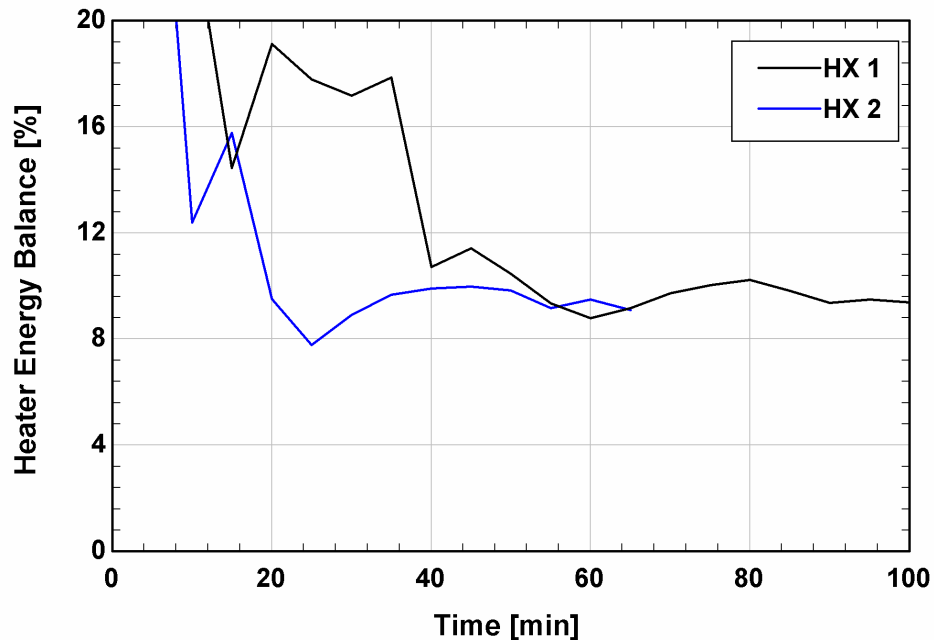


**Figure 4.11: Comparison of the coolant heat transfer rate to the heat dissipated by an electric heater for the first and second heat exchanger**

127

rate of the first heat exchanger is accurate as the energy balance for the second heat exchanger was within 5% in the fouling experiment at design conditions. The 10% difference between the coolant heat transfer rate and the heater power dissipated is attributed to electrical losses in the wiring and axial conduction along the length of the exhaust tube which is not as prevalent when exhaust is flowing. To eliminate the possibility of environmental factors influencing the energy balance, a heater test was performed outdoors for a duration of 14 hours. The heater energy balance results, along with the changing ambient temperature are shown in Figure 4.12. For this test, the heater energy balance is again at 10% throughout the duration of the test even though the ambient temperature changes significantly. The test was started before sunrise and stopped after sunset, which eliminates changing solar insolation as a possible reason for the energy
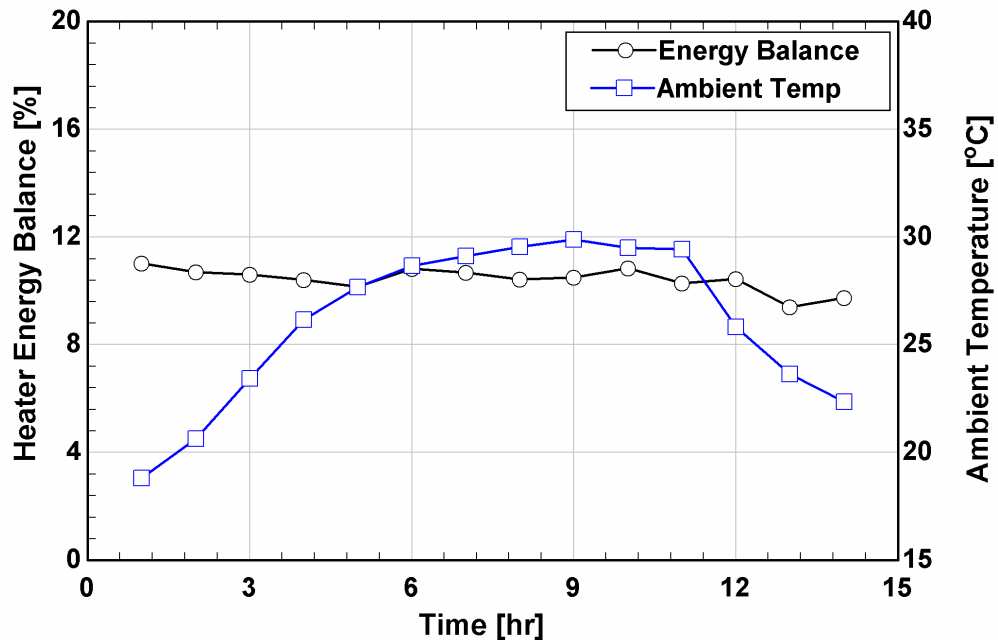


**Figure 4.12: Investigation of the effect of ambient conditions on heater energy balance for the first heat exchanger**

imbalance. Based on the results of both heater tests, the measurement of coolant heat transfer rate is deemed acceptable.

Other measurements that affect the calculation of fouling resistance are the exhaust temperatures and flowrate. The flowrate is not a likely cause for the deviation in the energy balance for the first heat exchanger because the exhaust is connected in series and the same measurement is used to calculate the heat transfer rate for second through fourth heat exchangers, which have acceptable energy balances. This leaves the exhaust temperature measurement as the remaining potential cause for the energy balance discrepancy. Since the energy balance of the first heat exchanger is initially within 5% and grows to 15%, it appears that a transient phenomenon is affecting the temperature measurement. One proposed explanation is that the thermocouple fouls throughout the experiment, causing a reduction in the measured temperature. To test this hypothesis, fouled thermocouples were removed and clean thermocouples were inserted into the exhaust, but no change in the exhaust temperature great enough to have an effect on the energy balance was observed. Radiation is also an unlikely explanation for inaccurate temperature measurement as a thorough accounting for this effect is made in the data reduction. The accuracy of the temperature and flow measurements are further validated by the measured heat transfer rates in the air test for exhaust side Nusselt number, which shown in Figure 4.4 have less than a 10% difference.

All of this information provides evidence that the heat transfer rate measurements are acceptable, suggesting that there is a physical mechanism causing a difference between the heat rejected from the exhaust and the heat gained by the coolant. The exhaust is a volatile, chemically reacting mixture, and there are several possibilities for this

phenomenon. One potential explanation is the evaporation of deposited hydrocarbons in the fouling layer. Hydrocarbons that were deposited at the beginning of the experiment could be evaporated after a fouling layer develops and the temperature of the surface of the fouling layer increases. The evaporation of the hydrocarbons would act as another heat sink that results in greater heat transfer from the exhaust than to the coolant; however, this process would not be continuous and lead to the steady growth in the observed energy imbalance. Once all of the hydrocarbons in the layer are evaporated, the energy imbalance should approach zero. This suggests that the evaporation of hydrocarbons is not the reason for the difference in the two heat transfer rates.

Another potential cause for the energy balance discrepancy could be an endothermic chemical reaction occurring in the exhaust. Such a reaction would require heat rejection from the exhaust that is not gained by the coolant. One potential reaction is the pyrolysis of unburned hydrocarbons in the exhaust. The reaction is not initiated, or at least not at noticeable levels, until the fouling layer grows in the first heat exchanger and the exhaust temperature increases throughout. The literature available for the pyrolysis reaction rates is limited for liquid hydrocarbons, but it is abundant for the pyrolysis of biomass. Reaction rate data for the conversion of biomass to gas, tar, and char through a pyrolysis reaction are reported by Haseli *et al.* (2011). The reaction rate constants for each reaction are modeled with the Arrhenius rate equation, as follows.

$$k = Ae^{\frac{E_a}{RT}} \tag{4.76}$$

The frequency factors ($A$) for the gas, tar and char reaction are reported to be $4.38 \times 10^8$, $1.08 \times 10^{10}$, and $3.27 \times 10^6$ s$^{-1}$, respectively. Similarly, the activation energy for each

reaction is 152.7, 148.0, and 111.7 kJ mol$^{-1}$, respectively. At a temperature of 400°C, the reaction rate constant for each reaction is determined. The global reaction rate is the sum of each individual reaction rate, and is calculated to be 0.024 s$^{-1}$. The mass conversion rate of hydrocarbons can be approximated with the reaction rate, the concentration of hydrocarbons in the exhaust, and the volume of the exhaust tube, as follows.

$$\dot{m}_{pyrolysis} = kC_{HC}V \tag{4.77}$$

The resulting conversion rate is $3.238 \times 10^{-9}$ kg s$^{-1}$. This value is multiplied by the enthalpy of the pyrolysis reaction, 418 kJ kg$^{-1}$, to determine the total heat transfer required for the reaction, as in Equation (4.78).

$$\dot{Q}_{pyrolysis} = \dot{m}_{pyrolysis} h_{pyrolysis} \tag{4.78}$$

The resulting heat transfer rate is 0.004 W, while the difference in the heat transfer rate in the first heat exchanger after 24 hours is 8.980 W. As the heat transfer required for the pyrolysis reaction rate is much less than the difference in the coolant and exhaust heat transfer difference, it is not likely that this is the cause of the energy balance discrepancy.

Although a specific cause for the energy balance discrepancy has not been determined, potential mechanisms that could be contributing to the additional heat rejected by the exhaust have been identified and discussed. Determining the exact mechanisms for the energy balance discrepancy is not necessary as long as the coolant heat transfer rate, exhaust flowrate, and exhaust temperature measurements are accurate. These measurement still yield an accurate estimate of the fouling resistance, the primary goal of the present investigation.

### 4.2.3    Steady State Experiments

Steady state experiments, in which the exhaust and coolant inlet temperatures were at steady state before exhaust entered the heat exchangers, are performed for a range of coolant temperatures, generator loads, and exhaust flow rates for both the series and parallel configurations. The goal of these experiments is to determine the worst case conditions for fouling. Experiments are performed for 10 hours, which provides enough time to establish differences and notice trends between different fouling conditions.

The fouling resistance results and predicted particulate matter and hydrocarbon deposition as a function of coolant temperature for the series configurations are shown in Figure 4.13. For any given test case, the fouling resistance of the first heat exchanger is
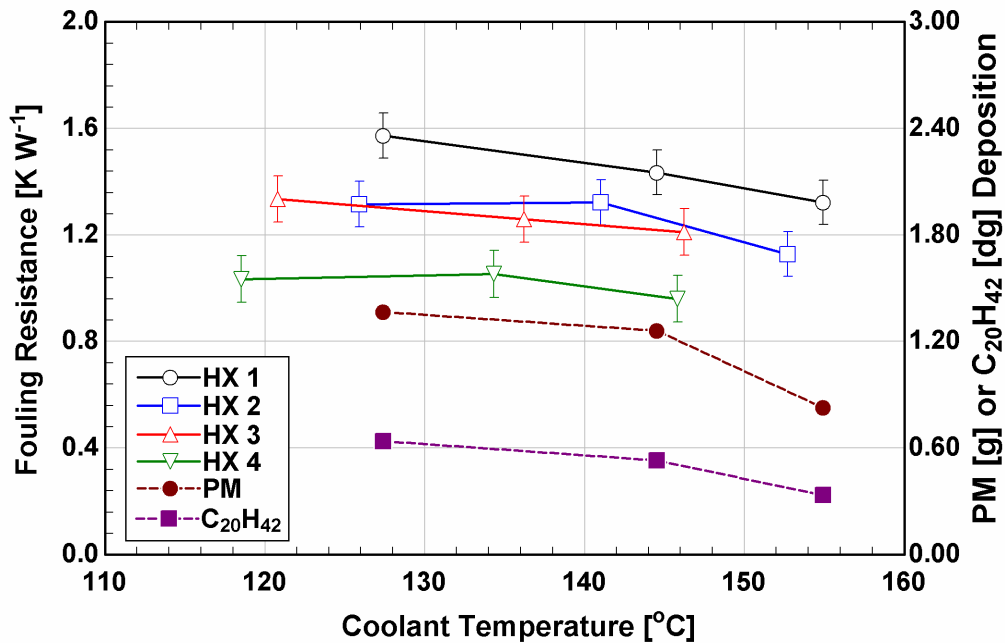


**Figure 4.13: Fouling resistance and model predicted deposition after 10 hours of exhaust exposure as a function of coolant temperature for the series configuration**

132

the greatest, the second and third heat exchanger are about equal, and the fourth heat exchanger has the least fouling resistance. This is attributed to the temperature difference between the exhaust and coolant and the particulate matter concentration in the exhaust decreasing in each subsequent heat exchanger, which both reduce the amount of thermophoretic deposition. Between cases, the fouling resistance generally decreases with increasing coolant temperature. This follows the trend of both the particulate matter and hydrocarbon deposition, which were predicted based on measured exhaust composition and temperature and calculated using the model described in Section 4.1.6. Thermophoresis increases with lower coolant temperature due to the increase in temperature difference, and hydrocarbon condensation increases with lower coolant temperature due to a lower tube surface temperature.
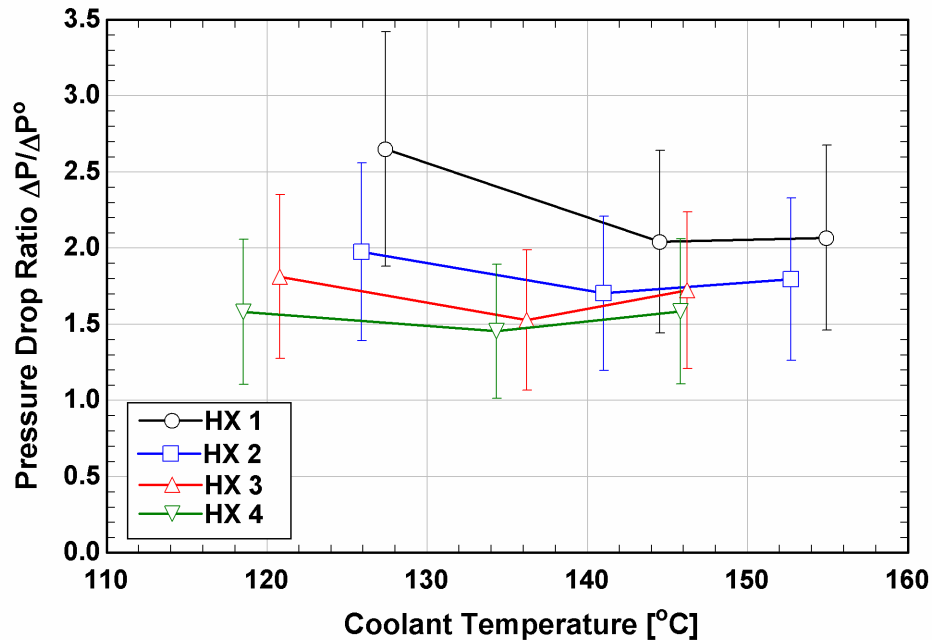


**Figure 4.14: Pressure drop ratio after 10 hours of exhaust exposure as a function of coolant temperature for the series configuration**

The pressure drop ratio results for the series configuration as a function of coolant temperature are shown in Figure 4.14. The pressure drop ratio shows trends similar to the fouling resistance. For a single test case, the pressure drop ratio decreases from the first to the fourth heat exchanger. The pressure drop ratio is greatest at the lowest coolant temperature. While the fouling resistance is dependent on both the fouling layer thickness and thermal conductivity, the pressure drop ratio is primarily dependent on the fouling layer thickness alone. Therefore, differences in the thermal conductivity of the fouling layer can lead to differences between the trends in pressure drop and resistance results. Measurement of the fouling layer thickness and resistance allows for a calculation of the effective thermal conductivity of the fouling layer using Equation (4.79).

$$k_{foul,i} = \frac{\ln\left(D_{IT,i} / \left(D_{IT,i} - 2t_{foul,i}\right)\right)}{2\pi D_{IT,i} R_{foul,i}}$$

(4.79)

The measured fouling layer thickness and calculated effective thermal conductivity as a function of coolant temperature are shown in Figure 4.15. The fouling layer thicknesses for the first and second heat exchangers are nearly constant across all coolant temperatures. The thicknesses for the third and fourth heat exchangers are much greater at the lowest coolant temperature case than at the higher temperatures. The fouling resistances for the third and fourth heat exchangers were only slightly greater at the lowest coolant temperature case than at the higher coolant temperature cases; therefore, the thermal conductivities of the layers for the third and fourth heat exchangers were calculated to be greater at the lower coolant temperature case. Greater fouling layer thermal conductivities at lower coolant temperatures were also noticed by several other researchers (Sluder and Storey (2008); Sluder *et al.* (2009); Bika *et al.* (2012); Salvi *et al.* (2014)), and were
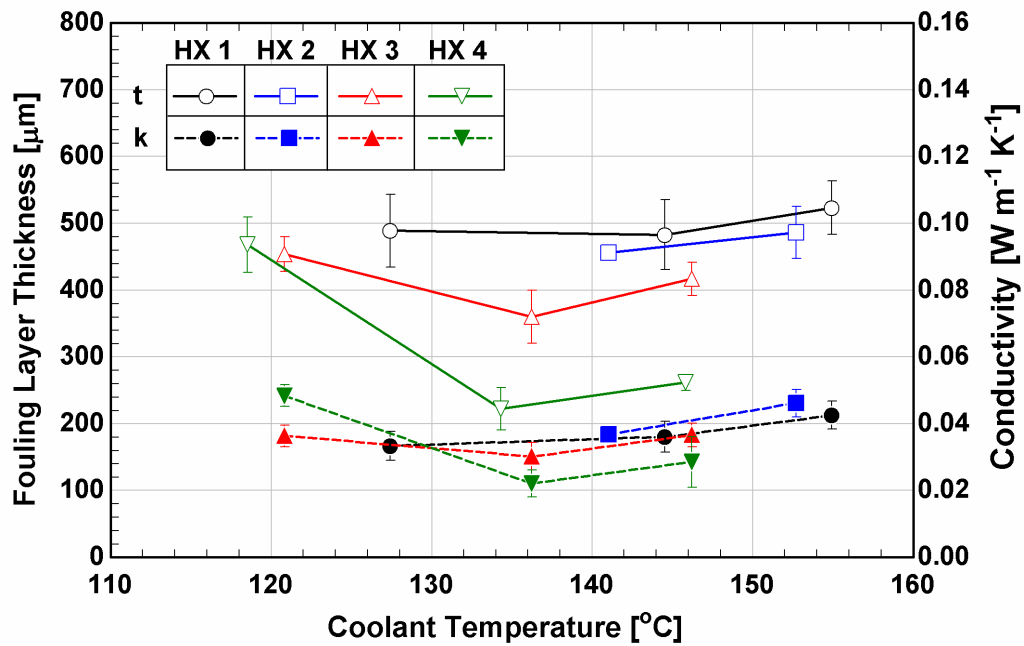
**Figure 4.15: Fouling layer thickness and thermal conductivity after 10 hours of exhaust exposure as a function of coolant temperature for the series configuration**

attributed to greater condensation of hydrocarbons onto the layer  The results in the present study support this hypothesis and demonstrate that hydrocarbon condensation increases both fouling layer thickness and thermal conductivity.  This has the potential to have varying effects on the fouling layer resistance.

The fouling resistance and predicted deposition results as a function of coolant temperature for the parallel configuration are shown in Figure 4.16.  The fouling resistance of the first heat exchanger is greatest at the lowest coolant temperature and decreases with increasing coolant temperature, which follows the same observed trend in the series experiments.  The fouling resistance in the second heat exchanger is actually lowest at the lowest coolant temperature.  This can be explained by the pressure drop results in Figure 4.17.  Contrary to the fouling resistance, the pressure drop ratio is actually greatest at the
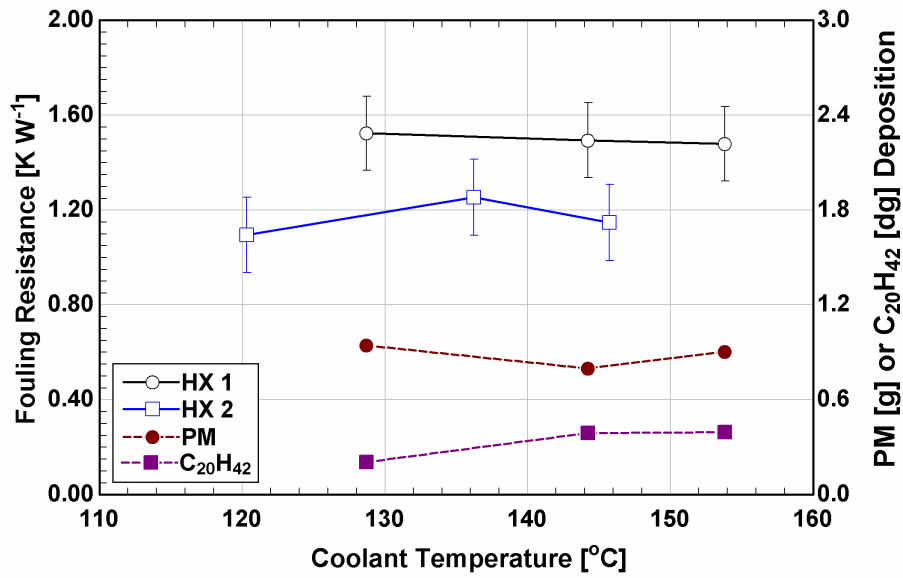
**Figure 4.16: Fouling resistance and predicted deposition after 10 hours of exhaust exposure as a function of coolant temperature for the parallel configuration**
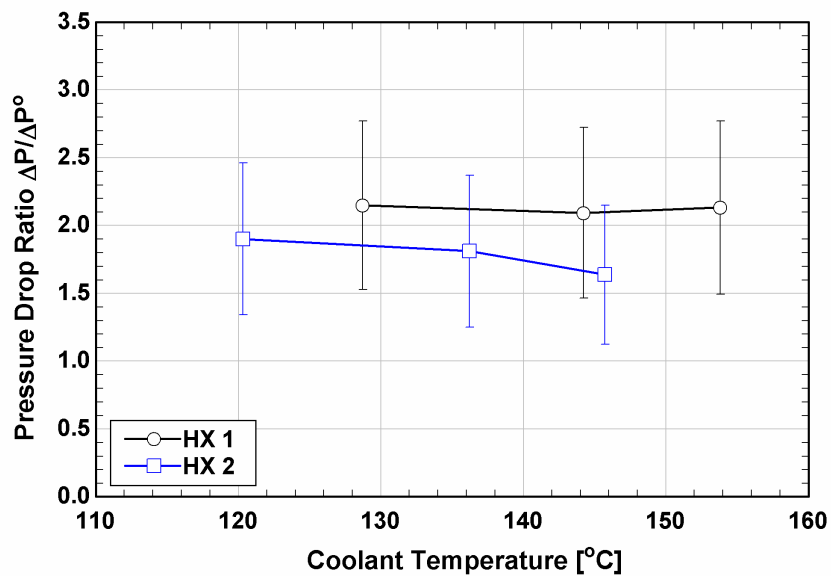


**Figure 4.17: Pressure drop ratio after 10 hours of exhaust exposure as a function of coolant temperature for the parallel configuration**

lowest coolant temperature, suggesting that the fouling layer thickness is greatest for this case. For the thickness to be greater at the lower coolant temperature than at the higher temperature while the fouling resistance is lower, the thermal conductivity of the layer at the lower coolant temperature must be greater. This supports the results found for the series configuration experiments that greater hydrocarbon condensation in the latter heat exchangers at the lowest coolant temperature results in a thicker but more conductive fouling layer.

Overall, the results of the series and parallel tests show that the fouling resistance and pressure drop ratio are most severe at the lowest coolant temperatures. For this reason, the lowest coolant temperature is used in the investigation of the effect of generator load. The generator load has a significant effect on both the exhaust temperature and composition. The exhaust temperature, particulate matter concentration, and hydrocarbon mole fraction on a $C_1$ basis are shown in Figure 4.18. The temperature is greatest at full load and decreases as load decreases. Below a load of 60%, the exhaust temperature becomes too low to be utilized, and experiments were not performed below this load. The particulate matter concentration is by far the greatest at 100%, sharply decreases at 90%, and remains approximately equal throughout the lower load points. The mole fraction of hydrocarbons is again greatest at full load, is approximately constant at the mid load points, and is lowest at 60%. These varying exhaust conditions have a significant effect on fouling resistance and pressure drop ratio results.
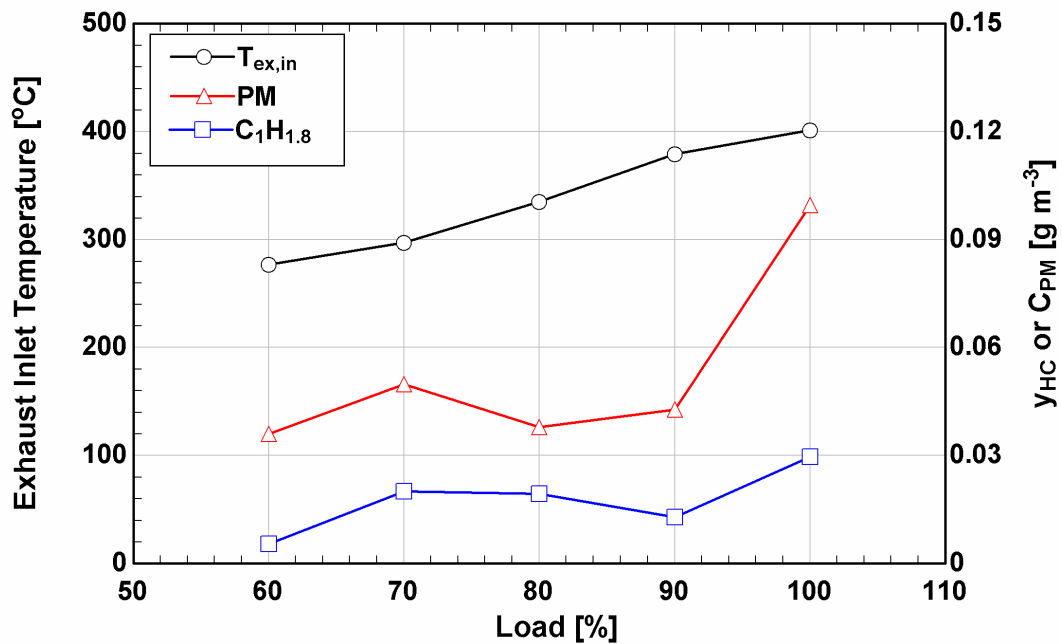
**Figure 4.18: Exhaust temperature and concentration as a function of generator load**

The fouling resistance results after 10 hours of exhaust exposure as a function of generator load for the series configuration are shown in Figure 4.19. As in the coolant temperature experiments, for a single load, the fouling resistance is greatest for the first heat exchanger, about equal for the second and third, and lowest for the fourth. Between load points, the fouling resistance is greatest at 60%, decreases to the lowest value at 80%, and increases again to 100%. This trend matches that of particulate matter deposition from 80% to 100%, but as the predicted deposition continues to slightly increases from 60% to 80%, the fouling resistance decreases considerably. This could be a result of the hydrocarbon condensation, which is much lower at 60% than 70 or 80%. The pressure drop ratio results for generator load in the series configuration are shown in Figure 4.20. The trend of pressure drop ratio is similar to that of fouling resistance except that the pressure drop ratio is greatest at 100% rather than 60%. This again suggests a difference
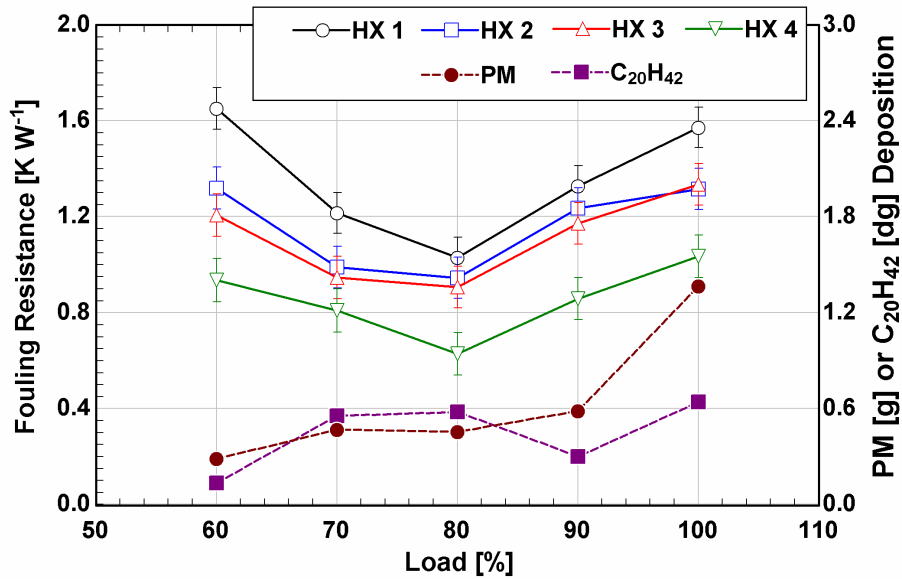
**Figure 4.19: Fouling resistance and predicted deposition after 10 hours of exhaust exposure as a function of generator load for the series configuration**
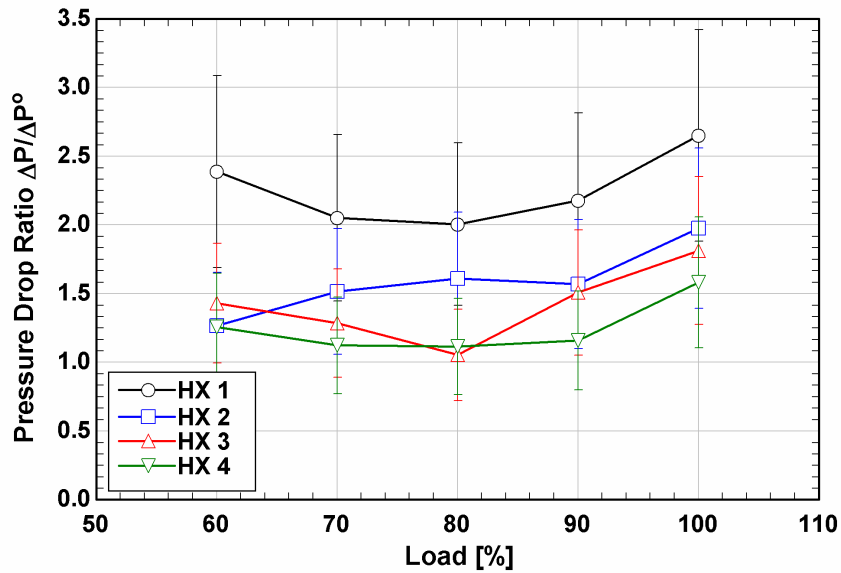


**Figure 4.20: Pressure drop ratio after 10 hours of exhaust exposure as a function of generator load for the series configuration**

in thermal conductivity of the fouling layer at different load conditions. The thermal conductivity and fouling layer thickness results are shown in Figure 4.21. The fouling layer thickness is the greatest at 100%, decreases at 80%, and slightly increases at 60%. The thermal conductivity of the fouling layer steadily decreases from 100% to 60%. While the thickness at 60% load is much less than that at 100%, the lower thermal conductivity explains why the fouling resistance is greater at 60% than 100%. The generator load that has the most severe effect on fouling was determined based on whether the percentage difference between the 60% and 100% load cases was greater for pressure drop ratio or fouling resistance. The fouling resistance at 60% load was 5.0% greater than that at 100% load, while the pressure drop ratio at 100% was 9.5% greater than that at 60% load;
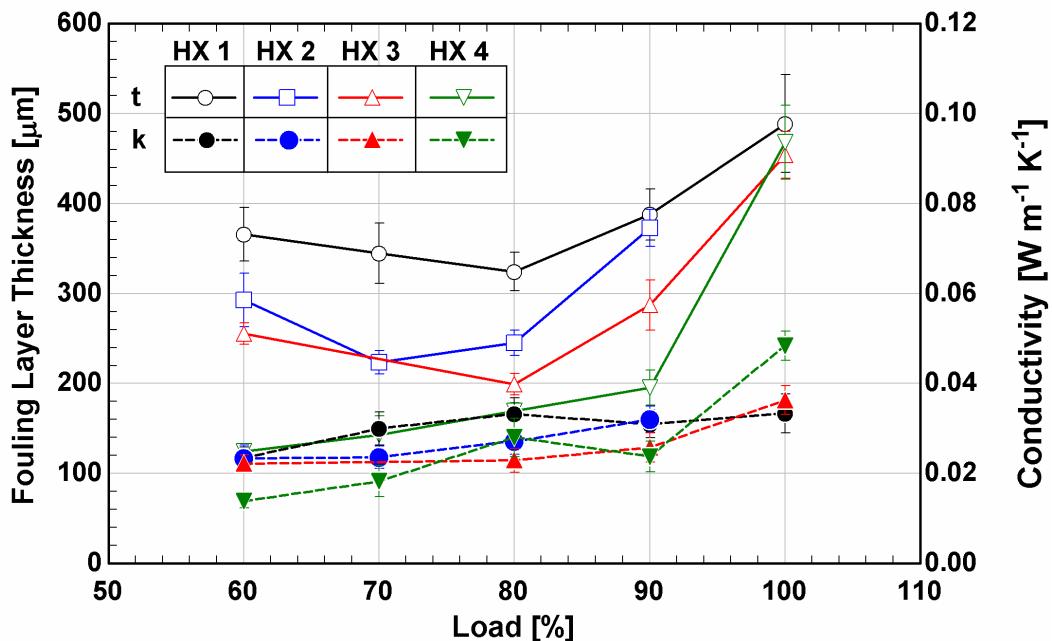


**Figure 4.21: Fouling layer thickness and thermal conductivity after 10 hours of exhaust exposure as a function of generator load for the series configuration**

therefore, the 100% load case was selected as the most severe generator load condition for fouling.

The fouling resistance results as a function of load for the parallel configuration are shown in Figure 4.22. The fouling resistance of the first heat exchanger follows a trend similar to that in series experiments; however, the fouling resistance is actually greatest at the full load case as opposed to the 60% load case. Interestingly, the predicted hydrocarbon condensation rate is lowest at 100% load for the parallel configuration while it was lowest for 60% load in the series configuration experiment. This likely promoted a less conductive layer and greater fouling resistance. The pressure drop ratio results, in Figure 4.23, show no significant difference for the pressure drop ratio of the first heat exchanger across all loads. The pressure drop ratio of the second heat exchanger is greatest at full load and
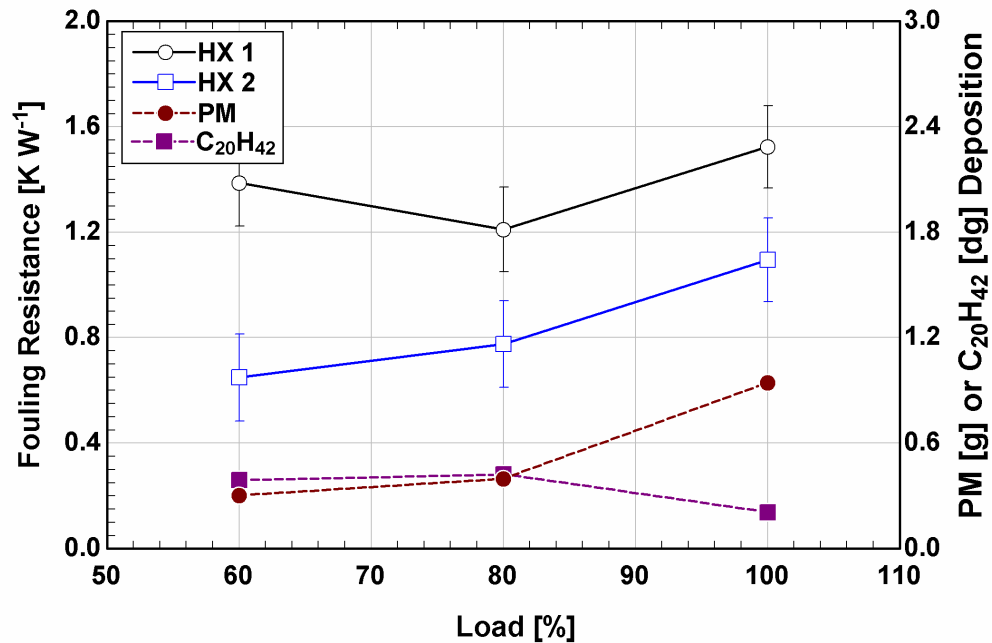


**Figure 4.22: Fouling resistance and predicted deposition after 10 hours of exhaust exposure as a function of generator load for the parallel configuration**
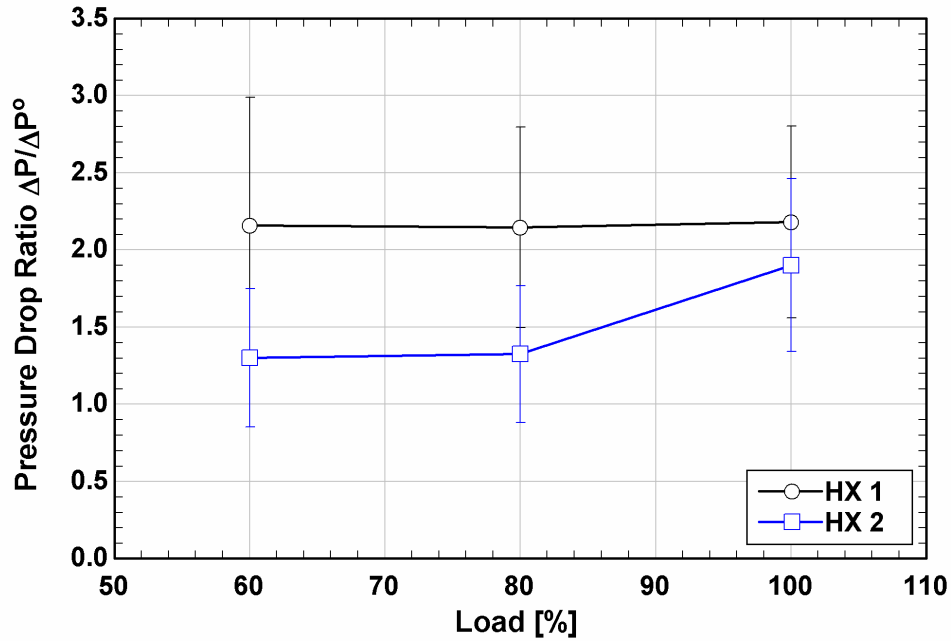
**Figure 4.23: Pressure drop ratio after 10 hours of exhaust exposure as a function of generator load for the parallel configuration**

approximately equal at the other load cases. For the parallel configuration experiments, the fouling resistance is greatest at full load with no significant difference in pressure drop ratio; therefore, full load generator operation has the most severe effect on performance. This was also the case for the series configuration; therefore, the generator is operated at full load in the evaluation of exhaust flow rate.

The fouling resistance and predicted deposition results for both the series and parallel configuration as a function of flow rate are plotted in Figure 4.24. The fouling resistance of all heat exchangers follows the trend of thermophoretic particulate matter deposition from a flow rate of 0.8 g s$^{-1}$ to 1.6 g s$^{-1}$; however, as predicted deposition increases for the 1.6 g s$^{-1}$ to 2.6 g s$^{-1}$ test cases, the fouling resistance decreases. This suggests that a removal mechanism is causing the fouling resistance to be lower at the

142
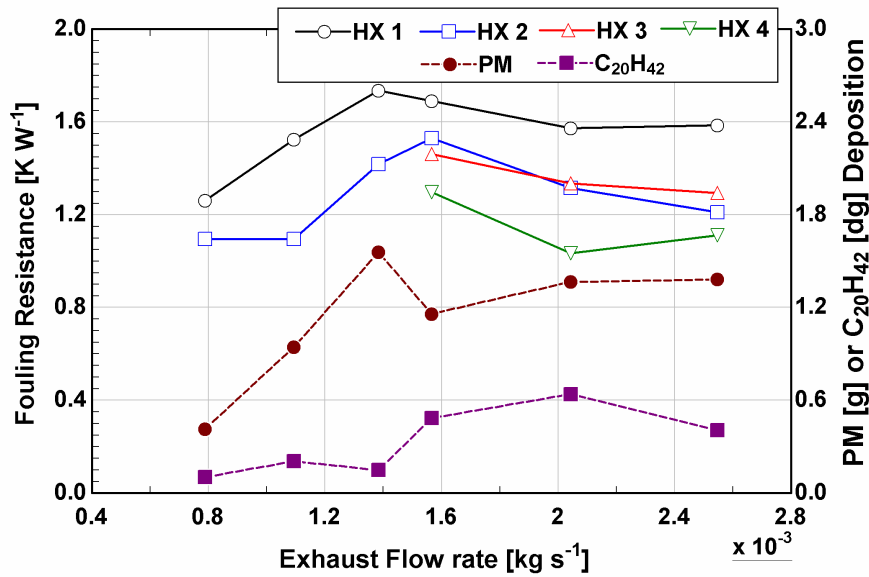
**Figure 4.24: Fouling resistance and deposition ratio after 10 hours of exhaust exposure as a function of exhaust flowrate for the series and parallel configuration**
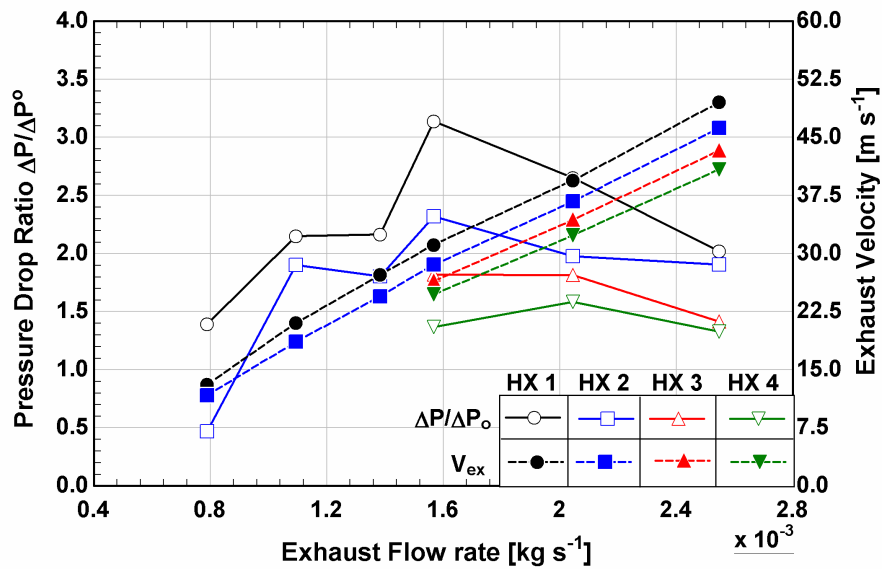


**Figure 4.25: Pressure drop ratio and exhaust velocity after 10 hours of exhaust exposure as a function of exhaust flowrate for the series and parallel configuration**

143

higher flow rates than at lower flow rates. The pressure drop ratio results as well as the calculated exhaust velocity are shown in Figure 4.25. The exhaust velocity is calculated such that no fouling layer has developed. At a single exhaust mass flow rate, the velocity is greatest in the first heat exchanger due to higher temperatures that result in a lower density, and decreases in subsequent heat exchangers. The pressure drop ratio decreases at the highest two flow rate test cases, a trend similar to that of fouling resistance. It is hypothesized that flow-induced shear removal of the fouling layer causes this reduction. Sluder *et al.* (2013) found that flow induced shear occurred at average exhaust velocities as low as 42 m s$^{-1}$. The exhaust velocities for the fourth through first heat exchanger at exhaust flowrates of 2.1 and 2.6 g s$^{-1}$ range from 32.3 to 39.42 m s$^{-1}$ and 40.9 and 49.6 m s$^{-1}$, respectively. The velocities at the 2.1 g s$^{-1}$ test case approach the threshold determined by Sluder *et al.* (2013), while the velocities at 2.6 g s$^{-1}$ exceed the threshold. This suggests that shear induced removal occurs at these test points and that greater exhaust velocity has the potential to reduce the steady state fouling thickness. The fouling layer thickness and thermal conductivity for the series flow rate experiments are shown in Figure 4.26. The thickness and thermal conductivity of the fouling layer are approximately constant for each heat exchanger across the flow rate range. This provides further evidence that the higher exhaust velocity limits the growth of the fouling layer.

The steady state testing results determined that fouling is most severe at the lowest coolant temperature and at full load generator operating conditions for both the series and parallel configuration. These are the conditions for which desorber is designed. The fouling results for exhaust flow rate are used to design a modified desorber that reduces the steady state fouling resistance and pressure drop. A comparison of the measured heat

144
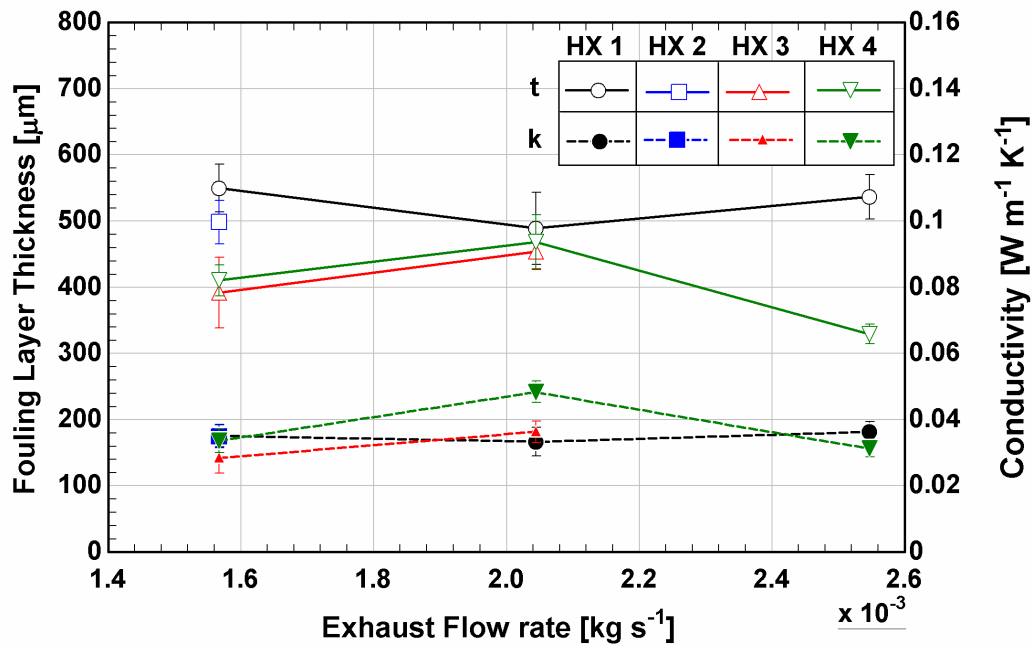
**Figure 4.26: Fouling layer thickness and thermal conductivity after 10 hours of exhaust exposure as a function of exhaust flowrate for the series configuration**

transfer rates for both the series and parallel experiments is shown in Figure 4.27. The difference in heat transfer rate between the exhaust and coolant is within 10% for the majority of the series experiments, with the only exceptions being those for the first heat exchanger in a few experiments. The energy balance for the first heat exchanger followed the same trend in which it began below 5% and grew throughout the experiment. The difference in heat transfer rates for the parallel experiments was greater, sometimes as much as 40% for the first heat exchanger. Heat transfer measurements were verified for parallel experiments with the same means discussed previously. This suggests that the mechanism causing the difference in the heat transfer rates is exacerbated at the lower exhaust flowrates. As stated previously, this does not affect the measurement of the fouling resistance.
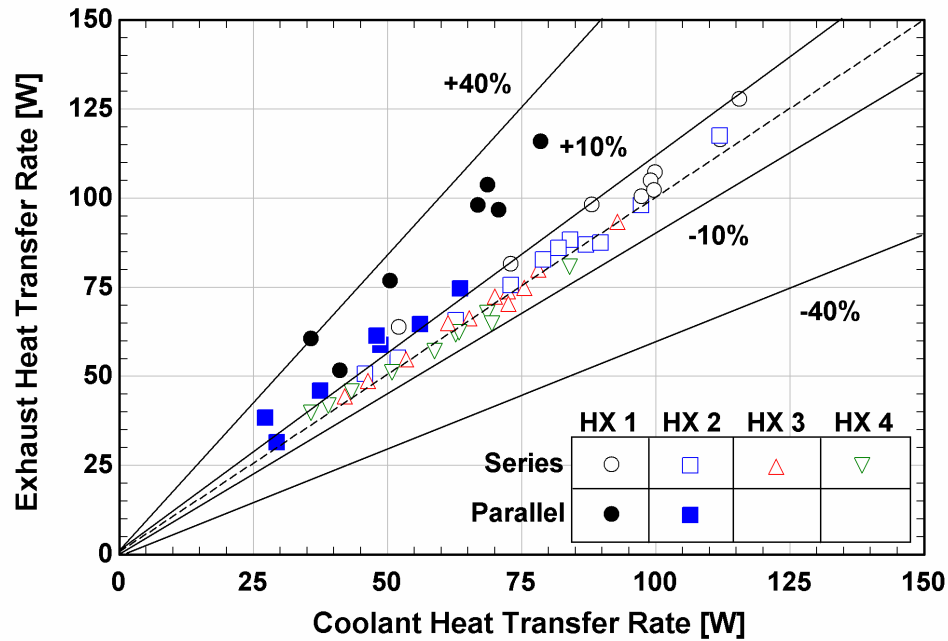
**Figure 4.27: Heat transfer rate comparison for the steady state experiments**

*4.2.4 Transient Experiments*

Transient experiments were performed to determine the effect of heat pump and generator start up on the fouling of the desorber. Two sets of experiments were performed. In the first set, referred to as the engine steady case, the generator is run until the exhaust reaches a steady temperature before it is directed into the experimental facility. In the second set, referred to as the engine start-up case, exhaust is directed into the experimental facility at the instant the generator is started. For both sets of experiments, the coolant start-up time, the time for the coolant inlet temperature to reach its steady state value, is varied between 0, 15, and 30 minutes. The zero-minute start-up time represents the results of the steady state experiments.

The transient experiments were performed at the nominal flowrate for the parallel configuration with the lowest coolant temperature and the generator at full load. The fouling resistance and predicted deposition results for the transient experiments after 10 hours of exhaust exposure are shown in Figure 4.28. As in the steady state experiments, the resistance of the first heat exchanger is greater than that of the second heat exchanger for any test point. There is an increase in the fouling resistance from 0 to 15-minute start-up time for both the engine steady and start-up cases. The predicted thermophoretic particulate matter deposition does not increase between 0 and 15 minutes for either case; therefore, there must be another mechanism for the increased deposition. The predicted hydrocarbon condensation does increase between these two test points due to the lower tube surface temperature at the start of the experiment. The results suggest that the
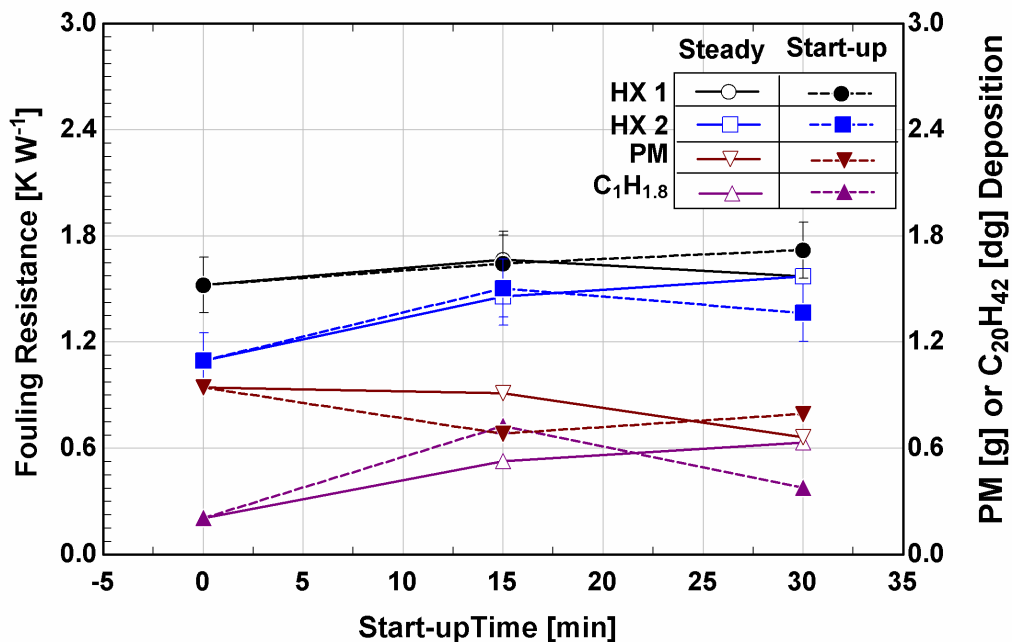


**Figure 4.28: Fouling resistance and predicted deposition results of the transient experiments after 10 hours of exhaust exposure**

additional deposition of hydrocarbons at the start of the experiment promotes deposition of particulate matter and results in a greater fouling resistance. There is no consistent difference in the fouling resistance between the 15 and 30 minute start-up times for the two cases. For the engine steady case, the fouling resistance for the first and second heat exchanger decreases slightly, but for the engine start-up case there is a slight increase. Both of these changes correspond with the change in predicted particulate matter deposition. From these results, it is concluded that the duration of the transient start-up does not have a significant effect on the fouling resistance, but any transient start-up in which the coolant is initially at a lower temperature causes a greater fouling resistance. The engine start-up case with a coolant start-up time of 30 minutes resulted in the greatest fouling resistance, and this case is used in the experiment to quantify the worst case steady state fouling resistance and pressure drop ratio.

The fouling resistance and pressure drop results as a function of exhaust flowrate from the steady state experiments are used as inputs to a desorber model to select an optimum configuration that minimizes fouling and meets the performance requirements for the heat pump. A thorough discussion of this selection process is provided in Chapter 5. The steady state fouling resistance of the 10-hour experiments was predicted based on the ratio of the 10-hour fouling resistance to the steady state fouling resistance in the initial full length experiment at design conditions. The per-tube exhaust flow rate predicted to meet heat transfer performance without exceeding the maximum back pressure on the engine is 1.6 g s$^{-1}$. To validate the prediction of the steady state fouling resistance was an accurate representation of the actual steady state fouling resistance, an experiment is performed in the series configuration for the exhaust flowrate of 1.6 g s$^{-1}$ until the fouling

resistance reaches steady state. The test was performed with the lowest coolant temperature, full generator load, and the 30-minute engine start-up transient, as these conditions lead to the worst case fouling. The fouling resistance and predicted particulate matter deposition results for every hour throughout the experiment are shown in Figure 4.29. The fouling resistance increases throughout the experiment until it reaches steady state after 23 hours of exhaust exposure. While the fouling resistance of all four heat exchangers levels off and slightly decreases in the last several hours, the predicted deposition does not. The predicted deposition does show some decay due to the increase in the fouling layer surface temperature, which reduces the temperature difference for thermophoresis, but it does not level off to the degree that the fouling resistance does. This suggests that a removal mechanism is partially responsible for the leveling of the fouling
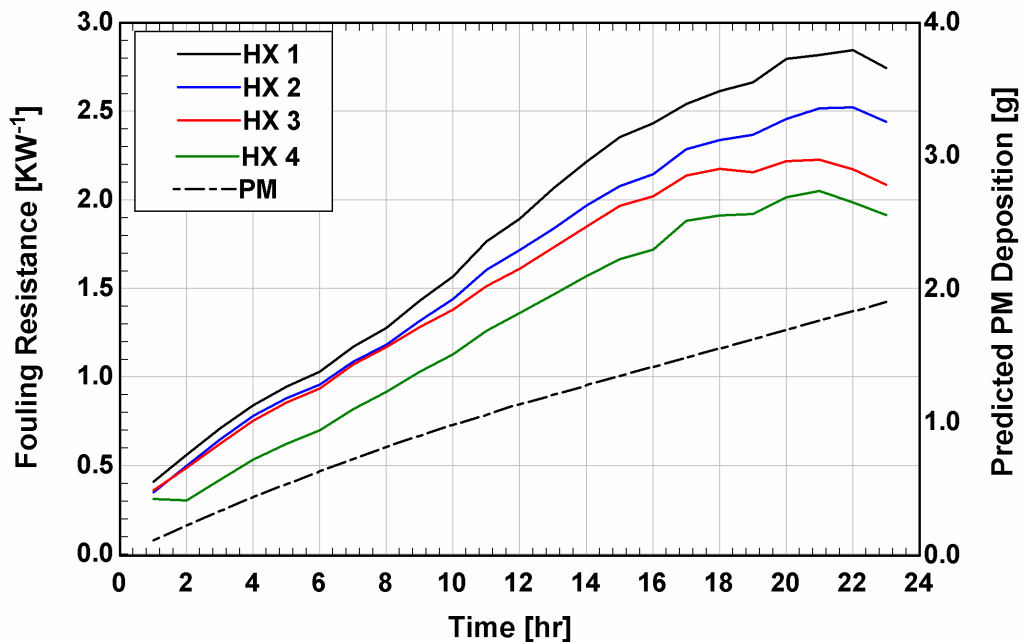


**Figure 4.29: Fouling resistance and predicted deposition as a function of time for the full length test at the worst case fouling conditions**

resistance.  This is further emphasized by the fact that the fouling resistance decreases in the final hour or two for each heat exchanger.

To investigate the potential for shear induced removal, the rate of change of fouling resistance per hour and the predicted exhaust velocity are examined.  The predicted exhaust velocity is the velocity accounting for the change in diameter due to growth of the fouling layer. The fouling layer thickness was measured at the end of the experiment and the layer thermal conductivity was calculated.  Assuming that the thermal conductivity of the layer was constant throughout the experiment, the fouling thickness throughout the experiment was back calculated.  The fouling layer thickness allowed for prediction of the velocity change. The predicted velocity and the rate of change in fouling resistance are shown in Figure 4.30.  The rate of change of fouling resistance begins to decrease sharply at 17 hours
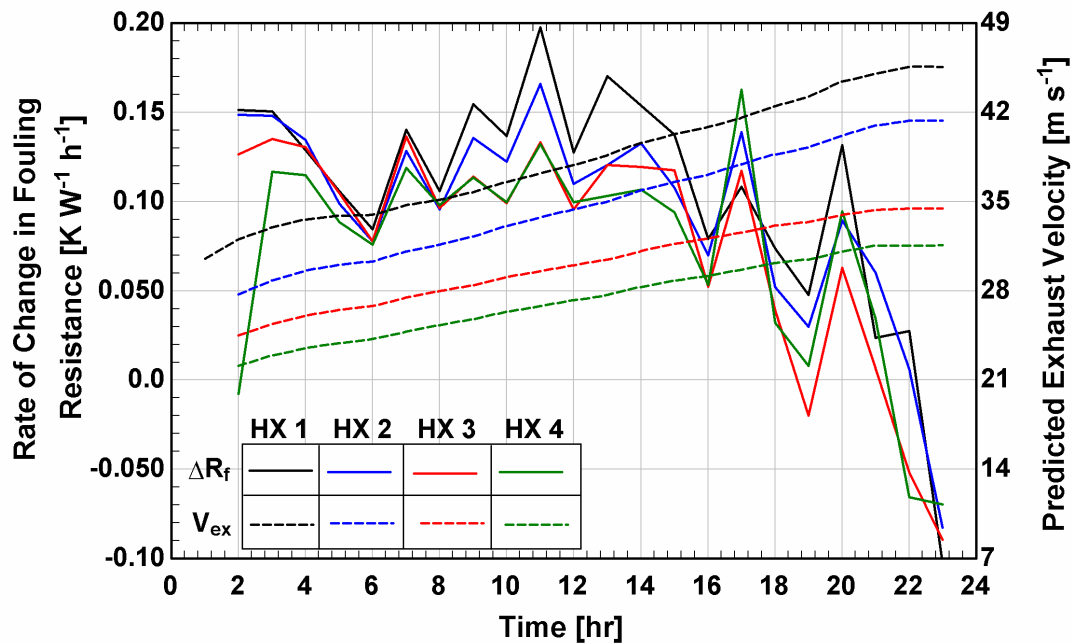


**Figure 4.30: Rate of change of fouling resistance and predicted exhaust velocity as a function of time for the full length test at the worst case fouling conditions**

150

from the beginning of the experiment. This signifies that the fouling resistance is leveling off. Interestingly, the exhaust velocity in the first heat exchanger is about 42 m s$^{-1}$ at this point, which is the velocity observed by Sluder *et al.* (2013) to initiate removal of the fouling layer by flow induced shear. The velocity of the exhaust in the remaining heat exchangers is similar to that in the steady state series configuration experiment at a flowrate of 2.1 g s$^{-1}$, in which removal is also apparent. These results suggest that removal of the fouling layer due to flow-induced shear is a contributor to the leveling of the fouling layer in time.

All of the previous experiments have been performed continuously without starting or stopping the generator throughout the duration of the test. To determine the effect of stopping and starting up the generator on the fouling resistance and pressure drop, a duty cycle test is performed in which the heat exchangers are exposed to exhaust for 10 hours each day for 5 consecutive days. This is consistent with the load requirements for the generator and the exhaust exposure of the desorber in a field application. The experiment is performed at the worst case fouling condition and the fouling resistance throughout is shown in Figure 4.31. The first cycle of five was only performed for 9 hours due to a fault that occurred with the generator. From the end of the first cycle to the beginning of the next, there is no difference in the trend of the fouling resistance. It continues to increase as if the generator was not shut down and started back up. In each subsequent cycle, the fouling resistance at start-up is much less that that at the end of the previous cycle. It is also noticed that the degree to which they differ is not consistent between cycles. The resistance of the fouling layer never exceeds the resistance determined from the continuous test at these conditions despite the fact that there is an additional 26 hours of exhaust
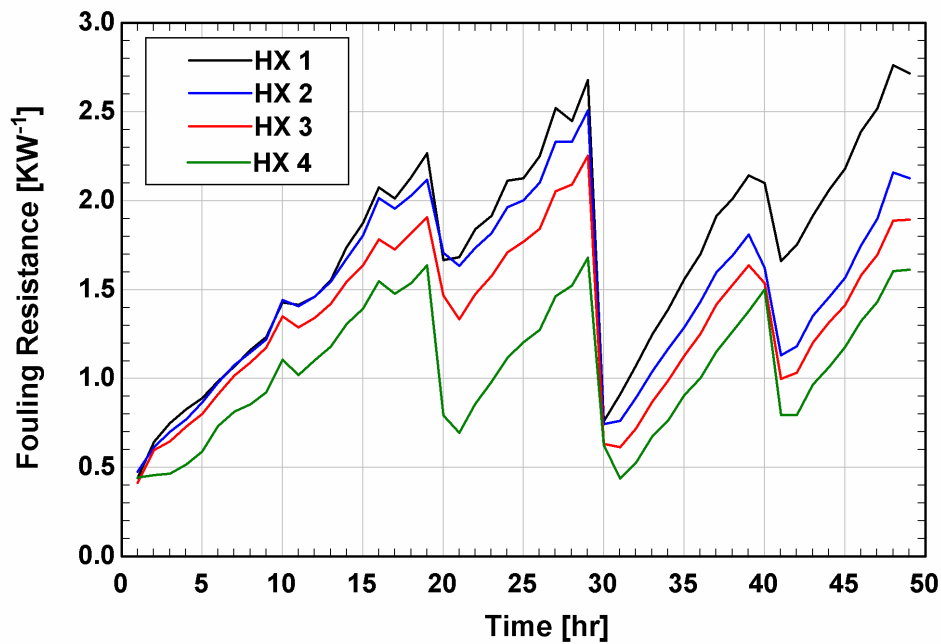
**Figure 4.31: Fouling resistance as a function of time for the duty cycle test at the worst case fouling conditions**

exposure in the duty cycle experiment.  It is also interesting that when the fouling resistance in the duty cycle test reaches the maximum value found from the continuous test, about 2.8 K W$^{-1}$, the fouling resistance again decreases as it did in the continuous test.

The variation of the fouling resistance between experiments could be attributed to the fouling layer structure. Storey *et al.* (2013) investigated deposit structures in EGR coolers and found that the layer at the tube surface that is initially formed is denser compared to the top portion of the layer. The top portion consists of thin dendritic structures that grow radially to increase fouling layer thickness.  This top layer could collapse in between cycles causing the layer to become thinner.  The top dendritic layer could also be removed due to shear stress as the exhaust enters the tube at the beginning of the next cycle. The fouling resistance would be reduced in either of these scenarios.  If the top dendritic

**Table 4.7: Comparison of fouling layer properties for the continuous and duty cycle tests**

| Test | Heat Exchanger | Resistance [K W$^{-1}$] | Thickness [μm] | Conductivity [W m$^{-1}$ K$^{-1}$] |
|---|---|---|---|---|
| Continuous (23 Hour) | 1 | 2.744 | 889.4 | 0.0362 |
| | 2 | 2.441 | 846.8 | 0.0385 |
| | 3 | 2.084 | 584.3 | 0.0303 |
| | 4 | 1.915 | 528.7 | 0.0297 |
| Duty Cycle (49 Hours) | 1 | 2.715 | 816.7 | 0.0333 |
| | 2 | 2.126 | 571.2 | 0.0290 |
| | 3 | 1.895 | - | - |
| | 4 | 1.613 | 351.1 | 0.0230 |

layer had not yet formed at the end of the first cycle, it could explain the lack of a decrease in the fouling resistance at the beginning of the second cycle.

The fouling layer resistance, thickness, and thermal conductivity after 23 hours of exposure in the continuous test and 49 hours of exposure in the duty cycle test are compared in Table 4.7 to further understand the difference in the development of the fouling layer. The fouling layer in the duty cycle test has a smaller thickness and is less conductive for all heat exchangers. If the difference in the fouling resistance at the end of one cycle and beginning of the next is due to compaction of the layer, it would become thinner, denser, and more conductive. A greater thermal conductivity is not observed in Table 4.7, and it seems more likely that a portion of the fouling layer is actually removed between experiments.

## 4.3 Comparison with Literature

The mass gain of soot in the first heat exchanger at worst case fouling conditions is determined for comparison with values in the literature. The mass gain is computed with Equation (4.80).

$$m_{soot,1} = \rho_{soot} L_{annulus} \frac{\pi}{4} \left( D_{IT,i}^2 - \left( D_{IT,i} - 2t_{foul,1} \right)^2 \right) \qquad (4.80)$$

The fouling thickness is known at 23 hours of exhaust exposure. This value is used to calculate the thermal conductivity of the fouling layer. Assuming that the thermal conductivity is constant throughout the experiment, it was used with the fouling resistance to calculate fouling thickness at any time throughout the experiment. The density of the soot was taken to be 0.0316 g cm$^{-3}$, which was measured by Lance *et al.* (2009) for a fouling layer developed with similar exhaust and coolant conditions.

A comparison of mass gain reported in the literature to the mass gain computed for the first heat exchanger at worst case fouling conditions in this study is shown in Table 4.8. The mass gain is compared on a per unit surface area basis to account for the difference in tube and heat exchanger geometries. Differences in the mass gains are attributed to differences in the exhaust and coolant conditions. The exhaust and coolant temperatures of this study best match those of Sluder and Storey (2008), and coincidentally the mass gains after 12 hours of exhaust exposure are very similar. The exhaust and coolant temperatures in the investigation by Hong *et al.* (2011) are also similar to those in this study, but the reduced exhaust mass flux results in less mass gain. The exhaust mass fluxes in the experiments of Sluder *et al.* (2009) and Bika *et al.* (2012) are the most similar to the mass flux in the present study; however, the mass gains are much lower. This is likely due

to the lower exhaust inlet temperatures of 200 and 250ºC, which reduce the temperature difference for thermophoresis. In general, the order of magnitude of the computed mass gain in this study compares well with those of the studies in the literature at each duration of exhaust exposure.

The fouling layer thickness and thermal conductivity results of the continuous test at the worst case fouling conditions are compared to results in the literature in Table 4.9. The fouling layer thickness is much greater in comparison to the other studies. For comparison to the study of Lance *et al.* (2009), the difference in thickness is attributed to the duration of exposure to exhaust, which is nearly half of that in this study. The duration of exhaust exposure for the study of Salvi *et al.* (2014) is similar to that for this study, but the lower temperature difference between the exhaust and coolant and the lower exhaust mass flux results in the lower fouling layer thickness. The thermal conductivity of the fouling layer should be independent of the duration of exhaust exposure, and the results of each study can be compared directly. The thermal conductivity of the fouling layer in this study is calculated to be slightly less than that in the previous research. However, the difference between the results of this study and those of Lance *et al.* (2009), whose deposit layer thickness measurements were also taken ex-situ, is only 12%.

Overall, the values for fouling resistance, thickness, and thermal conductivity compare well with the values of the literature. The results of the single-tube experiments provide valuable insight into the different mechanisms for fouling deposition and removal. These results are used in Chapter 5 to design a desorber that meets heat pump performance requirements after fouling has occurred. The desorber is fabricated and tested to validate its performance.

**Table 4.8: Comparison of the deposit mass gain of this study to that reported in the literature**

| Author(s) (Year) | Exhaust Inlet Temperature [ºC] | Exhaust Mass Flux [kg m$^{-2}$ s$^{-1}$] | Coolant Temperature [ºC] | Duration [hr] | Mass Gain [g m$^{-2}$] |
|---|---|---|---|---|---|
| Sluder and Storey (2008) | 375 | 37.3 | 95 | 12 | 19.6 |
| Sluder et al. (2009) | 250 | 16.0 | 85 | 2 | 3.8 |
| Hong et al. (2011) | 380 | 1.8 | 80 | 10 | 6.7 |
| Bika et al. (2012) | 200 | 22.1 | 90 | 1 | 0.4 |
| Present Study | 400 | 17.1 | 127 | 12 | 21.1 |
| | | | | 2 | 6.8 |
| | | | | 10 | 17.8 |
| | | | | 1 | 5.0 |

**Table 4.9: Comparison of the deposit thickness and thermal conductivity of this study to that reported in the literature**

| Author(s) (Year) | Exhaust Inlet Temperature [ºC] | Exhaust Mass Flux [kg m$^{-2}$ s$^{-1}$] | Coolant Temperature [ºC] | Duration [hr] | Thickness [micron] | Conductivity [W m$^{-1}$ K$^{-1}$] |
|---|---|---|---|---|---|---|
| Lance et al. (2009) | 375 | 37.3 | 95 | 12 | 410.0 | 0.041 |
| Salvi et al. (2013) | 280 | 4.8 | 70 | 24 | 379.0 | 0.047 |
| Present Study | 400 | 17.1 | 127 | 23 | 889.4 | 0.036 |

# CHAPTER 5.    DESORBER DESIGN AND EXPERIMENTS

In this chapter, the framework for the heat transfer and thermodynamic model of the fin-tray desorber is presented.  Results for fouling resistances of single-tube experiments are used in the model, and a parametric study is performed to select a desorber design that meets required performance after fouling has occurred.  The modified desorber is fabricated, fouling experiments are performed, and results are compared with those from single-tube experiments and model predictions.

### 5.1 Desorber Modeling

A heat transfer and thermodynamic model of the desorber is developed in Engineering Equation Solver (EES) to predict performance that meets performance requirements after fouling has occurred.  Desorber model boundary conditions are obtained from the heat pump cycle model and the single-tube fouling experiments. The concentrated solution inlet, dilute solution outlet, and exhaust inlet fluid properties are obtained from the heat pump cycle model at design ambient conditions.  These inputs are summarized in Table 5.1.  The worst-case fouling results from the single-tube experiments at a variety of exhaust flow rates are also input to the model. With these inputs, the model predicts the

**Table 5.1: Desorber model inputs from heat pump cycle model**

|  | Temperature [ºC] | Flow rate [g s$^{-1}$] | Quality | Pressure [kPa] | Concentration |
|---|---|---|---|---|---|
| **Exhaust** | 398.8 | 23.5 | - | 101.3 | - |
| **Concentrated Solution** | 137.6 | - | 0 | 2,889 | 0.60 |
| **Dilute Solution** | 190.4 | - | 0 | 2,889 | 0.29 |

total heat transfer rate, vapor generation rate, vapor concentration, and the exhaust pressure drop. These parameters are used in the evaluation and selection of the desorber design.

A segmented modeling approach is employed for improved heat transfer performance prediction. The segments are split vertically by desorber trays and horizontally by the two exhaust gas passes, as shown in Figure 5.1. The segments are numbered to follow the flow of the exhaust through each desorber column. The inlet exhaust temperature to the first segment is known from the heat pump cycle model and the inlet exhaust temperature to each subsequent segment is taken as the outlet temperature of the previous segment, as shown in Equation (5.1).

$$T_{ex,in,i} = T_{ex,out,i-1} \tag{5.1}$$
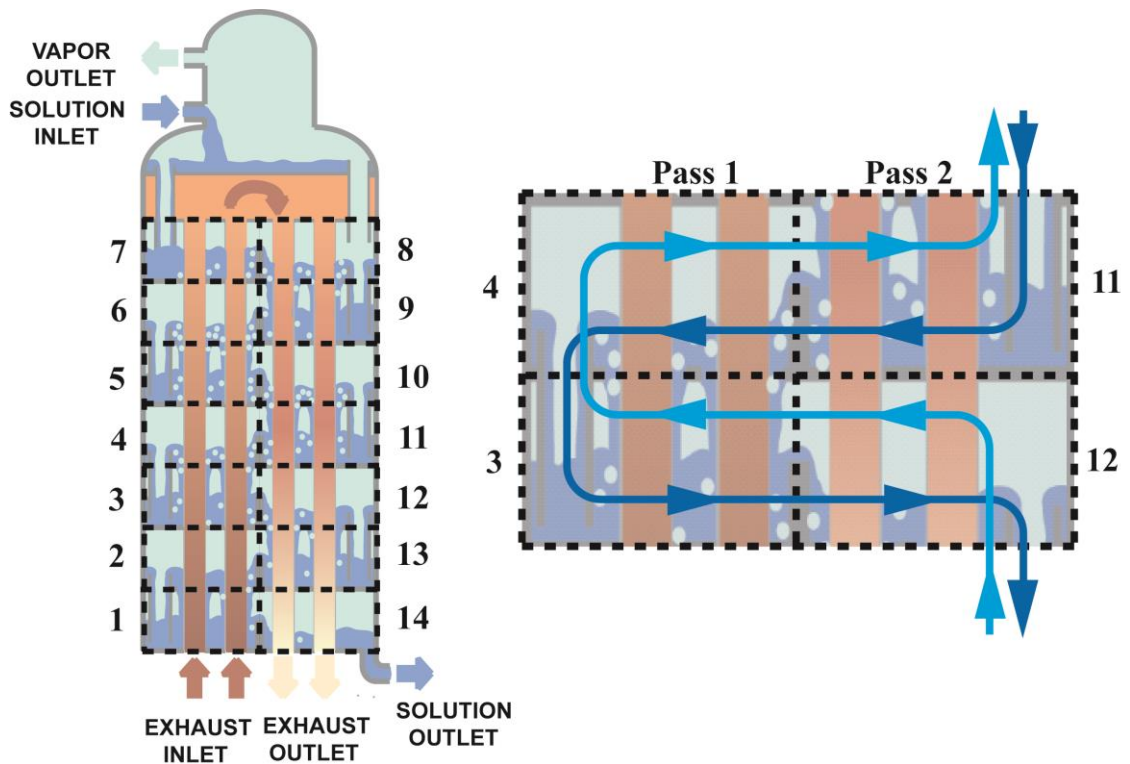


**Figure 5.1: Desorber model framework**

The subscript $i$ represents the segment number. The inlet liquid and vapor properties of each segment are also taken to be the outlet properties of the previous segment. Due to the serpentine flow of the vapor and liquid through the desorber, the number of the previous segment depends on the exhaust pass that the segment is in, the total number of segments, $n_{seg}$, and whether the current segment is even or odd. The upstream liquid and vapor segments are denoted with the counters $j$ and $k$, respectively. The counters are determined using Equations (5.2) and (5.3).

$$j = \begin{cases} n_{seg} + 1 - i & \text{if } i \text{ is even} \\ i + 1 & \text{if } i \text{ is odd} \end{cases} \right\} Pass\ 1 \\ \begin{cases} n_{seg} + 1 - i & \text{if } i \text{ is even} \\ i - 1 & \text{if } i \text{ is odd} \end{cases} \right\} Pass\ 2 \tag{5.2}$$

$$k = \begin{cases} i - 1 & \text{if } i \text{ is even} \\ n_{seg} + 1 - i & \text{if } i \text{ is odd} \end{cases} \right\} Pass\ 1 \\ \begin{cases} i + 1 & \text{if } i \text{ is even} \\ n_{seg} + 1 - i & \text{if } i \text{ is odd} \end{cases} \right\} Pass\ 2 \tag{5.3}$$

As an example, consider segment three. Segment three is in the first pass and is odd, using Equation (5.2) results in $j = 3 + 1 = 4$. The previous vapor segment is determined using Equation (5.3) to be $k = 14 + 1 - 3 = 12$. These values are represented in Figure 5.1. Using the counters $j$ and $k$, the inlet liquid and vapor flowrates and temperatures to each segment are represented byEquation (5.4) and (5.5), respectively.

$$\dot{m}_{l,in,i} = \dot{m}_{l,out,j}\ ,\ T_{l,in,i} = T_{l,out,j} \tag{5.4}$$

$$\dot{m}_{v,in,i} = \dot{m}_{v,out,k}\ ,\ T_{v,in,i} = T_{v,out,k} \tag{5.5}$$

The quality of the liquid and vapor entering and exiting each segment are assumed to be zero and unity, respectively. The solution pressure is also assumed to be constant throughout the desorber. In combination with the knowledge of enthalpy or temperature of the upstream segment, this defines the inlet states of liquid and vapor for each segment. The outlet fluid conditions are determined through a mass, species, and energy balance, respectively, as shown in the following equations.

$$\dot{m}_{l,in,i} + \dot{m}_{v,in,i} = \dot{m}_{l,out,i} + \dot{m}_{v,out,i} \tag{5.6}$$

$$\dot{m}_{l,in,i} x_{l,in,i} + \dot{m}_{v,in,i} x_{v,in,i} = \dot{m}_{l,out,i} x_{l,out,i} + \dot{m}_{v,out,i} x_{v,out,i} \tag{5.7}$$

$$\dot{Q}_i = \dot{m}_{l,out,i} h_{l,out,i} + \dot{m}_{v,out,i} h_{v,out,i} - \dot{m}_{l,in,i} h_{l,in,i} - \dot{m}_{v,in,i} h_{v,in,i} \tag{5.8}$$

A simple, conservative assumption is made to account for the heat and mass transfer resistance between the vapor and liquid. Due to the counter-flow orientation between the liquid and vapor, it is assumed that the outlet vapor temperature is at an average of the inlet vapor temperature and the inlet liquid temperature, as shown in Equation (5.9).

$$T_{v,out,i} = \left(T_{v,in,i} + T_{l,in,i}\right)/2 \tag{5.9}$$

The vapor outlet temperature is used to determine the vapor outlet concentration and enthalpy. The system of equations can be closed by employing a heat transfer resistance network to calculate heat transfer in Equation (5.8). The heat transfer rate is calculated based on the overall heat transfer conductance and log mean temperature difference between the exhaust and solution, as shown in Equation (5.10).

$$\dot{Q}_i = UA_i \Delta T_{lm,i} \tag{5.10}$$

The exhaust and solution are in counter-flow in the first pass and co-flow in the second pass, and the log mean temperature differences are determined using the equations presented in Chapter 3 for the respective flow direction. The *UA* in each segment is the inverse of the total thermal resistance, which is a parallel combination of the thermal resistance between the exhaust and coolant for each tube, as shown in Equation (5.11).

$$R_i = \frac{R_{tube,i}}{n_{p,tubes}} \tag{5.11}$$

The tube resistance is a combination of the exhaust, fouling layer, wall, and solution resistances as follows.

$$R_{tube,i} = R_{ex,i} + R_{foul,i} + R_{wall,i} + R_{s,i} \tag{5.12}$$

The exhaust resistance is dependent on the exhaust heat transfer coefficient, determined using the correlation of Churchill (1977a), the segment length, and the tube inner diameter, as shown in Equation (5.13).

$$R_{ex,i} = \frac{1}{h_{ex,i} \pi D_{tube,I} L_{seg}} \tag{5.13}$$

The fouling resistance is calculated based on the resistivity measured in single-tube experiments, as shown in Equation (5.14). Using the resistivity accounts for differences in tube length. The wall resistance is calculated using the relationship for radial conduction through a hollow cylinder, shown in Equation (5.15).

$$R_{foul,i} = R'_{foul,i} / L_{seg} \tag{5.14}$$

$$R_{wall,i} = \frac{\ln\left(D_{tube,O} / D_{tube,I}\right)}{2\pi k_{tube} L_{seg}} \tag{5.15}$$

The resistance of the ammonia-water solution is determined from the boiling heat transfer coefficient, the segment length, and the tube outer diameter, as follows.

$$R_{s,i} = \frac{1}{h_{s,i} \pi D_{tube,o} L_{seg}}$$

(5.16)

The effect of the fins on the solution side is not accounted for due to the solution resistance being much less than the exhaust and fouling layer resistance. The solution heat transfer coefficient is taken to be 3000 W m$^{-2}$ K$^{-1}$ for the reasons described in Chapter 3. These calculations and design selections enable the calculation of thermal resistance, $UA$, heat transfer rate, and the outlet liquid temperature and concentration for each segment. The vapor generation rate and concentration from the desorber column are taken to be the outlet of the final segment for vapor flow ($i = n_{seg}/2$), which is the seventh segment in Figure 5.1. The total heat transfer rate in a column is the sum of the heat transfer in each segment, as follows.

$$\dot{Q} = \sum_{i=1}^{n_{seg}} \dot{Q}_i$$

(5.17)

The exhaust outlet temperature from the segment is calculated using Equation (5.18). The specific heat of exhaust is calculated using the method described for the experimental facility model in Chapter 3.

$$T_{ex,out,i} = T_{ex,in,i} + \dot{Q}_i / \dot{m}_{ex} c_{p,ex,i}$$

(5.18)

The exhaust-side pressure drop is another important parameter for the design of the desorber. The total pressure drop must not exceed the back pressure limit of the generator.

162

The Kohler 10REOZDC diesel generator used in this study has a back pressure limit of 12 kPa. This is the maximum allowed gage pressure of the exhaust in the exhaust header of the engine; therefore, the pressure drop in the exhaust piping upstream of the desorber must also be accounted for. The piping from the exhaust header to the desorber has an inner diameter of 38 mm and a length of 1.5 m. The major losses are calculated using Equation (5.19).

$$\Delta P_{ex,pipe,maj} = \frac{f_{ex,pipe}}{D_{pipe}^5} \frac{8}{\pi^2} \frac{\dot{m}_{ex}^2 L_{pipe}}{\rho_{ex}} \tag{5.19}$$

The exhaust properties are calculated at the temperature of the exhaust at the inlet to the desorber. The friction factor is predicted using the correlation of Churchill (1977b). Several minor loss elements are also present in the exhaust piping: a contraction from the exhaust header to the pipe, an expansion and contraction in the muffler, two ninety-degree pipe elbows, and the exit of the exhaust from the desorber into the atmosphere. The loss coefficients for a contraction, expansion, elbow, and exit are taken from Munson *et al.* (1990) to be 0.5, 1, 1.5, and 0.5, respectively. The loss coefficients are summed to calculate the total loss coefficient, which is used to determine the minor losses using the following equation.

$$\Delta P_{ex,pipe,\min} = K_{L,tot} \frac{8}{\pi^2} \frac{\dot{m}_{ex}^2}{\rho_{ex} D_{pipe}^4} \tag{5.20}$$

The total pressure drop in the exhaust piping to and from the desorber is the sum of the major and minor losses, which is approximately 2.7 kPa. Therefore, the desorber pressure drop limit is about 9.3 kPa.

The desorber exhaust side pressure drop is calculated to insure that it does not exceed the limit. It is assumed that the exhaust flow rate is evenly distributed through each parallel tube in the desorber. The major pressure drop in an exhaust tube is calculated for each segment using Equation (5.21). The friction factor is determined from the correlation of Churchill (1977b). The major pressure drop for a clean tube is multiplied by the pressure drop ratio from single-tube experiments to predict the pressure drop of a fouled tube. Minor pressure losses are calculated for the entrance of exhaust into and exit out of each tube in the desorber column. The loss coefficient for an entrance and exit is specified by Munson *et al.* (1990) to be 0.5, which is used in Equations (5.22) and (5.23) to calculate the respective minor losses.

$$\Delta P_{ex,maj,i} = \left( \frac{\Delta P}{\Delta P_o} \right) \frac{f_{ex,i}}{D_{tube,I}^{5}} \frac{8}{\pi^2} \frac{\dot{m}_{ex}^2 L_{seg}}{\rho_{ex,i}} \tag{5.21}$$

$$\Delta P_{ex,ent} = K_{L,ent} \frac{8}{\pi^2} \frac{\dot{m}_{ex}^2}{\rho_{ex,1} D_{tube,I}^{4}} + K_{L,ent} \frac{8}{\pi^2} \frac{\dot{m}_{ex}^2}{\rho_{ex,n_{seg}/2+1} D_{tube,I}^{4}} \tag{5.22}$$

$$\Delta P_{ex,exit} = K_{L,exit} \frac{8}{\pi^2} \frac{\dot{m}_{ex}^2}{\rho_{ex,n_{seg}/2} D_{tube,I}^{4}} + K_{L,exit} \frac{8}{\pi^2} \frac{\dot{m}_{ex}^2}{\rho_{ex,n_{seg}} D_{tube,I}^{4}} \tag{5.23}$$

The major and minor losses are summed to determine the total pressure drop through each desorber column. Calculation of desorber heat duty, vapor generation rate, and pressure drop with the framework presented in this section provides a basis for desorber design. Sample calculations for the desorber model are provided in APPENDIX F.

## 5.2 Desorber Design Selection

To optimize desorber performance, the model allows for variation in tube length, tube diameter, the number of parallel tubes, and the number of tube passes through the solution. Height constraints in the heat pump packaged unit limit the tube and pressure drop constraints limit the tube diameter. The number of parallel tubes and number of tube passes are more practical means of varying the desorber design for performance improvement. The number of parallel tubes can either be varied by changing the number of tubes in each column or by adding another column in parallel. The number of tube passes through the solution is varied by adding columns in series. A single column has two tube passes; therefore, adding a second column results in four passes, a third in six passes, and so on.

The effects of changing tubes per pass and the number of passes on desorber heat duty and exhaust pressure drop are analyzed for a desorber without fouling in Figure 5.2. As the number of tubes per pass increases, the mass flow rate of exhaust through each tube decreases, as represented by Equation (5.24).

$$\dot{m}_{ex,pt} = \dot{m}_{ex}/n_{p,tubes} \qquad (5.24)$$

This explains the trend of decreasing pressure drop with increasing tubes per pass. As the mass flow rate decreases, the velocity decreases proportionally. Pressure drop is proportional to the square of velocity, which explains the asymptotic approach of pressure drop towards zero as the number of tubes per pass increases and velocity decreases. The heat transfer rate for both the two and four pass cases initially increases with the number of tubes per pass, reaches a maximum near 22 tubes per pass, decreases until about 38 tubes per pass, and again begins to increase. This trend is explained by Figure 5.3, which shows
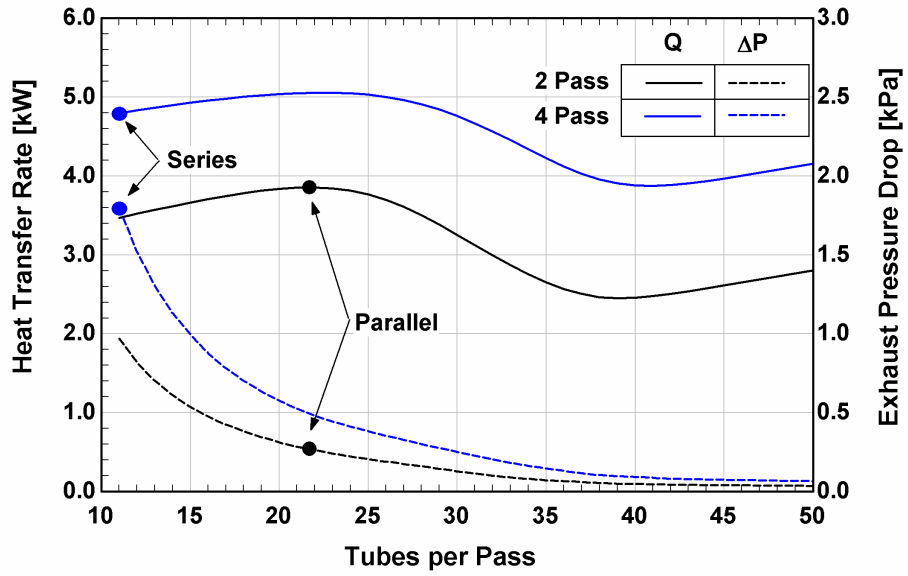
**Figure 5.2: Heat transfer rate and pressure as a function of tubes per pass and number of passes for a clean desorber**
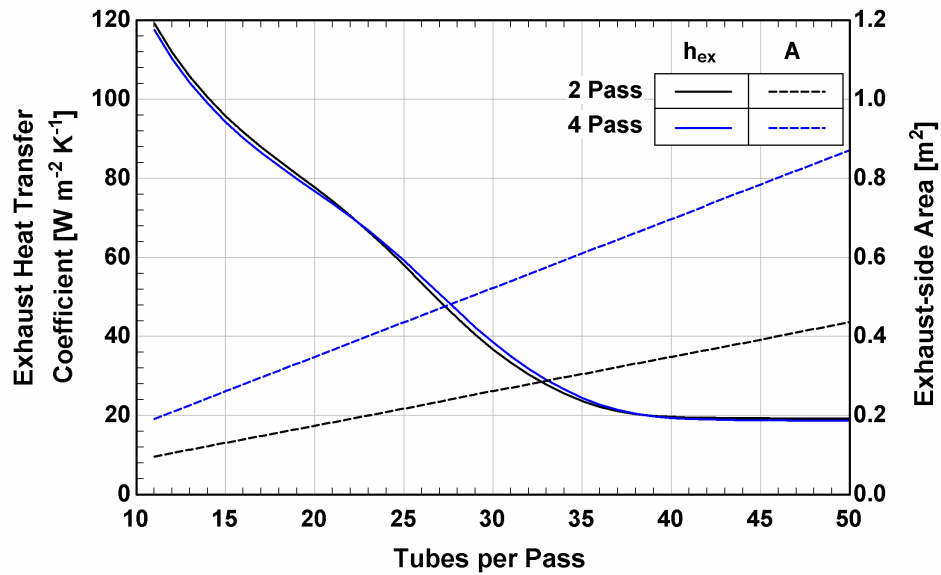


**Figure 5.3: Exhaust heat transfer coefficient and area as a function of tubes per pass and number of passes for a clean desorber**

166

exhaust heat transfer coefficient and area as a function of the number of tubes per pass. Increasing the number tubes per pass causes a decrease in gas velocity and Reynolds number, which results in a decrease in the heat transfer coefficient. Gas flow becomes laminar at about 38 tubes per pass, for which the heat transfer coefficient is constant for varying Reynolds numbers. The exhaust-side heat transfer area increases proportionally with the number of parallel tubes. The exhaust-side area and the heat transfer coefficient define the exhaust-side thermal resistance, which is the dominant resistance in the desorber. Due to the increasing area and decreasing heat transfer coefficient, the resistance reaches a minimum at about 22 tubes per pass, causing a maximum in heat transfer rate. The increasing area is outweighed by the decreasing heat transfer coefficient from about 22 to 38 tubes per pass, causing the decrease in heat transfer rate. As the heat transfer coefficient becomes constant at 38 tubes per pass, the heat transfer rate increases due to increasing area.

The effect of the number of tube passes is also demonstrated in Figure 5.2. A comparison is made between the series and parallel configuration of two of the baseline desorber column designs. This allows for comparison on an equal basis such that the designs have the same total heat transfer area. The series configuration corresponds to 4 passes of 11 tubes while the parallel configuration corresponds to 2 passes of 22 tubes. Connecting the two columns in series results in double the exhaust flow rate per tube and double the total tube length as compared to the parallel configuration. This results in an eight-fold increase in exhaust-side pressure drop. The increased flow rate per tube in the series design results in a greater exhaust heat transfer coefficient than in the parallel designs. This causes a reduction in the exhaust thermal resistance and about a 25% greater

heat transfer rate. The increase in heat transfer must be balanced by the corresponding increase in pressure drop.

The 3.8 kW heat duty of the parallel desorber configuration without fouling is used as the target value to be achieved by the modified desorber after fouling has occurred. To select the modified design, the thermal resistance and pressure drop ratio results of single-tube experiments are used with the model for a range of exhaust flow rates. Each of the flow rates correspond to a different number of tubes per pass in the desorber design. A parametric study was performed to evaluate six different designs. Designs with fewer tubes per pass require six passes, whereas designs with more tubes per pass require only four passes. The per-tube exhaust flow rate, number of tubes per pass, number of passes, and total tubes for each design are summarized in Table 5.2.

The number of tubes per pass is chosen to correspond to the various single-tube exhaust flowrates that were tested. Fouling results are input to the model based on the particular flowrate and the tube location in the desorber. For example, the fouling resistance and pressure drop ratio measured in the first tube-in-tube heat exchanger at a flow rate of 2.1 g s$^{-1}$ are used for the tubes in the first pass of the desorber design with 11 tubes per pass. Similarly, the results from the second tube-in-tube heat exchanger are used

**Table 5.2: Desorber designs evaluated in parametric study**

| Desorber Design | Exhaust Flowrate per Tube [g s$^{-1}$] | Tubes per Pass | Number of Passes | Total Number of Tubes |
|---|---|---|---|---|
| 1 | 2.9 | 8 | 6 | 48 |
| 2 | 2.1 | 11 | 6 | 66 |
| 3 | 1.7 | 14 | 6 | 84 |
| 4 | 1.4 | 17 | 6 | 102 |
| 5 | 1.4 | 17 | 4 | 68 |
| 6 | 1.1 | 22 | 4 | 88 |

for the second pass, and so on. The fouling experiments were either performed with two or four tube-in-tube heat exchangers, which corresponds to two or four tube passes. Therefore, fouling measurements are not available to correspond to the tubes in the final two desorber passes. To account for this, the fouling results of the last tube-in-tube heat exchanger in the experiments are used for the final passes in the desorber model. This is a conservative estimate as it was found that fouling effects were greatest in upstream heat exchangers.

The fouling resistances used in the model are a result of 10 hours of exhaust exposure and the fouling resistance had not yet reached steady state. The steady state fouling resistance and pressure drop are predicted by multiplying the 10 hour results by the ratio of the 24 hour to 10 hour results in the experiment performed to steady state at design conditions. This experiment was presented in Chapter 4, and the 24 hour to 10 hour fouling resistance and pressure drop ratios were 1.5 and 1.6, respectively. Using these factors allows for a prediction of the steady state fouling effects based on the 10 hour results.

The predicted steady state desorber heat transfer rate and pressure drop are presented in Figure 5.4 for each of the desorber designs investigated. The heat transfer target of 3.8 kW and the pressure drop limit of 9.3 kPa are also shown on the plot. The four designs with fourteen or greater tubes per pass have predicted pressure drops less than the limit. Of these designs, the only one that meets the heat transfer requirements has six passes of seventeen tubes. However, the six pass, 14 tube and four pass, 22 tube designs only fall short of the heat transfer target by about 5%. The total number of tubes for these two designs, 84 and 88 tubes respectively, is much less than the 102 total tubes in the six pass, 17 tube design. The additional tubes will result in a desorber that is larger and heavier
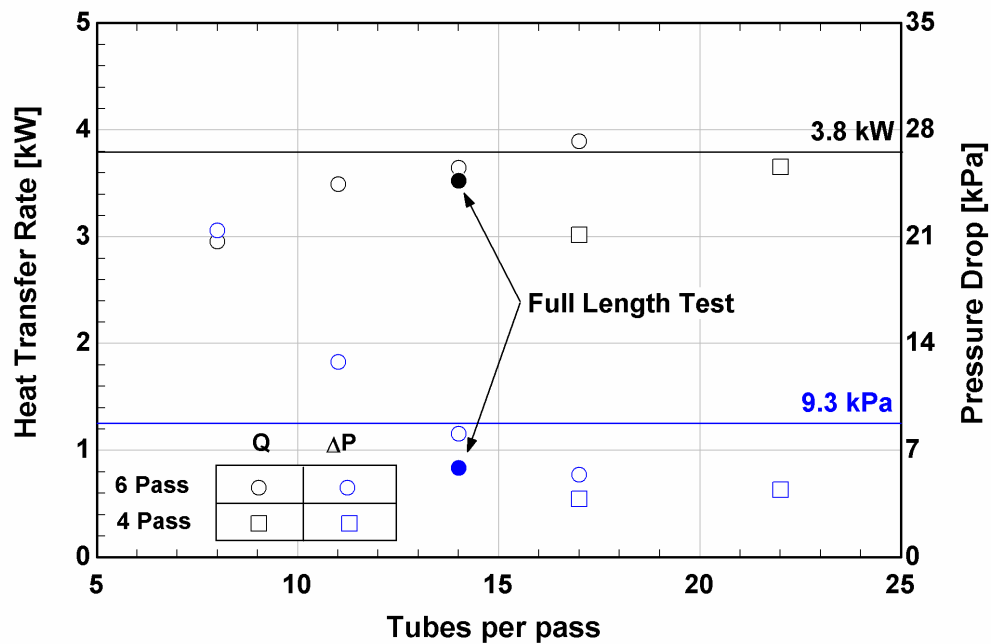
**Figure 5.4: Parametric study for predicted desorber steady state heat transfer rate and pressure drop after fouling has occurred**

than the other designs. For this reason, the six pass, 17 tube design was considered less preferable in comparison to the six pass 14 tube and four pass 22 tube designs.

The six pass, 14 tube (6:14) and four pass 22 tube (4:22) designs have very similar heat transfer results, and further examination of the vapor generation rate and purity of the two designs is required. Design 6:14 requires three desorber columns in series and Design 4:22 requires two series columns. Schematics of the two designs with the model predicted inlet and outlet fluid conditions and heat transfer rates are shown in Figure 5.5. In this comparison, the dilute solution outlet temperature is specified, and the concentrated solution inlet flow rate is allowed to vary for each column. Beginning with design 6:14, the heat transfer rate in the first column is greatest and decreases for each subsequent column. The heat transfer rate in the last column is 30% less than that in the first column,

170

which shows the need for the additional column. As a result of the decreasing heat transfer rate, the concentrated solution inlet flowrate also decreases in each column to maintain the same dilute solution outlet temperature. Similarly, the vapor generation rate decreases with each column and the vapor temperature increases. Overall, the desorber assembly has a heat transfer rate of 3.65 kW and a vapor generation rate of 1.745 g s$^{-1}$. The trends for heat transfer rate and vapor generation rate between each column of the four-pass twenty-two tube design match that of the six-pass fourteen-tube design. The heat transfer rate for the assembly is 3.60 kW, which is slightly less than that of the other design. This also results in a 2% lower vapor generation rate, but these differences are not significant enough to eliminate either design.

One concern with a three column design is the potential for variation of vapor purities and temperature between columns. This was not observed with the present model because the dilute solution outlet temperature was specified for each column. Achieving identical dilute solution temperatures with different heat transfer rates requires variation of concentrated solution flow rates. In actual heat pump design and operation, a flow control device will be required to tailor the solution flow of each column in this manner, increasing overall cost and complexity. To determine the effect of eliminating the flow control devices, the concentrated solution inlet flowrate for each column was specified to be equal. This represents a case in which a flow balancing header is used to distribute the flow equally. The total flow rate to the desorber assembly was taken to be the total predicted flowrate of the model while specifying dilute solution temperature. The results of specifying concentrated solution flowrate are shown in Figure 5.6.
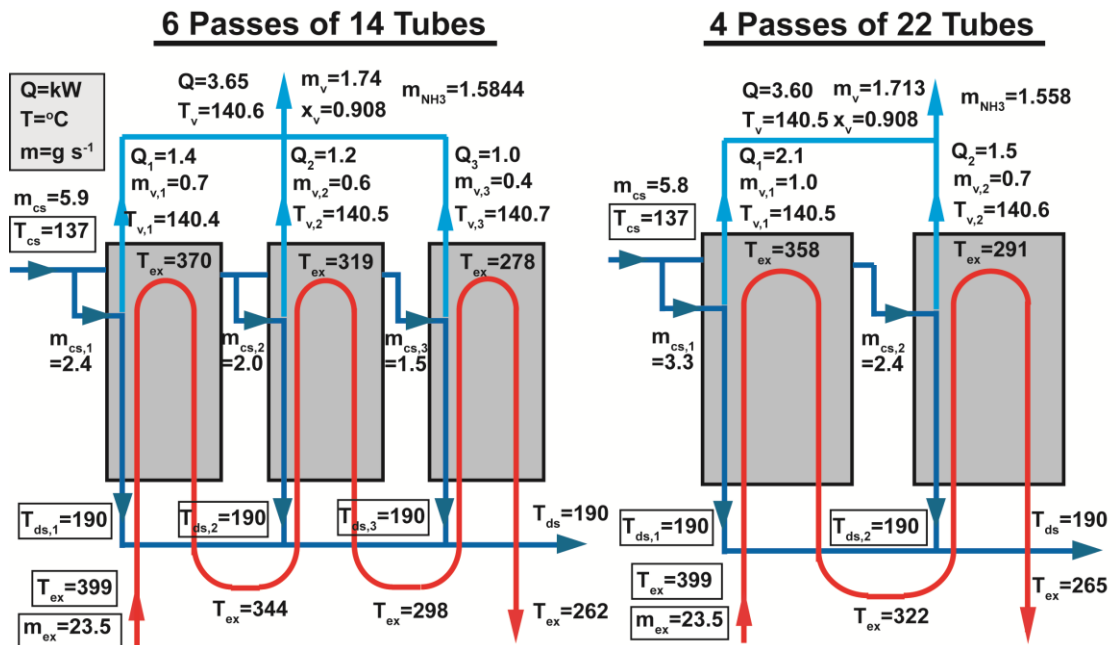
**Figure 5.5: Comparison of desorber designs with the dilute solution outlet temperature of each column specified**
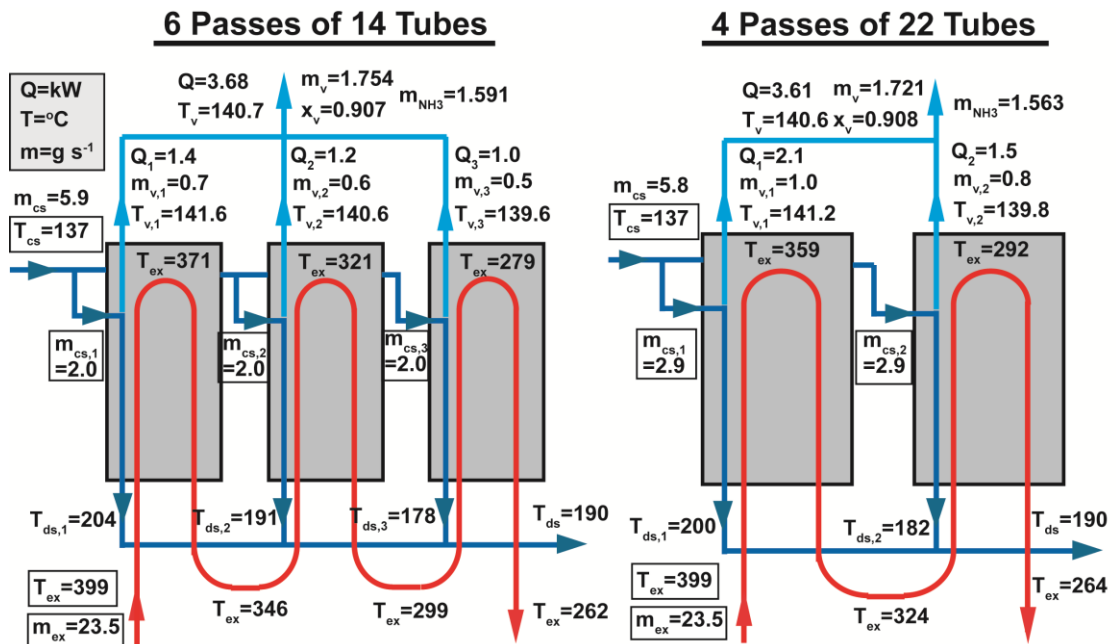


**Figure 5.6: Comparison of desorber designs with an equal concentrated solution flowrate specified for each column**

172

While the combined dilute solution outlet temperature of both desorber assemblies is still 190℃, the dilute solution outlet temperature of each column ranges from 178 to 204℃ for design 6:14 and 180 to 200℃ for design 4:22. This causes greater variation in vapor outlet temperature and a slightly lower vapor concentration as compared to the previous model. The lower purity is compensated for by a greater vapor generation rate such that the total amount of ammonia generated is greater for the equal solution flow rate case. The overall heat transfer rates are also slightly greater for this case because the temperature difference between the exhaust and coolant is greater in the latter columns. While having three columns instead of two produces slightly greater variation in vapor concentration between each column, the differences are not large enough to cause concern for system operation.

In comparing both designs and examining differences in heat transfer rate, vapor generation rates, and vapor concentrations, neither design provides a significant advantage over the other to justify a selection based on these criteria. A 3D CAD model was developed to determine the size and weight of each design. For the purposes of validating the fouling results in this study, simulation desorbers are designed with a single phase inlet and outlet. The simulation desorbers contain identical exhaust side geometry without detailed solution side fin-tray design required for liquid-vapor interaction. Given that the dominant thermal resistance is on the exhaust gas side, single phase simulation of the solution side allows for more accurate determination of fouling resistances of each column and more flexible experimental operation. The CAD models for both simulation desorber designs are shown in Figure 5.7.
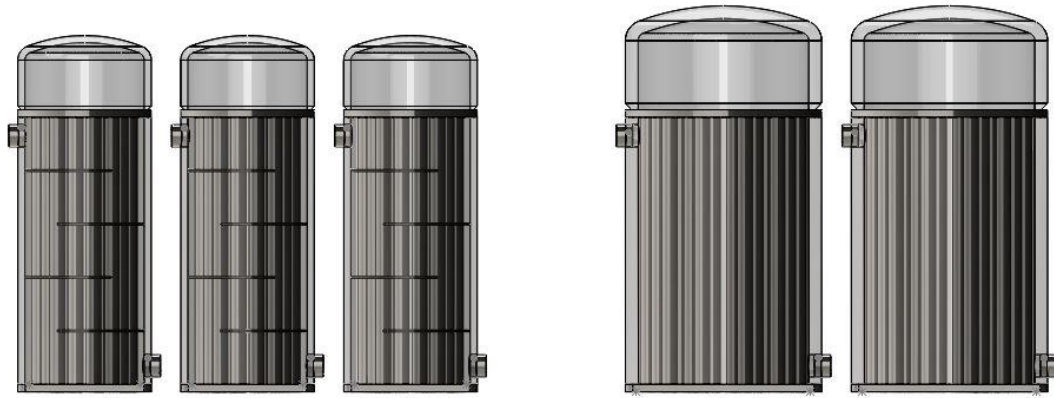
**Figure 5.7: CAD models of simulation desorber designs with six passes of
fourteen tubes (left) and four passes of twenty-two tubes (right)**

The exhaust tubes are 24.1 mm in length, 12.7 mm in outer diameter, and have a
wall thickness of 0.9 mm. The tubes Design 6:14 are contained in a stainless steel pipe
with 144 mm outside diameter (O.D.) and a wall thickness of 6 mm, while the tubes for
Design 4:22 are contained in a 168 mm O.D. stainless steel pipe with a wall thickness of
11 mm. The working fluid pressure requires a greater wall thickness for larger shell
diameters. As can be seen in Design 6:14, baffles are installed inside the shell. The baffles
improve tube stability, promote serpentine flow of the coolant, and increase coolant heat
transfer coefficient. The tubes are joined to the top and bottom of the outer shell with a 6.3
mm thick plate. A pipe cap is placed on the top plate to serve as the exhaust header.

The footprint, weight, and total heat transfer area for each of the designs is
compared in Table 5.3. The footprint and weight of Design 6:14 are much less than that
for Design 4:22 with a minimal decrease in the heat transfer area. Therefore, the six pass
twenty-two design is selected as the most desirable for meeting system performance
requirements and limiting component size and weight for incorporation into a heat pump.

174

**Table 5.3: Comparison of the physical characteristics of the simulation desorber designs**

| Desorber Design | Footprint [m²] | Heat Transfer Area [m²] | Weight [kg] |
|---|---|---|---|
| 6 Pass, 14 Tubes | 0.021 | 0.809 | 22.7 |
| 4 Pass, 22 Tubes | 0.045 | 0.847 | 38.5 |
| Percent Difference | -54% | -5% | -41% |

This design is fabricated for testing and validation of fouling results and heat transfer and pressure drop performance.

The fabricated simulation desorber column is shown in Figure 5.8. The coolant inlet and outlet are placed in a similar location as the concentrated solution inlet and dilute solution outlet of the actual desorber to facilitate similar temperature profiles. The bottom view of the desorber shows the placement of the tubes within the shell. The tubes are spaced to account for desorber internal tray geometries not included in the simulation desorber. A 6.3 mm gap between the inlet and outlet exhaust pass allows for the weir to be placed between the passes in the desorber and for a seal between the two passes of the exhaust on the bottom plate. A space is also placed in the center of each tube pass for the down comer tube that would be installed in an actual desorber. The three simulation desorber columns are sealed to an exhaust header. The header routes the exhaust through each pass of the entire assembly and contains the ports for exhaust pressure and temperature measurement. The assembly of the simulation desorber columns and the header are shown in Figure 5.9.
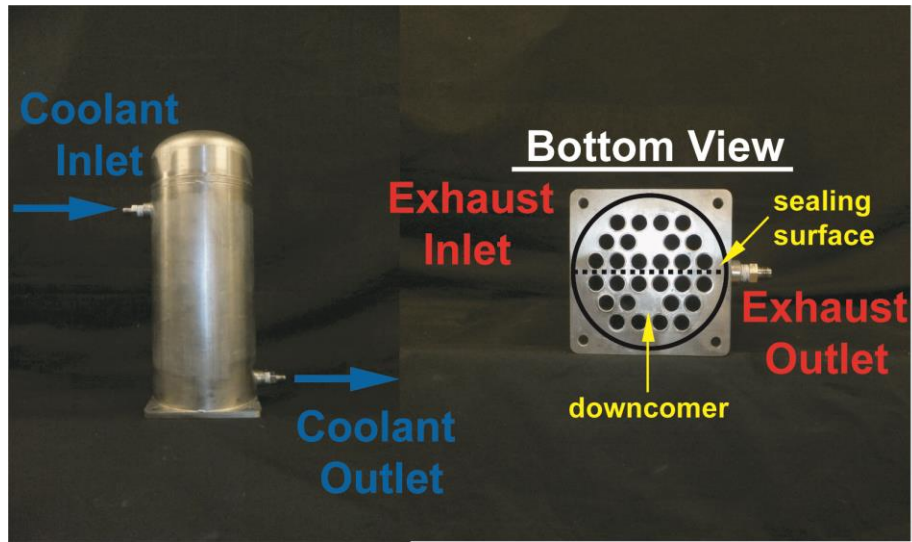
**Figure 5.8: Modified desorber column**
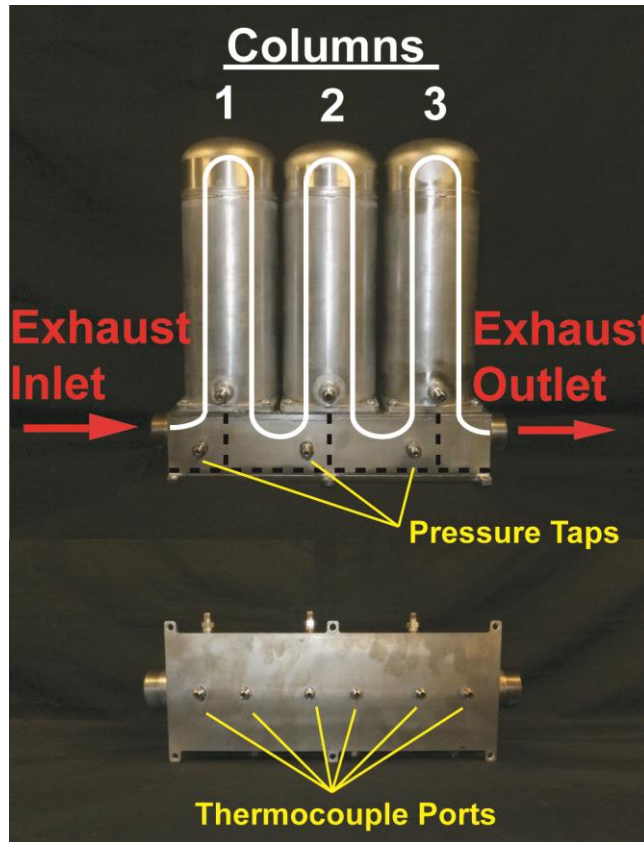


**Figure 5.9: Modified desorber assembly**

## 5.3 Experimental Set-up

The single-tube experimental facility was modified for the testing of the desorber assembly. A schematic of the modified facility is shown in Figure 5.10. Exhaust exits the generator and enters the experimental facility. A portion of the exhaust is directed to the exhaust gas analyzer and opacimeter for exhaust gas composition measurement. The remainder passes through the three desorber columns [1-4]. Temperature and pressure are measured between each desorber column. The exhaust flowrate is measured at the outlet of the last column [5]. The coolant loop begins at state point [6] where it splits into three
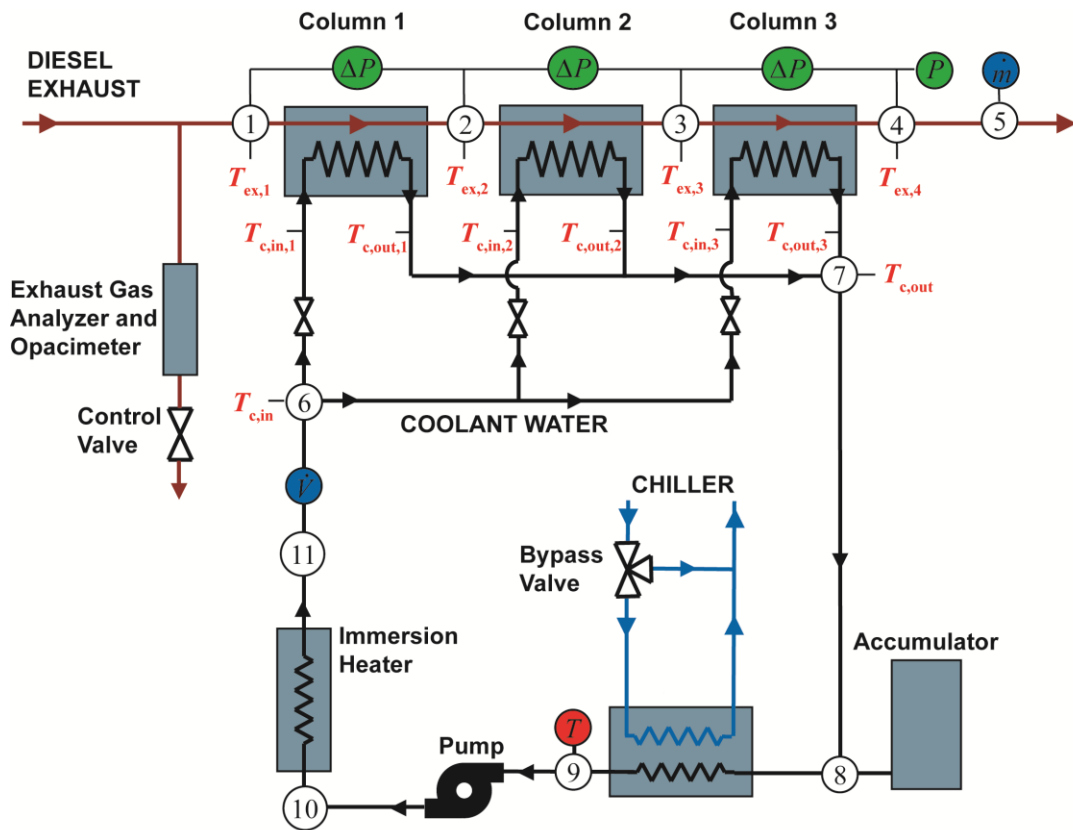


**Figure 5.10: Schematic of desorber test facility**

parallel paths to each column. The coolant flows to each column through a control valve and inlet and outlet temperature are measured before the three streams recombine [7]. An accumulator is installed at state point [8] to account for expansion and to reduce flow fluctuations. The coolant then flows through the chilled water heat exchanger where heat is rejected and the temperature is controlled with the bypass valve that varies the flow rate of chilled water through the heat exchanger [9]. The coolant is pressurized by the pump [10] and passes through the immersion heater [11]. Lastly, coolant flowrate is measured before it splits to each column [6].

Several of the components in the facility designed for the single-tube experiments described above are replaced to account for greater flow rates and heat transfer rates in this case. This includes the exhaust wedgemeter, the coolant pump, coolant flow meter, and chilled water heat exchanger. A list of the modified components along with their specifications is shown in Table 5.4. The facility was operated and controlled in same

**Table 5.4: Equipment and instrumentation in desorber experimental facility**

| Instrument/ Equipment | Type | Vendor and Model | Range | Accuracy |
|---|---|---|---|---|
| Coolant Pump | Gear | Concentric 1070049 | 30 LPM @ 6.8 Mpa | - |
| Pump Motor | DC | Leeson C4D17FK3G | 90 VDC, 7.5 A | - |
| Coolant Total Flow Meter | Magnetic | Rosemount 8711ASA30FRE5G1 | 35.5 LPM | 0.25% |
| Exhaust Flow Meter | Wedge Meter | Coin PCOCA2AH3Z1 | 0.0235 g s-1 @ 11.0 kPa | 0.50% |
| Chilled Water Heat Exchanger | Plate-Plate | BrazePak BP400-040 | 15 kW | - |

manner as the single-tube test facility, described in Chapter 3. Experiments are performed using the procedure described for engine start-up transient experiments.

**5.4 Data Analysis**

The data are analyzed to calculate exhaust and coolant heat transfer rates, the *UA* of each column, and the fouling resistance in each column.

*5.4.1    Heat Transfer Rates*

The heat transfer rate from the exhaust in each column is calculated based on the exhaust specific heat, exhaust mass flow rate, and the inlet and outlet exhaust temperature, as follows.

$$\dot{Q}_{ex,i} = \dot{m}_{ex} c_{p,ex,i} \left( T_{ex,i} - T_{ex,i+1} \right)$$
(5.25)

The subscript *i* specifies the column number. The specific heat is calculated based on the average exhaust temperature and composition of the exhaust measured with the exhaust gas analyzer, as done in single-tube experiments and explained in Chapter 4  The exhaust mass flow rate is determined based on the wedgemeter flow coefficient, diameter, and thermal expansion factor and the exhaust compressibility, density, and pressure difference through the wedgemeter, as shown in Equation (5.26).

$$\dot{m}_{ex} = K_p D_{wm}^2 FaY \sqrt{\rho_{ex,wm} \Delta P_{wm}}$$
(5.26)

The flow coefficient, diameter, and thermal expansion factor of the wedgemeter used in desorber experiments are specified by the manufacturer to be $3.04 \times 10^{-3}$, 26.6 mm, and 1.012, respectively. The density and compressibility are determined based on exhaust

temperature and pressure. The pressure drop across the wedgemeter is measured with a differential pressure transducer. This enables the calculation of exhaust mass flow rate and exhaust heat transfer rate in each column. The total desorber heat transfer rate from the exhaust is the sum of the heat transfer in each column, as follows.

$$\dot{Q}_{ex} = \sum_{i=1}^{3} \dot{Q}_{ex,i}$$

(5.27)

The total heat transfer rate to the coolant in the desorber assembly is calculated based on the total coolant flow rate, specific heat, and the inlet and outlet mixture temperatures, as shown in Equation (5.28).

$$\dot{Q}_c = \dot{m}_c c_{p,c} \left( T_{c,out} - T_{c,in} \right)$$

(5.28)

The flow rate and temperatures are measured and the specific heat is taken as that for water at the average of the inlet and outlet temperature. The total heat transfer to the coolant plus any heat losses to the ambient are equal to the heat transfer from the exhaust, as follows.

$$\dot{Q}_{ex} = \dot{Q}_c + \dot{Q}_{amb}$$

(5.29)

In the ideal case, the desorbers are perfectly insulated, eliminating all heat losses to the ambient. In practice, due to losses to the ambient, the coolant heat transfer rate is less than that of the exhaust. This difference can be minimized by insulating as well as possible. Experimental validation includes verification that the total coolant heat transfer rate is less than the exhaust heat transfer rate by an acceptable margin. The coolant heat transfer rate in each column is approximated by multiplying the exhaust heat transfer rate in each column by a ratio of the total coolant and exhaust heat transfer rate, in Equation (5.30).

$$\dot{Q}_{c,i} = \dot{Q}_{ex,i} \frac{\dot{Q}_c}{\dot{Q}_{ex}} \tag{5.30}$$

This assumes that the losses from each desorber column to the ambient are equal. The losses are dependent on the thermal resistance between the coolant and the ambient and their temperature difference, as shown in the following equation.

$$\dot{Q}_{amb,i} = \left( T_{cool,avg,i} - T_{amb} \right) / R_{amb,i} \tag{5.31}$$

All of the columns are identically insulated to ensure comparable thermal resistance to the ambient for each column. The ambient temperature is the same for all columns, and the coolant temperatures are also similar. This justifies the assumption that the losses from each column are equal for an approximation of coolant heat transfer rate in each column. The coolant heat transfer rate is used to determine the mass flow rate of coolant through each column using Equation (5.32).

$$\dot{m}_{c,i} = \frac{\dot{Q}_{c,i}}{c_{p,c,i}(T_{c,out,i} - T_{c,in,i})} \tag{5.32}$$

The coolant mass flow rate is used in the calculation of fouling resistance in each column.

### 5.4.2   Fouling Resistance

The total thermal resistance in each column is calculated using the $\varepsilon - NTU$ method for a shell-and-tube heat exchanger as presented by Bergman *et al.* (2011). The effectiveness of each column is defined as the ratio of the heat transfer rate to the maximum heat transfer rate in Equation (5.33). The maximum heat transfer rate is calculated based on the exhaust inlet temperature, coolant inlet temperature, and the minimum heat capacitance rate of the

181

two fluids. In this case, the exhaust has the minimum heat capacitance rate and is used to calculate the maximum heat transfer rate in Equation (5.34).

$$\varepsilon_i = \frac{\dot{Q}_{c,i}}{\dot{Q}_{max,i}} \tag{5.33}$$

$$\dot{Q}_{max,i} = \dot{m}_{ex} c_{p,ex,i} \left( T_{ex,in,i} - T_{c,in,i} \right) \tag{5.34}$$

The number of transfer units (*NTU*) for a shell-and-tube heat exchanger with a single shell pass and any even number of tube passes is dependent on the ratio of the heat capacitance rates, $C_r$, and the heat exchanger effectiveness. The relationship presented by Bergman *et al.* (2011) is shown in Equation (5.35) and (5.36).

$$E_i = \frac{2/\varepsilon_i - \left(1 + C_{r,i}\right)}{\left(1 + C_{r,i}^2\right)^{1/2}} \tag{5.35}$$

$$NTU_i = -\left(1 + C_{r,i}^2\right)^{-1/2} \ln \frac{E_i - 1}{E_i + 1} \tag{5.36}$$

*NTU* is defined as the ratio of the overall heat transfer conductance to the minimum heat capacitance ratio, and the *UA* for each column can be calculated with Equation (5.37). The thermal resistance of each column is the inverse of the overall heat transfer conductance, as shown in Equation (5.38).

$$UA_i = \dot{m}_{ex} c_{p,ex,i} NTU_i \tag{5.37}$$

$$R_i = 1/UA_i \tag{5.38}$$

The exhaust exchanges heat with the coolant in each column through both the exhaust tubes and the header plates at the top and bottom of the desorber. Therefore, the

total heat transfer resistance is a parallel combination of the header and tube resistances, as shown in Equation (5.39).

$$\frac{1}{R_i} = \frac{1}{R_{tubes,i}} + \frac{1}{R_{header,i}} \tag{5.39}$$

The resistance of all of the tubes in each desorber column is a parallel combination of the resistance from the exhaust to the coolant for each individual tube. Assuming that the resistance through each tube is equal, the total resistance of all of the tubes is represented by Equation (5.40).

$$R_{tubes,i} = R_{tube,i} / n_{p,tubes} \tag{5.40}$$

The resistance from the exhaust to the coolant for each individual tube is a series combination of the exhaust convective resistance, fouling resistance, wall resistance, and the coolant resistance, as follows.

$$R_{tube,i} = R_{ex,i} + R_{foul,i} + R_{wall,i} + R_{c,i} \tag{5.41}$$

The coolant heat transfer coefficient is calculated using the method of Kern (1950), who developed a correlation for shell-and-tube heat exchangers with a baffle cut of 25%. The cross sectional area of the shell is calculated using Equation (5.42) as a function of the shell diameter, tube pitch, tube clearance, and length between baffles, which are 102 mm, 15.8 mm, 3.18 mm, and 45.7 mm, respectively. The coolant mass flux of the coolant through the shell is a ratio of the coolant flowrate to the cross sectional area of the shell, as shown in Equation (5.43).

183

$$A_{x,shell} = \frac{D_{shell}}{P_{tube}} CL_b \qquad (5.42)$$

$$\dot{m}''_{c,shell,i} = \frac{\dot{m}_{c,i}}{A_{x,shell}} \qquad (5.43)$$

The effective diameter of the shell is dependent on the tube pitch and the tube outer diameter, as in Equation (5.44). The effective diameter, coolant mass flux through the shell, and coolant properties taken at the average of the coolant inlet and outlet temperature are used to calculate the heat transfer coefficient using Equation (5.45).

$$D_e = \frac{4\left(P_{tube}\big/2\times0.86P_{tube} - 0.5\left(\pi D_{tube,O}^2\big/4\right)\right)}{\pi D_{tube,O}\big/4} \qquad (5.44)$$

$$\frac{h_{c,i}D_e}{k_{c,i}} = 0.36\left(\frac{D_e \dot{m}'''_{c,shell,i}}{\mu_{c,i}}\right)^{0.55}\left(\frac{c_{p,i}\mu_{c,i}}{k_{c,i}}\right)^{1/3}\left(\frac{\mu_{c,i}}{\mu_{c,w,i}}\right)^{0.14} \qquad (5.45)$$

The coolant heat transfer coefficient is used to calculate the coolant thermal resistance using Equation (5.46). The wall resistance is calculated for radial conduction through a hollow cylinder using Equation (5.47). The exhaust heat transfer coefficient is calculated using the correlation of Churchill (1977a), and used to calculate the exhaust resistance in Equation (5.48).

The area for the resistances is calculated with two times the tube length to account for both an inlet and an outlet tube.

$$R_{c,i} = \frac{1}{h_{c,i}\pi D_{tube,O}\left(2L_{tube}\right)} \qquad (5.46)$$

184

$$R_{wall,i} = \frac{\ln\left(D_{tube,O}/D_{tube,I}\right)}{2\pi k_{tube}\left(2L_{tube}\right)}$$ (5.47)

$$R_{ex,i} = \frac{1}{h_{ex,i}\pi D_{tube,I}\left(2L_{tube}\right)}$$ (5.48)

This yields the thermal resistances for each tube. Prediction of the thermal resistance for the header will allow for calculation of the fouling resistance. The header resistance is a series combination of the exhaust, wall, and coolant resistances. The coolant heat transfer coefficient on the plate is approximated with the coolant heat transfer coefficient calculated using the method of Kern (1950). The coolant thermal resistance, calculated using Equation (5.49), is dependent on this heat transfer coefficient and two times the surface area of each header plate, which is $3.4 \times 10^{-3}$ m$^2$. The wall resistance of the header plate is calculated for conduction through a plane wall with Equation (5.50). The plate is 6.4 mm thick.

$$R_{header,c,i} = \frac{1}{h_{c,i}\left(2A_{surf,plate}\right)}$$ (5.49)

$$R_{header,wall,i} = \frac{t_{plate}}{k_{plate}A_{surf,plate}}$$ (5.50)

The exhaust heat transfer coefficient is calculated for flow over a flat plate. The Reynolds number of the exhaust at the end of the plate ranges from 3,790 to 4,360; therefore, the average Nusselt number of the exhaust across the plate is calculated for laminar flow with the relationship presented by Bergman *et al.* (2011), as follows.

$$\overline{Nu}_{ex,L,i} = 0.664\,\mathrm{Re}_{ex,L,i}^{1/2}\,\mathrm{Pr}_{ex,i}^{1/3} \tag{5.51}$$

The Reynolds number is calculated based on the exhaust density, velocity, and viscosity and the header plate length, as shown in Equation (5.52). The header plate length is half of the diameter of the plate, which is 63.5 mm, while the properties are determined at the average of the inlet and outlet temperature of each column.

$$\mathrm{Re}_{ex,L,i} = \frac{\rho_{ex,i} V_{ex,i} L_{plate}}{\mu_{ex,i}} \tag{5.52}$$

The velocity is calculated from the exhaust flow rate over the plate, the exhaust density, and the cross sectional area of the header, which is $7.28 \times 10^{-3}$ m$^3$. As the exhaust flows over the header plate, a portion of it flows into each row of the exhaust tubes. This causes a reduction of mass flow rate as the exhaust flows over the plate. It is assumed that the exhaust flow rate through each tube is the same, and the distribution of the tube flow rate across each tube row is depicted in Figure 5.11. The average mass flow rate over the entire plate is used to calculate the average exhaust velocity. The average exhaust mass flow rate is calculated using Equation (5.53), and is in turn used to calculate average velocity in Equation (5.54).

$$\overline{\dot{m}}_{ex,header} = \dot{m}_{ex}\left(1 + \frac{10}{14} + \frac{6}{14}\right)\Big/3 = \frac{15}{21}\dot{m}_{ex} \tag{5.53}$$

$$\overline{V}_{ex,header} = \frac{\overline{\dot{m}}_{ex,header}}{\rho_{ex,i} A_{x,header}} \tag{5.54}$$

186
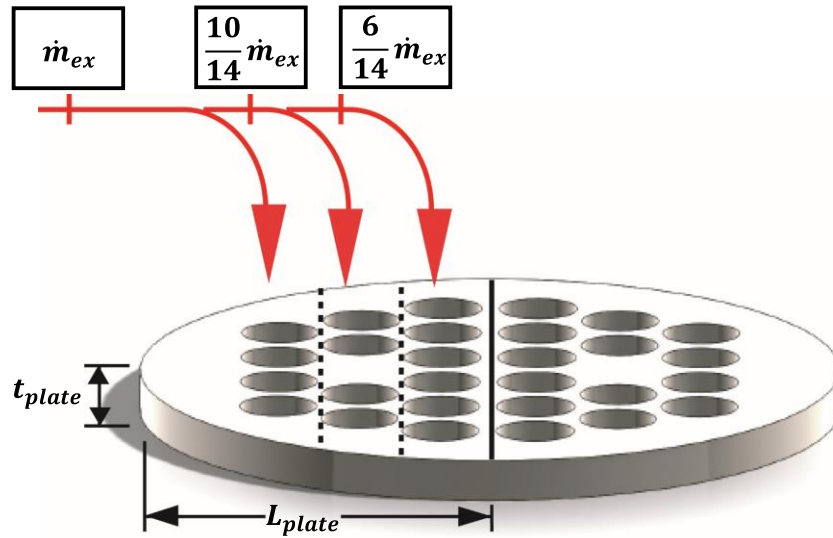
**Figure 5.11: Variation in mass flow rate over exhaust header plate**

Determination of exhaust velocity allows for calculation of the Reynolds number and Nusselt number. The Nusselt number is used to calculate exhaust heat transfer coefficient in Equation (5.55), and exhaust thermal resistance in Equation (5.56).

$$h_{ex,header,i} = \frac{Nu_{ex,L,i}k_{ex,i}}{L_{plate}} \tag{5.55}$$

$$R_{header,ex,i} = \frac{1}{h_{ex,header,i}\left(2A_{surf,plate}\right)} \tag{5.56}$$

The header thermal resistance calculated in this manner is used with Equation (5.39) to calculate the total tube resistance. With the total tube resistance, Equations (5.40) and (5.41) are solved to calculate the fouling resistance of an inlet and outlet tube of each column.

### 5.4.3    Pressure Drop

The effect of fouling on pressure drop for each column is also analyzed. Pressure drop measurements are made between the inlet and outlet header of each column in the desorber experiments. The measured pressure drop consists of both the major and minor frictional losses, shown in Equation (5.57).

$$\Delta P_{ex,i} = \Delta P_{ex,maj,i} + \Delta P_{ex,\min,i} \tag{5.57}$$

The minor pressure losses are due to the entrance and exit of the exhaust from each tube. As used previously for the desorber model, the loss coefficient from an entrance or exit is specified by Munson *et al.* (1990) to be 0.5. The minor pressure loss consists of a total of four entrances or exits, as shown in Equation (5.58).

$$\Delta P_{ex,\min,i} = 4K_{L,ent/ex} \frac{8}{\pi^2} \frac{\dot{m}_{ex}^2}{\rho_{ex,1} D_{tube,I}^4} \tag{5.58}$$

The major pressure loss is a result of flow through the exhaust tubes. There are also major pressure losses for the flow through the header; however, the cross-sectional area of the header is much larger and the length much shorter than that in the exhaust tubes, which will result in significantly less pressure drop. For this reason, only the pressure drop through the tube is considered in Equation (5.59).

$$\Delta P_{ex,maj,i} = \frac{f_i}{D_{foul,i}^5} \frac{8}{\pi^2} \frac{\dot{m}_{ex,pt}^2 L_{tube}}{\rho_{ex,i}} \tag{5.59}$$

188

The ratio of the friction factor to the diameter of the fouling layer to the fifth power is calculated from this equation, and is used to determine the pressure drop ratio as was done in the single-tube experiments, in Equation (5.60).

$$\frac{\Delta P_{ex,i}}{\Delta P_{ex,o,i}} = \frac{f_i / D_{foul,i}^5}{f_{o,i} / D_{tube,I}^5}$$

(5.60)

The friction factor for a clean tube is determined from the correlation of Churchill (1977b). Calculation of pressure drop ratio and fouling resistance of each column for desorber experiments allow for comparison with single-tube experimental results. Sample calculations for the desorber experiment data analysis are included in APPENDIX G.

### 5.5 Experimental Results

The desorber fouling experiment is performed at the worst-case fouling conditions determined from the single-tube experiments. The worst-case fouling effects corresponded to the lowest coolant temperature, the generator operating at full load, and simultaneous start-up of the generator and heat pump. The target exhaust flow rate is the total flow rate of 23.5 g s$^{-1}$. The average conditions of the experiment throughout its duration are summarized in Table 5.5. The generator load and coolant temperatures in the experiment match the target values well, but the exhaust flow rate is 12% less than the target. The

generator did not meet the maximum exhaust flow rate specified by the manufacturer and as a result did not produce the target exhaust flow rate. The exhaust flow rate from the generator for this naturally aspirated engine is primarily dependent on the engine displacement, engine speed, and intake air density. The displacement and engine speed is fixed for a desired generation frequency, which leaves intake density the only remaining factor. As air density increases, the exhaust flow rate will also increase. The intake air density is a function of the ambient temperature, which averaged 31ºC throughout the experiment. The generator is rated to operate in temperatures as low as 0ºC, at which the air density is 10% greater than at 31ºC. This is the most likely reason for the generator not meeting the specified maximum exhaust flow rate. Despite the lower-than-target exhaust mass flow rate, the average input conditions of the experiment are used in the desorber model to compare model predictions and experimental results.

In the experiment, the desorber assembly is exposed to exhaust continuously until fouling reaches steady state. The fouling resistance of each column is shown in Figure 5.12 as a function of time. Similar to the single-tube experiments, the fouling resistance

**Table 5.5: Summary of conditions in desorber fouling experiment**

| Condition | Target Value | Experimental Value |
|---|---|---|
| Generator Load [%] | 100 | 100 |
| Exhaust Flowrate [g s$^{-1}$] | 23.5 | 20.6 |
| Exhaust Inlet Temperature [ºC] | 398.8 | 420.3 |
| Coolant Inlet Temperature [ºC] | 95.3 | 94.9 |
| Coolant Outlet Temperature [ºC] | 160.4 | 158.6 |

grows quickly initially and begins to level off with time. The fouling resistance reaches

steady state, which is defined as a less than 2% change for two consecutive hours, after 27

hours of exhaust exposure.  This is similar to the 23 and 24 hours it took to reach steady

state in single-tube experiments at worst case and design conditions, respectively.

Comparing the differences between individual columns, the steady state fouling resistance

of the first and second column are approximately equal, while that of the third column is

noticeably lower.  The change in pressure drop throughout the experiment provides some

insights into this phenomenon.

The pressure drop ratio results are shown in Figure 5.13, and the same trend of the

fouling resistance with time is observed for the pressure drop ratio.  At steady state, the

pressure drop ratio of the first column is greater than that of the second column, which is
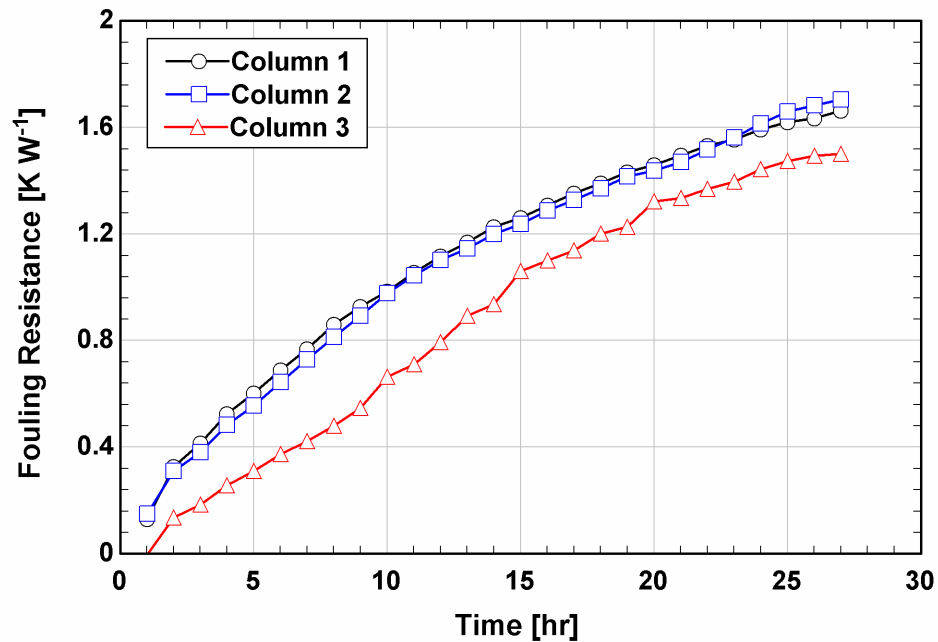


**Figure 5.12: Fouling resistance for a single-tube in each desorber column throughout duration of experiment**

greater than the pressure drop ratio of the third column. This is different from the fouling resistance values, which are approximately the same for the first and second column. A similar trend was observed in single-tube experiments for the second and third tube-in-tube heat exchanger, which had very similar fouling resistances but the pressure drop of the third tube-in tube heat exchanger was less than that of the second. This was found to be a due to the difference in thickness and thermal conductivities of the two fouling layers. In the second heat exchanger, the fouling layer was thicker and more conductive, but that of the third heat exchanger was thinner and less conductive. The larger diameter of the third heat exchanger resulted in lower pressure drop, but the lower thermal conductivity caused greater fouling resistance. A similar trend most likely causes this to occur for the first and second column in the desorber experiment.
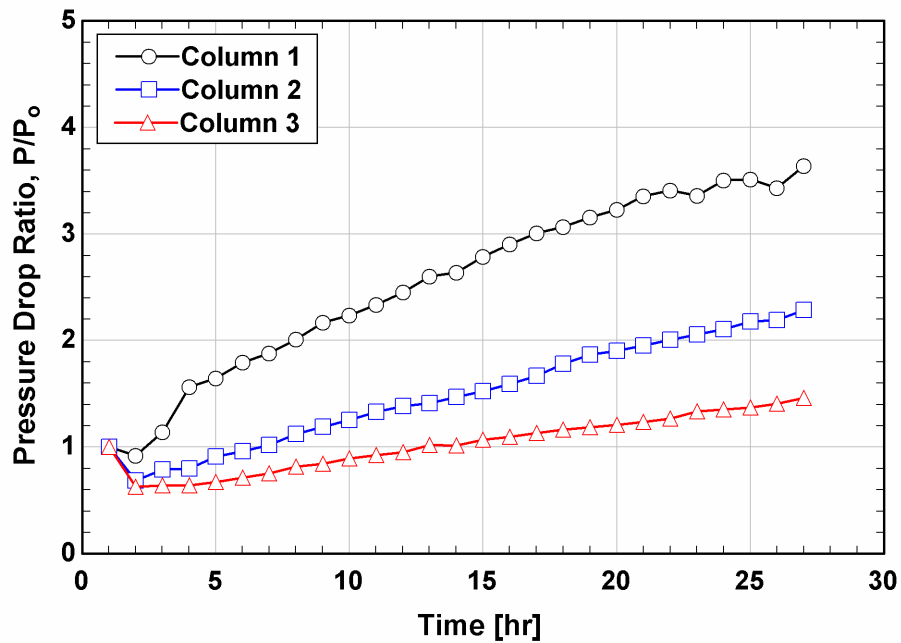


**Figure 5.13: Pressure drop ratio for each column throughout duration of the experiment**

The energy balance of the total coolant and exhaust heat transfer rates, defined by Equation (5.61), is plotted as a function of time in Figure 5.14.

$$EB = \frac{\dot{Q}_{ex} - \dot{Q}_c}{\dot{Q}_c} \times 100\% \qquad (5.61)$$

For the first eight hours of the experiment, the energy balance remains between 7 and 9%. Similar to single-tube experiments, the energy balance begins to increase as the experiment progresses. The time at which this occurs is approximately the same as that for the continuous single-tube experiment at design conditions. This further supports the conclusion that the increase in energy imbalance is not a result of systematic errors during single-tube experiments, rather it is a physical phenomenon that occurs both in the tube-in-tube heat exchangers and the desorber as they foul. A trend that was not observed in single-tube experiments was the sudden decrease in the energy imbalance at the end of the
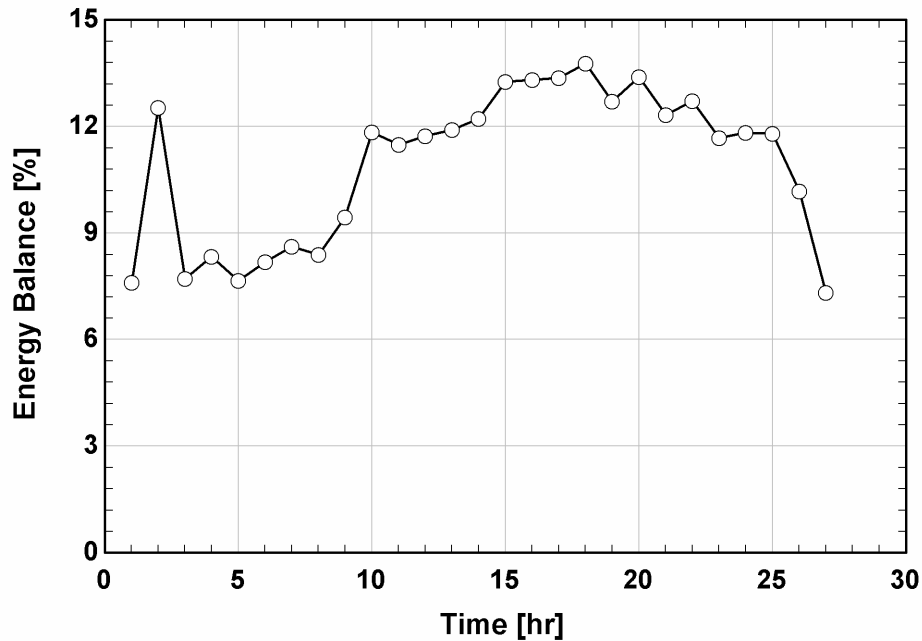


**Figure 5.14: Energy balance for desorber fouling experiment**

experiment. This occurred as fouling resistance reached steady-state and deposition decreased, which could suggest that the energy imbalance is a result of the fouling process. Overall, the minimal difference in heat transfer rates at the beginning of the experiment provides evidence of proper measurement of fluid properties that result in accurate calculation of fouling resistance.

Images of the bottom plate of each desorber column after the 27 hours of exhaust exposure are compared to an image of a clean bottom plate in Figure 5.15. A soot layer covers the portions of the bottom plate exposed to the exhaust and the inside surface of the exhaust tubes. A few tubes in the center of the third column do appear to have fouled more than the others, but this is due to gasket material that extended over a portion of the tube inlet. The remainder of the tubes appears to have fouled uniformly, which suggests equal distribution of exhaust flow between the tubes in each column. The fouling resistance and pressure drop results do suggest differences in fouling layer thickness between the columns. The fouling layer thickness of the first and fourth heat exchanger in the single-tube experiment differed by 360 µm. While this has a significant effect on fouling layer thermal resistance and exhaust pressure drop, it is difficult to observe visually without a magnified image. The comparison of any of the fouled columns with the clean
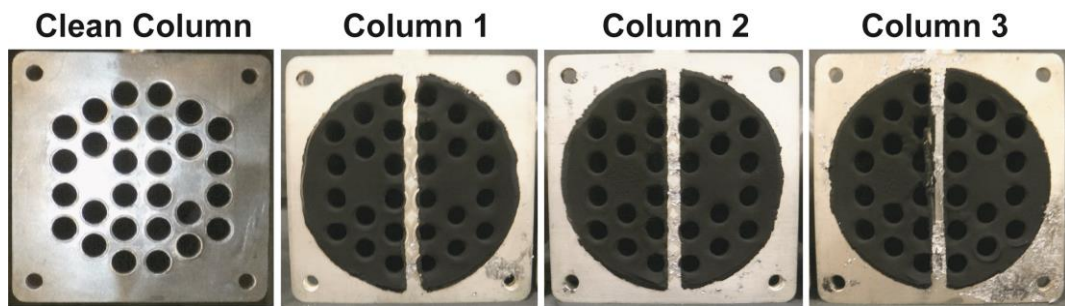


**Figure 5.15: Comparison of clean column to fouled columns after 27 hours of exhaust exposure**

column shows a considerable reduction in the exhaust tube diameter, and illustrates the importance of accounting for fouling in the design of the desorber.

### 5.6 Comparison of Results

#### 5.6.1    Single-Tube Experiments

To evaluate the ability of the single-tube experiments to predict the fouling resistance in the desorber, a direct comparison is made between the measured steady state fouling resistances.  The fouling resistances in the desorber experiments are calculated for the inlet and outlet pass of each column, and the length of the tube used to calculate the resistance in the desorber experiments is about twice the length of each tube-in-tube heat exchanger.  To compare the fouling resistances from the two experiments on an equal basis, the resistivity is calculated with Equations (5.62) and (5.63) for the single-tube and desorber experiments, respectively.

$$R'_{foul} = R_{foul} L_{annulus} \tag{5.62}$$

$$R'_{foul} = R_{foul} \left( 2 L_{tube} \right) \tag{5.63}$$

The data analysis of the desorber experiments provides one fouling resistance for each column, but the single-tube experiments provide fouling resistances for both the inlet and outlet tube in each column.  Therefore, the fouling resistance per unit length for both the first and second tube-in-tube heat exchangers are compared to the fouling resistance in the first column, and the fouling resistance per unit length for the third and fourth tube-in-tube heat exchangers are compared to the fouling resistance in the second column.  The fouling

resistance in the third column does not have a direct comparison to the single-tube experiments as this would have required six tube-in-tube heat exchangers.

The final fouling resistance measurements for the single-tube and desorber experiments are shown in Figure 5.16. The fouling resistance of the desorber is generally greater than that of the tube-in-tube heat exchangers. The results of the two experiments show best agreement for the first column, with the fouling resistance of both the first and second heat exchanger of the single-tube experiments falling within the uncertainty of the fouling resistance of the first column. The uncertainty for the desorber experiments is greater than that of the single-tube experiments because the exhaust heat transfer coefficient is calculated using the correlation of Churchill (1977a) with an assigned 25% uncertainty; whereas, in the single-tube experiments a correlation developed in this study is used with a 10% uncertainty. The fouling resistances for the third and fourth heat exchanger from the single-tube tests are 27% and 34% less than the fouling resistance in the second column for the desorber, respectively. The fouling resistance in the third column of the desorber is also considerably greater than that in the third and fourth heat exchangers from the single-tube tests.

A potential reason for these results is the added length of exhaust tube at the inlet and outlet of each tube-in-tube heat exchanger. The tubing at the inlet and outlet is 99 mm compared to the 285 mm long annulus. Although the tube length was minimized, it was required for sealing the fitting to the tube that contains the coolant and for installing a cross with thermocouple measurements between each heat exchanger. As the exhaust enters the first tube-in-tube heat exchanger, some deposition could occur in the inlet tubing, reducing the concentration of particulate matter, and causing a reduction in deposition in the annulus.

196
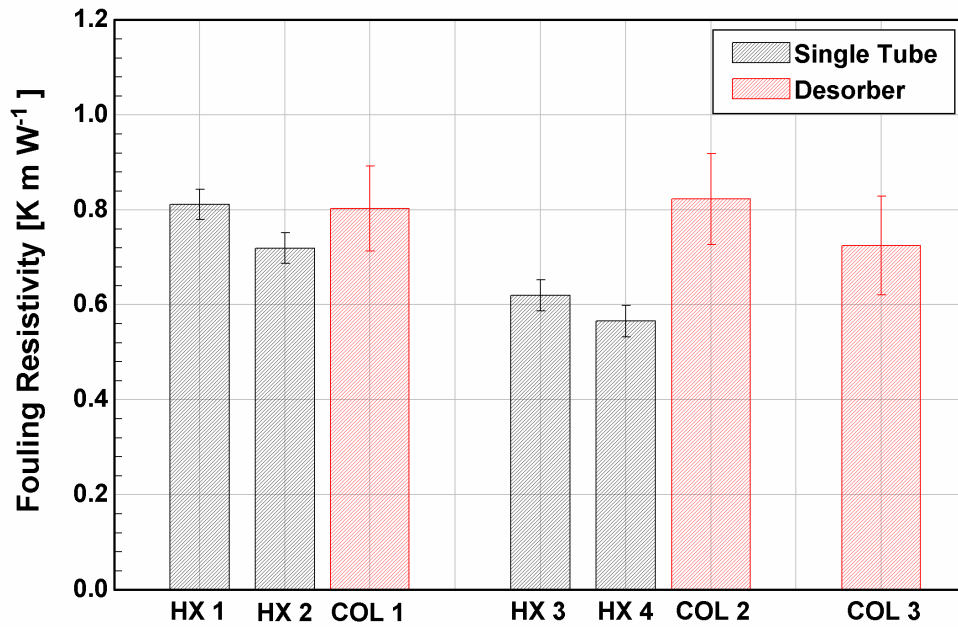
**Figure 5.16: Comparison of final fouling resistance from desorber and single-tube experiments**

This would have an even greater effect on subsequent heat exchangers as more particulate matter is deposited at each inlet and outlet, further reducing the particulate matter concentration in the exhaust..  This could explain the trend that the discrepancies between the single-tube and desorber fouling resistances are greater in downstream tube-in-tube heat exchangers and columns.

Another potential reason for the greater fouling resistance is the lower exhaust mass flow rate per tube in the desorber experiment than in the single-tube experiment.  Greater exhaust flow rates result in greater velocities, which were found to have a significant effect on the steadying of fouling layer growth in the single-tube experiments.  If fouling reaches a steady state due to a balancing of reduced thermophoretic deposition and removal due to flow induced shear, then steady state will not be reached until the exhaust velocity reaches

the threshold for deposit removal. At a lower mass flow rate, more fouling is required to reach the threshold velocity as the inner diameter of the tube must be smaller to achieve the same velocity. This could be the reason for both greater fouling resistance and the additional time required to reach steady state in the desorber experiment.

A comparison of the pressure drop ratio for the single-tube and desorber experiment is shown in Figure 5.17. The pressure drop ratios of the first and second column are slightly greater than those for the corresponding heat exchangers of the single-tube experiments. The pressure drop in the third column is significantly less than that in the second column, which was used to predict pressure drop in the third column for the desorber model. This should result in less pressure drop than the model predicted for the third column. In general, the pressure drop ratio results between the two experiments show better agreement than the
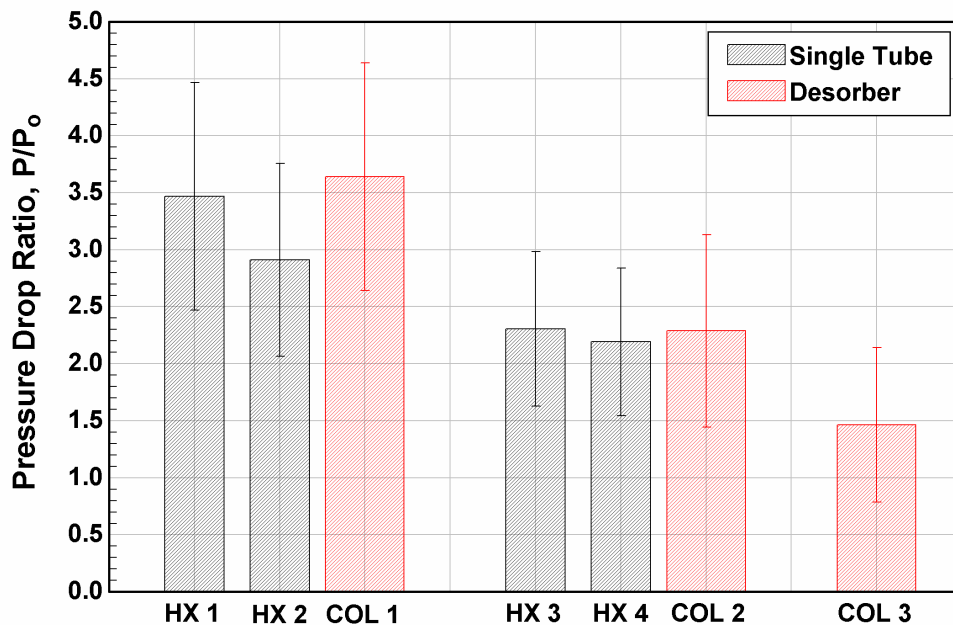


**Figure 5.17: Comparison of final pressure drop ratio from desorber and single-tube experiments**

fouling resistance results. The effects of the fouling resistance and pressure drop ratio results on heat transfer and exhaust pressure drop of the desorber are compared to model predictions in the following section.

### 5.6.2  Desorber Modeling

For direct comparison between the model predictions and the measured performance of the desorber, the exhaust inlet temperature, coolant temperatures, and exhaust flow rate from the desorber experiment were input to the model. These values were presented previously in Table 5.5. The single-tube fouling results at worst case conditions were used in the model to obtain baseline values for heat transfer and pressure drop performance of the desorber. The coolant heat transfer rate measured in experiments is corrected to account for heat transfer from the exhaust to coolant through the header surfaces in the column. The model only accounted for heat transfer in the tubes and not in the header. The coolant heat transfer rate in the tubes of each column is calculated using the log mean temperature difference and the tube resistance, shown in Equation (5.64).

$$\dot{Q}_{c,tubes,i} = \Delta T_{lm,i} / R_{tubes,i} \qquad (5.64)$$

The measured heat transfer rates in the experiment are compared with the target heat transfer rates predicted by the model in Figure 5.18. The heat transfer rates in the first

column are approximately equal, while the measured heat transfer rates of the second and third column are less than the model predictions. This trend is attributed to the greater fouling resistance of the second and third column in the desorber experiments than in the single-tube experiments. The total heat transfer rate of the desorber is 9.6% less than the target heat transfer rate predicted by the model. A comparison of the measured and predicted pressure drops is shown in Figure 5.19. The pressure drops are about equal in the first column, the measured pressure drop is slightly greater than the predicted pressure drop in the second column, and the pressure drop in the third column is less than predicted. The greater difference between the model and the experiments for the third column is due to the use of the fourth tube-in-tube heat exchanger pressure drop ratio in the model, which has been found to be greater than the pressure drop ratio in the third column. The total exhaust pressure drop is 4.7 kPa, which is 2.6% greater than the predicted value. This
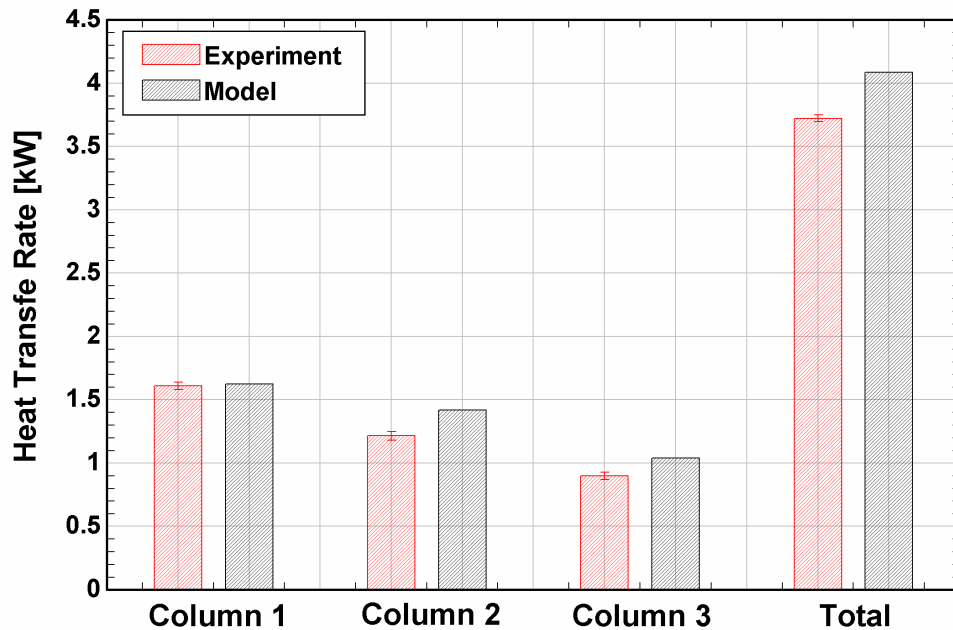


**Figure 5.18: Comparison of experimental and model results for desorber heat transfer rate**

pressure drop value cannot be compared directly to the back pressure limit of the generator because it is at a lower exhaust flow rate. The model predicted pressure drop at design exhaust flow rate was 8.3 kPa. A 2.6% increase results in a pressure drop of 8.5 kPa, which is less than the back pressure limit of 9.3 kPa.

Overall, incorporating the single-tube experimental results into the desorber model leads to prediction of the fouled desorber heat duty within 10%. More significantly, the steady state heat duty at design conditions of the modified desorber (3.35kW) is predicted to be 53% greater than that of the baseline desorber design (2.19 kW). The modified desorber design ensures consistence heat pump performance for direct coupled waste-heat recovery applications using a variety of diesel fuels.
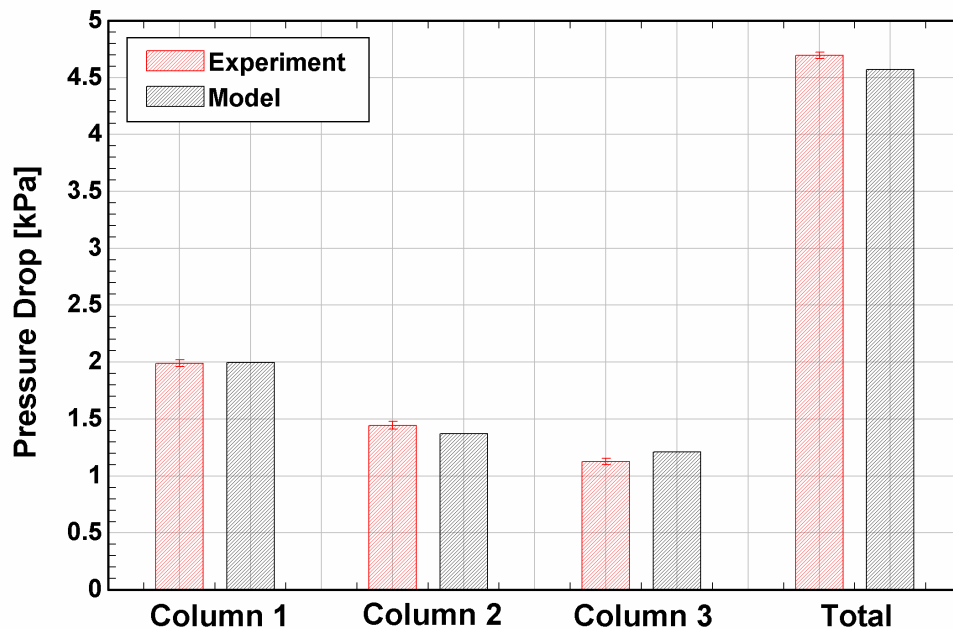


**Figure 5.19: Comparison of experimental and model results for desorber pressure drop**

# CHAPTER 6.    CONCLUSIONS AND

# RECOMMENDATIONS

### 6.1 Conclusions

A detailed investigation into the fouling mechanisms in waste heat recovery systems, with a 2.71 kW cooling capacity diesel engine exhaust driven absorption heat pump as a representative example, was performed.  The findings were used to guide the design of the desorber, the component that couples the diesel engine exhaust to the working fluid pair in the heat pump, such that it meets system performance requirements even after fouling has occurred.  A review of the literature showed that the performance of diesel exhaust coupled heat exchangers degrades over time due to the deposition of particulate matter and unburned hydrocarbons in the exhaust stream onto the heat exchanger surface.  The literature has also shown that fouling is highly dependent on exhaust temperature, chemical composition, velocity and the heat exchanger surface temperature. Fouling investigations in the literature were primarily performed on exhaust-gas recirculation (EGR) coolers in diesel engines, which experience different exhaust and coolant conditions than those of the desorber in a waste-heat driven absorption heat pump.  The lack of studies in the literature for fouling conditions in the desorber of interest prompted the study of fouling mechanisms and their effect on heat transfer and pressure drops specific to this application.

A cycle model of the 2.71 kW heat pump developed in the Engineering Equation Solver platform by  Forinash (2015) was utilized to determine the fluid inlet and outlet state points of the desorber over a range of potential operating conditions.  Exhaust gases were specified to enter the desorber at 398.8°C and a flow rate of 0.0235 kg s$^{-1}$, and for ambient

temperatures from 26.7 to 51.6 °C, the temperature of the concentrated solution inlet and dilute solution outlet ranged from 99.03 to 137.6 °C and 165.6 to 190.4 °C, respectively. These conditions were replicated in an experimental facility that simulated the shell-and-tube type desorber with multiple 12.7 mm diameter tubes using a set of tube-and-tube heat exchangers. The use of a single 12.7 mm tube improved the accuracy of heat transfer and fouling resistance measurement and made the testing of a wide range of fouling conditions possible. The exhaust from a 10 kW diesel generator was used in the experiments, and a load bank allowed for variation in engine operation, exhaust temperature, and exhaust composition. Experiments were performed for generator loads ranging from 60 to 100%, exhaust flow rates from 0.8 to 2.6 g s$^{-1}$, coupling fluid inlet temperatures from 95.3 to 129.8 °C, and coupling fluid outlet temperatures from 160.4 to 182.3 °C. Transient investigations on fouling were also performed for two different cases: one in which the generator is in steady operation and the heat pump starts up, and another in which the generator and heat pump start-up simultaneously.

Experiments were performed until the fouling thermal resistance and exhaust pressure drop reached steady state, which took approximately 24 hours. After the experiments were performed, the tubes were extracted from the tube-in-tube heat exchanger for ex-situ analysis of fouling layer thickness and thermal conductivity. The fouling layer thickness and thermal conductivity values were used to understand fouling deposition and removal mechanisms at various conditions. Fouling thickness increased with greater particulate matter inlet concentration and a greater driving temperature difference between the exhaust and coolant. Fouling layer thermal conductivity was greatest in the cases that promoted hydrocarbon condensation, including those with high inlet concentration or low coolant

temperature. Fouling layer thickness measurement also allowed for prediction of exhaust velocity based on the effective exhaust side flow area. It was observed that despite the continued thermophoretic deposition in the heat exchanger tubes, fouling thermal resistance reached a steady state as exhaust velocities approached 40 m s$^{-1}$. This led to the conclusion that shear induced fouling removal could be one of the primary balancing mechanisms by which fouling thermal resistance is limited.

Fouling effects were most severe in the transient case when the generator and heat pump start simultaneously with a coolant inlet temperature of 95.3 °C, coolant outlet temperature of 160.4 °C, and 100% generator load. At these conditions, the fouling thermal resistance at steady state was approximately 70% of the total thermal resistance ($R_{foul,1} = 2.85 \pm 0.11\ K\ W^{-1}, R_{tot,1} = 3.99 \pm 0.03\ K\ W^{-1}$), and the ratio of the steady state pressure drop to the initial pressure drop was 3.25. The fouling layer was 889 µm thick, which was used to deduce the thermal conductivity of 0.0362 W m$^{-1}$ K$^{-1}$. Sluder and Storey (2008) performed fouling experiments for 12 hours with an exhaust inlet temperature of 375 °C, coolant temperature of 95 °C, and exhaust mass flux of 37.3 kg m$^{-2}$ s$^{-1}$, which was similar to the conditions investigated in this study with an exhaust temperature of 400 °C, coolant temperature of 127 °C, and exhaust mass flux of 17.1 kg m$^{-2}$ s$^{-1}$. The mass gain per unit surface area for the experiments of Sluder and Storey (2008) and the present investigation were also similar at 19.6 and 21.1 g m$^{-2}$, respectively. The results of the present study are consistent with the results from the literature at similar testing conditions, and they confirm the significant effect that exhaust gas fouling has on heat exchanger performance and the importance of taking into account exhaust-side fouling for heat exchanger design and analysis.

To design a desorber that meets heat pump performance requirements after fouling has occurred, a computational model was developed on the Engineering Equation Solver software platform. The fouling resistance and pressure drop from single-tube experiments were selected as inputs into the model to predict desorber heat duty, vapor generation rate, vapor purity, and exhaust pressure drop. The number of exhaust tube passes and number of tubes per pass in the shell-and-tube desorber were parametrically varied to maximize desorber performance. The initial desorber design that did not consider the effects of fouling consisted of two passes of twenty-two parallel tubes, and was predicted to have a heat duty of 3.80 kW at the heat pump design conditions. The predicted desorber capacity was then specified as the target heat duty for the modified desorber design after fouling has occurred. The exhaust pressure drop limit is dependent on the maximum engine back pressure and was specified by the generator manufacturer to be 9.3 kPa. Two desorber designs were selected that best matched the target design specifications. The first design with six passes of fourteen tubes was predicted to transfer a heat duty of 3.65 kW and at a pressure drop of 8.10 kPa, while the second design of four passes of twenty-two tubes had a heat duty of 3.60 kW at a pressure drop of 4.41 kPa. Both designs had an exhaust pressure drop less than the allowable limit and approached the heat duty target to within 5%. Further improvements in heat duty would have required significant increases in heat transfer surface area. The two designs were predicted to have similar heat duties, vapor generation rates, and vapor purities; however, the six pass, fourteen tube design had a foot print and weight 54% and 41% less than that of the four pass, twenty-two tube design, respectively. For this reason, the six pass, fourteen tube design was selected and fabricated for validation experiments.

The single-tube experimental facility was modified to incorporate the modified desorber test section. A validation experiment was performed at the worst case fouling conditions. Fouling in the desorber followed a trend similar to that in the single-tube experiments, and steady-state conditions were reached after 27 hours of continuous exhaust exposure. The fouling resistances in the desorber experiment were slightly greater than those in the single-tube experiment at the same conditions. This resulted in a desorber heat duty 9.6% less than the heat duty predicted by the desorber model ($\dot{Q}_{des,exp} = 3.72 \pm 0.26, \dot{Q}_{des,mod} = 4.09 \ kW$). The measured exhaust pressure drop was only 2.6% greater than the pressure drop predicted by the model. Accounting for this higher pressure drop at design conditions, the total pressure drop would be 8.5 kPa, which is less than the imposed back pressure limit of 9.3 kPa.

Through the use of single-tube experiments, a wide range of fouling conditions were tested, enabling the determination of the worst case fouling thermal resistance and exhaust pressure drop. The use of these single tube results with the desorber model predicted heat transfer performance of the fouled desorber within 10%. This demonstrates the success of the single-tube facility to simulate the operating conditions in the desorber. At heat pump design conditions, the modified desorber design was predicted to have a heat duty of 3.35 kW after fouling, 53% greater than the predicted heat duty a fouled desorber of the original design of 2.19 kW. Furthermore, the pressure drop ratio of a fouled to clean desorber for the modified design was 43% less than that for the baseline design. These differences demonstrate a significant and necessary improvement to the desorber design. While this study focused on the design of a desorber in an absorption heat pump, the results from single-tube fouling experiments can be applied to any number of diesel engine exhaust

waste-heat recovery applications in which similar operating conditions are experienced. A thorough understanding of the mechanisms for deposition and removal of particulate matter and hydrocarbons enables the design of compact and efficient exhaust coupled heat exchangers. These factors are crucial for realizing the maximum cost savings as well as the viability of waste-heat recovery technologies.

## 6.2 Recommendations

Several pathways are present for continued development of diesel engine exhaust coupled heat exchangers for waste heat recovery systems.

### 6.2.1 Fundamental Fouling Relationships

While several researchers have quantified fouling thermal resistances, thicknesses, and thermal conductivities for a range of applications and heat exchanger geometries, there has not been an effort to develop fundamental relationships for these parameters. These relationships would correlate the effects of fouling to inlet conditions such as exhaust temperature, composition, tube temperature, and heat exchanger geometry. Experiments to develop these relationships would require the ability to simulate the exhaust temperature and composition of particulate matter and hydrocarbons in the exhaust independently. A variety of tube diameters and geometries would also have to be studied. The relationships would have to consider the effect of both deposition and removal mechanisms. Developing relationships of this nature would minimize the need to perform fouling experiments for each new application of diesel exhaust coupled heat exchangers, and it would drastically improve the ability to design such heat exchangers.

## 6.2.2    *System Level Implementation*

In this study, desorber performance was evaluated after fouling reached steady state, so that the heat pump would meet the rated cooling capacity after fouling has occurred. Before the desorber has completely fouled, the heat duty and vapor generation rates of the desorber are greater. This could lead to mismatch between the desorber capacity and the balance of the system as the other components in the system are not be designed for the higher capacities. When continuously exposed to exhaust gas flow, the desorber reached steady state conditions in approximately 24 hours. However, single-tube duty cycle testing demonstrated that the transient fouling resistance decreased considerably from the end of one cycle to the beginning of the next. This could cause challenges throughout the heat pump lifetime due to variations in desorber performance. Future studies should be performed to determine the control strategies required to manage these thermal resistance fluctuations. One potential strategy for mitigating this problem would be to install an exhaust bypass valve to control the exhaust flow rate to the desorber. When the fouling resistance of the desorber is lower, the flow rate to the desorber could be reduced to control the exhaust outlet temperature, which would affect desorber heat duty and vapor generation rate. This strategy would require an additional component in the absorption system and would lead to additional capital cost and increased complexity. Further control strategies should also be investigated to determine whether previously controlled variables in the system, such as solution flow rate and various valve positions, can be manipulated to account for the predicted fluctuation in desorber performance. The strategies should then be compared for their impact on system cost and complexity.

### 6.2.3 Exhaust-Side Tube Enhancement

While it has been demonstrated that exhaust fouling is minimized by manipulating the heat exchanger arrangement, the effects of fouling can also be reduced through exhaust-side tube enhancements. One potential means of doing this is through surface coatings that reduce fouling buildup. Investigations into different surface coatings and their effect on fouling and heat exchanger performance could provide a number of innovative solutions to improve the performance of exhaust gas coupled heat exchangers. While these coatings may reduce the fouling layer thickness, they could also add a thermal resistance between the exhaust and coupling fluid. The beneficial effect of the coating on fouling resistance must be greater than the impact of the additional resistance of the coating itself. The coatings should also be tested for durability throughout heat exchanger life time. If the coating is degraded over time, the desorber would presumably still reach the steady state fouling thickness in time. Another means of reducing fouling through exhaust-side enhancement is the installation of extended surfaces. Such a method would increase the effective exhaust side heat transfer area and reduce the exhaust convective thermal resistance; however, it would also increase the area for deposition of particulate matter that could adversely affect the heat exchanger. The presence of fins, mixers, or turbulators would also induce higher local exhaust velocities. As noticed in the experiments in this investigation, exhaust velocity and shear induced removal have a significant effect on the final fouling layer thickness. This physical mechanism could be taken advantage of through the use of extended surfaces, but the performance gains must not be outweighed by the additional back pressure imparted on the diesel engine. For both the surface coatings

and tube enhancements, the additional materials and fabrication costs should be considered in comparison with plain tubes.

### 6.2.4    *Exhaust Emission Treatment*

Exhaust emission treatment devices, such as diesel particulate filters (DPF) or diesel oxidation catalysts (DOC) could also be investigated as a means to reduce fouling in the diesel engine exhaust coupled heat exchanger. Zhan *et al.* (2009) found that an in-line diesel particulate filter significantly reduced fouling in EGR coolers. The primary barrier to the implementation of this technology is the cost and complexity of operation. DPFs rely on either active or passive regeneration of the soot trapped in the filter. Active DPFs require that a combustible fluid is sprayed in the exhaust stream once the back pressure on the engine is too high to burn out the soot in the filter, while a passive DPF auto-regenerates as exhaust temperature increases due to increased engine back pressure. There are benefits and drawbacks to both DPF designs, and selection based on the specific application requirements is necessary. Previous studies have investigated the use of DOCs, which reduce unburned hydrocarbons in the exhaust stream. Warey *et al.* (2014) found that the elimination of hydrocarbons resulted in a dryer and more brittle fouling layer. The layer was more easily removed through water condensation and caused natural regeneration of the EGR cooler. Both DPFs and DOCs should be investigated for their use with diesel engine exhaust driven waste-heat recovery systems. The additional size and cost of the exhaust treatment equipment should be compared to that of designing the desorber with additional heat transfer surface area to account for increased fouling thermal resistance, as was conducted in the present investigation.

The fouling experiments from the present study have provided a basis for understanding the fouling mechanisms in diesel engine exhaust coupled heat exchangers. The study has shown that through surface area addition and heat exchanger arrangement optimization, the effect of fouling on these heat exchangers can be minimized and accounted for. A number of recommendations for future research are presented to further develop the understanding of complex fouling mechanisms and improve the compactness and efficiency of diesel engine exhaust coupled heat exchangers for implementation in absorption heat pumps.

# APPENDIX A. TEST FACILICTY PRESSURE DROP MODELING

Coolant pressure drop modeling is required to size the pump and flow control valves in the system. Pressure drop values are calculated for each major component in the coolant loop of the system. Total coolant pressure drop across the system, shown in Equation (A.1), is the sum of the pressure drop across the immersion heater, Coriolis flow meter, chilled water heat exchanger, the pressure drop between the two headers at points [7] and [16] in Figure 3.6, and the pressure drop in the plumbing between components.

$$\Delta P_{c,tot} = \Delta P_{c,heater} + \Delta P_{c,coriolis} + \Delta P_{c,chiller} + \Delta P_{c,7 \rightarrow 16} + \Delta P_{c,plumbing} \qquad (A.1)$$

Pressure drop through the plumbing between components in the system is not included in this analysis because of its minimal contribution to total pressure drop. As an example, major pressure loss through three meters of tube 4.6 mm in inner diameter at the greatest flow rate of 1.88 g s$^{-1}$ is 120 Pa. This is several orders of magnitude less than the pressure drop through other components in the system. The immersion heater and chilled water heat exchanger are constructed of similar tubing that does not contribute significantly to the system pressure drop and are also not considered in this analysis. The pressure drop between the two headers at points [7] and [16] is represented by Equation (A.2) as the sum of the pressure drop across the flow control valve, turbine flow meter, and tube-in-tube heat exchanger along any of the four flow paths between the two headers.

$$\Delta P_{c,7 \rightarrow 16} = \Delta P_{c,v,i} + \Delta P_{c,TM,i} + \Delta P_{c,HX,i} \qquad (A.2)$$

Pressure drop through each tube-in-tube heat exchanger consists of both major and minor frictional losses. Major pressure losses are calculated using Equation (A.3) based on the velocity through the annulus of the heat exchanger.

$$\Delta P_{c,HX,maj,i} = f_{c,i} \frac{l_{annulus}}{D_h} \frac{\rho_{c,i} V_{c,i}^2}{2}$$  (A.3)

The friction factor to Reynolds number relationship for laminar flow through a concentric annulus is shown by Munson *et al.* (1990) to be a function of the ratio of the inner and outer diameter. For a ratio of 0.77, the friction factor Reynolds number relationship is as follows.

$$f_{c,i} \, \mathrm{Re}_{c,i} = 95.8$$  (A.4)

The largest pressure drop occurs in the first heat exchanger for the series configuration at the highest coolant temperatures. The pressure drop is largest at higher temperature despite the lower coolant density because the mass flow rate is the largest for this case, as shown previously in Figure 3.9. Sample calculations for this operating condition are presented throughout this section. For a Reynolds number of 191, velocity of 0.0095 m s$^{-1}$, and average density of 911 kg m$^{-3}$, the major pressure losses in the tube-in-tube heat exchanger annulus are 1.37 Pa.

Minor pressure losses are dependent on the flow restrictions in the tube-in-tube heat exchanger. The flow undergoes an expansion from a 4.6 mm to a 10.9 mm inner diameter tube, two ninety-degree turns through tee fittings, and a contraction from a 10.9 mm to a 4.6 mm inner diameter tube. The loss coefficients for the expansion and contraction, taken from Munson *et al.* (1990), are dependent on the cross-sectional area ratios of the two tubes

and were determined to be 0.65 and 0.45, respectively. The loss coefficient for branch flow through a tee was assumed to be 2. The minor pressure loss for each restriction is calculated with Equation (A.5) where the velocities for the expansion and contraction are those through the smaller tube and the velocity through the tee is that through the larger tube.

$$\Delta P_{c,HX,min,i} = \frac{1}{2} K_L \rho_{c,i} V_{c,i}^2 \tag{A.5}$$

The sum of the minor losses for the first heat exchanger is 1.5 Pa. The total pressure drop through each heat exchanger is equal to the sum of the major and minor losses.

$$\Delta P_{c,HX,i} = \Delta P_{c,HX,maj,i} + \Delta P_{c,HX,min,i} \tag{A.6}$$

The total pressure drop through the first tube-in-tube heat exchanger is 2.87 Pa, which is also insignificant in comparison to the pressure drop through the flow meters and flow control valves.

The maximum pressure drop specified by the manufacturer for the Coriolis flowmeter is 176 Pa, and this value was used as a conservative estimate at all flow rates. The turbine flow meters are made with a small orifice that is the primary contributor to pressure drop. The manufacturer specifies a maximum pressure drop of 69,000 Pa at a flow rate of $5 \times 10^{-6} \ m^3 \ s^{-1}$. Using these values, a loss coefficient for flow through the orifice is calculated using Equation (A.7).

$$K_{L,TM} = \frac{2 \Delta P_{c,TM,max}}{\rho_c V_{c,TM,max}^2} \tag{A.7}$$

For a coolant density of 936 kg m$^{-3}$ and an inlet velocity of 0.31 m s$^{-1}$, the loss coefficient is 1,560. With the loss coefficient determined, pressure drop through the flow meter at lower flowrates is approximated by Equation (A.8).

$$\Delta P_{c,TM,i} = \frac{1}{2} K_{L,TM} \rho_{c,i} V_{c,i}^2 \tag{A.8}$$

The frictional pressure drops through the turbine flow meters for the first through fourth heat exchangers are 1,830, 790, 420, and 170 Pa. The pressure drop decreases with each subsequent heat exchanger because of lower flow through those components.

Control valves are used to modulate the flow rate to each heat exchanger, and sizing the flow coefficient is critical to having proper flow control. The flow coefficient is defined by Equation (A.9).

$$C_{v,i} = \dot{V}_{c,i} \sqrt{\frac{\gamma}{\Delta P_{c,v,i}}} \tag{A.9}$$

The coolant flow rate for each heat exchanger is known from the heat transfer modeling. The flow rate through the first heat exchanger is greatest; therefore, the valve in-line with this heat exchanger requires the greatest flow coefficient. A valve is selected by assigning the fully open flow coefficient to the valve in line with the first heat exchanger. The flow coefficient for the other heat exchangers can be achieved by using the same valve turned down to the required position. Specifying the flow coefficient for the valve in line with the first heat exchanger determines the pressure drop across that valve. This valve pressure drop, along with the pressure drop across the turbine flow meter and tube-in-tube heat exchanger, when used in Equation (A.2), yields the pressure drop between the headers at

points [7] and [16]. With $\Delta P_{c,6\rightarrow15}$ known, the flow coefficient for each valve is obtained by combining Equation (A.9) and (A.2) to yield Equation (A.10).

$$C_{v,i} = \sqrt{\frac{\dot{V}_{c,i}^2 \gamma}{\Delta P_{c,7\rightarrow16} - \Delta P_{c,TM,i} - \Delta P_{c,HX,i}}} \tag{A.10}$$

A valve with a fully open flow coefficient of $3.04 \times 10^{-9}$ m$^3$ s$^{-1}$ Pa$^{-0.5}$ is selected to be used for all four heat exchangers. For the series configuration at the greatest coolant temperature, this results in a pressure drop across the valves in line with the first through fourth heat exchangers of 68.9, 70.0, 70.4, and 70.6 kPa. The total pressure drop across the system is 71.0 kPa, which consists primarily of the valve pressure drop. The valve pressure drop could have been reduced by selecting a valve with a greater fully open flow coefficient, but increasing the valve coefficient increases the valve turn down ratio that is required to achieve the lower flow rates. The turn down ratio is defined here as the ratio of the fully open flow coefficient to the actual flow coefficient, as shown in Equation (A.11).

$$r_{TD} = C_{v,fo} / C_{v,i} \tag{A.11}$$

Increasing the turn down ratio results in more sensitivity in valve position and reduces fine flow control. The turn down ratio for the valve in line with each heat exchanger is shown for a variety of fully open flow coefficients in Figure A.1. At the selected fully open flow coefficient, the turn down ratio is minimized and a reasonable pressure drop across the system is maintained.
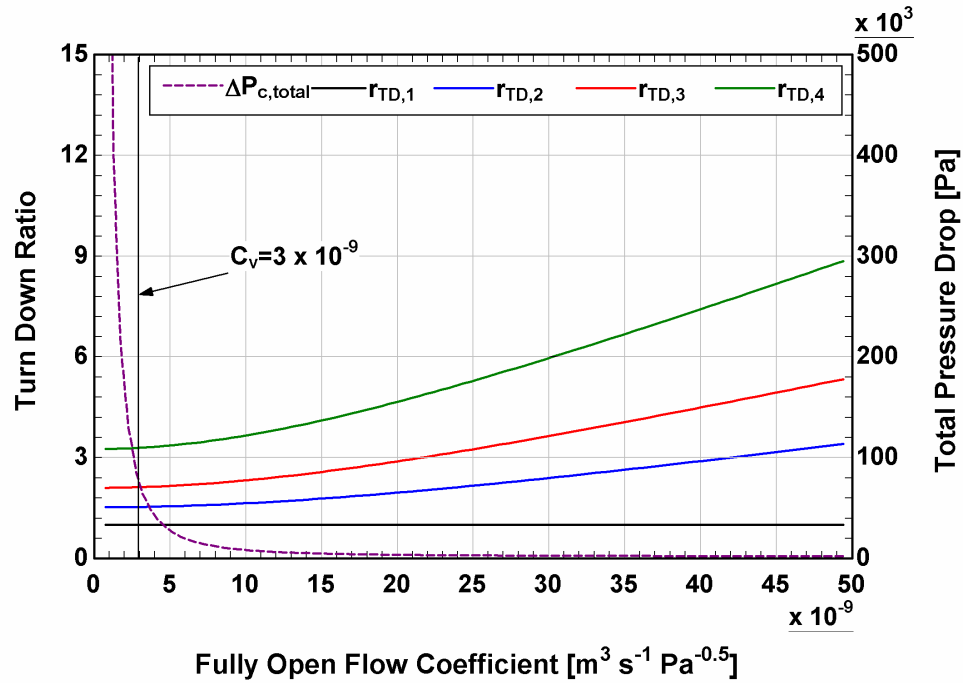
**Figure A.1: Parametric study for valve selection for the series configuration at the greatest average coolant temperature**

A parametric study of the total system pressure drop and the required turn down ratio of each heat exchanger over both test stand configurations and all coolant temperatures was performed and the results are shown in Figure A.2. Turn down ratio shows very little change with coolant temperature, but some decrease is observed due to a decrease in the ratio of the heat exchanger coolant flow rates as coolant temperature increases. Total system pressure drop increases with coolant temperature due to the increase in flowrates with temperature and is maximum for the series configuration at the highest coolant temperature. The total pressure drop across the system is equal to the differential pressure gain across the pump.

The maximum differential pressure across the pump is 71.0 kPa. The required pumping power is expressed by Equation (A.12) for an incompressible fluid.
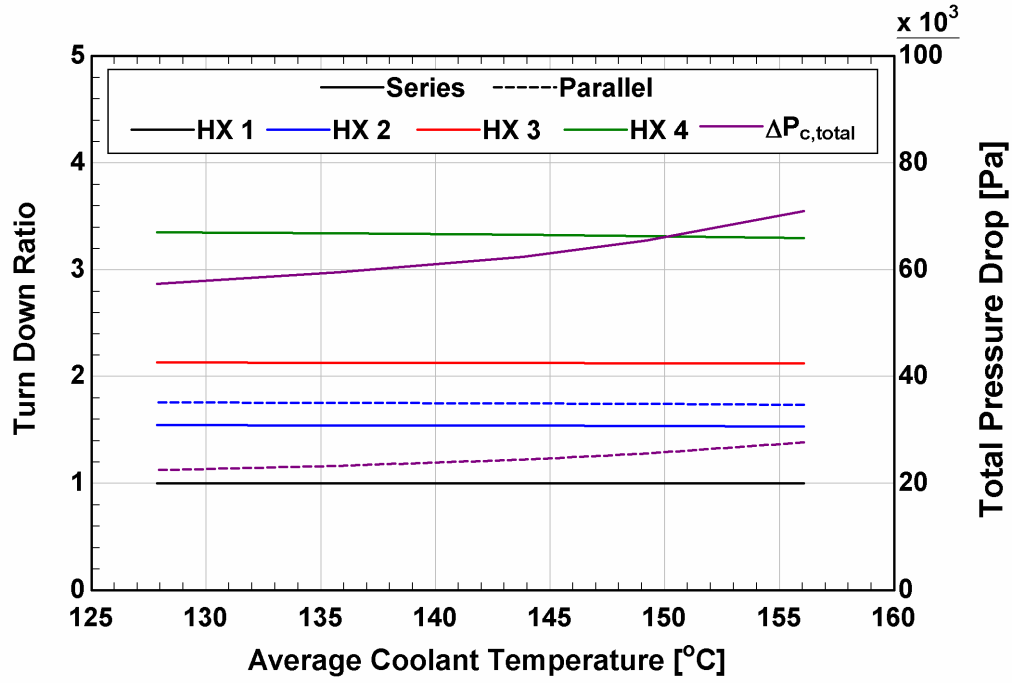
**Figure A.2: Parametric study of turn down ratio and total coolant pressure drop for the range of coolant temperature in both the parallel and series configuration**

$$\dot{W}_{pump} = \dot{V}_{c,pump} \Delta P_{c,tot} \qquad (A.12)$$

For a volumetric flow rate of $1.78 \times 10^{-6}$ m$^3$ s$^{-1}$ and pressure differential of 71 kPa, the pump work is 0.13 W. The electrical power input for the pump required to size the pump motor is determined using a pump and electric motor efficiency, as shown in Equation (A.13).

$$\dot{W}_{pump,elec} = \frac{\dot{W}_{pump}}{\eta_{pump}\eta_{elec}} \qquad (A.13)$$

For a pumping efficiency of 0.6 and electric motor efficiency of 0.9, the required electrical power input is 0.23 W.

218

A model of the exhaust pressure drop across the test facility is used to select pressure measurement instrumentation. The pressure drop must also be less than the allowable back pressure on the diesel engine. The total exhaust pressure drop across the system is equal to the sum of the pressure drop across the four heat exchangers, the pressure drop across the wedge meter used to measure exhaust flow rate, and the pressure drop in the tubing at the outlet of the test stand, as shown in Equation (A.14).

$$\Delta P_{ex,total} = \sum_{i=1}^{n} \Delta P_{ex,HX,i} + \Delta P_{ex,wm} + \Delta P_{ex,outlet} \qquad \text{(A.14)}$$

The pressure drop across each heat exchanger consists of both major and minor losses as follows.

$$\Delta P_{ex,HX,i} = \Delta P_{ex,HX,maj,i} + \Delta P_{ex,HX,min,i} \qquad \text{(A.15)}$$

The major losses are represented by Equation (A.16).

$$\Delta P_{ex,HX,maj,i} = f_{ex,i} \frac{l_{annulus}}{D_{IT,I}} \frac{\rho_{ex,i} V_{ex,i}^{2}}{2} \qquad \text{(A.16)}$$

The friction factor is calculated using the correlation of Churchill (1977b), as shown in Equation (3.16). For the series configuration at the highest coolant temperature, the first heat exchanger is subjected to an exhaust velocity of 39.0 m s$^{-1}$, density of 0.58 kg m$^{-3}$, and friction factor of 0.035, resulting in a major pressure drop of 363 Pa. Minor losses are calculated for flow through the union crosses between heat exchangers that are used for pressure and temperature measurement. The loss coefficient is taken to be 0.9, which is recommended by Munson *et al.* (1990) for line flow through a tee. The minor loss is calculated using Equation (A.17).

$$\Delta P_{ex,HX,\min,i} = \frac{1}{2} K_{L,tee} \rho_{ex,i} V_{ex,i} \tag{A.17}$$

For the conditions listed for the major loss calculation, the minor pressure loss is 800 Pa, which results in a total pressure drop across the first heat exchanger of 1163 Pa.

The frictional pressure loss across the wedge flow meter at the series arrangement exhaust flow rate of 2.1 g s$^{-1}$ is specified by the manufacturer to be 673 Pa. This was used as an estimate of the pressure drop for both the series and parallel configurations.

The pressure drop at the outlet of the test stand consists of major losses through one meter of tubing with an inner diameter of 10.9 mm and minor losses through an elbow and out the exit of the tube into the atmosphere. The major and minor losses are calculated using Equations (A.18) and (A.19), respectively.

$$\Delta P_{ex,outlet,maj} = f_{ex,outlet} \frac{l_{outlet}}{D_{IT,I}} \frac{\rho_{ex,outlet} V_{ex,outlet}^2}{2} \tag{A.18}$$

$$\Delta P_{ex,outlet,\min} = \frac{1}{2} (K_{L,elbow} + K_{L,exit}) \rho_{ex,outlet} V_{ex,outlet} \tag{A.19}$$

The loss coefficients through the elbow and exit are taken to be 1.5 and 1, as specified by Munson *et al.* (1990). The resulting major losses and minor losses are 1,100 and 885 Pa, respectively, summing to a total pressure drop at the outlet of 1,985 Pa. The total exhaust pressure drop across the entire test stand for the series configuration at the highest coolant temperature is 6,771 Pa.

The pressure drop across each heat exchanger and the total pressure drop are shown for all coolant temperatures and test stand configurations in Figure A.3. Comparing heat
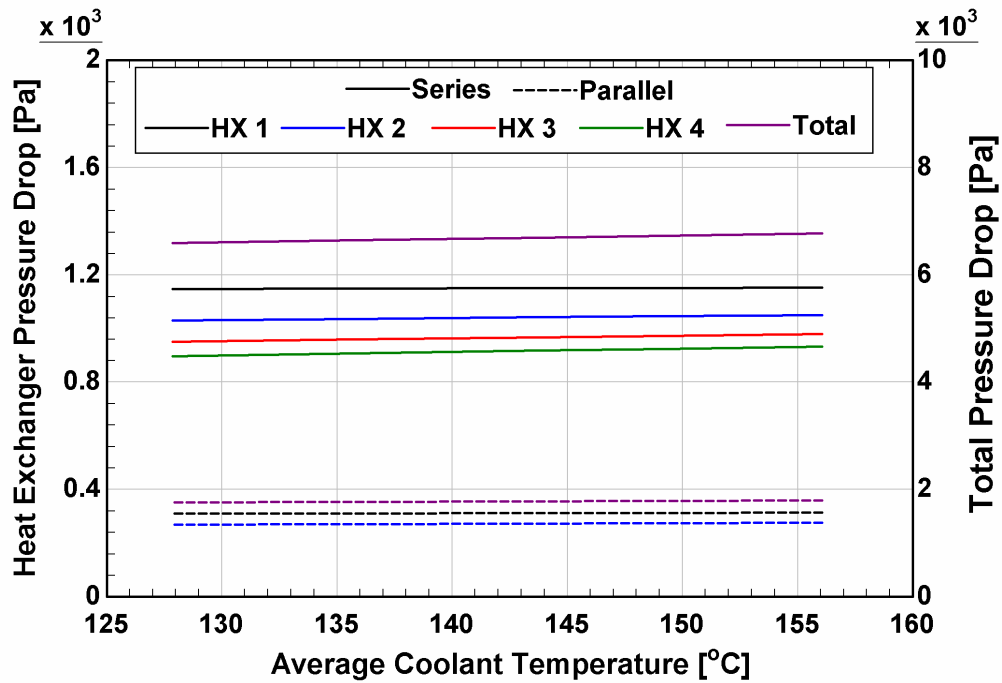
**Figure A.3: Total and heat exchanger pressure drop over coolant temperature range for both test stand configurations**

exchangers for either configuration at a single coolant temperature, the pressure drop is greatest in the first heat exchanger and decreases in subsequent heat exchangers. This is because the temperature is greater in the first heat exchanger, which results in a lower density and greater velocity. The viscosity of the exhaust also increases with temperature, which contributes to the higher pressure drop. For a single heat exchanger, and as the coolant temperature increases, the pressure drop increases as well because the greater coolant temperature causes exhaust temperature at the outlet of each heat exchanger to be greater. Comparing the two configurations, the total pressure drop for the series cases is about four times that of the parallel case. This is because the mass flow rate is double for the series case and pressure drop is approximately dependent on the square of velocity. The heat exchanger pressure drops range from 228 to 1153 Pa, which is important for selection

of the differential pressure transducer to measure these pressure drops.  Total exhaust

pressure drop has a maximum of 6,771 Pa, which is well below the engine manufacturer

specified maximum allowable back pressure of 12,000 Pa.

# APPENDIX B.    THERMOCOUPLE RADIATION

# CORRECTION

At steady state, the convection and radiation heat transfer rates must be equal, as in Equation (B.1).

$$\dot{Q}_{tc,conv,i} = \dot{Q}_{tc,rad,i} \tag{B.1}$$

The thermocouple is idealized as a sphere suspended in the center of the exhaust flow. The convective heat transfer rate is dependent on the heat transfer coefficient, the area of the sphere, and the temperature difference between the exhaust and the thermocouple.

$$\dot{Q}_{tc,conv,i} = h_{tc,i} \left( 4\pi r_{tc}^2 \right) \left( T_{ex,i} - T_{tc,i} \right) \tag{B.2}$$

The thermocouple radius is 1.6 mm, which is half of the outer diameter of the thermocouple sheath. The convective heat transfer coefficient is determined from the Nusselt number for external flow over a sphere calculated with the correlation of Whitaker (1972), as follows.

$$Nu_{tc,i} = 2 + \left( 0.4\,\mathrm{Re}_{tc,ex,i}^{1/2} + 0.06\,\mathrm{Re}_{tc,ex,i}^{2/3} \right) \mathrm{Pr}_{ex,i}^{0.4} \left( \frac{\mu_{ex,i}}{\mu_{s,tc,i}} \right)^{1/4} \tag{B.3}$$

All properties are calculated at the bulk temperature of the exhaust, except for $\mu_s$, which is determined at the surface temperature of the thermocouple. The heat transfer coefficient is calculated from the Nusselt number and the thermal conductivity of exhaust in Equation (B.4), which is predicted as that for air at the bulk temperature of the exhaust.

$$h_{tc,i} = \frac{Nu_{tc,i} D_{tc}}{k_{ex,i}} \tag{B.4}$$

It is assumed that the radiation heat transfer is between a relatively small thermocouple surface and large surroundings. The surroundings consist of the internal surface of the cross and the inner surface of the inner tube in the heat exchanger on either side of the cross. This is shown schematically in Figure B.4.

Further assumptions include that each of the surrounding surfaces are black bodies at a constant temperature, the thermocouples are grey and diffuse, and the thermocouples only radiate to the heat exchangers on either side of them, not to heat exchangers further up or downstream. Assuming that the surrounding surfaces are black bodies results in the maximum potential radiation heat transfer rate from the thermocouple to the surroundings. The radiation heat transfer rate for each thermocouple is represented by Equation (B.5).



**Figure B.4: Radiation heat transfer from exhaust thermocouple in union cross between heat exchangers**

$$\dot{Q}_{rad,i} = \dot{Q}_{tc,rad,i} = F_{tc,tube}e_{tc}\sigma_{SB}\left(4\pi r_{tc}^2\right)\left(T_{tc,i}^4 - T_{IT,I,i-1}^4\right) + F_{tc,cross}e_{tc}\sigma_{SB}\left(4\pi r_{tc}^2\right)\left(T_{tc,i}^4 - T_{cross,i}^4\right)$$
$$+ F_{tc,tube}e_{tc}\sigma_{SB}\left(4\pi r_{tc}^2\right)\left(T_{tc,i}^4 - T_{IT,I,i}^4\right) \tag{B.5}$$

For the first thermocouple, there is no heat exchanger upstream of the measurement, and the first term in the equation is removed. Similarly for the fifth thermocouple, there is no heat exchanger downstream, and the last term is removed from the equation.

It is observed in experiments that the thermocouple surface becomes covered in a thin layer of particulate matter; therefore, the emissivity assigned to the thermocouple is that of soot adhered to a solid surface, 0.96. The temperature of the inner surface of each cross is calculated based on the exhaust heat loss in the inlet and outlet of the heat exchanger and the thermal resistance of the exhaust. The temperature of the inner surface of the inner tube in each heat exchanger is calculated from the exhaust heat transfer rate and the exhaust convective resistance.

The view factor from the thermocouple to the tube in each heat exchanger is calculated with a relationship for a view factor between a sphere and a coaxial disc. The disc represents the opening in the cross that the exhaust flows through. According to Howell (1998), the view factor is dependent on the radius ratio of the sphere to the disk, $r = r_{tc}/r_{IT,I}$, and the ratio of the distance between the sphere and the disc to the radius of the disc, $h = h_{tc,disc}/r_{IT,I}$, as shown in the following equation.

$$F_{tc,tube} = 2r^2\left(1 - \frac{1}{\sqrt{1 + 1/h^2}}\right) \tag{B.6}$$

The view factors of the thermocouple must sum to one; therefore, the view factor from the thermocouple to the cross for the first and fifth thermocouple is represented with Equation (B.7) and for the second through fourth heat exchanger with Equation (B.8).

$$F_{tc,cross,1/5} = 1 - F_{tc,tube} \tag{B.7}$$

$$F_{tc,cross,2-4} = 1 - 2F_{tc,tube} \tag{B.8}$$

With the system of equations for the convective and radiation heat transfer rates of each heat exchanger, the exhaust temperature at the location of each thermocouple is calculated. The measured and corrected exhaust temperatures for a test at design conditions are shown in Table B.1. The correction for the first thermocouple, 1.9°C, is the greatest and the correction for the last thermocouple, 0.3°C, is the least. The effect on

**Table B.1: Comparison of corrected and measured exhaust temperatures**

| TC | Measured Temperature [°C] | Corrected Temperature [°C] | Difference [°C] |
|----|--------------------------|---------------------------|-----------------|
| 1 | 377.8 | 379.7 | 1.9 |
| 2 | 301.7 | 303.1 | 1.4 |
| 3 | 245.9 | 246.7 | 0.8 |
| 4 | 208.6 | 209.2 | 0.6 |
| 5 | 181.2 | 181.5 | 0.3 |

**Table B.2: Effect of temperature correction on exhaust heat transfer rate**

| Heat Exchanger | Change in Temperature Difference [°C] | Percent of Temperature Difference [%] |
|----------------|---------------------------------------|---------------------------------------|
| 1 | 0.5 | 0.7 |
| 2 | 0.6 | 1.1 |
| 3 | 0.2 | 0.5 |
| 4 | 0.3 | 1.1 |

temperature difference across each heat exchanger is shown in Table B.2. The temperature

difference is affected by a maximum of 1.1%, which will result in the same difference in

exhaust heat transfer rate.

# APPENDIX C.    PREDICTED DEPOSITION

Particulate matter deposition is calculated due to thermophoresis, as this was determined to be the dominant mechanism in a scaling analysis performed by Abarham *et al.* (2010a). A relationship for the thermophoretic deposition efficiency, the ratio of particulate mass deposited to that entering the tube, was developed by Housiadas and Drossinos (2005) for turbulent flow through an infinitely long tube. For an infinitely long tube, the exhaust temperature approaches the tube wall temperature; therefore, this equation is most applicable to calculate the total mass deposited across all four heat exchangers in the series configuration and two heat exchangers in the parallel configuration. The relationship is shown in Equation (C.1).

$$E_{th,\infty} = 1 - \left( \frac{T_{foul,i}}{T_{ex,in,1}} \right)^{\Pr K} \tag{C.1}$$

The mass of particulate matter entering the test facility is predicted based on the measurement of exhaust opacity. The smoke opacity measurement is dependent on the attenuation of a light beam according to Beer's Law, as in the following equation.

$$Opacity = 1 - e^{\left( -A_E C_{PM} L_{opac} \right)} \tag{C.2}$$

Where $C_{PM}$ is the mass concentration of particulate matter, $L_{opac}$ is the length of the beam between the transmitter and receiver of the opacimeter, and $A_E$ is the specific optical extinction. The specific optical extinction is dependent on the exhaust properties; however, it was determined by Roessler (1982) that for exhaust that is the product of lean combustion, the specific optical extinction is a constant value of approximately 3 $m^2$ $g^{-1}$.

Using this value, the measured opacity, and the beam length of 0.05 m allows for the prediction of particulate matter concentration. The concentration is converted to a mass flow rate of particulate matter using Equation (C.3), where the density is calculated at the inlet temperature of the exhaust to the test stand.

$$\dot{m}_{PM,in} = \frac{C_{PM,in,1}\dot{m}_{ex}}{\rho_{ex,in,1}}$$
(C.3)

The fouling layer surface temperature is calculated based on the coolant heat transfer rate, the average coolant temperature, and the resistance of the coolant, tube, and fouling layer, as shown in the following equation.

$$T_{foul,i} = \frac{\dot{Q}_{c,i}}{R_{c,i} + R_{IT,i} + R_{foul,i}} + T_{c,avg,i}$$
(C.4)

The fouling layer temperature of each heat exchanger is averaged and input to Equation (4.70). The exhaust inlet temperature to the first heat exchanger is measured and the Prandtl number is determined for that of air at the average temperature of exhaust across the test stand. The thermophoretic coefficient, $K$, is calculated using the method presented by Abarham $et\ al.$ (2009b) in Equation (C.5) and (C.6).

$$K = \frac{2C_s C'}{1+3C_m Kn} \times \frac{k_g/k_p + C_t Kn}{1+2k_g/k_p + 2C_t Kn}$$
(C.5)

$$C' = 1 + Kn\left(A + Be^{-C/Kn}\right)$$
(C.6)

The coefficients $A$, $B$, $C$, $C_s$, $C_m$, $C_t$ are 1.2, 0.41, 0.88, 1.14, 1.17, and 2.18, respectively. The thermal conductivity of the gas is taken to be for air at the average exhaust temperature

and the thermal conductivity of graphite, 5 W m$^{-1}$ K$^{-1}$, is used for the particulate. The thermal conductivity of graphite was used for particulate matter in the EGR cooler fouling modeling efforts of Abarham *et al.* (2010b), which showed good agreement with experiments. The Knudsen number is dependent on the mean free path and diameter of the particle as shown in Equation (C.7). The most frequent diameter of particulate matter in diesel exhaust was measured by Bika *et al.* (2012) to be about 100 nm. As diameter increases, Knudsen number decreases, causing a decrease in the thermophoretic coefficient, and a corresponding decrease in the thermophoretic efficiency. For this diameter, the mean free path is calculated using Equation (C.8).

$$Kn = \frac{2\lambda}{D_{PM}} \tag{C.7}$$

$$\lambda = \frac{2\mu_{ex,avg}}{\rho_{ex,avg}} \sqrt{\frac{\pi M_{ex}}{8R_u T_{ex,avg}}} \tag{C.8}$$

The viscosity and density are the average of that in each heat exchanger. The universal gas constant is 8.314 J mol$^{-1}$ K$^{-1}$. With these values, thermophoretic coefficient and deposition efficiency can be calculated. The rate of deposition is found from the mass flow rate of particulate matter and the deposition efficiency.

$$\dot{m}_{PM,dep} = \dot{m}_{PM,in} E_{th,\infty} \tag{C.9}$$

This value is numerically integrated for each data point over the duration of the experiment to predict the total deposition mass of particulate matter.

The mass rate of hydrocarbons that condense onto the deposit surface of each heat exchanger is dependent on the surface area of the inner tube, mass transfer coefficient, and the mole fraction of hydrocarbons in the bulk and at the interface, as shown in Equation (4.72).

$$\dot{m}_{g,i} = K_{g,i} A_{IT,i} \ln\left(\frac{1 - \tilde{y}_{C_{20}H_{42},\text{int},i}}{1 - \tilde{y}_{C_{20}H_{42},b,i}}\right) \tag{C.10}$$

After performing ex-situ analysis on the deposit layer, Sluder *et al.* (2009) found that eicosane ($C_{20}H_{42}$) is the most prevalent hydrocarbon that deposits onto the fouling layer. For simplicity, it is assumed that all of the hydrocarbons in the exhaust are eicosane, which is sufficient to show the trend of hydrocarbon condensation at different operating conditions. The mole fraction of hydrocarbons that is calculated on a $C_1$ basis at the inlet of the test facility is converted to the mole fraction of eicosane with the following equation.

$$\tilde{y}_{C_{20}H_{42},b,in,1} \approx \tilde{y}_{C_1H_{1.8},b,in}\big/20 \tag{C.11}$$

The mass flow rate of eicosane entering the heat exchanger is dependent on the mass fraction at the inlet and the mass flow rate of exhaust, as shown in Equation (C.12). The bulk mole fraction of eicosane is taken as the average of the inlet and outlet concentration, where the outlet concentration is determined based on the mass deposited in the heat exchanger using Equation (C.13).

$$\dot{m}_{C_{20}H_{42},b,in,i} = y_{C_{20}H_{42}} \dot{m}_{ex} \tag{C.12}$$

$$\dot{m}_{C_{20}H_{42},b,out,i} = \dot{m}_{C_{20}H_{42},b,in,i} - \dot{m}_{g,i} \tag{C.13}$$

The mass flow rate, and therefore mole fraction, at the outlet of one heat exchanger is taken to be equal to the corresponding value at the inlet to the subsequent heat exchanger. This results in a reduction in the mole fraction as the exhaust flows through each heat exchanger. The vapor pressure of eicosane at the interface is determined from the Antoinne relationship for vapor pressure of a pure fluid, as shown in the following equation.

$$\log\left(P_{C_{20}H_{42},\text{int},i}\right) = AA - BB/(T_{foul,i} + CC) \tag{C.14}$$

The coefficients AA, BB, and CC for eicosane are 7.122, 2032.700, and 132.100. From the vapor pressure, the mole fraction at the interface is calculated as a ratio of the vapor pressure to the exhaust pressure.

$$\tilde{y}_{C_{20}H_{42},\text{int},i} = P_{C_{20}H_{42},\text{int},i}/P_{ex} \tag{C.15}$$

The mass transfer coefficient is predicted using the analogy of Chilton and Colburn (1934), shown in Equation (C.16). The recommended correlation for the Fanning friction factor for turbulent pipe flow is shown in Equation (C.17).

$$St_{m,i}Sc_i^{2/3} = C_{f,i}^2 \tag{C.16}$$

$$C_{f,i} = 0.046\,\mathrm{Re}_{ex,i}^{-0.2} \tag{C.17}$$

The Schmidt number is dependent on the exhaust viscosity, density, and the mass diffusivity of eicosane in the exhaust.

$$Sc_i = \frac{\mu_{ex,i}}{\rho_{ex,i}d_{12}} \tag{C.18}$$

The mass diffusivity was calculated using the empirical relationship proposed by Holman (1997) shown in Equation (C.19).

$$d_{12} = 0.04357 \frac{\left(T_{ex,avg,i} + 273.15\right)^{3/2}}{P_{ex}\left(V_1^{1/3} + V_2^{1/3}\right)^2} \sqrt{\frac{1}{M_1} + \frac{1}{M_2}} \qquad (C.19)$$

It is idealized that fluid two, the exhaust, is pure nitrogen. The diffusion volume of hydrocarbon and nitrogen, $V_1$ and $V_2$, are taken from Tang *et al.* (2015) to be 415.02 and 9.08 m$^3$, respectively. This allows for the calculation of the Schmidt number, which along with the Fanning friction factor, is input to Equation (C.16) to determine the Stanton number for mass transfer. The Stanton number is used to calculate the Sherwood number in Equation (C.20), which is subsequently used to calculate the mass transfer coefficient in Equation (C.21).

$$Sh_i = St_{m,i}\, \mathrm{Re}_{ex,i}\, Sc_i \qquad (C.20)$$

$$K_{g,i} = \frac{Sh_i d_{12} \rho_{ex,i}}{D_{IT,I}} \qquad (C.21)$$

The determination of mass transfer coefficient enables the calculation of the condensation rate of hydrocarbons in each heat exchanger, which is numerically integrated to determine the total mass of deposition throughout an experiment.

# APPENDIX D.    TEST FACILITY MODEL SAMPLE CALCULATIONS

| Inputs | Equations | Results |
|---|---|---|
| **Exhaust composition** | | |
| $a = 1$ | $n_{O_2} = 1 + b/4a$ | $n_{O_2} = 1.45$ |
| $b = 1.8$ | $n_{prod} = 3.773 \dfrac{n_{O_2}}{\varphi \tilde{y}_{N_2}}$ | $n_{prod} = 11.98$ |
| $\varphi = 0.6$ | | |
| $M_{CO_2} = 44.01$ kg kmol$^{-1}$ | $\tilde{y}_{CO_2} = a/n_{prod}$ | $\tilde{y}_{CO_2} = 0.083$ |
| $M_{H_2O} = 18.02$ kg kmol$^{-1}$ | $\tilde{y}_{H_2O} = b/2n_{prod}$ | $\tilde{y}_{H_2O} = 0.075$ |
| $M_{O_2} = 32$ kg kmol$^{-1}$ | $\tilde{y}_{O_2} = \dfrac{n_{O_2}}{\varphi n_{prod}} - \tilde{y}_{CO_2} - \dfrac{1}{2}\tilde{y}_{H_2O}$ | $\tilde{y}_{O_2} = 0.081$ |
| $M_{N_2} = 28.01$ kg kmol$^{-1}$ | | |
| | $\tilde{y}_{N_2} = 1 - \tilde{y}_{H_2O} - \tilde{y}_{CO_2} - \tilde{y}_{O_2}$ | $\tilde{y}_{N_2} = 0.76$ |
| | $M_{tot} = n_p \left( \tilde{y}_{CO_2} M_{CO_2} + \tilde{y}_{H_2O} M_{H_2O} + \tilde{y}_{O_2} M_{O_2} + \tilde{y}_{N_2} M_{N_2} \right)$ | $M_{tot} = 346.6$ kg kmol$^{-1}$ |
| | $y_{CO_2} = \tilde{y}_{CO_2} M_{CO_2} / M_{tot}$ | $y_{CO_2} = 0.127$ |
| | $y_{H_2O} = \tilde{y}_{H_2O} M_{H_2O} / M_{tot}$ | $y_{H_2O} = 0.047$ |
| | $y_{O_2} = \tilde{y}_{O_2} M_{O_2} / M_{tot}$ | $y_{O_2} = 0.089$ |
| | $y_{N_2} = \tilde{y}_{N_2} M_{N_2} / M_{tot}$ | $y_{N_2} = 0.740$ |

| Heat Transfer Rate in First Heat Exchanger | | |
|---|---|---|
| $\dot{m}_{ex,des} = 0.0235 \, \text{kg s}^{-1}$ | $\dot{m}_{ex,pt} = \dot{m}_{ex,des} / n_{p,tubes}$ | $\dot{m}_{ex,pt} = 0.00213 \, \text{kg s}^{-1}$ |
| $n_{p,tubes} = 11$ | $c_{p,ex,1} = y_{CO_2} c_{p,CO_2,1} + y_{H_2O} c_{p,H_2O,1}$ $+ y_{O_2} c_{p,O_2,1} + y_{N_2} c_{p,N_2,1}$ | $c_{p,ex,1} = 1129 \, \text{J kg}^{-1} \, \text{K}^{-1}$ |
| $y_{CO_2} = 0.127$ | | |
| $y_{H_2O} = 0.047$ | | |
| $y_{O_2} = 0.089$ | $\text{Re}_{ex,1} = \dfrac{4\dot{m}_{ex,pt}}{\pi D_{IT,I} \mu_{ex,1}}$ | $\text{Re}_{ex,1} = 7935$ |
| $y_{N_2} = 0.74$ | | |
| $D_{IT,I} = 0.0109 \, \text{m}$ | Friction factor for smooth tubes over all flow regimes (Churchill, 1977b) | $f_{ex,1} = 0.0352$ |
| $D_{IT,O} = 0.0127 \, \text{m}$ | $f_{ex,1} = 8\left[\left(\dfrac{8}{\text{Re}_{ex,1}}\right)^{12} + 1 \Big/ \left(2.457\ln\left(\dfrac{1}{\left(7/\text{Re}_{ex,1}\right)^{0.9} + \left(0.27\varepsilon/D_{IT,I}\right)}\right)^{16} + \left(37530/\text{Re}_{ex,1}\right)^{16}\right)^{1.5}\right]^{1/12}$ | |
| $D_{OT,I} = 0.0166 \, \text{m}$ | | |
| $L_{annulus} = 0.254 \, \text{m}$ | | |
| $\varepsilon = 1.5 \times 10^{-5} \, \text{m}$ | | |
| $T_{ex,in,1} = 400 \, ^\circ\text{C}$ | Nusselt number for smooth tubes over all flow regimes Churchill (1977a) | $Nu_{ex,1} = 24.42$ |
| $\mu_{ex,1} = 3.14 \times 10^{-5} \, \text{kg m}^{-1} \, \text{s}^{-1}$ | $Nu_{ex,1}^{10} = 4.364^{10} + \left[\dfrac{e^{(2200-\text{Re}_{ex,1})/365}}{4.364^2} + 1\Big/\left(\dfrac{6.3 + 0.079(f_{ex,1}/8)^{1/2}\,\text{Re}_{ex,1}\,\text{Pr}_{ex,1}}{\left(1 + \text{Pr}_{ex,1}^{4/5}\right)^{5/6}}\right)\right]^{-5}$ | |
| $k_{ex,1} = 0.048 \, \text{W m}^{-1} \, \text{K}^{-1}$ | | |
| $\text{Pr}_{ex,1} = 0.69$ | | |
| $c_{p,CO_2,1} = 1096 \, \text{J kg}^{-1} \, \text{K}^{-1}$ | $h_{ex,1} = Nu_{ex,1} k_{ex,1} / D_{IT,I}$ | $h_{ex,1} = 107.3 \, \text{W m}^{-2} \, \text{K}^{-1}$ |
| $c_{p,H_2O,1} = 2041 \, \text{J kg}^{-1} \, \text{K}^{-1}$ | $R_{ex,1} = \dfrac{1}{h_{ex,1}\pi D_{IT,I} L_{annulus}}$ | $R_{ex,1} = 1.069 \, \text{K W}^{-1}$ |
| $c_{p,O_2,1} = 1014 \, \text{J kg}^{-1} \, \text{K}^{-1}$ | | |
| $c_{p,N_2,1} = 1086 \, \text{J kg}^{-1} \, \text{K}^{-1}$ | $R_{tube,1} = \dfrac{\ln(D_{IT,O}/D_{IT,I})}{2\pi k_{tube,1} L_{tube}}$ | $R_{tube,1} = 0.0060 \, \text{K W}^{-1}$ |
| $k_{tube,1} = 15.63 \, \text{W m}^{-1} \, \text{K}^{-1}$ | | |
| | $r = D_{IT,I} / D_{OT,I}$ | $r = 0.77$ |

| | | |
|---|---|---|
| $T_{cs} = 137.6\,^{\circ}\text{C}$ <br> $T_{ds} = 190.4\,^{\circ}\text{C}$ <br> $k_{c,1} = 0.665\,\text{W m}^{-1}\,\text{K}^{-1}$ <br> $c_{p,c,1} = 4332\,\text{J kg}^{-1}\,\text{K}^{-1}$ <br> $h_s = 3000\,\text{W m}^{-2}\,\text{K}^{-1}$ | Nusselt Number for fully-developed laminar flow through a concentric annulus ($0.50 \le r \le 1.00$) (Bergman *et al.* (2011)) <br> $$Nu_c = \frac{4.86-5.74}{1.00-0.50}(r-0.50)+5.74$$ | $Nu_{c,1} = 5.27$ |
| | $D_h = D_{OT,I} - D_{IT,O}$ | $D_h = 3.86\,\text{mm}$ |
| | $h_{c,1} = Nu_c k_{c,1}/D_h$ | $h_{c,1} = 908.9\,\text{W m}^{-2}\,\text{K}^{-1}$ |
| | $$R_{c,1} = \frac{1}{h_{c,i}\pi D_{IT,O}L_{annulus}}$$ | $R_{c,i} = 0.109\,\text{K W}^{-1}$ |
| | $R_1 = R_{ex,1} + R_{tube,1} + R_{e,1}$ | $R_1 = 1.184\,\text{K W}^{-1}$ |
| | $UA_1 = 1/R_1$ | $UA_1 = 0.845\,\text{W K}^{-1}$ |
| | $$LMTD_1 = \frac{\left(T_{ex,in,1}-T_{c,out,1}\right)-\left(T_{ex,out,1}-T_{c,in,1}\right)}{\ln\left(\left(T_{ex,in,1}-T_{c,out,1}\right)/\left(T_{ex,out,1}-T_{c,in,1}\right)\right)}$$ | $LMTD_1 = 207.4\,^{\circ}\text{C}$ |
| | $\dot{Q}_1 = UA_1 \times LMTD_1$ | $\dot{Q}_1 = 175.1\,\text{W}$ |
| | $$T_{c,in,1} = T_{cs} - \frac{\dot{Q}_1}{A_{IT,O}}\left(\frac{1}{h_{c,1}}-\frac{1}{h_s}\right)$$ | $T_{c,in,1} = 129.8\,^{\circ}\text{C}$ |
| | $$T_{c,out,1} = T_{ds} - \frac{\dot{Q}_1}{A_{IT,O}}\left(\frac{1}{h_{c,1}}-\frac{1}{h_s}\right)$$ | $T_{c,out,1} = 182.3\,^{\circ}\text{C}$ |
| | $\dot{m}_{c,1} = \dot{Q}_1 \big/ \left(c_{p,c,1}(T_{c,out,1}-T_{c,in,1})\right)$ | $\dot{m}_{c,1} = 7.7 \times 10^{-4}\,\text{kg s}^{-1}$ |
| | $T_{ex,out,1} = T_{ex,in,1} - \dot{Q}_1 \big/ \left(\dot{m}_{ex,pt}c_{p,ex,1}\right)$ | $T_{ex,out,1} = 327.2\,^{\circ}\text{C}$ |

| **Coolant Pressure Drop Model** | | |
|---|---|---|
| **Tube –in-Tube heat exchanger pressure drop** | | |
| $A_{annulus} = 8.87 \times 10^{-5}\,\text{m}^2$ <br> $D_{IT,O} = 0.0109\,\text{m}$ | $\text{Re}_{c,1} = \dfrac{\dot{m}_{c,1} D_h}{\mu_{c,1} A_{annulus}}$ | $\text{Re}_{c,1} = 191.4$ |
| $D_h = 0.0039\,\text{m}$ <br> $D_{small-tube} = 0.0046\,\text{m}$ <br> $D_{large-tube} = 0.0109\,\text{m}$ | Friction factor for laminar flow through a concentric annulus ($0.50 \leq r \leq 1.00$) (Munson *et al.*, 1990) <br><br> $f_{c,1}\,\text{Re}_{c,1} = \dfrac{96.0 - 95.6}{1.00 - 0.60}(r - 0.6) + 95.6$ | $f_{c,1} = 0.500$ |
| $r = 0.77$ <br> $L_{annulus} = 0.254\,\text{m}$ | $V_{c,1} = \dfrac{\dot{m}_{c,1}}{\rho_{c,1} A_{annulus}}$ | $V_{c,1} = 0.00953\,\text{m s}^{-1}$ |
| $\dot{m}_{c,1} = 7.7 \times 10^{-4}\,\text{kg s}^{-1}$ <br> $\mu_{c,1} = 1.75 \times 10^{-4}\,\text{kg m}^{-1}\,\text{s}^{-1}$ | $V_{c,small-tube,1} = \dfrac{4\dot{m}_{c,1}}{\rho_{c,1} \pi D_{tube}^2}$ | $V_{c,small-tube,1} = 0.0516\,\text{m s}^{-1}$ |
| $\rho_{c,1} = 911\,\text{kg m}^{-3}$ <br> $K_{L,\exp} = 0.65$ | $V_{c,large-tube,1} = \dfrac{4\dot{m}_{c,1}}{\rho_{c,1} \pi D_{large-tube}^2}$ | $V_{c,large-tube,1} = 0.0090\,\text{m s}^{-1}$ |
| $K_{L,con} = 0.45$ <br> $K_{L,elbow} = 1.5$ | $\Delta P_{c,HX,maj,1} = f_{c,1} \dfrac{L_{annulus}}{D_h} \dfrac{\rho_{c,1} V_{c,1}^2}{2}$ | $\Delta P_{c,HX,maj,1} = 1.366\,\text{Pa}$ |
| Munson *et al.* (1990) for $A_1/A_2 = 0.2$ | $\Delta P_{c,HX,\exp,1} = \dfrac{1}{2} K_{L,\exp} \rho_{c,1} V_{c,small-tube,1}^2$ | $\Delta P_{c,HX,\exp,1} = 0.788\,\text{Pa}$ |
| $n_{elbow} = 2$ | $\Delta P_{c,HX,con,1} = \dfrac{1}{2} K_{L,con} \rho_{c,1} V_{c,small-tube,1}^2$ | $\Delta P_{c,HX,con,1} = 0.546\,\text{Pa}$ |
| | $\Delta P_{c,HX,elb,1} = \dfrac{1}{2} n_{elb} K_{L,elb} \rho_{c,1} V_{c,1}^2$ | $\Delta P_{c,HX,elb,1} = 0.166\,\text{Pa}$ |
| | $\Delta P_{c,HX,\min,1} = \Delta P_{c,HX,\exp,1} + \Delta P_{c,HX,con,1} + \Delta P_{c,HX,elbow,1}$ | $\Delta P_{c,HX,\min,1} = 1.500\,\text{Pa}$ |
| | $\Delta P_{c,HX,1} = \Delta P_{c,HX,maj,1} + \Delta P_{c,HX,\min,1}$ | $\Delta P_{c,HX,1} = 2.866\,\text{Pa}$ |

| Turbine flow meter pressure drop | | |
|---|---|---|
| $D_{small-tube} = 0.0046\,\text{m}$<br>$\dot{V}_{c,max} = 5 \times 10^{-6}\,\text{m}^3\,\text{s}^{-1}$<br>$\Delta P_{c,TM,max} = 69,000\,\text{Pa}$<br>$\rho_{c,in,1} = 936.3\,\text{kg m}^{-3}$<br>$\rho_{c,in,2} = 936.3\,\text{kg m}^{-3}$<br>$\rho_{c,in,3} = 936.3\,\text{kg m}^{-3}$<br>$\rho_{c,in,4} = 936.3\,\text{kg m}^{-3}$<br>$\dot{m}_{c,1} = 7.7 \times 10^{-4}\,\text{kg s}^{-1}$<br>$\dot{m}_{c,2} = 5.1 \times 10^{-4}\,\text{kg s}^{-1}$<br>$\dot{m}_{c,3} = 3.7 \times 10^{-4}\,\text{kg s}^{-1}$<br>$\dot{m}_{c,4} = 2.7 \times 10^{-4}\,\text{kg s}^{-1}$ | $V_{c,max} = \dfrac{4\dot{V}_{c,TM,max}}{\pi D_{small-tube}^2}$ | $V_{c,max} = 0.31\,\text{m s}^{-1}$ |
| | $K_{L,TM} = \dfrac{2\Delta P_{c,TM,max}}{\rho_c V_{c,TM,max}^2}$ | $K_{L,TM} = 1560$ |
| | $V_{c,TM,1} = \dfrac{4\dot{m}_{c,1}}{\rho_{c,in,1}\pi D_{tube,small}^2}$ | $V_{c,TM,1} = 0.050\,\text{m s}^{-1}$ |
| | $V_{c,TM,2} = \dfrac{4\dot{m}_{c,2}}{\rho_{c,in,2}\pi D_{tube,small}^2}$ | $V_{c,TM,2} = 0.033\,\text{m s}^{-1}$ |
| | $V_{c,TM,3} = \dfrac{4\dot{m}_{c,3}}{\rho_{c,in,3}\pi D_{tube,small}^2}$ | $V_{c,TM,3} = 0.024\,\text{m s}^{-1}$ |
| | $V_{c,TM,4} = \dfrac{4\dot{m}_{c,1}}{\rho_{c,in,4}\pi D_{tube,small}^2}$ | $V_{c,TM,4} = 0.0154\,\text{m s}^{-1}$ |
| | $\Delta P_{c,TM,1} = \dfrac{1}{2}K_{L,TM}\rho_{c,in,1}V_{c,TM,1}^2$ | $\Delta P_{c,TM,1} = 1830\,\text{Pa}$ |
| | $\Delta P_{c,TM,2} = \dfrac{1}{2}K_{L,TM}\rho_{c,in,2}V_{c,TM,2}^2$ | $\Delta P_{c,TM,2} = 795\,\text{Pa}$ |
| | $\Delta P_{c,TM,3} = \dfrac{1}{2}K_{L,TM}\rho_{c,in,3}V_{c,TM,3}^2$ | $\Delta P_{c,TM,3} = 421\,\text{Pa}$ |
| | $\Delta P_{c,TM,4} = \dfrac{1}{2}K_{L,TM}\rho_{c,in,4}V_{c,TM,4}^2$ | $\Delta P_{c,TM,4} = 173\,\text{Pa}$ |

| Control Valve Sizing | | |
|---|---|---|
| $C_{v,1} = 3.04 \times 10^{-9} \text{ m}^3 \text{ s}^{-1} \text{ Pa}^{-0.5}$ | $\dot{V}_{c,1} = \dot{m}_{c,1} / \rho_{c,in,1}$ | $\dot{V}_{c,1} = 8.24 \times 10^{-7} \text{ m}^3 \text{ s}^{-1}$ |
| $\Delta P_{c,HX,1} = 2.87 \text{ Pa}$ | $\dot{V}_{c,2} = \dot{m}_{c,2} / \rho_{c,in,2}$ | $\dot{V}_{c,2} = 5.41 \times 10^{-7} \text{ m}^3 \text{ s}^{-1}$ |
| $\Delta P_{c,HX,2} = 1.55 \text{ Pa}$ | $\dot{V}_{c,3} = \dot{m}_{c,3} / \rho_{c,in,3}$ | $\dot{V}_{c,3} = 3.92 \times 10^{-7} \text{ m}^3 \text{ s}^{-1}$ |
| $\Delta P_{c,HX,3} = 0.99 \text{ Pa}$ | $\dot{V}_{c,4} = \dot{m}_{c,4} / \rho_{c,in,4}$ | $\dot{V}_{c,4} = 2.53 \times 10^{-7} \text{ m}^3 \text{ s}^{-1}$ |
| $\Delta P_{c,HX,4} = 0.56 \text{ Pa}$ | $\Delta P_{c,v,1} = \dfrac{\dot{V}_{c,1}^{\,2} \gamma}{C_{v,1}^{\,2}}$ | $\Delta P_{c,v,1} = 69000 \text{ Pa}$ |
| $\Delta P_{c,TM,1} = 1838 \text{ Pa}$ | | |
| $\Delta P_{c,TM,2} = 794 \text{ Pa}$ | $\Delta P_{c,7 \to 16} = \Delta P_{c,v,1} + \Delta P_{c,TM,1} + \Delta P_{c,HX,1}$ | $\Delta P_{c,7 \to 16} = 70800 \text{ Pa}$ |
| $\Delta P_{c,TM,3} = 417 \text{ Pa}$ | $C_{v,2} = \sqrt{\dfrac{\dot{V}_{c,2}^2 \gamma}{\Delta P_{c,7 \to 16} - \Delta P_{c,TM,2} - \Delta P_{c,HX,2}}}$ | $C_{v,2} = 1.98 \times 10^{-9} \text{ m}^3 \text{ s}^{-1} \text{ Pa}^{-0.5}$ |
| $\Delta P_{c,TM,4} = 173 \text{ Pa}$ | | |
| $\gamma = 0.94$ | $C_{v,3} = \sqrt{\dfrac{\dot{V}_{c,3}^2 \gamma}{\Delta P_{c,7 \to 16} - \Delta P_{c,TM,3} - \Delta P_{c,HX,3}}}$ | $C_{v,3} = 1.43 \times 10^{-9} \text{ m}^3 \text{ s}^{-1} \text{ Pa}^{-0.5}$ |
| | $C_{v,4} = \sqrt{\dfrac{\dot{V}_{c,4}^2 \gamma}{\Delta P_{c,7 \to 16} - \Delta P_{c,TM,4} - \Delta P_{c,HX,4}}}$ | $C_{v,4} = 9.21 \times 10^{-10} \text{ m}^3 \text{ s}^{-1} \text{ Pa}^{-0.5}$ |

| **Pump Power** | | |
|---|---|---|
| $\Delta P_{c,coriolis} = 176\,\text{Pa}$ | $\Delta P_{c,tot} = \Delta P_{c,coriolis} + \Delta P_{c,7\rightarrow16}$ | $\Delta P_{c,tot} = 70976\,\text{Pa}$ |
| $\Delta P_{c,7\rightarrow16} = 70800\,\text{Pa}$ | $\dot{m}_{c,tot} = \dot{m}_{c,1} + \dot{m}_{c,2} + \dot{m}_{c,3} + \dot{m}_{c,4}$ | $\dot{m}_{c,tot} = 0.0019\,\text{kg s}^{-1}$ |
| $\dot{m}_{c,1} = 7.7 \times 10^{-4}\,\text{kg s}^{-1}$ | $\dot{V}_{c,pump} = \dot{m}_{c,tot} / \rho_{c,pump}$ | $\dot{V}_{c,pump} = 1.8 \times 10^{-6}\,\text{m}^3\,\text{s}^{-1}$ |
| $\dot{m}_{c,2} = 5.1 \times 10^{-4}\,\text{kg s}^{-1}$ | $\dot{W}_{pump} = \dot{V}_{c,pump} \Delta P_{c,total}$ | $\dot{W}_{pump} = 0.13\,\text{W}$ |
| $\dot{m}_{c,3} = 3.7 \times 10^{-4}\,\text{kg s}^{-1}$ | $\dot{W}_{pump,elec} = \dfrac{\dot{W}_{pump}}{\eta_{pump}\eta_{elec}}$ | $\dot{W}_{pump,elec} = 0.23\,\text{W}$ |
| $\dot{m}_{c,4} = 2.7 \times 10^{-4}\,\text{kg s}^{-1}$ | | |
| $\rho_{c,pump} = 1026\,\text{kg m}^{-3}$ | | |
| $\eta_{pump} = 0.9$ | | |
| $\eta_{elec} = 0.6$ | | |

| **Exhaust Pressure Drop** | | |
|---|---|---|
| $l_{annulus} = 0.254\,\mathrm{m}$ <br> $D_{IT,I} = 0.0109\,\mathrm{m}$ | $V_{ex,1} = \dfrac{4\dot{m}_{ex,pt}}{\rho_{ex,1}\pi D_{IT,i}^2}$ | $V_{ex,1} = 38.6\,\mathrm{m\ s^{-1}}$ |
| $\rho_{ex,1} = 0.59\,\mathrm{kg\ m^3}$ <br> $f_{ex,1} = 0.035$ | $\Delta P_{ex,HX,maj,1} = f_{ex,1}\dfrac{l_{annulus}}{D_{IT,I}}\dfrac{\rho_{ex,1}V_{ex,1}^{\ 2}}{2}$ | $\Delta P_{ex,HX,maj,1} = 360\,\mathrm{Pa}$ |
| $K_{L,tee} = 0.9$ | $\Delta P_{ex,HX,\min,1} = \dfrac{1}{2}n_{tee}K_{L,tee}\rho_{ex,1}V_{ex,1}^2$ | $\Delta P_{ex,HX,\min,1} = 790\,\mathrm{Pa}$ |
| $n_{tee} = 2$ <br> Munson *et al.* (1990) | $\Delta P_{ex,HX,1} = \Delta P_{ex,HX,maj,1} + \Delta P_{ex,HX,\min,1}$ | $\Delta P_{ex,HX,1} = 1150\,\mathrm{Pa}$ |
| $\rho_{ex,outlet} = 0.735\,\mathrm{kg\ m^{-3}}$ <br> $\mu_{ex,outlet} = 2.65\times10^{-5}\,\mathrm{kg}$ <br> $\mathrm{m^{-1}\ s^{-1}}$ | $V_{ex,outlet} = \dfrac{4\dot{m}_{ex,pt}}{\rho_{ex,outlet}\pi D_{IT,I}^2}$ | $V_{ex,outlet} = 31.0\,\mathrm{m\ s^{-1}}$ |
| $\varepsilon = 1.5\times10^{-5}\,\mathrm{m}$ <br> $l_{outlet} = 1\,\mathrm{m}$ | $\mathrm{Re}_{ex,outlet} = \dfrac{4\dot{m}_{ex,pt}}{\pi D_{IT,I}\mu_{ex,outlet}}$ | $\mathrm{Re}_{ex,1} = 9395$ |
| $K_{L,elbow} = 1.5$ <br> $K_{L,exit} = 1$ <br> Munson *et al.* (1990) <br> $\Delta P_{ex,HX,1} = 1150\,\mathrm{Pa}$ | $f_{ex,outlet} = 8\left[\left(\dfrac{8}{\mathrm{Re}_{ex,outlet}}\right)^{12} + 1\Big/\left(\begin{array}{c}2.457\ln\left(\dfrac{1}{\left(7/\mathrm{Re}_{ex,outlet}\right)^{0.9}+\left(0.27\varepsilon/D_{IT,I}\right)}\right)^{16}\\ +\left(37530/\mathrm{Re}_{ex,outlet}\right)^{16}\end{array}\right)^{1.5}\right]^{1/12}$ | $f_{ex,6} = 0.0337$ |
| $\Delta P_{ex,HX,2} = 1050\,\mathrm{Pa}$ <br> $\Delta P_{ex,HX,3} = 980\,\mathrm{Pa}$ | $\Delta P_{ex,outlet,maj} = f_{ex,outlet}\dfrac{l_{outlet}}{D_{IT,I}}\dfrac{\rho_{ex,outlet}V_{ex,outlet}^{\ 2}}{2}$ | $\Delta P_{ex,outlet,maj} = 1090\,\mathrm{Pa}$ |
| $\Delta P_{ex,HX,4} = 930\,\mathrm{Pa}$ <br> $\Delta P_{ex,wm} = 673$ | $\Delta P_{ex,outlet,\min} = \dfrac{1}{2}(K_{L,elbow}+K_{L,exit})\rho_{ex,outlet}V_{ex,outlet}^2$ | $\Delta P_{ex,outlet,\min} = 880\,\mathrm{Pa}$ |
| | $\Delta P_{ex,outlet} = \Delta P_{ex,outlet,maj} + \Delta P_{ex,outlet,\min}$ | $\Delta P_{ex,outlet} = 1970\,\mathrm{Pa}$ |
| | $\Delta P_{ex,total} = \sum_{i=1}^{n}\Delta P_{ex,HX,i} + \Delta P_{ex,wm} + \Delta P_{ex,outlet}$ | $\Delta P_{ex,total} = 6760\,\mathrm{Pa}$ |

| **Heater and Chiller Sizing** | | |
|---|---|---|
| $\dot{m}_{19} = 0.00190\,\text{kg s}^{-1}$<br>$T_7 = 129.8\,^\circ\text{C}$<br>$T_{amb} = 20\,^\circ\text{C}$<br>$c_{p,c,avg} = 4184\ \text{J kg}^{-1}\,\text{K}^{-1}$ | $\dot{Q}_{heater} = \dot{m}_{19}c_{p,c,avg}\left(T_7 - T_{amb}\right)$ | $\dot{Q}_{heater} = 870\,\text{W}$ |
| $D_{IT,i,cwhx} = 0.00457\,\text{m}$<br>$\dot{m}_{17} = 1.90\,\text{g s}^{-1}$<br>$\mu_{c,cwhx} = 1.8\times10^{-4}\,\text{kg m}^{-1}\ \text{s}^{-1}$<br>$\text{Pr}_{c,cwhx} = 1.17$<br>$k_{c,cwhx} = 0.6658\,\text{Wm}^{-1}\text{K}^{-1}$<br>$\varepsilon = 1.5\times10^{-5}\,\text{m}$<br>$D_{IT,O,cwhx} = 0.00635\,\text{m}$<br>$D_{OT,I,cwhx} = 0.01092\,\text{m}$ | $\text{Re}_{c,cwhx} = \dfrac{4\dot{m}_{17}}{\pi D_{IT,I,cwhx}\mu_{c,cwhx}}$ | $\text{Re}_{c,cwhx} = 2990$ |
| | $f_{c,cwhx} = 8\left[\left(\dfrac{8}{\text{Re}_{c,cwhx}}\right)^{12} + 1\Big/\left(2.457\ln\left(\dfrac{1}{\left(7/\text{Re}_{c,cwhx}\right)^{0.9} + \left(0.27\varepsilon/D_{IT,I,cwhx}\right)}\right)^{16} + \left(37530/\text{Re}_{c,cwhx}\right)^{16}\right)^{1.5}\right]^{1/12}$ | $f_{c,cwhx} = 0.045$ |
| | $Nu_{c,cwhx}{}^{10} = 4.364^{10} + \left[\dfrac{e^{(2200-\text{Re}_{c,cwhx})/365}}{4.364^2} + 1\Big/\left(\dfrac{6.3 + 0.079(f_{c,cwhx}/8)^{1/2}\,\text{Re}_{c,cwhx}\,\text{Pr}_{c,cwhx}}{\left(1 + \text{Pr}_{c,cwhx}{}^{4/5}\right)^{5/6}}\right)^2\right]^{-5}$ | $Nu_{c,cwhx} = 10.37$ |
| | $h_{c,cwhx} = \dfrac{Nu_{c,cwhx}k_{c,cwhx}}{D_{IT,I,cwhx}}$ | $h_{c,cwhx} = 1510$<br>$\text{W m}^{-2}\,\text{K}^{-1}$ |
| | $r_{cwhx} = D_{IT,O,cwhx}/D_{OT,I,cwhx}$ | $r_{cwhx} = 0.59$ |
| | Nusselt Number for fully-developed laminar flow through a concentric annulus ( $0.50 \le r \le 1.00$ )<br>$Nu_{cw,cwhx} = \dfrac{4.86 - 5.74}{1.00 - 0.50}\left(r_{cwhx} - 0.50\right) + 5.74$ | $Nu_{cw,cwhx} = 5.59$ |

| | | |
|---|---|---|
| $k_{cw,cwhx} = 0.463\,\text{W m}^{-1}\,\text{K}^{-1}$ | $D_{h,cwhx} = D_{OT,I,cwhx} - D_{IT,O,cwhx}$ | $D_{h,cwhx} = 0.00457\,\text{m}$ |
| $T_{17} = 182.3\,^{\circ}\text{C}$ | $h_{cw,cwhx} = \dfrac{Nu_{cw,cwhx} k_{cw,cwhx}}{D_{h,cwhx}}$ | $h_{cw,cwhx} = 566\,\text{W m}^{-2}\,\text{K}^{-1}$ |
| $T_{18} = 129.8\,^{\circ}\text{C}$ | | |
| $c_{p,c,avg} = 4332\,\text{J kg}^{-1}\,\text{K}^{-1}$ | $\dot{Q}_{cwhx} = \dot{m}_{17} c_{p,c,avg} (T_{17} - T_{18})$ | $\dot{Q}_{cwhx} = 430\,\text{W}$ |
| $T_{21} = 12.8\,^{\circ}\text{C}$ | $T_{22} = \dfrac{\dot{Q}_{cwhx}}{\dot{m}_{20} c_{p,cw,avg}} + T_{21}$ | $T_{22} = 13.8\,^{\circ}\text{C}$ |
| $\dot{m}_{20} = 0.1\,\text{kg s}^{-1}$ | | |
| $c_{p,cw,avg} = 4115\,\text{J kg}^{-1}\,\text{K}^{-1}$ | $LMTD_{cwhx} = \dfrac{(T_{17} - T_{22}) - (T_{18} - T_{21})}{\ln\left((T_{17} - T_{22})/(T_{18} - T_{21})\right)}$ | $LMTD_{cwhx} = 141\,^{\circ}\text{C}$ |
| | $UA_{cwhx} = \dot{Q}_{cwhx}/LMTD_{cwhx}$ | $UA_{cwhx} = 3.05\,\text{W K}^{-1}$ |
| | $R_{cwhx} = 1/UA_{cwhx}$ | $R_{cwhx} = 0.33\,\text{K W}^{-1}$ |
| | $L_{cwhx} = \dfrac{1}{R_{cwhx}} \left( \dfrac{1}{h_{c,cwhx} \pi D_{IT,I,cwhx}} + \dfrac{\ln(D_{IT,O,cwhx}/D_{IT,I,cwhx})}{2\pi k_{tube}} + \dfrac{1}{h_{cw,cwhx} \pi D_{IT,O,cwhx}} \right)$ | $L_{cwhx} = 0.42\,\text{m}$ |

# APPENDIX E.    SINGLE-TUBE EXPERIMENTS SAMPLE CALCULATIONS

| Input | Equations | Results |
|---|---|---|
| **Exhaust Composition** | | |
| $a = 1$ <br> $b = 1.8$ <br> $\tilde{y}_{O_2,dry} = 0.0670 \pm 0.0025$ <br> $\tilde{y}_{CO_2,dry} = 0.1020 \pm 0.0020$ <br> $\tilde{y}_{CO,dry} = 0.0006 \pm 0.0005$ | $n_{O_2} = a + b/4$ | $n_{O_2} = 1.45$ |
| | $\tilde{y}_{O_2} = \tilde{y}_{O_2,dry} \left( 1 - \tilde{y}_{H_2O} \right)$ | $\tilde{y}_{O_2} = 0.061$ |
| | $\tilde{y}_{CO_2} = \tilde{y}_{CO_2,dry} \left( 1 - \tilde{y}_{H_2O} \right)$ | $\tilde{y}_{CO_2} = 0.093$ |
| | $\tilde{y}_{CO} = \tilde{y}_{CO,dry} \left( 1 - \tilde{y}_{H_2O} \right)$ | $\tilde{y}_{CO} = 0.0005$ |
| | $a = n_{prod} \left( a\tilde{y}_{C_aH_b} + \tilde{y}_{CO} + \tilde{y}_{CO_2} \right)$ | $\tilde{y}_{C_aH_b} = 0.016$ |
| | $b = n_{prod} \left( b\tilde{y}_{C_aH_b} + 2\tilde{y}_{H_2O} \right)$ | $\tilde{y}_{H_2O} = 0.085$ |
| | $2n_{O_2}/\varphi = n_{prod} \left( \tilde{y}_{CO} + 2\tilde{y}_{CO_2} + \tilde{y}_{H_2O} \right)$ | $n_{prod} = 9.1$ |
| | $7.546 n_{O_2}/\varphi = n_{prod} \left( 2\tilde{y}_{N_2} \right)$ | $\varphi = 0.808$ |
| | $\tilde{y}_{N_2} + \tilde{y}_{H_2O} + \tilde{y}_{CO_2} + \tilde{y}_{CO} + \tilde{y}_{O_2} + \tilde{y}_{C_aH_b} = 1$ | $\tilde{y}_{N_2} = 0.744$ |
| $M_{CO_2} = 44.01$ kg kmol$^{-1}$ <br> $M_{H_2O} = 18.02$ kg kmol$^{-1}$ <br> $M_{O_2} = 32$ kg kmol$^{-1}$ <br> $M_{N_2} = 28.01$ kg kmol$^{-1}$ <br> $M_{CO} = 28.01$ kg kmol$^{-1}$ <br> $M_{C_aH_b} = 13.82$ kg kmol$^{-1}$ | $M_{tot} = n_{prod} \left( \tilde{y}_{CO_2}M_{CO_2} + \tilde{y}_{H_2O}M_{H_2O} + \tilde{y}_{O_2}M_{O_2} + \tilde{y}_{N_2}M_{N_2} + \tilde{y}_{Co}M_{CO} + \tilde{y}_{C_aH_b}M_{C_aH_b} \right)$ | $M_{tot} = 28.7$ kg kmol$^{-1}$ |
| | $y_{CO_2} = \tilde{y}_{CO_2}M_{CO_2} / M_{tot}$ | $y_{CO_2} = 0.143$ |
| | $y_{H_2O} = \tilde{y}_{H_2O}M_{H_2O} / M_{tot}$ | $y_{H_2O} = 0.053$ |
| | $y_{O_2} = \tilde{y}_{O_2}M_{O_2} / M_{tot}$ | $y_{O_2} = 0.068$ |
| | $y_{N_2} = \tilde{y}_{N_2}M_{N_2} / M_{tot}$ | $y_{N_2} = 0.73$ |
| | $y_{CO} = \tilde{y}_{CO}M_{CO} / M_{tot}$ | $y_{CO} = 0.0005$ |
| | $y_{C_aH_b} = \tilde{y}_{C_aH_b}M_{C_aH_b} / M_{tot}$ | $y_{C_aH_b} = 0.0077$ |

| Inputs | Equations | Results |
|---|---|---|
| **Exhaust Flow Rate** | | |
| $T_{ex,wm} = 199.4 \pm 1.1\ ^{\circ}\text{C}$ | $P_{CO_2} = \tilde{y}_{CO_2} P_{ex}$ | $P_{CO_2} = 9{,}717\ \text{Pa}$ |
| $P_{ex} = 104{,}067 \pm 68\ \text{Pa}$ | $P_{O_2} = \tilde{y}_{O_2} P_{ex}$ | $P_{O_2} = 6{,}383\ \text{Pa}$ |
| $\rho_{CO_2,wm} = 0.1088\ \text{kg m}^{-3}$ | $P_{N_2} = \tilde{y}_{N_2} P_{ex}$ | $P_{N_2} = 77{,}451\ \text{Pa}$ |
| $\rho_{O_2,wm} = 0.0520\ \text{kg m}^{-3}$ | $P_{CO} = \tilde{y}_{CO} P_{ex}$ | $P_{CO} = 57\ \text{Pa}$ |
| $\rho_{H_2O,wm} = 0.0404\ \text{kg m}^{-3}$ | $P_{C_aH_b} = \tilde{y}_{C_aH_b} P_{ex}$ | $P_{C_aH_b} = 1661\ \text{Pa}$ |
| $\rho_{N_2,wm} = 0.552\ \text{kg m}^{-3}$ | $P_{H_2O} = \tilde{y}_{H_2O} P_{ex}$ | $P_{H_2O} = 8{,}797\ \text{Pa}$ |
| $\rho_{CO,wm} = 0.0004\ \text{kg m}^{-3}$ | $\rho_{ex,wm} = \rho_{CO_2,wm} + \rho_{O_2,wm} + \rho_{H_2O,wm} + \rho_{N_2,wm} + \rho_{CO,wm} + \rho_{C_aH_b,wm}$ | $\rho_{ex,wm} = 0.7599\ \text{kg m}^{-3}$ |
| $\rho_{C_aH_b,wm} = 0.0061\ \text{kg m}^{-3}$ | | |
| $K_p = (1.16 \pm 0.02) \times 10^{-3}$ | $\dot{m}_{ex} = K_p D_{wm}^2 Fa Y \sqrt{\rho_{ex,wm} \Delta P_{wm}}$ | $\dot{m}_{ex} = 0.002058\ \text{kg s}^{-1}$ |
| $D_{wm} = 0.158\ \text{m}$ | | |
| $Fa = 1.012$ | | |
| $Y = 1$ | | |
| $\Delta P_{wm} = 6719 \pm 31\ \text{Pa}$ | | |
| **Exhaust Measured Heat Transfer Rate** | | |
| $T_{ex,1} = 428.5\ ^{\circ}\text{C}$ | $T_{ex,avg,1} = (T_{ex,1} + T_{ex,2})/2$ | $T_{ex,avg,1} = 401.8\ ^{\circ}\text{C}$ |
| $T_{ex,2} = 375.1\ ^{\circ}\text{C}$ | $c_{p,ex,1} = y_{CO_2} c_{p,CO_2,1} + y_{H_2O} c_{p,H_2O,1} + y_{O_2} c_{p,O_2,1} + y_{N_2} c_{p,N_2,1}$ | $c_{p,ex,1} = 1139\ \text{J kg}^{-1}\ \text{K}^{-1}$ |
| $c_{p,CO_2,1} = 1115\ \text{J kg}^{-1}\ \text{K}^{-1}$ | $+ y_{CO} c_{p,CO,1} + y_{C_aH_b} c_{p,C_aH_b,1}$ | |
| $c_{p,H_2O,1} = 2065\ \text{J kg}^{-1}\ \text{K}^{-1}$ | | |
| $c_{p,O_2,1} = 1024\ \text{J kg}^{-1}\ \text{K}^{-1}$ | | |
| $c_{p,N_2,1} = 1088\ \text{J kg}^{-1}\ \text{K}^{-1}$ | $\dot{Q}_{ex,meas,1} = c_{p,ex,1} \dot{m}_{ex} (T_{ex,1} - T_{ex,2})$ | $\dot{Q}_{ex,meas,1} = 125.3 \pm 4.0\ \text{W}$ |
| $c_{p,CO,1} = 1108\ \text{J kg}^{-1}\ \text{K}^{-1}$ | | |
| $c_{p,C_aH_b,1} = 518\ \text{J kg}^{-1}\ \text{K}^{-1}$ | | |
| $\dot{m}_{ex} = 0.002058$ | | |

| Inputs | Equations | Results |
|---|---|---|
| **Exhaust Inlet Losses** | | |
| $T_{ex,1} = 428.5\ ^{\circ}\text{C}$ | $T_{ex,in,avg,1} = \left(T_{ex,1} + T_{ex,in,1}\right)/2$ | $T_{ex,in,avg,1} = 427.5\ ^{\circ}\text{C}$ |
| $T_{ex,in,1} = 426.5\ ^{\circ}\text{C}^{*}$<br><br>$\dot{m}_{ex} = 0.002058\ \text{kg s}^{-1}$ | $\text{Re}_{ex,in,1} = \dfrac{4\dot{m}_{ex}}{\pi D_{IT,I}\mu_{ex,in,1}}$ | $\text{Re}_{ex,in,1} = 7170$ |
| $\mu_{ex,in,1} = 3.346\times10^{-5}\ \text{kg}$ $\text{m}^{-1}\text{s}^{-1}$<br><br>$k_{ex,in,1} = 0.0517\ \text{W m}^{-1}\text{K}^{-1}$<br><br>$\rho_{ex,in,1} = 0.5175\ \text{kg m}^{-3}$<br><br>$\text{Pr}_{ex,in,1} = 0.6954$<br><br>$D_{IT,I} = 0.0109\ \text{m}$<br><br>$\varepsilon = 1.5\times10^{-5}\ \text{m}$<br><br>$L_{ex,in} = 0.097\ \text{m}$<br><br>$^{*}$Determined through iteration | Friction factor for fully-developed flow through smooth tubes (Churchill, 1977b)<br><br>$f_{ex,in,1} = 8\left[\left(\dfrac{8}{\text{Re}_{ex,in,1}}\right)^{12} + 1\Big/\left(\left(2.457\ln\left(\dfrac{1}{\left(7/\text{Re}_{ex,in,1}\right)^{0.9} + \left(0.27\varepsilon/D_{IT,I}\right)}\right)\right)^{16} + \left(37530/\text{Re}_{ex,in,1}\right)^{16}\right)^{1.5}\right]^{1/12}$ | $f_{ex,in,1} = 0.0360$ |
| | Nusselt number for fully-developed flow through smooth tubes (Churchill, 1977a)<br><br>$Nu_{ex,in,1}^{10} = 4.364^{10} + \left[\dfrac{e^{(2200-\text{Re}_{ex,in,1})/365}}{4.364^{2}} + 1\Big/\left(\dfrac{6.3 + \dfrac{0.079(f_{ex,in,1}/8)^{1/2}\text{Re}_{ex,in,1}\text{Pr}_{ex,in,1}}{\left(1+\text{Pr}_{ex,in1}^{4/5}\right)^{5/6}}}{}\right)\right]^{-5}$ | $Nu_{ex,in,1} = 22.9$ |
| | $h_{ex,in,1} = Nu_{ex,in,1}k_{ex,in,1}\big/D_{IT,i}$ | $h_{ex,in,i} = 108\ \text{W m}^{-2}\text{K}^{-1}$ |
| | $R_{ex,in,1} = \dfrac{1}{h_{ex,in,1}\pi D_{IT,1}L_{ex,in}}$ | $R_{ex,in,1} = 2.77\ \text{K W}^{-1}$ |

| | | |
|---|---|---|
| $k_{tube,ex,1} = 19.89 \ \text{W m}^{-1} \text{K}^{-1}$ <br> $k_{ins,ex,1} = 0.0530 \ \text{W m}^{-1} \text{K}^{-1}$ | $R_{tube,ex,in,1} = \dfrac{\ln\left(D_{IT,O}/D_{IT,I}\right)}{2\pi k_{tube,ex,1} L_{ex,in}}$ | $R_{tube,ex,in,1} = 0.012 \ \text{K W}^{-1}$ |
| $D_{IT,O} = 0.0127 \ \text{m}$ <br> $D_{ins,O} = 0.172 \ \text{m}$ | $R_{ins,ex,in,1} = \dfrac{\ln\left(D_{ins,O}/D_{IT,O}\right)}{2\pi k_{ins,ex,1} L_{ex,in,1}}$ | $R_{ins,ex,in,1} = 80.60 \ \text{K W}^{-1}$ |
| $T_{amb} = 18.07 \pm 0.25 \ \text{°C}$ <br> $T_{ins,ex,in,i} = 46.8 \ \text{°C}^{*}$ | $Ra_{air,ex,in,1} = \dfrac{g\beta_{air}\left(T_{ins,ex,in,1}-T_{amb}\right)D_{ins,O}^3}{\upsilon_{air}\alpha_{air}}$ | $Ra_{air,ex,in,1} = 1.034 \times 10^7$ |
| $P_{amb} = 101,325 \ \text{Pa}$ <br> $g = 9.81 \ \text{m s}^{-2}$ <br> $\beta_{air} = 0.003346 \ \text{K}^{-1}$ <br> $\upsilon_{air} = 1.568 \times 10^{-5} \ \text{m}^2 \text{ s}^{-1}$ <br> $\alpha_{air} = 2.154 \times 10^{-5} \ \text{m}^2 \text{ s}^{-1}$ <br> $\text{Pr}_{air} = 0.7279$ <br> $k_{air} = 0.0256 \ \text{W m}^{-1} \text{K}^{-1}$ | Free convection over a horizontal cylinder (Churchill and Chu, 1975) <br><br> $Nu_{air,ex,in,1} = \left[0.60 + \dfrac{0.387 Ra_{air}^{1/6}}{\left(1+\left(\dfrac{0.559}{\text{Pr}_{air}}\right)^{9/16}\right)^{8/27}}\right]^2$ | $Nu_{air,ex,in,1} = 28.64$ |
| $\varepsilon_{ins} = 0.85$ | $h_{air,ex,in,1} = \dfrac{Nu_{air,ex,in,1}k_{air}}{D_{ins,O}}$ | $h_{air,ex,in,1} = 4.269 \ \text{W m}^{-2} \text{K}^{-1}$ |
| $\sigma_{SB} = 5.67 \times 10^{-8} \ \text{W m}^{-2} \text{K}^{-4}$ <br> $T_{amb} = 298.7 \pm 0.25 \ \text{K}$ | $R_{amb,conv,in,1} = \dfrac{1}{h_{air,in,1}\pi D_{ins,O}L_{ex,in,1}}$ | $R_{amb,conv,in,1} = 4.482 \ \text{K W}^{-1}$ |
| $T_{ins,ex,in,i} = 319.8 \ \text{K}$ <br><br> $^{*}$ Determined through iteration | $R_{amb,rad,in,1} = \dfrac{1}{e_{ins}\pi D_{ins,O}L_{ex}\sigma_{SB}\left(T_{ins,ex,1}^2 + T_{amb}^2\right)\left(T_{ins,ex,1}+T_{amb}\right)}$ | $R_{amb,rad,in,i} = 3.35 \ \text{K W}^{-1}$ |
| | $R_{amb,ex,in,1} = \left(R_{amb,conv,in,1}\times R_{amb,rad,in,1}\right)/\left(R_{amb,conv,in,1}+R_{amb,rad,in,1}\right)$ | $R_{amb,ex,i} = 1.92 \ \text{K W}^{-1}$ |
| | $R_{tot,ex,in,1} = R_{ex,in,1} + R_{tube,ex,in,1} + R_{ins,ex,in,1} + R_{amb,ex,in,1}$ | $R_{tot,ex,in,1} = 85.5 \ \text{K W}^{-1}$ |
| | $\dot{Q}_{ex,loss,in,1} = \left(T_{ex,in,avg,1}-T_{amb}\right)/R_{tot,ex,in,1}$ | $\dot{Q}_{ex,loss,in,1} = 4.710 \pm 0.116 \ \text{W}$ |
| | $T_{ex,in,1} = T_{ex,1} - \dot{Q}_{ex,loss,in,1}/\dot{m}_{ex}c_{p,ex,in,1}$ | $T_{ex,in,1} = 426.5 \ \text{°C}$ |
| | $T_{ins,ex,in,1} = T_{air} + \dot{Q}_{ex,loss,in,1}R_{amb,ex,in,1}$ | $T_{ins,ex,in,1} = 46.8 \ \text{°C}$ |

| Inputs | Equations | Results |
|---|---|---|
| **Exhaust Heat Transfer Rate** | | |
| $\dot{Q}_{ex,meas,1} = 125.3 \pm 4.0\,\text{W}$ $\dot{Q}_{ex,loss,in,1} = 4.710 \pm 0.141\,\text{W}$ $\dot{Q}_{ex,loss,out,1} = 3.816 \pm 0.117\,\text{W}$ | $\dot{Q}_{ex,1} = \dot{Q}_{ex,meas,1} - \dot{Q}_{ex,loss,in,1} - \dot{Q}_{ex,loss,out,1}$ | $\dot{Q}_{ex,1} = 116.60 \pm 3.99\,\text{W}$ |
| **Exhaust Heat Transfer Rate Uncertainty** | | |
| $\dfrac{\partial \dot{Q}_{ex,1}}{\partial \dot{Q}_{ex,meas,1}} = 1$ $U_{\dot{Q}_{ex,meas,1}} = 3.981\,\text{W}$ $\dfrac{\partial \dot{Q}_{ex,1}}{\partial \dot{Q}_{ex,loss,in,1}} = 1$ $U_{\dot{Q}_{ex,loss,in,1}} = 0.141\,\text{W}$ $\dfrac{\partial \dot{Q}_{ex,1}}{\partial \dot{Q}_{ex,loss,out,1}} = 1$ $U_{\dot{Q}_{ex,loss,out,1}} = 0.117\,\text{W}$ | $U^2_{\dot{Q}_{ex,1}} = \left( \dfrac{\partial \dot{Q}_{ex,1}}{\partial \dot{Q}_{ex,meas,1}} U_{\dot{Q}_{ex,meas,1}} \right)^2 + \left( \dfrac{\partial \dot{Q}_{ex,1}}{\partial \dot{Q}_{ex,loss,in,1}} U_{\dot{Q}_{ex,loss,in,1}} \right)^2$ $+ \left( \dfrac{\partial \dot{Q}_{ex,1}}{\partial \dot{Q}_{ex,loss,out,1}} U_{\dot{Q}_{ex,loss,out,1}} \right)^2$ | $U_{\dot{Q}_{ex,meas,1}} = 3.985\,\text{W}$ |

| Inputs | Equations | Results |
|---|---|---|
| **Exhaust Thermocouple Radiation** | | |
| $r_{tc} = 0.003176\,\text{m}$ | $r = r_{tc}/r_{IT,I}$ | $r = 0.31$ |
| $r_{tc} = 0.001588\,\text{m}$ | $h = h_{tc,disc}/r_{IT,I}$ | $h = 2.59$ |
| $r_{IT,I} = 0.0055\,\text{m}$ | $F_{tc,tube} = 2r^2\left(1 - \dfrac{1}{\sqrt{1+1/h^2}}\right)$ | $F_{tc,tube} = 0.0336$ |
| $h_{tc,disc} = 0.0132\,\text{m}$ | | |
| $\dot{Q}_{ex,loss,in,1} = 4.170\,\text{W}$ | $F_{tc,cross,1} = 1 - F_{tc,tube}$ | $F_{tc,cross,1} = 0.9664$ |
| $R_{ex,in,1} = 2.77\,\text{K W}^{-1}$ | $T_{cross,1} = T_{ex,1} - \dot{Q}_{ex,loss,in,1}/R_{ex,loss,in,1}$ | $T_{cross,1} = 415.5\ ^{\circ}\text{C}$ |
| $T_{c,avg,1} = 154.9\ ^{\circ}\text{C}$ | $T_{IT,I,1} = T_{c,avg,1} + \dot{Q}_{c,1}/\left(R_{c,i,1} + R_{tube,1}\right)$ | $T_{IT,i,1} = 282.0\ ^{\circ}\text{C}$ |
| $\dot{Q}_{c,1} = 112.0\,\text{W}$ | $\dot{Q}_{tc,rad,1} = F_{tc,cross}\varepsilon_{tc}\sigma_{SB}\left(4\pi r_{tc}^2\right)\left(T_{tc,1}^4 - T_{cross,1}^4\right)$ | $\dot{Q}_{tc,rad,1} = 0.032\,\text{W}$ |
| $R_{c,i,1} = 0.091\,\text{K W}^{-1}$ | $+F_{tc,tube}\varepsilon_{tc}\sigma_{SB}\left(4\pi r_{tc}^2\right)\left(T_{tc,1}^4 - T_{IT,I,1}^4\right)$ | |
| $R_{tube,1} = 0.005\,\text{K W}^{-1}$ | $\dot{Q}_{tc,conv,1} = \dot{Q}_{tc,rad,1}$ | $\dot{Q}_{tc,conv,1} = 0.032\,\text{W}$ |
| $\varepsilon_{tc} = 0.96$ | $\text{Re}_{tc,ex,1} = \dfrac{4\dot{m}_{ex}}{\pi D_{tc}\mu_{ex,tc,1}}$ | $\text{Re}_{tc,ex,1} = 2082$ |
| $\sigma_{SB} = 5.67\times10^{-8}\,\text{W m}^{-2}\,\text{K}^{-4}$ | | |
| $T_{tc,1} = 699.4 \pm 1.1\,\text{K}$ | $Nu_{tc,1} = 2 + \left(0.4\,\text{Re}_{tc,ex,1}^{1/2} + 0.06\,\text{Re}_{tc,ex,1}^{2/3}\right)\text{Pr}_{ex,1}^{\,0.4}\left(\dfrac{\mu_{ex,1}}{\mu_{s,tc,1}}\right)^{1/4}$ | $Nu_{tc,i} = 26.25$ |
| $T_{cross,1} = 688.6\,\text{K}$ | | |
| $T_{IT,i,1} = 555.2\,\text{K}$ | | |
| $\dot{m}_{ex} = 0.002058\,\text{kg s}^{-1}$ | $h_{tc,1} = Nu_{tc,1}k_{ex,tc,1}/D_{tc}$ | $h_{tc,1} = 428\,\text{W m}^{-2}\,\text{K}^{-1}$ |
| $\mu_{ex,tc,1} = 3.349\times10^{-5}\,\text{kg m}^{-1}\,\text{s}^{-1}$ | $T_{ex,i} = \dfrac{\dot{Q}_{tc,conv,i}}{h_{tc,i}\left(4\pi r_{tc}^2\right)} + T_{tc,i}$ | $T_{ex,1} = 428.5\ ^{\circ}\text{C}$ |
| $k_{ex,tc,1} = 0.05178\,\text{W m}^{-1}\,\text{K}^{-1}$ | | |
| $\text{Pr}_{ex,tc,1} = 0.6954$ | | |
| $\mu_{s,tc,i} = 3.342\times10^{-5}\,\text{kg m}^{-1}\,\text{s}^{-1}$ | | |

| Inputs | Equations | Results |
|---|---|---|
| **Coolant Measured Heat Transfer Rate** | | |
| $T_{c,in,1} = 127.60 \pm 0.25\,^{\circ}\text{C}$ | $T_{c,avg,1} = \left(T_{c,in,1} + T_{c,out,1}\right)/2$ | $T_{c,avg,1} = 154.9\,^{\circ}\text{C}$ |
| $T_{c,out,1} = 182.3 \pm 0.25\,^{\circ}\text{C}$ | $K_{factor,1} = 128{,}000\ln\left(\dot{V}_{c,GPM,meas,1}\right) + 1{,}298{,}000$ | $K_{factor,1} = 7.00 \times 10^5$ |
| $P_c = \left(1.852 \pm 0.013\right) \times 10^6\,\text{Pa}$ | | |
| $k_{c,1} = 0.6683\,\text{W m}^{-1}\,\text{K}^{-1}$ | $\omega_{HZ,1} = \dfrac{K_{factor,1}\dot{V}_{c,GPM,1}}{timebase}$ | $\omega_{HZ,1} = 109\,\text{Hz}$ |
| $\mu_{c,1} = 2.178 \times 10^{-4}\,\text{kg m}^{-1}\,\text{s}^{-1}$ | | |
| $\rho_{c,in,1} = 937.8\,\text{kg m}^{-3}$ | $\omega_1 = 2\pi\omega_{HZ,1}$ | $\omega_1 = 685.1\,\text{rad s}^{-1}$ |
| $\nu_{c,1} = 2.323 \times 10^{-7}\,\text{m}^2\,\text{s}^{-1}$ | $D_{TM,1} = D_{TM,o}\left(1 + \alpha_M\left(T_{c,in,1} - T_o\right)\right)^{1/3}$ | $D_{TM,1} = 0.01272\,\text{m}$ |
| $c_{p,c,1} = 4320\,\text{J kg}^{-1}\,\text{K}^{-1}$ | $Ro_1 = \dfrac{f_1 D_{TM}^2}{\nu_{c,1}}$ | $Ro_1 = 6075$ |
| $\dot{V}_{c,GPM,meas,1} = 0.00934 \pm 0.0002\,\text{GPM}$ | | |
| $timebase = 60\,\text{s min}^{-1}$ | $St_1 = 286\ln\left(Ro_1\right) - 220$ | $St_1 = 2274$ |
| $D_{TM,o} = 0.01270\,\text{m}$ | $V_{c,1} = \dfrac{\omega_1 D_{TM,1}}{St_1}$ | $V_{c,1} = 3.83 \times 10^{-3}\,\text{m s}^{-1}$ |
| $\alpha_M = 1.721 \times 10^{-5}\,\text{K}^{-1}$ | | |
| $T_o = 23.9\,^{\circ}\text{C}$ | $\dot{m}_{c,1} = \rho_{c,in,1}V_{c,1}\pi D_{TM,1}^2/4$ | $\dot{m}_{c,1} = 4.57 \times 10^{-4}\,\text{kg s}^{-1}$ |
| | $\dot{Q}_{c,meas,1} = \dot{m}_{c,1}c_{p,c,1}\left(T_{c,out,1} - T_{c,in,1}\right)$ | $\dot{Q}_{c,meas,1} = 108.20 \pm 0.79\,\text{W}$ |

| Inputs | Equations | Results |
|---|---|---|
| **Coolant Losses** | | |
| $T_{c,in,1} = 127.60 \pm 0.25\,^{\circ}\text{C}$ | $T_{c,avg,1} = \left( T_{c,in,1} + T_{c,out,1} \right)/2$ | $T_{c,avg,1} = 154.9\,^{\circ}\text{C}$ |
| $T_{c,out,1} = 182.3 \pm 0.25\,^{\circ}\text{C}$ | $D_h = D_{OT,I} - D_{IT,O}$ | $D_h = 0.00386\,\text{m}$ |
| $P_c = (1.852 \pm 0.013) \times 10^6\,\text{Pa}$ | $\text{Re}_{c,1} = \dfrac{4\dot{m}_{c,1}}{\pi D_h \mu_{c,1}}$ | $\text{Re}_{c,1} = 692$ |
| $k_{c,1} = 0.6683\,\text{W m}^{-1}\,\text{K}^{-1}$ | | |
| $\mu_{c,1} = 2.178 \times 10^{-4}\,\text{kg m}^{-1}\,\text{s}^{-1}$ | $q_I^{''} = \dfrac{\dot{Q}_{c,1}}{\pi D_{IT,O} L_{annulus}}$ | $q_I^{''} = 9849\,\text{W m}^{-2}$ |
| $\rho_{c,in,1} = 937.8\,\text{kg m}^{-3}$ | | |
| $\nu_{c,1} = 2.323 \times 10^{-7}\,\text{m}^2\,\text{s}$ | $q_O^{''} = \dfrac{\dot{Q}_{c,loss,1}}{\pi D_{OT,I} L_{annulus}}$ | $q_O^{''} = 257\,\text{W m}^{-2}$ |
| $c_{p,c,1} = 4320\,\text{J kg}^{-1}\,\text{K}^{-1}$ | | |
| $D_{IT,O} = 0.0127\,\text{m}$ | $Nu_{c,O,1} = \dfrac{Nu_\infty}{1 - \left( q_I^{''}/q_O^{''} \right)\theta_O^*}$ | $Nu_{c,O,1} = 0.432$ |
| $D_{OT,I} = 0.0166\,\text{m}$ | | |
| $L_{annulus} = 0.285\,\text{m}$ | $h_{c,O,1} = \dfrac{Nu_{c,O,1} k_{c,1}}{D_h}$ | $h_{c,O,1} = 74.78\,\text{W m}^{-2}\,\text{K}^{-1}$ |
| $\dot{m}_{c,1} = 4.57 \times 10^{-4}\,\text{kg s}^{-1}$ | | |
| $\dot{Q}_{c,i} = 112.00\,\text{W}$ | $R_{c,O,1} = \dfrac{1}{h_{c,O,1}\pi D_{OT,I} L_{annulus}}$ | $R_{c,O,1} = 0.901\,\text{K W}^{-1}$ |
| $\dot{Q}_{c,loss,i} = 3.83\,\text{W}^{\,*}$ | | |
| $Nu_\infty = 5.217$ | $R_{OT,c,1} = \dfrac{\ln\left( D_{OT,O}/D_{OT,O} \right)}{2\pi k_{tube,c,1} L_{annulus}}$ | $R_{OT,c,1} = 0.005\,\text{ K W}^{-1}$ |
| $\theta_o^* = 0.290$ | | |
| $k_{tube,c,1} = 15.61\,\text{W m}^{-1}\,\text{K}^{-1}$ | $R_{ins,c,1} = \dfrac{\ln\left( D_{ins,O}/D_{OT,O} \right)}{2\pi k_{c,1} L_{annulus}}$ | $R_{ins,c,1} = 32.02\,\text{ K W}^{-1}$ |
| $k_{ins,c,1} = 0.0383\,\text{W m}^{-1}\,\text{K}^{-1}$ | | |
| $^{*}$ Determined through iteration | | |

| | | |
|---|---|---|
| $T_{amb} = 25.7 \pm 0.25\,^{\circ}\mathrm{C}$ <br> $T_{ins,c,i} = 28.9\,^{\circ}\mathrm{C}^{*}$ <br> $P_{amb} = 101,325\,\mathrm{Pa}$ <br> $g = 9.81\,\mathrm{m\ s^{-2}}$ <br> $\beta_{air} = 0.003346\,\mathrm{K^{-1}}$ <br> $\upsilon_{air} = 1.568 \times 10^{-5}\,\mathrm{m^2\ s^{-1}}$ <br> $\alpha_{air} = 2.154 \times 10^{-5}\,\mathrm{m^2\ s^{-1}}$ <br> $k_{air} = 0.0256\,\mathrm{W\ m^{-1}\ K^{-1}}$ <br> $\varepsilon_{ins} = 0.85$ <br> $\sigma_{SB} = 5.67 \times 10^{-8}\,\mathrm{W\ m^{-2}\ K^{-4}}$ <br> $T_{amb} = 298.7 \pm 0.25\,\mathrm{K}$ <br> $T_{ins,c,i} = 302.1\,\mathrm{K}^{*}$ <br><br> $^{*}$Determined through iteration | $Ra_{air,c,1} = \dfrac{g\beta_{air}\left(T_{ins,c,1} - T_{amb}\right)D_{ins,O}^{3}}{\upsilon_{air}\alpha_{air}}$ | $Ra_{air,c,1} = 1.586 \times 10^{6}$ |
| | Correlation for natural convection about a horizontal cylinder <br><br> $Nu_{air,c,1} = \left[ 0.60 + \dfrac{0.387 Ra_{air}^{1/6}}{\left(1 + \left(\dfrac{0.559}{\mathrm{Pr}_{air}}\right)^{9/16}\right)^{8/27}} \right]^{2}$ | $Nu_{air,c,1} = 16.61$ |
| | $h_{air,c,1} = \dfrac{Nu_{air,c,1}k_{air}}{D_{ins,O}}$ | $h_{air,c,1} = 2.47\,\mathrm{W\ m^{-2}\ K^{-1}}$ |
| | $R_{amb,conv,c,1} = \dfrac{1}{h_{air,c,1}\pi D_{ins,O}L_{annulus}}$ | $R_{amb,conv,c,1} = 2.63\,\mathrm{K\ W^{-1}}$ |
| | $R_{amb,c,1} = \dfrac{1}{e_{ins}\pi D_{ins,O}L_{annulus}\sigma_{SB}\left(T_{ins,c,1}^{2} + T_{amb}^{2}\right)\left(T_{ins,c,1} + T_{amb}\right)}$ | $R_{amb,rad,c,1} = 1.248\,\mathrm{K\ W^{-1}}$ |
| | $R_{amb,c,1} = \dfrac{R_{amb,conv,c,1} \times R_{amb,rad,c,1}}{R_{amb,conv,c,1} + R_{amb,rad,c,1}}$ | $R_{amb,c,i} = 0.846\,\mathrm{K\ W^{-1}}$ |
| | $R_{tot,c,1} = R_{c,1} + R_{OT,1} + R_{ins,c,1} + R_{amb,c,1}$ | $R_{tot,c,1} = 33.77\,\mathrm{K\ W^{-1}}$ |
| | $\dot{Q}_{c,loss,1} = \left(T_{c,avg,1} - T_{amb}\right)/R_{tot,c,1}$ | $\dot{Q}_{c,loss,1} = 3.826 \pm 0.129\,\mathrm{W}$ |
| | $T_{ins,c,1} = T_{air} + \dot{Q}_{c,loss,1}R_{amb,conv,c,1}$ | $T_{ins,c,1} = 28.9\,^{\circ}\mathrm{C}$ |
| **Coolant Heat Transfer Rate** | | |
| $\dot{Q}_{c,loss,1} = 3.826 \pm 0.129\,\mathrm{W}$ <br> $\dot{Q}_{c,meas,i} = 108.20 \pm 0.79\,\mathrm{W}$ | $\dot{Q}_{c,1} = \dot{Q}_{c,meas,1} + \dot{Q}_{c,loss,1}$ | $\dot{Q}_{c,1} = 112.00 \pm 0.80\,\mathrm{W}$ |

| Inputs | Equations | Results |
|---|---|---|
| **Fouling Resistance Calculation** | | |
| $T_{ex,in,1} = 426.5\,^\circ\text{C}$ | $LMTD_1 = \dfrac{\left(T_{ex,in,1} - T_{c,out,1}\right) - \left(T_{ex,out,1} - T_{c,in,1}\right)}{\ln\left(\left(T_{ex,in,1} - T_{c,out,1}\right)/\left(T_{ex,out,1} - T_{c,in,1}\right)\right)}$ | $LMTD_1 = 246.7\,^\circ\text{C}$ |
| $T_{ex,out,1} = 376.8\,^\circ\text{C}$ | | |
| $T_{c,in,1} = 127.6 \pm 0.25\,^\circ\text{C}$ | $R_1 = LMTD_1 / \dot{Q}_{c,1}$ | $R_1 = 2.203\,\text{K W}^{-1}$ |
| $T_{c,out,1} = 182.3 \pm 0.25\,^\circ\text{C}$ | $R_{IT,1} = \dfrac{\ln\left(D_{IT,O}/D_{IT,I}\right)}{2\pi k_{tube,c,1} L_{annulus}}$ | $R_{IT,1} = 0.0054 \pm 0.0001\,\text{K W}^{-1}$ |
| $\dot{Q}_{c,1} = 112.00 \pm 0.80\,\text{W}$ | | |
| $D_{IT,I} = 0.0109\,\text{m}$ | | |
| $D_{IT,O} = 0.0127\,\text{m}$ | $Nu_{c,i,1} = \dfrac{Nu_{II}}{1 - \left(q_O''/q_I''\right)\theta_I^*}$ | $Nu_{c,i,i} = 5.575$ |
| $L_{annulus} = 0.285\,\text{m}$ | | |
| $k_{tube,c,1} = 15.61\,\text{W m}^{-1}\,\text{K}^{-1}$ | $h_{c,I,1} = \dfrac{Nu_{c,I,1} k_{c,1}}{D_h}$ | $h_{c,i,1} = 965\,\text{W m}^{-2}\,\text{K}^{-1}$ |
| $Nu_{II} = 5.635$ | | |
| $\theta_I^* = 0.413$ | $R_{c,I,1} = \dfrac{1}{h_{c,I,i}\pi D_{IT,O} L_{annulus}}$ | $R_{c,i,1} = 0.091 \pm 0.025\,\text{K W}^{-1}$ |
| $q_I'' = 9849\,\text{W m}^{-2}$ | | |
| $q_O'' = 257\,\text{W m}^{-2}$ | $\text{Re}_{ex,1} = \dfrac{4\dot{m}_{ex}}{\pi D_{IT,I}\mu_{ex,1}}$ | $\text{Re}_{ex,1} = 7345$ |
| $k_{c,1} = 0.6683\,\text{W m}^{-1}\,\text{K}^{-1}$ | | |
| $\dot{m}_{ex} = 0.002058\,\text{kg s}^{-1}$ | Correlation fit Nusselt number of clean tube with air $Nu_{ex,1} = 0.0045\,\text{Re}_{ex,1}^{0.995}\,\text{Pr}_{ex,1}^{0.3}$ | $Nu_{ex,1} = 28.34$ |
| $\mu_{ex,1} = 3.266\times10^{-5}\,\text{kg m}^{-1}\,\text{s}^{-1}$ | $h_{ex,1} = \dfrac{Nu_{ex,1} k_{ex,1}}{D_{IT,I}}$ | $h_{ex,1} = 130.4\,\text{W m}^{-2}\,\text{K}^{-1}$ |
| $\text{Pr}_{ex,1} = 0.6946$ | | |
| $D_{IT,i} = 0.0109\,\text{m}$ | $R_{ex,1} = \dfrac{1}{h_{ex,1}\pi D_{IT,I} L_{annulus}}$ | $R_{ex,1} = 0.784 \pm 0.081\,\text{K W}^{-1}$ |
| $k_{ex,1} = 0.0502\,\text{W m}^{-1}\,\text{K}^{-1}$ | | |
| | $R_{foul,1} = R_1 - R_{ex,1} - R_{IT,1} - R_{c,i,1}$ | $R_{foul,1} = 1.322 \pm 0.084$ |

| Inputs | Equations | Results |
|---|---|---|
| **Pressure Drop** | | |
| $T_{ex,in,1} = 426.5\,^{\circ}\mathrm{C}$ $T_{ex,out,1} = 376.8\,^{\circ}\mathrm{C}$ $\mathrm{Re}_{ex,1} = 7345$ $\rho_{ex,1} = 0.532\,\mathrm{kg\,m^{-3}}$ $\dot{m}_{ex} = 0.002058\,\mathrm{kg\,s^{-1}}$ $\varepsilon = 1.5\times10^{-5}\,\mathrm{m}$ $\Delta P_{ex,meas,1} = 1754 \pm 62\,\mathrm{Pa}$ | $T_{ex,avg,1} = \left(T_{ex,in,1} + T_{ex,out,1}\right)/2$ | $T_{ex,avg,1} = 401.8\,^{\circ}\mathrm{C}$ |
| | $\Delta P_{ex,\min,1} = 8 K_{L,cross}\,\dfrac{\dot{m}_{ex}^2}{\rho_{ex,1}\pi^2 D_{IT,I}^4}$ | $\Delta P_{ex,\min,1} = 408.2\,\mathrm{Pa}$ |
| | $\Delta P_{ex,maj,1} = 2\dfrac{f_1}{D_{foul,1}^5}\dfrac{8}{\pi^2}\dfrac{\dot{m}_{ex}^2 L_{ex}}{\rho_{ex,1}}$ | $\Delta P_{ex,maj,1} = 482.8\,\mathrm{Pa}$ |
| | $\Delta P_{ex,annulus,1} = \dfrac{f_1}{D_{foul,1}^5}\dfrac{8}{\pi^2}\dfrac{\dot{m}_{ex}^2 L_{ex,annulus}}{\rho_{ex,1}}$ | $\Delta P_{ex,annulus,1} = 862.6\,\mathrm{Pa}$ |
| | $\Delta P_{ex,meas,i} = \Delta P_{ex,\min,1} + \Delta P_{ex,maj,1} + \Delta P_{ex,annulus,1}$ | $\dfrac{f_1}{D_{foul,1}^5} = 4.69\times10^8\,\mathrm{m^{-5}}$ |
| | Friction factor correlation for fully developed flow in smooth tubes(Churchill, 1977b) $$f_{o,1} = 8\left[\left(\frac{8}{\mathrm{Re}_{ex,1}}\right)^{12} + 1\bigg/\left(2.457\ln\left(\frac{1}{\left(7/\mathrm{Re}_{ex,1}\right)^{0.9}+\left(0.27\varepsilon/D_{IT,I}\right)}\right)^{16} + \left(37530/\mathrm{Re}_{ex,1}\right)^{16}\right)^{1.5}\right]^{1/12}$$ | $f_{o,1} = 0.0358$ |
| | $\dfrac{\Delta P_{ex,annulus,i}}{\Delta P_{ex,annulus,o,i}} = \dfrac{f_i\big/D_{foul,i}^5}{f_{o,i}\big/D_{IT,I}^5}$ | $\dfrac{\Delta P_{ex,annulus,i}}{\Delta P_{ex,annulus,o,i}} = 2.01$ |

## Particulate Matter Deposition

| | | |
|---|---|---|
| $A_E = 3\,\text{m}^2\,\text{g}^{-1}$<br>$Opacity = 0.021 \pm 0.001$ | $C_{PM,Opac} = \dfrac{-\ln(1 - Opacity)}{A_E L}$ | $C_{PM,Opac} = 0.141\,\text{g m}^{-3}$ |
| $L = 0.05\,\text{m}$<br>$T_{amb} = 298.7\,\text{K}$ | $C_{PM.STP} = C_{PM,Opac}\,\dfrac{T_{amb}}{273.15\,K}$ | $C_{PM.STP} = 0.150\,\text{g m}^{-3}$ |
| $\rho_{ex,1} = 0.532\,\text{kg m}^{-3}$<br>$\dot{m}_{ex} = 0.002058\,\text{kg s}^{-1}$ | $C_{PM.in,1} = C_{PM,STP}\,\dfrac{273.15\,K}{T_{ex,in,1}}$ | $C_{PM.in,1} = 0.0585\,\text{g m}^{-3}$ |
| $\dot{Q}_{c,1} = 112.00 \pm 0.80\,\text{W}$<br>$R_{c,i,1} = 0.091 \pm 0.025\,\text{K W}^{-1}$ | $\dot{m}_{PM,in} = \dfrac{C_{PM}\,\dot{m}_{ex}}{\rho_{ex,in,1}}$ | $\dot{m}_{PM,in} = 2.26 \times 10^{-4}\,\text{g s}^{-1}$ |
| $R_{IT,1} = 0.0054 \pm 0.0001\,\text{K W}^{-1}$<br>$R_{foul,i} = 1.322 \pm 0.084\,\text{K W}^{-1}$ | $T_{foul,1} = \dfrac{\dot{Q}_{c,1}}{R_{c,1} + R_{IT,1} + R_{foul,1}} + T_{c,avg,1}$ | $T_{foul,1} = 313.8\,^\circ\text{C}$ |
| $T_{c,avg,1} = 154.9\,^\circ\text{C}$<br>$\mu_{ex,avg} = 3.049 \times 10^{-5}\,\text{kg m}^{-1}\,\text{s}^{-1}$ | $\lambda = \dfrac{2\mu_{ex,avg}}{\rho_{ex,avg}}\sqrt{\dfrac{\pi M_{ex}}{8 R_u T_{ex,avg}}}$ | $\lambda = 1.86 \times 10^{-7}\,\text{m}$ |
| $\rho_{ex,avg} = 0.5936\,\text{kg m}^{-3}$<br>$MW_{ex} = 28.97\,\text{kg kmol}^{-1}$ | $Kn = \dfrac{2\lambda}{D_{PM}}$ | $Kn = 3.72$ |
| $T_{ex,avg} = 675.0\,\text{K}$<br>$R = 8134\,\text{J kmol}^{-1}\,\text{K}^{-1}$ | $C' = 1 + Kn\left(A + B e^{-C/Kn}\right)$ | $C' = 6.70$ |
| $D_{PM} = 1.00 \times 10^{-7}\,\text{m}$<br>$A = 1.2,\ B = 0.41,\ C = 0.88$<br>$C_s = 1.14,\ C_t = 2.18,\ C_m = 1.17$ | **Thermophoretic Coefficient**<br>$K = \dfrac{2 C_s C'}{1 + 3 C_m Kn} \times \dfrac{k_g/k_p + C_t Kn}{1 + 2 k_g/k_p + 2 C_t Kn}$ | $K = 0.4975$ |
| $k_g = 0.0463\,\text{W m}^{-1}\,\text{K}^{-1}$<br>$k_p = 5\,\text{W m}^{-1}\,\text{K}^{-1}$<br>$T_{foul,avg} = 536.2\,\text{K}$<br>$T_{ex,in,1} = 699.7\,\text{K}$ | Thermophoretic deposition efficiency for infinitely long tube (Housiadas and Drossinos, 2005)<br>$E_{th,\infty} = 1 - \left(\dfrac{T_{foul,avg}}{T_{ex,in,1}}\right)^{\Pr_{ex,avg} K}$ | $E_{th,\infty} = 0.0878$ |
| | $\dot{m}_{PM,dep} = \dot{m}_{PM,in}\,E_{th,\infty}$ | $\dot{m}_{PM,dep} = 1.98 \times 10^{-5}\,\text{g s}^{-1}$ |

| Inputs | Equations | Results |
|---|---|---|
| **Hydrocarbon Condensation (First Hour)** | | |
| $\tilde{y}_{C_1H_{1.8}} = 7.54\times10^{-3}$ | $\tilde{y}_{C_{20}H_{42},b,in,1} = \tilde{y}_{C_1H_{1.8}}/20$ | $\tilde{y}_{C_{20}H_{42},b,in,1} = 3.77\times10^{-4}$ |
| $M_{C_{20}H_{42}} = 282.5\,\text{kg kmol}^{-1}$ | $y_{C_{20}H_{42},b,in,1} = \tilde{y}_{C_{20}H_{42},b,in,1}\, M_{C_{20}H_{42}}/M_{tot}$ | $y_{C_{20}H_{42}b,in,1} = 3.70\times10^{-3}$ |
| $M_{tot} = 28.7\,\text{kg kmol}^{-1}$ | $\dot{m}_{C_{20}H_{42},b,in,1} = y_{C_{20}H_{42}}\,\dot{m}_{ex}$ | $\dot{m}_{C_{20}H_{42},b,in,1} = 7.64\times10^{-6}\,\text{kg s}^{-1}$ |
| $\dot{m}_{ex} = 0.002058\,\text{kg s}^{-1}$ | $\dot{m}_{C_{20}H_{42},b,out,1} = \dot{m}_{C_{20}H_{42},b,in,1} - \dot{m}_{g,1}$ | $\dot{m}_{C_{20}H_{42},b,out,1} = 7.55\times10^{-6}\,\text{kg s}^{-1}$ |
| $\dot{m}_{g,1} = 8.52\times10^{-8}\,\text{kg s}^{-1}{}^{*}$ | $y_{C_{20}H_{42},b,out,1} = \dot{m}_{C_{20}H_{42},b,out,1}/\dot{m}_{ex}$ | $y_{C_{20}H_{42},b,out,1} = 3.66\times10^{-3}$ |
| $AA = 7.122$ | $\tilde{y}_{C_{20}H_{42},b,out,1} = y_{C_{20}H_{42},b,in,1}\, M_{tot}/M_{C_{20}H_{42}}$ | $\tilde{y}_{C_{20}H_{42},b,out,1} = 3.73\times10^{-4}$ |
| $BB = 2032.700$ | $\tilde{y}_{C_{20}H_{42},b,avg,1} = \left(\tilde{y}_{C_{20}H_{42},b,in,1} + \tilde{y}_{C_{20}H_{42},b,out,1}\right)/2$ | $\tilde{y}_{C_{20}H_{42},b,avg,1} = 3.75\times10^{-4}$ |
| $CC = 132.100$ | | |
| $T_{foul,1} = 204.4\,^{\circ}\text{C}$ | $\log\left(P_{C_{20}H_{42},int,1}\right) = AA - BB/(T_{foul,1}+CC)$ | $P_{C_{20}H_{42},int,1} = 12.94\,\text{Pa}$ |
| $P_{ex} = 103,890 \pm 68\,\text{Pa}$ | $\tilde{y}_{C_{20}H_{42},int,i} = P_{C_{20}H_{42},int,i}/P_{ex}$ | $\tilde{y}_{C_{20}H_{42},int,i} = 1.24\times10^{-4}$ |
| $\text{Re}_{ex,1} = 7831$ | $C_{f,1} = 0.046\,\text{Re}_{ex,1}^{-0.2}$ | $C_{f,1} = 0.00766$ |
| $T_{ex,avg,1} = 614.6\,\text{K}$ | $d_{12} = 0.04357\dfrac{\left(T_{ex,avg,1}\right)^{3/2}}{P_{ex}\left(V_1^{1/3}+V_2^{1/3}\right)^2}\sqrt{\dfrac{1}{M_1}+\dfrac{1}{M_2}}$ | $d_{12} = 1.389\times10^{-5}\,\text{m}^2\,\text{s}^{-1}$ |
| $V_1 = 415.02\,\text{m}^3$ | | |
| $V_2 = 9.08\,\text{m}^3$ | | |
| $M_1 = 282.5\,\text{kg kmol}^{-1}$ | $Sc_1 = \mu_{ex,1}/\left(\rho_{ex,1}d_{12}\right)$ | $Sc_1 = 3.776$ |
| $M_2 = 28.01\,\text{kg kmol}^{-1}$ | $St_{m,1}Sc_1^{2/3} = C_{f,1}^2$ (Chilton and Colburn, 1934) | $St_{m,1} = 1.579\times10^{-3}$ |
| $\mu_{ex,1} = 3.073\times10^{-5}\,\text{kg m}^{-1}\,\text{s}^{-1}$ | $Sh_1 = St_{m,1}\,\text{Re}_{ex,1}\,Sc_1$ | $Sh_1 = 46.68$ |
| $\rho_{ex,1} = 0.5858\,\text{kg m}^{-3}$ | $K_{g,1} = Sh_1 d_{12}\rho_{ex,1}/D_{IT,I}$ | $K_{g,1} = 0.0348\,\text{kg m}^{-2}\,\text{s}^{-1}$ |
| $A_{IT,I} = 0.00978\,\text{m2}$ | $\dot{m}_{g,1} = K_{g,1}A_{IT,I}\,\ln\left(\dfrac{1-\tilde{y}_{C_{20}H_{42},i,1}}{1-\tilde{y}_{C_{20}H_{42},b,1}}\right)$ | $\dot{m}_{g,1} = 8.52\times10^{-8}\,\text{kg s}^{-1}$ |

# APPENDIX F.    DESORBER MODEL SAMPLE CALCULATIONS

| Input | Equations | Results |
|---|---|---|
| **Fluid Inlet Properties** | | |
| $n_{seg} = 18$ | $i = n_{seg}/2$ | $i = 9$ |
| $T_{ex,out,8} = 388.6\,^\circ\text{C}$ | $T_{ex,in,9} = T_{ex,out,8}$ | $T_{ex,in,9} = 388.6\,^\circ\text{C}$ |
| $\dot{m}_{cs} = 2.30 \times 10^{-3}\,\text{kg s}^{-1}$ | $k = n_{seg} + 1 - i$ | $k = 10$ |
| $T_{cs} = 95.0\,^\circ\text{C}$ | $\dot{m}_{l,in,9} = \dot{m}_{cs}$ | $\dot{m}_{l,in,9} = 2.30 \times 10^{-3}\,\text{kg s}^{-1}$ |
| $P_s = 2889\,\text{kPa}$ | $T_{l,in,9} = T_{cs}$ | $T_{l,in,9} = 95.0\,^\circ\text{C}$ |
| $q_{l,in,9} = 0$ | $x_{l,in,9} = f\left(T_{l,in,9}, P_s, q_{l,in,9}\right)^\dagger$ | $x_{l,in,9} = 0.60$ |
| $\dot{m}_{v,out,10} = 9.46 \times 10^{-4}\,\text{kg s}^{-1}$ | $h_{l,in,9} = f\left(T_{l,in,9}, P_s, q_{l,in,9}\right)^\dagger$ | $h_{l,in,9} = 2.165 \times 10^{5}\,\text{J kg}^{-1}$ |
| $T_{v,out,10} = 99.76\,^\circ\text{C}$ | $\dot{m}_{v,in,9} = \dot{m}_{v,out,10}$ | $\dot{m}_{v,in,9} = 9.46 \times 10^{-4}\,\text{kg s}^{-1}$ |
| $q_{v,out,10} = 1$ | $T_{v,in,9} = T_{v,out,10}$ | $T_{v,in,9} = 99.76\,^\circ\text{C}$ |
| $^\dagger$Determined with framework of Nagavarapu (2012) | $x_{v,in,9} = f\left(T_{v,in,9}, P_s, q_{v,in,9}\right)^\dagger$ | $x_{v,in,9} = 0.9857$ |
| | $h_{v,in,9} = f\left(T_{v,in,9}, P_s, q_{v,in,9}\right)^\dagger$ | $h_{v,in,9} = 1.427 \times 10^{6}\,\text{J kg}^{-1}$ |

| **Heat Transfer Rate** | | |
|---|---|---|
| $L_{tube} = 0.241$ m | $L_{seg} = 2L_{tube}/n_{seg}$ | $L_{seg} = 0.0268\,\text{m}$ |
| $n_{tubes/pass} = 14$ | $\dot{m}_{ex,pt} = \dot{m}_{ex}/n_{tubes/pass}$ | $\dot{m}_{ex,pt} = 1.47\times10^{-3}\ \text{kg s}^{-1}$ |
| $D_{tube,I} = 0.0109$ m | $\text{Re}_{ex,9} = \dfrac{4\dot{m}_{ex,pt}}{\pi D_{tube,I}\mu_{ex,9}}$ | $\text{Re}_{ex,9} = 5330$ |
| $D_{tube,O} = 0.0127$ m | | |
| $\dot{m}_{ex} = 0.0206$ kg s$^{-1}$ | Correlation for friction factor in smooth tubes (Churchill (1977b)) | $f_{ex,9} = 0.05147$ |
| $\mu_{ex,9} = 3.218\times10^{-5}\text{kg}$ m$^{-1}$ s$^{-1}$ | $f_{ex,9} = 8\left[\left(\dfrac{8}{\text{Re}_{ex,9}}\right)^{12} + 1\Big/\left(2.457\ln\left(\dfrac{1}{\left(7/\text{Re}_{ex,9}\right)^{0.9}+\left(0.27\varepsilon/D_{tube,I}\right)}\right)^{16} + \left(37530/\text{Re}_{ex,9}\right)^{16}\right)^{1.5}\right]^{1/12}$ | |
| $\text{Pr}_{ex,9} = 0.6943$ | | |
| $k_{ex,9} = 0.04937$ W m$^{-1}$ K$^{-1}$ | | |
| $c_{p,ex,9} = 1131\,\text{J kg}^{-1}$ | | |
| $R'_{f,9} = 0.8105$ m W$^{-1}$ | | |
| | Correlation for Nusselt number in smooth tubes (Churchill (1977a)) | $Nu_{ex,9} = 20.99$ |
| | $Nu_{ex,9}{}^{10} = 4.364^{10} + \left[\dfrac{e^{(2200-\text{Re}_{ex,9})/365}}{4.364^2} + 1\Big/\left(\dfrac{6.3 + 0.079(f_{ex,9}/8)^{1/2}\,\text{Re}_{ex,9}\,\text{Pr}_{ex,9}}{\left(1+\text{Pr}_{ex,9}{}^{4/5}\right)^{5/6}}\right)^2\right]^{-5}$ | |
| | $h_{ex,9} = Nu_{ex,9}k_{ex,9}/D_{tube,I}$ | $h_{ex,9} = 94.86$ W m$^{-2}$ K$^{-1}$ |
| | $R_{ex,9} = \dfrac{1}{h_{ex,9}\pi D_{tube,I}L_{seg}}$ | $R_{ex,9} = 11.46$ K W$^{-1}$ |
| | $R_{f,9} = R'_{f,9}/L_{seg}$ | $R_{f,9} = 30.23$ K W$^{-1}$ |

| | | |
|---|---|---|
| $k_{tube} = 16.03$ W m$^{-1}$ K$^{-1}$<br>$h_{s,9} = 3000$ W m$^{-2}$ K$^{-1}$<br>Delahanty (2015)<br>$T_{l,out,9} = 97.13$ $^{o}$C*<br>*Determined iteratively | $R_{wall,9} = \dfrac{\ln\left(D_{tube,O}/D_{tube,I}\right)}{2\pi k_{tube}L_{seg}}$ | $R_{wall,9} = 0.0527$ K W$^{-1}$ |
| | $R_{s,9} = \dfrac{1}{h_{s,i}\pi D_{tube,O}L_{seg}}$ | $R_{s,9} = 0.312$ K W$^{-1}$ |
| | $R_{tube,9} = R_{ex,9} + R_{foul,9} + R_{wall,9} + R_{s,9}$ | $R_{tube,9} = 42.05$ K W$^{-1}$ |
| | $R_{9} = \dfrac{R_{tube,9}}{n_{tubes/pass}}$ | $R_{9} = 3.003$ K W$^{-1}$ |
| | $\Delta T_{lm,9} = \dfrac{\left(T_{ex,in,9} - T_{l,out,9}\right) - \left(T_{ex,out,9} - T_{l,in,9}\right)}{\ln\left(\left(T_{ex,in,9} - T_{l,out,9}\right)/\left(T_{ex,out,9} - T_{l,in,9}\right)\right)}$ | $\Delta T_{lm,9} = 290.4$ $^{o}$C |
| | $\dot{Q}_{9} = \Delta T_{lm,9}/R_{9}$ | $\dot{Q}_{9} = 96.70$ W |
| | $T_{ex,out,9} = T_{ex,in,9} - \dot{Q}_{9}/\dot{m}_{ex}c_{p,ex,9}$ | $T_{ex,out,9} = 384.5$ $^{o}$C |
| **Solution Outlet Properties** | | |
| $q_{l,out,9} = 0$<br>$q_{v,out,9} = 1$ | $\dot{m}_{l,in,9} + \dot{m}_{v,in,9} = \dot{m}_{l,out,9} + \dot{m}_{v,out,9}$ | $\dot{m}_{l,out,9} = 2.225\times10^{-4}$ kg s$^{-1}$ |
| | $\dot{m}_{l,in,9}x_{l,in,9} + \dot{m}_{v,in,9}x_{v,in,9} = \dot{m}_{l,out,9}x_{l,out,9} + \dot{m}_{v,out,9}x_{v,out,9}$ | $\dot{m}_{v,out,9} = 1.02\times10^{-3}$ kg s$^{-1}$ |
| | $\dot{Q}_{9} = \dot{m}_{l,out,9}h_{l,out,9} + \dot{m}_{v,out,9}h_{v,out,9} - \dot{m}_{l,in,9}h_{l,in,9} - \dot{m}_{v,in,9}h_{v,in,9}$ | $h_{l,out,9} = 2.226\times10^{5}$ J kg$^{-1}$ |
| | $x_{l,out,9} = f\left(h_{l,out,9},P_{s},q_{l,out,9}\right)^{\dagger}$ | $x_{l,out,9} = 0.5858$ |
| | $T_{l,out,9} = f\left(h_{l,out,9},P_{s},q_{l,out,9}\right)^{\dagger}$ | $T_{l,out,9} = 97.13$ $^{o}$C |
| | $T_{v,out,9} = \left(T_{v,in,9} + T_{l,in,9}\right)/2$ | $T_{v,out,9} = 97.38$ $^{o}$C |
| | $x_{v,out,9} = f\left(T_{v,out,9},P_{s},q_{v,out,9}\right)^{\dagger}$ | $x_{v,out,9} = 0.9876$ |
| | $h_{v,out,9} = f\left(T_{v,out,9},P_{s},q_{v,out,9}\right)^{\dagger}$ | $h_{v,out,9} = 1.420\times10^{6}$ kJ kg$^{-1}$ |

**Exhaust Pressure Drop**

| | | |
|---|---|---|
| $\left(\dfrac{\Delta P}{\Delta P_o}\right) = 3.249$ | $\Delta P_{ex,maj,9} = \left(\dfrac{\Delta P}{\Delta P_o}\right) \dfrac{f_{ex,9}}{D_{tube,O}{}^5} \dfrac{8}{\pi^2} \dfrac{\dot{m}_{ex,pt}^2 L_{seg}}{\rho_{ex,9}}$ | $\Delta P_{ex,maj,9} = 96.13\,\text{Pa}$ |
| $\rho_{ex,1} = 0.5024\,\text{kg m}^{-3}$ $\rho_{ex,9} = 0.5267\,\text{kg m}^{-3}$ | $\Delta P_{ex,maj} = \displaystyle\sum_{1}^{i=n_{seg}} \Delta P_{ex,maj,i}$ | $\Delta P_{ex,maj} = 1566\,\text{Pa}$ |
| $\rho_{ex,10} = 0.5301\,\text{kg m}^{-3}$ $\rho_{ex,18} = 0.5558\,\text{kg m}^{-3}$ | $\Delta P_{ex,ent} = K_{L,ent} \dfrac{8}{\pi^2} \dfrac{\dot{m}_{ex,pt}^2}{\rho_{ex,1} D_{tube,I}{}^4} + K_{L,ent} \dfrac{8}{\pi^2} \dfrac{\dot{m}_{ex,pt}^2}{\rho_{ex,10} D_{tube,I}{}^4}$ | $\Delta P_{ex,ent} = 239.0\,\text{Pa}$ |
| $K_{L,ent} = 0.5$ $K_{L,exit} = 0.5$ | $\Delta P_{ex,exit} = K_{L,exit} \dfrac{8}{\pi^2} \dfrac{\dot{m}_{ex}^2}{\rho_{ex,9} D_{tube,I}{}^4} + K_{L,exit} \dfrac{8}{\pi^2} \dfrac{\dot{m}_{ex}^2}{\rho_{ex,18} D_{tube,I}{}^4}$ | $\Delta P_{ex,exit} = 228.0\,\text{Pa}$ |
| | $\Delta P_{ex,col,1} = \Delta P_{ex,maj} + \Delta P_{ex,ent} + \Delta P_{ex,exit}$ | $\Delta P_{ex,col,1} = 2033\,\text{Pa}$ |

| **Column Total** | | |
|---|---|---|
| | $\dot{Q}_{col,1} = \sum\limits_{i=1}^{n_{seg}} \dot{Q}_i$ | $\dot{Q}_{col,1} = 1627$ W |
| | $T_{v,out,col,1} = T_{v,out,9}$ | $T_{v,out,col,1} = 97.38$ ºC |
| | $x_{v,out,col,1} = x_{v,out,9}$ | $x_{v,out,col,1} = 0.9876$ |
| | $\dot{m}_{v,out,col,1} = \dot{m}_{v,out,9}$ | $\dot{m}_{v,out,col,1} = 1.02 \times 10^{-3}$ kg s$^{-1}$ |
| | $T_{l,out,col,1} = T_{l,out,18}$ | $T_{l,out,col,1} = 158.6$ ºC |
| | $x_{l,out,col,1} = x_{l,out,9}$ | $x_{l,out,col,1} = 0.2902$ |
| | $\dot{m}_{ds,col,1} = \dot{m}_{l,out,18}$ | $\dot{m}_{ds,col,1} = 1.28 \times 10^{-3}$ kg s$^{-1}$ |
| **Desorber Total** | | |
| $\dot{m}_{ds,col,2} = 1.11 \times 10^{-3}$ kg s$^{-1}$<br>$\dot{m}_{ds,col,3} = 8.17 \times 10^{-4}$ kg s$^{-1}$<br>$\dot{m}_{v,out,col,2} = 0.893 \times 10^{-3}$ kg s$^{-1}$<br>$\dot{m}_{v,out,col,3} = 0.653 \times 10^{-3}$ kg s$^{-1}$<br>$x_{ds,col,2} = 0.2902$<br>$x_{ds,col,3} = 0.2902$<br>$x_{v,out,col,2} = 0.9876$<br>$x_{v,out,col,3} = 0.9875$<br>$\Delta P_{ex,col,2} = 1409$ Pa<br>$\Delta P_{ex,col,3} = 1243$ Pa | $\dot{Q}_{des} = \sum\limits_{i=1}^{3} \dot{Q}_{col,i}$ | $\dot{Q}_{des} = 4089$ W |
| | $\dot{m}_{ds,des,out} = \sum\limits_{i=1}^{3} \dot{m}_{ds,col,i}$ | $\dot{m}_{ds,des,out} = 3.21 \times 10^{-3}$ kg s$^{-1}$ |
| | $\dot{m}_{v,des,out} = \sum\limits_{i=1}^{3} \dot{m}_{v,out,col,i}$ | $\dot{m}_{v,des,out} = 2.57 \times 10^{-3}$ kg s$^{-1}$ |
| | $x_{ds,des,out} = \left( \sum\limits_{i=1}^{3} \dot{m}_{ds,col,i} x_{ds,col,i} \right) \Big/ \dot{m}_{ds,des,out}$ | $x_{ds,des,out} = 0.2902$ |
| | $x_{v,des,out} = \left( \sum\limits_{i=1}^{3} \dot{m}_{v,out,col,i} x_{v,out,col,i} \right) \Big/ \dot{m}_{v,des,out}$ | $x_{v,des,out} = 0.9876$ |
| | $\Delta P_{ex,des} = \sum\limits_{i=1}^{3} \Delta P_{ex,col,i}$ | $\Delta P_{ex,des} = 4686$ Pa |

# APPENDIX G.  DESORBER EXPERIMENTS SAMPLE CALCULATIONS

| Input | Equations | Results |
|---|---|---|
| **Heat Transfer Rates** | | |
| $T_{ex,1} = 443.7 \pm 1.1\,^{\circ}\text{C}$ | $T_{ex,avg,1} = \left(T_{ex,1} + T_{ex,2}\right)/2$ | $T_{ex,avg,1} = 401.7\ ^{\circ}\text{C}$ |
| $T_{ex,2} = 359.7 \pm 1.1\ ^{\circ}\text{C}$ | $\dot{m}_{ex} = K_p D_{wm}^2 FaY\sqrt{\rho_{ex,wm}\Delta P_{wm}}$ | $\dot{m}_{ex} = 0.01979 \pm 0.0001\,\text{kg s}^{-1}$ |
| $K_p = 8.07 \times 10^{-3}$ | | |
| $D_{wm} = 0.0266\,\text{m}$ | $\dot{Q}_{ex,1} = \dot{m}_{ex}c_{p,ex,1}\left(T_{ex,1} - T_{ex,2}\right)$ | $\dot{Q}_{ex,1} = 1840 \pm 39\,\text{W}$ |
| $Fa = 1.012$ | $\dot{Q}_{ex} = \sum_{i=1}^{3}\dot{Q}_{ex,i}$ | $\dot{Q}_{ex} = 4244 \pm 59\ \text{W}$ |
| $T_{ex,4} = 247.1 \pm 1\ ^{\circ}\text{C}$ | | |
| $Y = 1$ | $T_{c,avg} = \left(T_{c,in} + T_{c,out}\right)/2$ | $T_{c,avg} = 124.3\ ^{\circ}\text{C}$ |
| $\rho_{ex,wm} = 0.675\,\text{kg m}^{-3}$ | $\dot{m}_c = \rho_c\dot{V}_c$ | $\dot{m}_c = 0.01601\ \text{kg s}^{-1}$ |
| $\Delta P_{wm} = 12586 \pm 31\,\text{Pa}$ | $\dot{Q}_c = \dot{m}_c c_{p,c}\left(T_{c,out} - T_{c,in}\right)$ | $\dot{Q}_c = 3951 \pm 27\ \text{W}$ |
| $P_{ex} = 105904 \pm 68\ \text{Pa}$ | | |
| $c_{p,ex,1} = 1107\ \text{J kg}^{-1}$ | $\dot{Q}_{c,1} = \dot{Q}_{ex,1}\dfrac{\dot{Q}_c}{\dot{Q}_{ex}}$ | $\dot{Q}_{c,1} = 1713 \pm 30\ \text{W}$ |
| $\dot{Q}_{ex,2} = 1386\ \text{W}$ | | |
| $\dot{Q}_{ex,3} = 1018\ \text{W}$ | $T_{c,avg,1} = \left(T_{c,in,1} + T_{c,out,1}\right)/2$ | $T_{c,avg,1} = 128.6\ ^{\circ}\text{C}$ |
| $T_{c,in} = 95.33 \pm 0.25\ ^{\circ}\text{C}$ | $\dot{m}_{c,1} = \dfrac{\dot{Q}_{c,1}}{c_{p,c,1}(T_{c,out,1} - T_{c,in,1})}$ | $\dot{m}_{c,1} = 0.00604\ \text{kg s}^{-1}$ |

| **Total Thermal Resistance** | | |
|---|---|---|
| $T_{c,out} = 153.4 \pm 0.25$ °C | $\dot{Q}_{max,1} = \dot{m}_{ex} c_{p,ex,1} \left( T_{ex,1} - T_{c,in,1} \right)$ | $\dot{Q}_{max,1} = 7632$ W |
| $\rho_c = 962.4$ kg m$^{-3}$ | $\varepsilon_1 = \dot{Q}_{c,1} / \dot{Q}_{max,1}$ | $\varepsilon_1 = 0.2244$ |
| $\dot{V}_c = 0.9982 \pm 0.0025$ | $C_{r,1} = \dfrac{\dot{m}_{ex} c_{p,ex,1}}{\dot{m}_{c,1} c_{p,c,1}}$ | $C_{r,1} = 0.8518$ |
| $c_{p,c} = 4255$ J kg$^{-1}$ | | |
| $T_{c,in,1} = 95.33 \pm 0.25$ °C | $\varepsilon - NTU$ relationship for shell and tube heat exchanger with one shell pass and any even number of tube passes (Bergman *et al.* (2011)) | $E_1 = 5.374$ |
| $T_{c,out,1} = 162.7 \pm 0.25$ °C | | $NTU_1 = 0.2767$ |
| $c_{p,c,1} = 4261$ J kg$^{-1}$ | $E_1 = \dfrac{2/\varepsilon_1 - \left(1 + C_{r,1}\right)}{\left(1 + C_{r,1}^2\right)^{1/2}}$ | |
| | $NTU_1 = -\left(1 + C_{r,1}^2\right)^{-1/2} \ln \dfrac{E_1 - 1}{E_1 + 1}$ | |
| | $UA_1 = \dot{m}_{ex} c_{p,ex,i} NTU_1$ | $UA_1 = 6.062$ W K$^{-1}$ |
| | $R_1 = 1/UA_1$ | $R_1 = 0.1650$ K W$^{-1}$ |
| | $\Delta T_{lm,1} = \dot{Q}_{c,1} R_1$ | $\Delta T_{lm,1} = 282.5$ |
| **Header Thermal Resistance** | | |
| $A_{s,plate} = 3.358 \times 10^{-3}$ m$^2$ | $R_{header,c,1} = \dfrac{1}{h_{c,1} \left( 2 A_{s,plate} \right)}$ | $R_{header,c,1} = 0.1143$ K W$^{-1}$ |
| $h_{c,1} = 651.4$ W m$^{-2}$ K$^{-1}$ | | |
| Correlation of Kern (1950) | $R_{header,wall,1} = \dfrac{t_{plate}}{k_{plate} A_{s,plate}}$ | $R_{header,wall,1} = 0.03113$ K W$^{-1}$ |
| $t_{plate} = 0.00635$ m | | |
| $k_{plate} = 15.19$ W m$^{-1}$ K$^{-1}$ | | |
| $A_{x,header} = 7.258 \times 10^{-3}$ m$^2$ | $\overline{\dot{m}}_{ex,header} = 15 \dot{m}_{ex} / 21$ | $\overline{\dot{m}}_{ex,header} = 0.01414$ kg s$^{-1}$ |
| | $\overline{V}_{ex,header} = \dfrac{\overline{\dot{m}}_{ex,header}}{\rho_{ex,1} A_{x,header}}$ | $\overline{V}_{ex,header} = 3.743$ m s$^{-1}$ |

| | | |
|---|---|---|
| $L_{plate} = 0.0635\,\text{m}$ <br> $\mu_{ex,1} = 3.266 \times 10^{-5}\,\text{kg m}^{-1}\,\text{s}^{-1}$ <br> $\rho_{ex,1} = 0.5204\,\text{kg m}^{-3}$ <br> $\text{Pr}_{ex,1} = 0.6947$ <br> $k_{ex,1} = 0.05024\,\text{W m}^{-1}\,\text{K}^{-1}$ | $\text{Re}_{ex,L,1} = \dfrac{\rho_{ex,1}\overline{V}_{ex,1}L_{plate}}{\mu_{ex,1}}$ | $\text{Re}_{ex,L,1} = 5047$ |
| | $\overline{Nu}_{ex,L,1} = 0.664\,\text{Re}_{ex,L,1}^{1/2}\,\text{Pr}_{ex,1}^{1/3}$ | $\overline{Nu}_{ex,L,1} = 36.19$ |
| | $h_{ex,header,1} = \dfrac{Nu_{ex,L,1}k_{ex,1}}{L_{plate}}$ | $h_{ex,header,1} = 28.64\,\text{W m}^{-2}\,\text{K}^{-1}$ |
| | $R_{header,ex,1} = \dfrac{1}{h_{ex,header,1}\left(2A_{s,plate}\right)}$ | $R_{header,ex,1} = 2.60\,\text{K W}^{-1}$ |
| | $R_{header,1} = R_{header,ex,1} + R_{header,wall,1} + R_{header,c,1}$ | $R_{header,1} = 2.745\,\text{K W}^{-1}$ |

**Fouling Thermal Resistance**

| | | |
|---|---|---|
| $D_{shell} = 0.102\,\text{m}$ <br> $P_{tube} = 0.0158\,\text{m}$ <br> $C = 0.00318\,\text{m}$ <br> $L_b = 0.0457\,\text{m}$ <br> $\mu_{c,1} = 2.158 \times 10^{-4}\,\text{kg m}^{-1}\,\text{s}^{-1}$ <br> $c_{p,1} = 4261\,\text{J kg}^{-1}$ <br> $k_{c,1} = 0.6704\,\text{W m}^{-1}\,\text{K}^{-1}$ <br> $\mu_{c,w,1} = 2.028 \times 10^{-4}\,\text{kg m}^{-1}\,\text{s}^{-1}$ | $R_{tubes,1} = \dfrac{R_1 - R_{header,1}}{R_1 R_{header,1}}$ | $R_{tubes,1} = 0.1755\,\text{K W}^{-1}$ |
| | $\dot{Q}_{c,tubes,1} = \Delta T_{lm,1}/R_{tubes,1}$ | $\dot{Q}_{c,tubes,1} = 1610\,\text{W}$ |
| | $R_{tube,1} = R_{tubes,1}n_{tubes/pass}$ | $R_{tube,1} = 2.457\,\text{K W}^{-1}$ |
| | $A_{x,shell} = \dfrac{D_{shell}}{P_{tube}}CL_b$ | $A_{x,shell} = 9.351 \times 10^{-3}\,\text{m}^2$ |
| | $\dot{m}''_{c,shell,1} = \dot{m}_{c,1}/A_{x,shell}$ | $\dot{m}''_{c,shell,1} = 6.455\,\text{kg s}^{-1}\,\text{m}^{-2}$ |
| | $D_e = \dfrac{4\left(P_{tube}/2 \times 0.86P_{tube} - 0.5\left(\pi D_o^2/4\right)\right)}{\pi D_o/4}$ | $D_e = 9.029 \times 10^{-3}\,\text{m}$ |
| | Correlation of Kern (1950) for heat transfer coefficient on shell side of shell-and-tube heat exchanger with a 25% baffle cut <br><br> $h_{c,1} = 0.36\left(\dfrac{D_e \dot{m}''_{c,shell,1}}{\mu_{c,1}}\right)^{0.55}\left(\dfrac{c_{p,1}\mu_{c,1}}{k_{c,1}}\right)^{1/3}\left(\dfrac{\mu_{c,1}}{\mu_{c,w,1}}\right)^{0.14}\left(\dfrac{k_{c,1}}{D_e}\right)$ | $h_{c,1} = 651.4\,\text{W m}^{-2}\,\text{K}^{-1}$ |

| | | |
|---|---|---|
| $k_{tube} = 15.19 \, \text{W m}^{-1} \, \text{K}^{-1}$<br><br>$L_{tube} = 0.241 \, \text{m}$<br><br>$D_{tube,I} = 0.0109 \, \text{m}$<br><br>$D_{tube,O} = 0.0127 \, \text{m}$ | $R_{c,1} = 1/\left( h_{c,1} \pi D_{tube,O} \left( 2L_{tube} \right) \right)$ | $R_{c,1} = 0.07973 \, \text{K W}^{-1}$ |
| | $R_{wall,1} = \ln\left( D_{tube,O} / D_{tube,I} \right) / \left( 2\pi k_{tube} \left( 2L_{tube} \right) \right)$ | $R_{wall,1} = 0.00328 \, \text{K W}^{-1}$ |
| | $\dot{m}_{ex,pt} = \dot{m}_{ex} / n_{p,tubes}$ | $\dot{m}_{ex,pt} = 1.414 \times 10^{-3} \, \text{kg s}^{-1}$ |
| | $\text{Re}_{ex,1} = 4\dot{m}_{ex,pt} / \left( \pi D_{tube,I} \mu_{ex,1} \right)$ | $\text{Re}_{ex,1} = 5047$ |
| | Correlation of Churchill (1977b)<br><br>$f_{ex,1} = 8 \left[ \left( \dfrac{8}{\text{Re}_{ex,1}} \right)^{12} + 1 / \left( 2.457 \ln\left( \dfrac{1}{\left( 7/\text{Re}_{ex,1} \right)^{0.9} + \left( 0.27 \varepsilon / D_{tube,I} \right)} \right)^{16} + \left( 37530/\text{Re}_{ex,1} \right)^{16} \right)^{1.5} \right]^{1/12}$ | $f_{ex,1} = 0.04411$ |
| | $Nu_{ex,1}{}^{10} = 4.364^{10} + \left[ \dfrac{e^{(2200 - \text{Re}_{ex,1})/365}}{4.364^2} + 1 / \left( 6.3 + \dfrac{0.079(f_{ex,1}/8)^{1/2} \, \text{Re}_{ex,1} \, \text{Pr}_{ex,1}}{\left( 1 + \text{Pr}_{ex,1}{}^{4/5} \right)^{5/6}} \right)^2 \right]^{-5}$ | $Nu_{ex,1} = 18.45$ |
| | $h_{ex,1} = Nu_{ex,1} k_{ex,1} / D_{tube,I}$ | $h_{ex,1} = 84.9 \pm 21.5 \, \text{W m}^{-2} \, \text{K}^{-1}$ |
| | $R_{ex,1} = 1/\left( h_{ex,1} \pi D_{tube,I} \left( 2L_{tube} \right) \right)$ | $R_{ex,1} = 0.7113 \, \text{K W}^{-1}$ |
| | $R_{foul,1} = R_{tube,1} - R_{ex,1} - R_{wall,1} - R_{c,1}$ | $R_{foul,1} = 1.663 \pm 0.185 \, \text{K W}^{-1}$ |
| | $R'_{foul,1} = R_{foul,1} \left( 2L_{tube} \right)$ | $R'_{foul,1} = 0.802 \pm 0.090 \, \text{m K W}^{-1}$ |

**Pressure Drop**

| $k_{ent/ex} = 0.5$ | $\Delta P_{ex,min,1} = 4 k_{ent/ex} \dfrac{8}{\pi^2} \dfrac{\dot{m}_{ex}^2}{\rho_{ex,1} D_{tube,I}^{~4}}$ | $\Delta P_{ex,min,1} = 437.6$ Pa |
|---|---|---|
| $\Delta P_{ex,1} = 1990 \pm 31$ Pa | | |
| $f_{o,1} = 0.04411$ | $\Delta P_{ex,maj,1} = \Delta P_{ex,1} - \Delta P_{ex,min,1}$ | $\Delta P_{ex,maj,1} = 1553$ Pa |
| | $\Delta P_{ex,maj,1} = \dfrac{f_{ex,1}}{D_{foul,i}^5} \dfrac{8}{\pi^2} \dfrac{\dot{m}_{ex,pt}^2 L_{tube}}{\rho_{ex,1}}$ | $\dfrac{f_{ex,1}}{D_{foul,i}^5} = 1.033 \times 10^9 \ \text{m}^{-5}$ |
| | $\dfrac{\Delta P_{ex,1}}{\Delta P_{ex,o,1}} = \dfrac{f_1 / D_{foul,1}^5}{f_{o,1} / D_{tube,I}^5}$ | $\dfrac{\Delta P_{ex,1}}{\Delta P_{ex,o,1}} = 3.64 \pm 1.06$ |

# REFERENCES

Abarham, M., T. Chafekar, J. W. Hoard, A. Salvi, D. J. Styles, C. S. Sluder and D. Assanis (2013a), "In-Situ Visualization of Exhaust Soot Particle Deposition and Removal in Channel Flows," *Chemical Engineering Science* Vol. 87 pp. 359-370.

Abarham, M., J. Hoard, D. Assanis, D. Styles, E. W. Curtis and N. Ramesh (2010a), "Review of Soot Deposition and Removal Mechanisms in EGR Coolers," *SAE International Journal of Fuels and Lubricants* Vol. 3(1) pp. 690-704.

Abarham, M., J. Hoard, D. Assanis, D. Styles, E. W. Curtis, N. Ramesh, C. S. Sluder and J. M. Storey (2009a), "Modeling of Thermophoretic Soot Deposition and Hydrocarbon Condensation in EGR Coolers," *SAE International Journal of Fuels and Lubricants* Vol. 2(1) pp. 921-931.

Abarham, M., J. W. Hoard, D. Assanis, D. Styles, C. S. Sluder and J. M. Storey (2010b), "An Analytical Study of Thermophoretic Particulate Deposition in Turbulent Pipe Flows," *Aerosol Science and Technology* Vol. 44(9) pp. 785-795.

Abarham, M., J. W. Hoard, D. Styles, E. W. Curtis, N. Ramesh, S. Sluder and J. M. Storey (2009b). Numerical Modeling and Experimental Investigations of EGR Cooler Fouling in a Diesel Engine. Oak Ridge National Laboratory (ORNL); Fuels, Engines and Emissions Research Centerp.

Abarham, M., P. Zamankhan, J. W. Hoard, D. Styles, C. S. Sluder, J. M. Storey, M. J. Lance and D. Assanis (2013b), "CFD Analysis of Particle Transport in Axi-Symmetric Tube Flows under the Influence of Thermophoretic Force," *International Journal of Heat and Mass Transfer* Vol. 61 pp. 94-105.

Abd-Elhady, M., C. Rindt, J. Wijers, A. Van Steenhoven, E. Bramer and T. H. Van der Meer (2004), "Minimum Gas Speed in Heat Exchangers to Avoid Particulate Fouling," *International Journal of Heat and Mass Transfer* Vol. 47(17) pp. 3943-3955.

Abd-Elhady, M., T. Zornek, M. Malayeri, S. Balestrino, P. Szymkowicz and H. Müller-Steinhagen (2011), "Influence of Gas Velocity on Particulate Fouling of Exhaust Gas Recirculation Coolers," *International Journal of Heat and Mass Transfer* Vol. 54(4) pp. 838-846.

ANSYS, C. (2012), "User Manual, Ansys," *Inc., Canonsburg, PA*.

Bari, S. and S. N. Hossain (2013), "Waste Heat Recovery from a Diesel Engine Using Shell and Tube Heat Exchanger," *Applied Thermal Engineering* Vol. 61(2) pp. 355-363.

Bergman, T. L., F. P. Incropera and A. S. Lavine (2011). *Fundamentals of Heat and Mass Transfer*, John Wiley & Sons.

Bika, A. S., A. Warey, D. Long, S. Balestrino and P. Szymkowicz (2012), "Characterization of Soot Deposition and Particle Nucleation in Exhaust Gas Recirculation Coolers," *Aerosol Science and Technology* Vol. 46(12) pp. 1328-1336.

Bombarda, P., C. M. Invernizzi and C. Pietra (2010), "Heat Recovery from Diesel Engines: A Thermodynamic Comparison between Kalina and ORC Cycles," *Applied Thermal Engineering* Vol. 30(2) pp. 212-219.

Chilton, T. H. and A. P. Colburn (1934), "Mass Transfer (Absorption) Coefficients Prediction from Data on Heat Transfer and Fluid Friction," *Industrial & Engineering Chemistry* Vol. 26(11) pp. 1183-1187.

Churchill, S. W. (1977a), "Comprehensive Correlating Equations for Heat, Mass and Momentum Transfer in Fully Developed Flow in Smooth Tubes," *Industrial & Engineering Chemistry Fundamentals* Vol. 16(1) pp. 109-116.

Churchill, S. W. (1977b), "Friction-Factor Equation Spans All Fluid-Flow Regimes," *Chemical Engineering* Vol. 84(24) pp. 91-92.

Churchill, S. W. and H. H. Chu (1975), "Correlating Equations for Laminar and Turbulent Free Convection from a Horizontal Cylinder," *International Journal of Heat and Mass Transfer* Vol. 18(9) pp. 1049-1053.

Delahanty, J. C. (2015), "Desorption of Ammonia-Water Mixtures in Microscale Geometries for Miniaturized Absorption Systems."

Determan, M. D. and S. Garimella (2012), "Design, Fabrication, and Experimental Demonstration of a Microscale Monolithic Modular Absorption Heat Pump," *Applied Thermal Engineering* Vol. 47 pp. 119-125.

Dongzi, Z., N. J. Nussbaum, H. D. Kuhns, M. C. O. Chang, D. Sodeman, S. Uppapalli, H. Moosmüller, J. C. Chow and J. G. Watson (2009), "In-Plume Emission Test Stand 2: Emission Factors for 10- to 100-kW U.S. Military Generators," *Journal of the Air & Waste Management Association (Air & Waste Management Association)* Vol. 59(12) pp. 1446-1457.

Durbin, T. D., D. R. Cocker, A. A. Sawant, K. Johnson, J. W. Miller, B. B. Holden, N. L. Helgeson and J. A. Jack (2007), "Regulated Emissions from Biodiesel Fuels from On/Off-Road Applications," *Atmospheric Environment* Vol. 41(27) pp. 5647-5658.

EIA, U. (2013), "Annual Energy Outlook 2013," *US Energy Information Administration, Washington, DC* pp. 60-62.

Fernández-Seara, J., A. Vales and M. Vázquez (1998), "Heat Recovery System to Power an Onboard NH3-H2O Absorption Refrigeration Plant in Trawler Chiller Fishing Vessels," *Applied Thermal Engineering* Vol. 18(12) pp. 1189-1205.

Forinash, D. M. (2015), "Novel Air-Coupled Heat Exchangers for Waste Heat-Driven Absorption Heat Pumps."

Garimella, S., C. M. Keinath, J. C. Delahanty, D. C. Hoysall, M. A. Staedter, A. Goyal and M. A. Garrabrant (2016), "Development and Demonstration of a Compact Ammonia–Water Absorption Heat Pump Prototype with Microscale Features for Space-Conditioning Applications," *Applied Thermal Engineering* Vol. 102 pp. 557-564.

Harris, S. J. and M. M. Maricq (2001), "Signature Size Distributions for Diesel and Gasoline Engine Exhaust Particulate Matter," *Journal of Aerosol Science* Vol. 32(6) pp. 749-764.

Haseli, Y., J. Van Oijen and L. De Goey (2011), "Modeling Biomass Particle Pyrolysis with Temperature-Dependent Heat of Reactions," *Journal of Analytical and Applied Pyrolysis* Vol. 90(2) pp. 140-154.

Hatami, M., D. Ganji and M. Gorji-Bandpy (2014), "A Review of Different Heat Exchangers Designs for Increasing the Diesel Exhaust Waste Heat Recovery," *Renewable and Sustainable Energy Reviews* Vol. 37 pp. 168-181.

Heywood, J. B. (1988). *Internal Combustion Engine Fundamentals*, Mcgraw-hill New York.

Hong, K. S., K. S. Lee, S. Song, K. M. Chun, D. Chung and S. Min (2011), "Parametric Study on Particle Size and SOF Effects on EGR Cooler Fouling," *Atmospheric Environment* Vol. 45(32) pp. 5677-5683.

Hornig, G., P. Volk, G. Wachtmeister and R. Niessner (2011), "Fouling of EGR Heat Exchangers-Investigations of Mechanisms Involved in Soot Particle Deposition," *Proceedings of International Conference on Heat Exchanger Fouling & Cleaning IX, Greece*

Horuz, I. (1999), "Vapor Absorption Refrigeration in Road Transport Vehicles," *Journal of Energy Engineering* Vol. 125(2) pp. 48-58.

Housiadas, C. and Y. Drossinos (2005), "Thermophoretic Deposition in Tube Flow," *Aerosol Science and Technology* Vol. 39(4) pp. 304-318.

Howell, J. "A Catalog of Radiation Heat Transfer Configuration Factors, 1998," *Eletronic version available at http://sage. me. utexas. edu/howell/index. html*.

Keinath, C. M., J. C. Delahanty, S. Garimella and M. A. Garrabrant (2012), "Diesel Engine Waste-Heat Driven Ammonia-Water Absorption System for Space-Conditioning Applications."

Kern, D. Q. (1950). *Process Heat Transfer*, Tata McGraw-Hill Education.

Kim, H.-M., S.-K. Park, K.-S. Choi, H.-M. Wang, D.-H. Lee, D.-K. Lee, Y.-S. Cha, J.-S. Lee and J. Lee (2008), "Investigation on the Flow and Heat Transfer Characteristics of Diesel Engine EGR Coolers," *International Journal of Automotive Technology* Vol. 9(2) pp. 149-153.

Klein, S. (2016), "Engineering Equation Solver," *F-Chart Software, Madison, WI* Vol. 1.

Kuosa, M., J. Kaikko and L. Koskelainen (2007), "The Impact of Heat Exchanger Fouling on the Optimum Operation and Maintenance of the Stirling Engine," *Applied Thermal Engineering* Vol. 27(10) pp. 1671-1676.

Lambert, M. and B. Jones (2006), "Automotive Adsorption Air Conditioner Powered by Exhaust Heat. Part 1: Conceptual and Embodiment Design," *Proceedings of the Institution of Mechanical Engineers, Part D: Journal of Automobile Engineering* Vol. 220(7) pp. 959-972.

Lance, M. J., C. S. Sluder, H. Wang and J. M. Storey (2009). Direct Measurement of EGR Cooler Deposit Thermal Properties for Improved. SAE 2009-01-1461p.

Little, A. B. and S. Garimella (2011), "Comparative Assessment of Alternative Cycles for Waste Heat Recovery and Upgrade," *Energy* Vol. 36(7) pp. 4492-4504.

MathWorks, I. (2014). *Matlab*. Natik, Massachusetts.

Mattingly, G. (1992), "The Characterization of a Piston Displacement-Type Flowmeter Calibration Facility and the Calibration and Use of Pulsed Output Type Flowmeters," *Journal of Research-National Institute of Standards and Technology* Vol. 97 pp. 509-509.

Mavridou, S., G. Mavropoulos, D. Bouris, D. Hountalas and G. Bergeles (2010), "Comparative Design Study of a Diesel Exhaust Gas Heat Exchanger for Truck Applications with Conventional and State of the Art Heat Transfer Enhancements," *Applied Thermal Engineering* Vol. 30(8) pp. 935-947.

Mosburger, M., J. Fuschetto, D. Assanis, Z. Filipi and H. McKee (2008). Impact of High Sulfur Military JP-8 Fuel on Heavy Duty Diesel Engine EGR Cooler Condensate. DTIC Documentp.

Munson, B. R., D. F. Young and T. H. Okiishi (1990), "Fundamentals of Fluid Mechanics," *New York* Vol. 3(4).

Nagavarapu, A. K. (2012), "Binary Fluid Heat and Mass Exchange at the Microscale in Internal and External Ammonia-Water Absorption."

Prabhakar, B. and A. L. Boehman (2013), "Effect of Engine Operating Conditions and Coolant Temperature on the Physical and Chemical Properties of Deposits from an Automotive Exhaust Gas Recirculation Cooler," *Journal of Engineering for Gas Turbines and Power* Vol. 135(2) p. 022801.

Rattner, A. S. and S. Garimella (2011), "Energy Harvesting, Reuse and Upgrade to Reduce Primary Energy Usage in the USA," *Energy* Vol. 36(10) pp. 6172-6183.

Roessler, D. M. (1982). Opacity and Photoacoustic Measurements of Diesel Particle Mass Emissions. SAE Technical Paper, 0148-7191p.

Saidur, R., M. Rezaei, W. Muzammil, M. Hassan, S. Paria and M. Hasanuzzaman (2012), "Technologies to Recover Exhaust Heat from Internal Combustion Engines," *Renewable and Sustainable Energy Reviews* Vol. 16(8) pp. 5649-5659.

Saiyasitpanich, P., M. Lu, T. C. Keener, F. Liang and S.-J. Khang (2005), "The Effect of Diesel Fuel Sulfur Content on Particulate Matter Emissions for a Nonroad Diesel Generator," *Journal of the Air & Waste Management Association* Vol. 55(7) pp. 993-998.

Salvi, A., J. Hoard, M. Bieniek, M. Abarham, D. Styles and D. Assanis (2014), "Effect of Volatiles on Soot Based Deposit Layers," *Journal of Engineering for Gas Turbines and Power* Vol. 136(11) p. 111401.

Salvi, A. A., J. Hoard, P. K. Jagarlapudi, T. Pornphaithoonsakun, K. Collao, D. N. Assanis, D. J. Styles, M. Abarham and E. W. Curtis (2013). Optical and Infrared in-Situ Measurements of EGR Cooler Fouling. SAE Technical Paper, 0148-7191p.

Semler, T., J. Bogue, S. Henslee and L. Casper (1982). Fouling of a Finned-Tube Diesel-Flue-Gas Heat Recuperator. Idaho National Engineering Lab., Idaho Falls (USA); Honeywell, Inc., Plymouth, MN (USA)p.

Shah, S. D., D. R. Cocker Iii, K. C. Johnson, J. M. Lee, B. L. Soriano and J. W. Miller (2006), "Emissions of Regulated Pollutants from in-Use Diesel Back-up Generators," *Atmospheric Environment* Vol. 40(22) pp. 4199-4209.

Sluder, C. S., J. Storey, M. J. Lance and T. Barone (2013), "Removal of EGR Cooler Deposit Material by Flow-Induced Shear," *SAE International Journal of Engines* Vol. 6(2) pp. 999-1008.

Sluder, C. S. and J. M. Storey (2008). EGR Cooler Performance and Degradation: Effects of Biodiesel Blends. SAE Technical Paper, 0148-7191p.

Sluder, C. S., J. M. Storey, S. A. Lewis, D. Styles, J. Giuliano and J. W. Hoard (2009), "Hydrocarbons and Particulate Matter in EGR Cooler Deposits: Effects of Gas Flow Rate, Coolant Temperature, and Oxidation Catalyst," *SAE International Journal of Engines* Vol. 1(1) pp. 1196-1204.

Staedter, M. A., K. Keniar and S. Garimella (2016), "Hydrodynamic Considerations for Optimal Thermal Compressor Design," *International Refrigeration and Air Conditioning Conference at Purdue*.

Storey, J. M., C. S. Sluder, M. J. Lance, D. J. Styles and S. J. Simko (2013), "Exhaust Gas Recirculation Cooler Fouling in Diesel Applications: Fundamental Studies of Deposit Properties and Microstructure," *Heat Transfer Engineering* Vol. 34(8-9) pp. 655-664.

Talbi, M. and B. Agnew (2002), "Energy Recovery from Diesel Engine Exhaust Gases for Performance Enhancement and Air Conditioning," *Applied Thermal Engineering* Vol. 22(6) pp. 693-702.

Tang, M., M. Shiraiwa, U. Pöschl, R. Cox and M. Kalberer (2015), "Compilation and Evaluation of Gas Phase Diffusion Coefficients of Reactive Trace Gases in the Atmosphere: Volume 2. Diffusivities of Organic Compounds, Pressure-Normalised Mean Free Paths, and Average Knudsen Numbers for Gas Uptake Calculations," *Atmospheric Chemistry and Physics* Vol. 15(10) pp. 5585-5598.

Tassou, S., G. De-Lille and Y. Ge (2009), "Food Transport Refrigeration–Approaches to Reduce Energy Consumption and Environmental Impacts of Road Transport," *Applied Thermal Engineering* Vol. 29(8) pp. 1467-1477.

Taylor, B. N. and C. E. Kuyatt (1994), "NIST Technical Note 1297 1994 Edition," *US Government Printing Office*.

Wang, L., R. Wang, J. Wu, K. Wang and S. Wang (2004), "Adsorption Ice Makers for Fishing Boats Driven by the Exhaust Heat from Diesel Engine: Choice of Adsorption Pair," *Energy Conversion and Management* Vol. 45(13) pp. 2043-2057.

Wang, T., Y. Zhang, Z. Peng and G. Shu (2011), "A Review of Researches on Thermal Exhaust Heat Recovery with Rankine Cycle," *Renewable and Sustainable Energy Reviews* Vol. 15(6) pp. 2862-2871.

Warey, A., A. S. Bika, D. Long, S. Balestrino and P. Szymkowicz (2013), "Influence of Water Vapor Condensation on Exhaust Gas Recirculation Cooler Fouling," *International Journal of Heat and Mass Transfer* Vol. 65 pp. 807-816.

Warey, A., A. S. Bika, A. Vassallo, S. Balestrino and P. Szymkowicz (2014), "Combination of Pre-EGR Cooler Oxidation Catalyst and Water Vapor Condensation to Mitigate Fouling," *SAE International Journal of Engines* Vol. 7(1) pp. 21-31.

Whitaker, S. (1972), "Forced Convection Heat Transfer Correlations for Flow in Pipes, Past Flat Plates, Single Cylinders, Single Spheres, and for Flow in Packed Beds and Tube Bundles," *AIChE Journal* Vol. 18(2) pp. 361-371.

Yost, D. M., D. A. Montalvo and E. A. Frame (1996). Us Army Investigation of Diesel Exhaust Emissions Using JP-8 Fuels with Varying Sulfur Content. SAE Technical Paper, 0148-7191p.

Zhan, R., S. T. Eakle, J. W. Miller and J. W. Anthony (2009), "EGR System Fouling Control," *SAE International Journal of Engines* Vol. 1(1) pp. 59-64.

Zhang, R., F. Charles, D. Ewing, J.-S. Chang and J. Cotton (2004). Effect of Diesel Soot Deposition on the Performance of Exhaust Gas Recirculation Cooling Devices. SAE Technical Paper, 0148-7191p.